Microstructural Control in Inconel 718 Manufactured by Laser Powder Bed Fusion

Elaine Livera

Thesis submitted for the degree of Doctor of Philosophy

Department of Materials Science and Engineering

The University of Sheffield

October 2023

Abstract

Additive Manufacturing promises intricate and high performance parts to be manufactured with less waste. However, more research is required into defect and temperature control in complex geometries, as well as on the production of functionally graded parts.

This thesis covers the initial concepts of a new method of achieving a homogeneous temperature distribution in a complex part by cutting laser hatch lines in to mini hatches and allowing a different set of laser parameters to be assigned to each hatch. This method should also allow for the generation of parts with consistent quality that contain microstructurally and mechanically distinct regions.

Further to this, a new method of achieving alternate microstructures using the additive manufacturing process has been investigated in Inconel 718. Traditional additive manufacturing produces a microstructure that comprises of long columnar grains. This new method exploits lack of fusion and keyhole defects as well as unmelted powder present in the central region of a printed component in order to generate a wide range of microstructures after hot isostatic pressing. As well as enabling a variation in tensile properties to be achieved in a multi-microstructural part, this method has been shown to be able to produce components using a fraction of the time and energy required in a standard additive manufacturing build.

These findings have implications for the broader field of additive manufacturing, with increased consistency providing a route for simpler part qualification in safety critical industries, and microstructural control providing a higher level of material functionality in complex parts.

Acknowledgements

Thank you so much to Jamie for always being there and always telling me that it (whatever 'it' is changes on a daily basis) will be fine, and forever being up for whatever crazy adventure we decide to go on that day. If not for Jamie, I wouldn't have stuck this out! I also want to thank Frances for being an awesome sister who knows me inside and out. I can't think of a more caring, and emotionally and scientifically adept, woman – Doing the same PhD as your sister definitely helps you get through it. Thanks also to my parents who have always supported me, and been there for me, no matter what. I love you all.

A massive thank you goes to Kathy for (everything!) providing endless guidance and answers to all the questions I have, and Iain for always being optimistic and enthusiastic. Felicity also deserves a huge thank you for always taking time to talk through all my weird and wonderful worries, chilling me out a little, and helping find a solution to any issue that came up. Our office was always a fun place and it made coming in every morning not a chore - a huge shout out goes to all the friends I wouldn't have had if I had not done this PhD; Lucy (whose near constant positivity has made all the difference during this PhD, and who doubles as an amazing conference buddy and amazing friend – I can't wait to see how far you can go!), Kavi, George, Lova, Original Alex, New Alex, Hugh, Connor, Henry, Fran, Josh, Ben, Martin, Jonah, Matt, and Will for always being up for an office chat in the middle of the afternoon. I appreciate it all more than you will ever know.

Thank you goes to several people who have helped me in the lab; George (now Dr Maddison) for answering so many Aconity questions and coming to the rescue when the errors start popping up, Dr Vahid Nekouie, Richard Pears, Will Pulfrey, and Jorge Elkin (University of Sheffield) for performing multiple HIP cycles for me, Neil Hind and Lisa Hollands (University of Sheffield) for performing the heat treatment procedures, Dr Le Ma (Sorby Centre for Electron Microscopy, University of Sheffield) for collecting some of the first raw EBSD data, Zilei Chen (PhD Student, University of Sheffield) for helping me run the DIC equipment and tensile testing, Rob Hillier (Master's Student 2022/2023) for preparing and imaging a number of melt pool samples, Jonah Shrive (PhD Student, Modern AlChEME Group) for helping with the etching of my samples as well as my first SEM and EDS sessions, Dr Geoff West (University of Warwick) for producing my TEM samples, James Miller (PhD Student, University of Cambridge) for producing some stunning TEM images.

This work was supported by the UK Engineering and Physical Sciences Research Council [EP/L016273/1], the Advanced Metallic Systems Centre for Doctoral Training, the Manufacture using Advanced Powder Processes (MAPP) EPSRC Future Manufacturing Hub EP/P006566/1, and by Solar Turbines Incorporated. Access to the Aconity3D Mini at The University of Sheffield was granted by the Henry Royce Institute for Advanced Materials, funded through EPSRC grants EP/R00661X/1 and EP/S019367/1.

I wanted to share a quote that one of the most amazing people in the world lived by: "If they respect you, respect them. If they disrespect you, still respect them. Don't allow the actions of others to decrease your good manners because you represent yourself, not others". Jess died suddenly in late December 2020 and I spend every day trying to live up to the goodness that she radiated on a daily basis. She was kind, loyal, thoughtful, and extremely intelligent. Just a reminder for anyone who happens to stumble across this message – **be more Jess**.

Contents

List of Abbreviations

Abbreviation	Description
CAD	Computer Aided Design
CCD	Charged-Coupled Device
CMOS	Complementary Metal Oxide Semiconductor
CSL	Coincident Site Lattice
CSRX	Continuous Static Recrystallisation
CT	Computed Tomography
CTE	Coefficient of Thermal Expansion
DED	Directed Energy Deposition
DOE	Design of Experiments
DSRX	Discontinuous Static Recrystallisation
EBSD	Electron Backscattered Diffraction
EDM	Electrical Discharge Machining
FCC	Face Centred Cubic
FDM	Fused Deposition Modelling
FIB	Focused Ion Beam
FOV	Field of View
GAM	Grain Average Misorientation
GBE	Grain Boundary Engineering
GOS	Grain Orientation Spread
HAGB	High Angle Grain Boundary
HIP	Hot Isostatic Press
HT	Heat Treatment
IPA	Isopropan-2-ol
IPF	Inverse Pole Figure
KAM	Kernel Average Misorientation
LAGB	Low Angle Grain Boundary
LOF	Lack of Fusion
LPBF	Laser Powder Bed Fusion
PBF	Powder Bed Fusion
SAED	Selected Area Electron Diffraction
SEM	Scanning Electron Microscope
TEM	Transmission Electron Microscope
UTS	Ultimate Tensile Strength
VED	Volumetric Energy Density

List of Symbols

Symbol	**Description**	**Units**
P	Laser Power	W
v	Laser Velocity	mms^{-1}
A_b	Laser Beam Area	μm^2
r_b	Laser Beam Radius	μm
D	Laser Beam Diameter	μm
l	Layer Thickness	μm
h	Hatch Spacing	μm
${E_o}^*$	Normalised Equivalent Energy Density	-
A	Absorption Coefficient	-
ρ	Density	kgm^{-2}
C_p	Specific Heat Capacity	$Jkg^{-1}°C^{-1}$
T_0	Room Temperature	K
T_m	Melt Temperature	K
T_L	Actual Liquidus Temperature	K
T_e	Equilibrium Liquidus Temperature	K
ε^*	Strain Parameter	-
E	Young's Modulus	Pa
I	Second Moment of Inertia	m^4
F	Fourier Number	-
α	Thermal Diffusivity	m^2s^{-1}
L	Characteristic Length	m
H	Heat Input per Length	-
t_{int}	Interaction Time	s
G	Temperature Gradient in the Liquid	Km^{-1}
R	Solidification Growth Rate	ms^{-1}
θ	Contact Angle	-
Δm	Mass Change	g
w_0	Initial Mass	g
w_t	Mass at time t	g
s_0	Surface Area	mm^2

1 Introduction

1.1 Problem Statement

In present day industry, innovation is largely driven not only by performance but also through waste reduction and increased efficiency. These pose monetary risks and, where already functioning components have a good level of heritage and demand, there is little need, commercially, to drastically alter them. However, there is a constant drive to increase functionality and quality of existent parts, while delivering the product at the lowest possible cost.

The materials and processes used to manufacture these advanced engineering components plays a large role in keeping products as competitive as possible. For example, additive manufacturing (AM) allows the geometry of a component to be completely ‘free-form’, negating the need to design with expensive moulds or machining tool access requirements in mind, as well as enabling the alteration of material microstructure in specific locations in order to manufacture components with site specific properties. This method of processing product components therefore has the potential to greatly increase the functionality and quality of a product on the market. The additive nature of the process, as opposed to subtractive processes, also leads to less material waste, reducing the cost of production and waste management.

However, the AM process is highly complex. This is due to the fact that the heat dissipation within the built part, and therefore the processing conditions, fluctuate with every change in geometry. This makes control over the material microstructure difficult and can lead to the introduction of defects if the input process parameters are not monitored. A large body of work within the AM sector is focused on the *in-situ* monitoring and autonomous correction of process parameters. Although research in this area is still in its relative infancy, it is not difficult to predict the use case of this work for the manufacture of components with graded microstructures.

One example of a product in which AM could be used to create site specific microstructures and mechanical properties, leading to increased component efficiency and functionality is in gas turbine engines. Through various stages of compression, a high pressure gas is produced which is ignited with fuel before the combustion gasses are passed through several turbine stages. The rotation of the turbine produces work, some of which is used to spin the compressor, and the remaining portion is used to either generate energy or, in the more commonly known use of a gas turbine, produce thrust.

Both the compressor and turbine contain rows of stationary and rotating blades. The rotating blades found in the turbine section in particular are continuously exposed to high stresses at elevated temperatures in highly oxidative and corrosive conditions. The blade is made up of two very distinct sections, the airfoil, which experiences the hot gasses, and the blade hub, which slots in to the turbine disc (and rotating engine shaft) by means of a fir tree shape in order to hold it in place. It is clear here that the airfoil experiences directional loads at high temperatures, meaning it requires high directional strength as well as low thermal expansion coefficients and low creep rates. At the same time, the blade hub requires a different set of mechanical properties, high isotropic strength and toughness, particularly as fretting and fatigue can significantly limit the life of the fir tree root. Notionally, these properties can be obtained via the engineering of a fine, equiaxed metallic microstructure whilst the former properties, required in the airfoil, require larger and more elongated grains. In theory, these microstructures are a result of the solidification conditions imposed on the molten material; an aspect that is highly tailorable in metal AM.

This is only an example of a simple component that demonstrates the need for conflicting microstructures. In general, industry can benefit substantially from microstructure control, helping to both improve component performance as well as reduce the number of functional materials utilised, therefore also improving recycling potential.

1.2 Aims and Objectives

The overriding aim of this thesis is to demonstrate the ability to produce site-specific microstructural control and mechanical performance using AM. This then provides the base to introduce these processes in the design of specific components within a gas turbine, allowing the ever-evolving requirement for enhanced functionality and performance to be achieved.

The high-level objectives that need to be fulfilled to achieve this are:

- Identify a set of process parameters that will enable fully dense samples to be built in Inconel 718 using an Aconity Mini LPBF machine.
- Identify the sensitivity of each of the LPBF process parameters in terms of the density distribution, grain morphology and residual stress levels within each printed sample.
- Investigate and analyse a method of tuning the microstructure of a part using AM.
- Analyse the relative effects on mechanical properties for each designed microstructure.

1.3 Thesis Structure

In order to achieve the outlined objectives, several chapters of work have been produced. Chapter 2 contains a literature review in to metal additive manufacturing. More specifically, laser powder bed fusion. It covers topics such as the build process, controllable parameters, common defects that may be generated, methods of controlling the process and the printing of Inconel 718.

Chapter 3 contains the general materials and methods used throughout all the experimental chapters. Any experimental details that are unique to a given chapter have been outlined within those.

Chapter 4 is the first experimental chapter and contains experimental data on the selection process of a useable set of AM process parameters for all builds in this thesis. The sensitivity of the AM process has also been tested as part of this work.

Chapter 5 details the initial conceptual design of a new method of control in AM systems. This system is different to many control systems published in the literature. Along with this, the measured pyrometry intensity distribution of a set of initial experimental builds have been discussed.

Chapter 6 covers the work performed to explore a new technique of generating different microstructures within a single part in LPBF. This chapter contains a large volume of EBSD data showing differences in grain size, sub-grain misorientation, and twin structures between each microstructure produced.

Chapter 7 analyses the precipitate structures of each microstructure introduced in Chapter 6. This information is used to inform and explain the similarities in hardness attained for each microstructure. This chapter uses SEM, EDS and TEM analysis to identify differentiating characteristics for each sample.

Chapter 8 details both the tensile mechanical performance and oxidation performance of the various different grain structures produced in the previous chapter.

Chapter 9 contains the final conclusions and remarks about the thesis and how this work fits in with the wider body of AM research. A number of recommendations for further work have also been proposed.

2 Literature Review

2.1 Additive Manufacturing

Additive manufacturing (AM) enables whole three-dimensional parts to be manufactured in a single processing step. This is achieved by manufacturing the component layer by layer based on information provided by computer aided design (CAD) data that has been sliced in to thin layers [1], [2]. There are several different types of AM, all of which differ in their material processing capabilities. As such, each comes with their own specific advantages and limitations [3]. The variety of AM technologies available has made it possible to produce complex parts using a range of different materials such as metals, polymers and ceramics, and with significantly varied costs.

Fused Deposition Modelling, which operates by extruding softened plastic into a predefined shape, is likely the most well-known AM technology. Metal AM is a more complex process due to the elevated temperatures that need to be reached in order to melt the metal [4]. Therefore, the fundamentals of the process differ vastly [4]. However, with this additional complexity also comes increased potential functionality. This thesis will focus on achieving an increased level of functionality from the laser-based powder bed fusion (LPBF) metal AM process.

2.1.1 Advantages of Additive Manufacturing for Industry

AM has often been described as a disruptive technology due to the large number of impactful advantages it can provide. These include:

- Ability to manufacture parts on site when required, reducing storage requirements [5], [6].
- Producing less material waste than machining methods due to powder reuse [5].
- Reduction of tooling requirements and associated costs such as those required for casting and machining [5].
- Enabling high levels of design flexibility (thin walls, internal channels and overhang structures) which subsequently allows more complex and efficient geometries to be manufactured [7].
- Enabling multi part components to be manufactured in a single unit, reducing weight as well as reducing losses to cost and time associated with assembly operations [8].
- Potential for better component efficiency through the production of parts with spatially distinct mechanical properties and alloy compositions [4], [9].

Many companies, including General Electric Aviation and Airbus, already boast their AM capabilities in components such as fuel injectors for gas turbine engines, and antenna mounting brackets on satellites. Both AM parts have led to reduced assembly times and costs [8], [10]–[12].

2.1.2 Understanding the Limitations of Additive Manufacturing

Whilst the benefits of metal AM are impressive, it is a relatively difficult process to implement as a quality controlled manufacturing process. This is because the process is associated with a lot of controllable parameters, such as the more commonly known laser speed or power, and less commonly known, inert gas flow rate or atmospheric pressure [13]. If any of the controllable parameters are sub-optimal, defects are easily introduced to the part. These are usually impossible to detect from the outside of the part, necessitating costly and time consuming non-destructive evaluation.

Additionally, most parts are produced using a single set of 'optimum' printing parameters. These are determined using time consuming design of experiments (DOE) based on dissimilar geometries to the final part. As changes in component geometry affect the local cooling rates, it is possible that unknown variations in microstructure and defect populations can be produced across a complex geometry, or during the scale up from test piece to final component. This has the potential to spatially alter the mechanical properties of a component in a random manner. As every different material or alloy also has different thermophysical properties, a different set of process parameters is required for each new material printed [2], [14].

These issues make the qualification of AM parts for safety critical industries, such as the aerospace industry, challenging. The resolution of these issues is currently the focus of metallic AM research. In general, the research is divided in to the following sections:

- The development of monitoring and sensing capabilities to detect defects as a component is manufactured.
- The development of control algorithms that can predict the formation of a defect, and auto-correct the process parameters, in order to prevent this from occurring.
- Further developing the link between the input process parameters, component geometry, and post process treatments, on the mechanical performance of the material or component.

The work in this thesis sits at the intersection between the first and last bullet points. It will focus on the link between input process parameters and the resulting microstructures and mechanical properties, making use of material post processing and pyrometry intensity data collected during the build process. All of the work culminates to the manufacture of functionally graded and multi-modal microstructures using methods not possible without AM.

2.2 Laser Powder Bed Fusion

2.2.1 The Laser Powder Bed Fusion Process

In laser powder bed fusion, a laser source is used to melt a thin layer of metal powder (typically 30-50µm thick [15]) in a predefined shape corresponding to a 2D slice of a 3D component. Partial remelting of the previous layer ensures adequate fusion between layers which minimises defects in the component. Once a layer has been scanned, the build plate drops by the height of a single layer, a new layer of powder is deposited in the build chamber using a wiper blade, and the process repeats until the full part has been produced [7]. Once completed, the part is removed from the chamber and the surrounding powder is cleaned away. This is collected and recycled for successive builds [16]. The last operation is the removal of the part from the baseplate, which is usually performed using wire electro discharge machining (EDM).

The laser usually has a wavelength in the order of 1060-1080nm, and a power of 100-400W, but this depends on the machine used [13]. In order to scan the required 2D shape, galvanometers are used to direct the laser to the required position on the baseplate. The whole process operates under an inert atmosphere to prevent oxidation of the material [2], [15]. A schematic of the process is shown in Figure 1.

During lasing, the powder particles on the surface layer both absorb and reflect the laser deeper into the bed. This causes thermal energy to be imparted to the local area, melting all the material to a given depth under the surface. As the laser is continuously moving during this process, the molten region also moves across the surface of the powder bed, solidifying quickly when the laser has moved to a different position. Because of this, the melt pool is very small and usually takes the form of a teardrop, with a width of approximately 75-100µm, and a depth of about 50µm. This is highly dependent on the laser parameters and machine utilised, and both larger and smaller melt pools are common. The melt pool is immediately surrounded by cooled, solid material. This leads to the presence of large thermal gradients between the edges and centre of the melt pool [17].

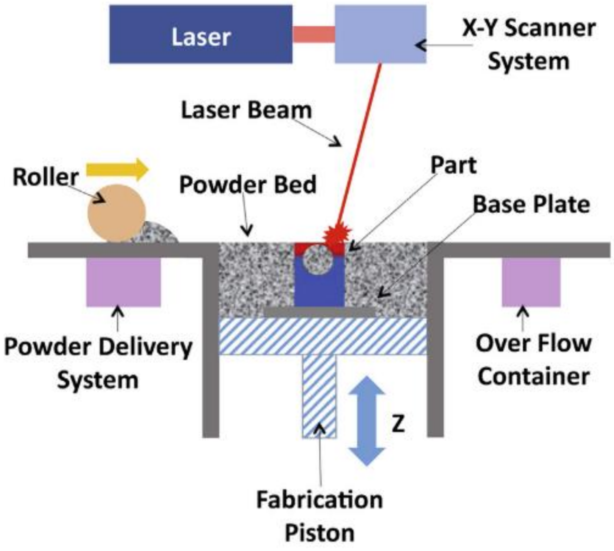

Figure 1: Schematic of LPBF process [18]**. During a build, the X-Y scanner changes the position of the laser beam on the surface of the powder bed, melting the powder. After a layer has been scanned, the build plate moves down by a distance set by the layer thickness, the powder delivery system moves up to dose a specific amount of powder, and the roller moves the dosed powder on to the powder bed. Any excess powder is rolled in to the overflow container. This process repeats until the part is completed. Reproduced with permission.**

As well as the large thermal gradients present, the high scanning velocities of the laser induce high cooling rates in the processed region. Although this is dependent on geometry, cooling rates of approximately 10^6 -10^8K/s have been reported [7]. This leads to rapid solidification resulting in the introduction of non-equilibrium solidification effects such as regions of supersaturated solid solutions separated by fine sub grain structures [7], [19]. As the previously solidified material acts as a heat sink, AM solidification structures grow in the build direction, and are therefore highly anisotropic. Each region then undergoes further thermal cycling within the space of seconds or milliseconds as subsequent layers are printed. As such, the microstructures obtained by LPBF are distinctive, and vary greatly from those obtained in the same material when processed in more traditional manner such as casting and forging.

2.2.2 Controllable Parameters in the LPBF Build

Although there are many controllable parameters in LPBF as detailed in [13], the main parameters typically discussed in LPBF are the laser power, beam diameter, laser scan velocity, hatch spacing and layer thickness [2], [13], [20], [21]. Some of these are shown schematically in Figure 2.

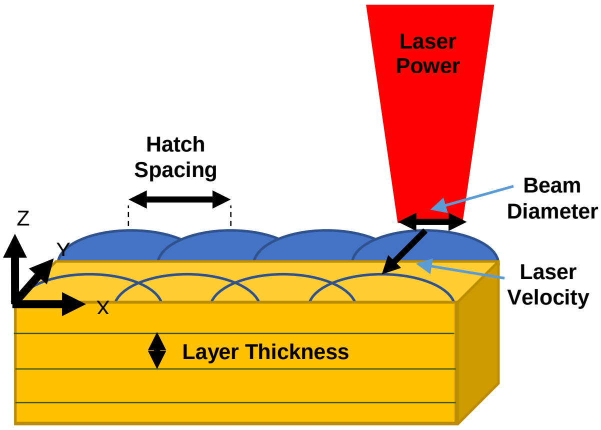

Figure 2: Main controllable process parameters in a LPBF AM build.

The laser power (P) is measured in watts and so is defined by the amount of energy provided to the powder bed per second. The laser beam diameter can be altered by moving the laser focal point relative to the laser. Depending on the machine used, the laser profile is usually either Gaussian or top hat in shape.

The laser scan velocity (V) is measured in mm/s and determines how quickly the laser is passed over the powder bed. This determines the amount of energy that is delivered to each voxel in the part. The laser scanning pattern used to melt each layer can be varied, however a back and forth raster scan is most common. Usually, the initial direction of the laser is rotated between each layer in order to achieve more homogeneous heating throughout the whole part cross section.

The hatch spacing (h) is measured in micrometres and determines the distance between neighbouring laser scan passes. At small distances, there may be excessive heat build-up in the material, and at large distances, the melt pool boundaries may not overlap, leading to unmelted powder.

The layer thickness (l) is usually determined by the powder size range in order to maximise powder utilisation. When using a range of 15-45μm, it is common to set a layer thickness of 30μm. Physically, this is the distance that the build plate moves downwards between each layer. This parameter can be altered as desired as long as the laser is able to melt the previously solidified material to form a strong bond between each layer.

Control of the size and shape of the melt pool is one of the most important aspects of the process. This is because the melt pool characteristics are determined by the local thermal conditions. If these can be kept constant so can the solidification behaviour, and subsequent mechanical properties, in the printed component [22]. This is achieved by implementing optimised printing process parameters for the machine, component geometry, and material used.

2.2.3 Additive Manufacturing Printability Maps

Due to the large amount of controllable parameters, a need was identified across the research society to unify and understand the effects of different combinations of these parameters on crucial aspects of the material.

For simplistic geometries, successful process parameters are typically described in terms of their collective energy density, however one standard method of calculating this is not available. Table 1 provides an overview of the different methods of calculating the energy densities used in the literature. By altering the applied energy density and relating these to the quality of the built part, conclusions can be drawn as to what energy density value should be used to manufacture a component.

Table 1: Different methods of calculating the energy density imposed on the material during LPBF

Description of energy density equation	Equation
Volumetric energy density (J/m^3) based on laser spot area [23] (or beam diameter [24])	$VED = \frac{P}{v\ x\ A_b}, \qquad where\ A_b = \pi\ {D_b}^2/4$
Volumetric energy density (J/mm^3) based on laser beam diameter and powder bed layer thickness [25]	$VED = \frac{P}{v\ x\ D_b\ x\ l}$
Volumetric energy density (J/mm^3) based on hatch distance and powder bed layer thickness [26]–[28]	$VED = \frac{P}{V\ x\ h\ x\ l}$
Linear energy density (J/mm) [26], [29]–[31]	$LED = \frac{P}{V}$
Normalised equivalent energy density [32]	${E_0}^* = \frac{q^*}{v^* l^* h^*} = \frac{Aq}{2vlh} \cdot \frac{1}{\rho C_p (T_m - T_0)}$

Printability maps are a way to display the limits of successful operation for a given material in terms of the applied energy density. These can then be used to compare the processing space for different materials [14], [32]–[34].

Thomas *et al.* [32] produced a modification of a process map initially created for continuous CO$_2$ laser welding for electron beam powder bed fusion [14]. Using dimensionless parameters, they proposed that the minimum energy per unit volume required to raise the temperature of a powder bed to the melting point per scan line is given by ${E_{min}}^*$ (Equation 1). In order to account for the hatch spacing in the analysis, the dimensionless hatch spacing, h^* (Equation 2), was also defined. The product of $\frac{1}{h^*}$ and

${E_{min}}^*$ gives the normalised equivalent energy density, ${E_0}^*$ (Equation 3). Higher values of ${E_0}^*$ indicate higher levels of heat input, with the possibility of causing part swelling and introducing keyhole defects [32]. Lower levels of ${E_0}^*$ lead to lack of fusion porosity due to insufficient heat input [32]. The process map is shown in Figure 3, and will be used extensively in Chapter 4.

$$\boldsymbol{{E_{min}}^* = \frac{q^*}{v^* l^*} = \frac{Aq}{2vlr_b} \cdot \frac{1}{\rho C_p (T_m - T_0)}}$$

Equation 1

$$\boldsymbol{h^* = \frac{h}{r_b}}$$

Equation 2

$$\boldsymbol{{E_0}^* = \frac{q^*}{v^* l^* h^*} = \frac{Aq}{2vlh} \cdot \frac{1}{\rho C_p (T_m - T_0)}}$$

Equation 3

Where;

q^* - dimensionless laser power

v^* - dimensionless laser velocity

l^* - dimensionless layer thickness

h^* - dimensionless hatch spacing

r_b – beam radius at focal point

A – surface absorptivity

T_0 – initial temperature of the material

q – laser power

v – laser velocity

l – layer thickness

h - hatch spacing

ρ – material density

C_p – specific heat capacity

T_m – melting temperature of the material

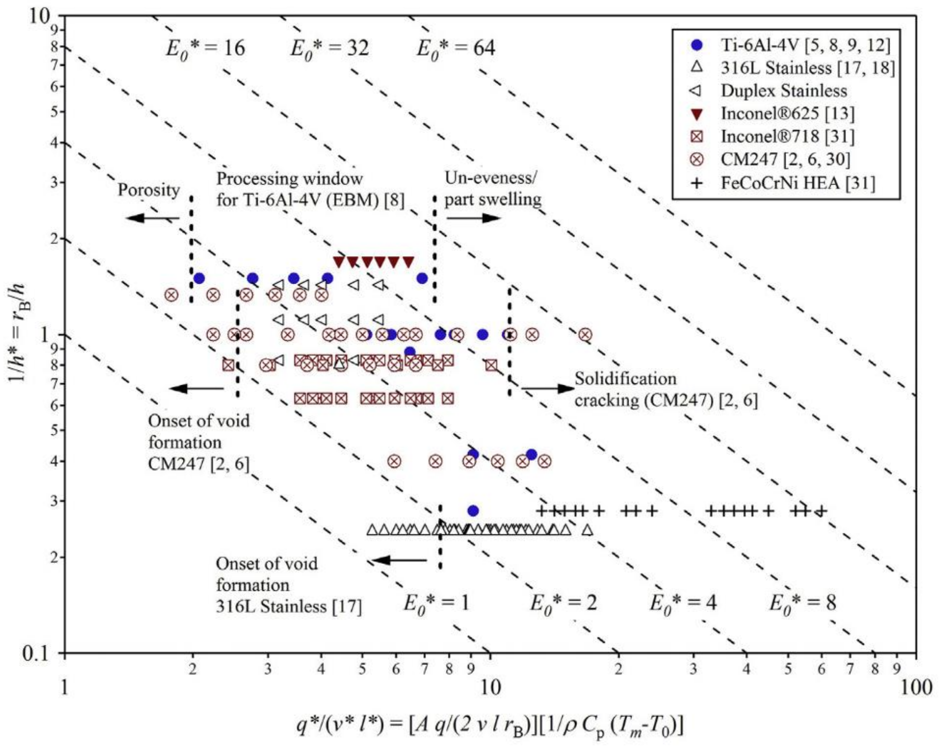

Figure 3: Alloy printability map for electron beam powder bed fusion showing the printability space for different materials [32]**. (Permission not required for reproduction).**

2.2.4 Defects in LPBF

Although process maps can provide assistance in selecting process parameters, they do not take geometry in to account and as such can only be used as a guide. The speed and turbulence associated with the melting process, as well as the complexity of heat dissipation through different geometries, make defects such as porosity, cracking, surface roughness and residual stress common in AM components. All defects cause the material to weaken and as they are largely stochastic in nature, they often lead to unpredictable mechanical properties. While post-processing stages like hot isostatic pressing (HIP) or machining can be used to improve component quality, this may not be possible for all unique or complex parts.

2.2.4.1 Porosity

Porosity can be introduced into a part due to several different means; incorrect processing parameters [35], changes in heat dissipation within specific build regions (e.g. inclined surfaces [23] or changes in geometry [22]), or by the feedstock powder [36]. The three main types of porosity observed in LPBF builds are gas porosity, keyhole porosity or lack of fusion porosity. These are shown in Figure 4.

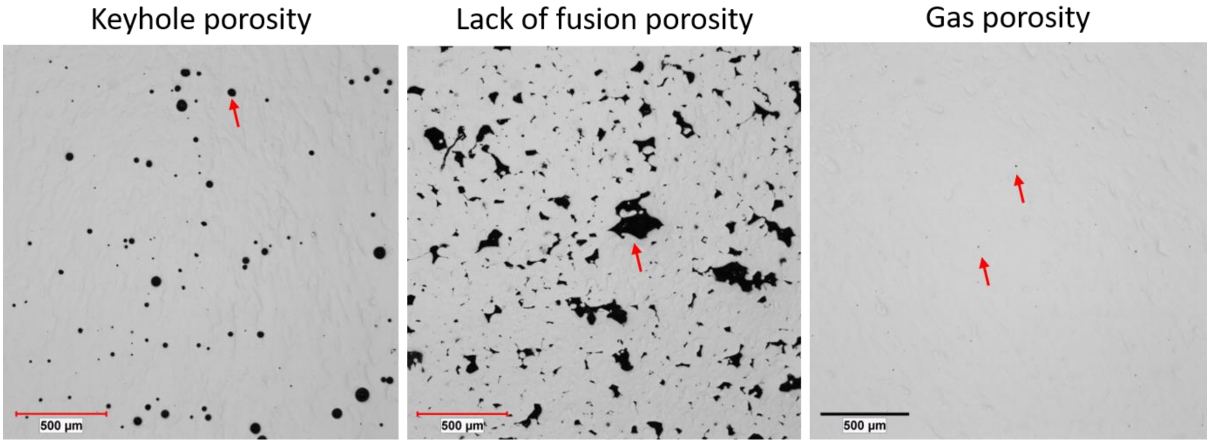

Figure 4: Examples of different types of porosity in Inconel 718.

Gas Porosity

As the powder utilised in LPBF is usually manufactured by gas atomisation, it is common for gas pores to be present within individual powder particles. Therefore, gas porosity is usually caused by the release of these gas bubbles when the powder melts. Gas porosity can also be caused when the inert gas from the surrounding build chamber is trapped by splashing melt pool flows during processing [36]. Due to the turbulent nature of the process, and the rapid solidification, these bubbles can become trapped within the melt pool [37]. Once present, the release of the gas bubble is dependent on the resulting effects of the speed of solidification, the melt pool convection and Marangoni forces, and the buoyancy forces acting on the bubble. Gas pores are typically small and spherical and can be observed even when lasing with optimum processing parameters. The position of these defects in the material is also unpredictable.

Keyhole Porosity

While the presence of gas porosity is relatively random in nature, keyhole porosity is caused by a local excess of input energy. The porosity can occur over a range of different sizes, and is commonly observed to be generally spherical in shape when analysed by 2D optical analysis. However, x-ray tomography by Kasperovich *et al.* [33] exposed that some keyhole pores can sometimes also have sharp internal edges that resemble ripples. In some cases, keyhole porosity can also take a more elongated shape, making it more difficult to distinguish it from lack of fusion porosity.

Upon an excessive energy input, usually caused by an excessive laser power, slow laser velocity or small hatch spacing, the molten material can vaporise. The expansion of the vaporised gas pushes away the local molten material and creates a deep cavity in the bottom of the melt pool [37], [38]. This allows the laser to reflect downward along the melt pool walls, enabling it to penetrate deeper into the previously processed material below. A schematic of this is shown in Figure 5. The intensity of the process can cause liquid on the top of the melt pool to be forced into the air. These can then land on the previously solidified melt track, producing spatter defects [37], [39], [40].

Turbulence within the melt pool can act to trap any gas bubbles formed during vaporisation making it difficult for them to escape prior to solidification. The keyhole pore is formed by the subsequent and sudden collapse of the molten material once the laser has passed. Fast solidification then traps this larger pore within the material as shown in Figure 5 [41], [42].

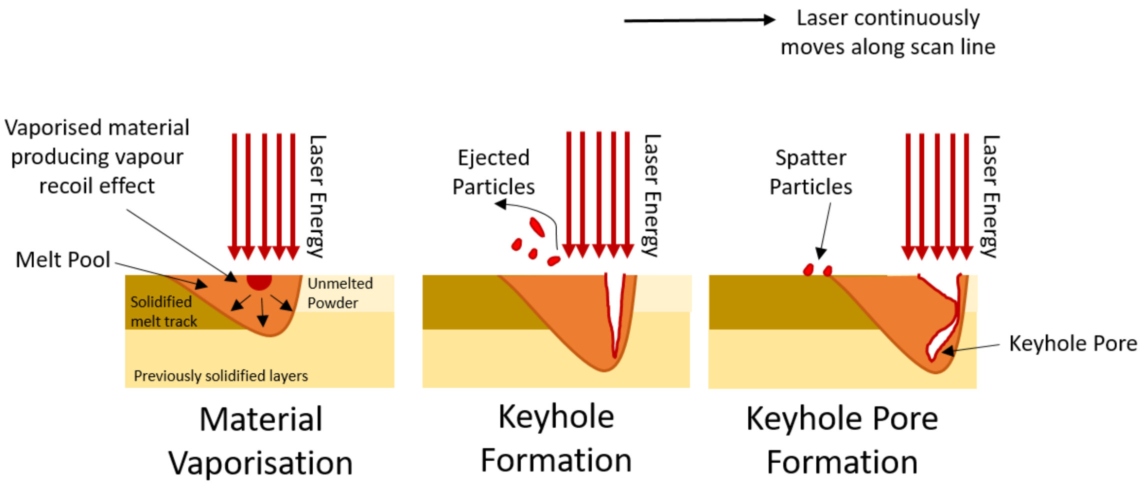

Figure 5: Schematic showing the process of keyhole formation. Under the application of excess energy input, the material may boil, producing a vapour bubble. The expansion of this bubble exerts pressure on the molten fluid, pushing it away and allowing the laser to penetrate deeper in to the material. As the laser moves on, the keyhole collapses, trapping the vapour bubble.

Lack of Fusion Porosity

Lack of fusion (LOF) porosity is produced when an insufficient amount of energy is delivered to the melt pool as a result of a low laser power, or a high scanning velocity, hatch spacing or layer thickness. Attenuation of the laser by the plasma plume that forms above the melt pool is also possible if the flow of protective gas travelling over the build surface is too low. This can cause LOF to occur even if the laser parameters are optimised [43].

LOF porosity is characterised by large, sometimes interconnected, and irregularly shaped, pores at the interface between adjacent layers or hatches [33], [44]. These defects also often contain unmelted powder particles [45]. Several different effects can occur as a result of the low applied energy. Firstly, a small, cooler, melt track is produced which exhibits high surface tension. This reduces the wettability of the molten region over the previously deposited layer leading to the introduction of open space between melt tracks. Secondly, LOF can be produced if the energy is not sufficient to penetrate the full height of the powder layer. Lastly, if the deposition of an even thickness of powder is impeded by things such as spatter particles [46], this can lead to regions whereby the layer is too thick for the laser to sufficiently melt the material, producing an uneven melt track.

Reducing Part Defects through Hot Isostatic Pressing

Generally, keyhole and LOF porosity can be eliminated by selecting appropriate AM process parameters for the material and geometry to be printed. However, as gas porosity can be caused by porosity in the powder feedstock, or by entrapment of the surrounding process gas, it may not be possible to eliminate all of these through process parameter optimisation.

Instead, it is common to apply a hot isostatic press (HIP) cycle. This form of post processing applies an elevated temperature and an isostatic pressure simultaneously. A schematic of a HIP is shown in Figure 6. The increased temperature reduces the yield stress of the material whilst the gas pressure leads to plastic deformation, squashing the pore. Subsequent atomic diffusion leads to the elimination of the previous boundary [47]. In some cases, the trapped gas diffuses into the material lattice, however this is dependent on the type of the gas. The plastic flow is aided by creep processes such as Nabarro-Herring creep, Coble creep, as well as dislocation creep [48].

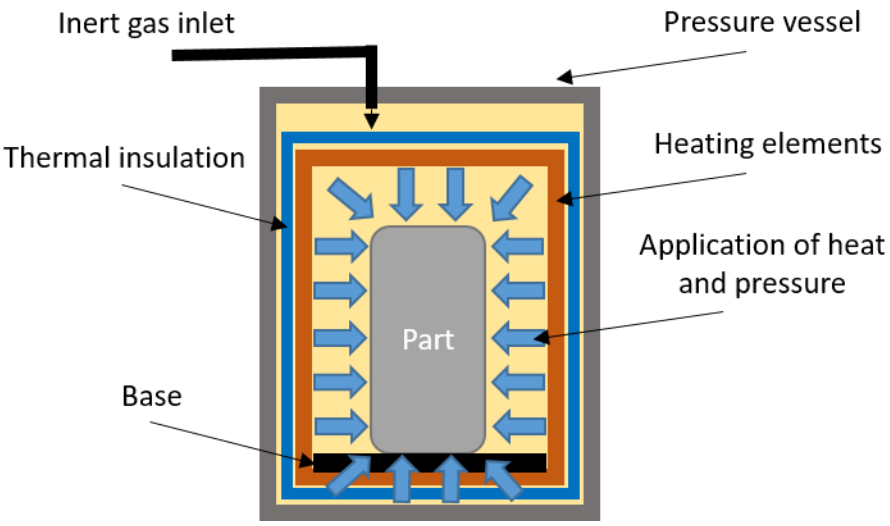

Figure 6: Schematic of a HIP [49]**.**

There are a few limitations of the process; Tillmann *et al.* [50] have found that when the gas is not able to be dissolved in to the lattice, the pressure due to expansion of the gas under elevated temperature can in some cases counteract the pressure induced by the HIP process meaning the pore will only shrink to the point at which the internal pore pressure equals the pressure due to HIP. Additionally, if the pore is connected to the surface of the component, the gas providing the isostatic pressure will infiltrate it, causing pressure equalisation between the pore interior and component exterior. This prevents the necessary plastic deformation from occurring [48], [51]–[54].

The reduction of gas porosity to below the resolution of high resolution x-ray computed tomography (CT) (<5µm) was achieved in two studies [51], [55]. Using a resolution of 8µm, Tillmann *et al.* [50] reported on a post HIP porosity of only 0.0019%. The reduction of Keyhole porosity (example, 0.298% to 0.0007%) and LOF porosity (example, 0.351% to 0.0039%) has also been shown possible by HIP [51], [56], as has the densification of encapsulated powder up to 2mm in diameter [51], [57]. Although precision to this amount of decimal places is unrealistic, it shows how little residual porosity can remain in the material after HIP.

HIP heat treatments are commonly followed by solution and aging heat treatments in order to enable precipitation strengthened alloys to reach their required mechanical properties. As gas porosity typically contains argon trapped from the LPBF process, which does not dissolve in to the metal matrix, the application of heat after HIP has been shown to cause porosity re-growth [51], [55]. However, if subsequent heat treatments are performed under isostatic pressure, regrowth can be reduced [57]. Although several papers have been written on the HIP process, it is difficult to ascertain under which conditions the trapped gas diffuses into the lattice or remains present in a single, compressed pore.

2.2.4.2 Surface Roughness

The LPBF process produces parts with a higher surface roughness than if the components were machined. This roughness produces regions of elevated stress under loading, leading to crack nucleation sites which significantly affect the mechanical properties of the material, particularly in terms of fatigue resistance [23]. Additionally, for components that require assembly joining operations, a tolerance exists on the maximum acceptable surface roughness. This is usually less than that of an as-built AM component. Therefore, machining of the AM surface is usually required. Several effects that increase the roughness of LPBF samples are presented below.

Swelling or Overbuilding

Overbuilding is observed by an increase in part height from the surface of the powder bed during printing. This may damage the wiper which prevents an even layer of powder from being deposited for future layers. The increase in part height also brings the component surface out of the laser focus region meaning less power is available to melt the subsequent layer. The phenomena of swelling have not been studied extensively in the literature, however from personal experience swelling can be caused by the presence of any of the following; keyhole or LOF defects at the sub-surface of the part or delamination in prior layers. Printing with parameters that cause keyhole or LOF defects cause instabilities in the melt pool which, along with delamination, causes the surface of the part to increase in roughness. This effect amplifies over a number of layers.

Stair Step Effect

The stair step effect is associated with surfaces built at an angle between 0-90^{o} from the build plate. It is caused by limitations in the resolution of the laser movement and layer height. As such, it is difficult for the laser to fill positions on an inclined surface in an analogue manner [19]. As build productivity is directly associated with the layer height, a trade-off exists between this and the surface roughness.

Edge Effects

Edge effects manifest as an increase in the height of the solidified material at the edge of a layer and are believed to be caused by a range of different mechanisms. As the thermal conductivity of the powder bed is lower than that of the solid part, less heat can be dissipated during the first scan line of a new layer. This creates a larger melt pool. Upon solidification of the next melt track, heat can dissipate down into the previously deposited layer, or into the neighbouring solidified melt track, producing a smaller melt pool. This effect creates a region of elevated material during the first hatch of each layer which can propagate throughout the height of the build [22], [58].

Edge effects can also be caused by the acceleration and deceleration of the laser at the start or end of a hatch, or due to the scanning pattern utilised. Because of these effects, the laser spends more time at these locations. Combined with the fact that the end of a hatch is surrounded by more powder which has a lower thermal conductivity, a larger melt pool is produced in these regions [22].

Edge Effects due to Powder Denudation

Edge effects can also be caused by powder denudation which is the clearance of powder from an area surrounding the laser scan path [59]–[61]. Therefore, while the initial scan line of a layer is able to melt the maximum volume of powder available to it, the denudation zone means that the second hatch is printed on a region with less powder, producing a smaller hatch.

The science behind powder denudation is complex and has been shown to be affected by several aspects of the AM process. These are, the surface tension and capillary forces that act at the interface between the powder bed and the melt track [40], [60], the argon pressure within the build chamber and the interaction between this and the plasma plume that forms above the melt pool [59], [62], and the interaction between the incident laser power and velocity with the plasma plume [61]. The exact mechanisms behind the formation of a denudation zone are not applicable to this literature review however the referenced papers provide insight if interested.

Hatch rotation strategies are implemented to prevent this geometric inaccuracy from always occurring at the same position as this would cause the part to swell out of tolerance in that location. This could result in potential damage to the wiper blade [58] and lead to an uneven deposition of powder for the subsequent layer.

Dross Formation on Overhang Structures

During the printing of an overhang, there is no solidified material directly under the top layer of powder. Due to the random packing nature of the powder bed, and the resulting fluctuation in thermal conductivity through it, the stability of the melt pool in these regions is much lower [63]. Regions of reduced conductivity lead to overheating of the melt pool, material vaporisation, recoil pressures, and the resulting ability for the melt pool to sink deeper into the powder bed before solidifying. This results in the formation of dross, whereby the bottom face of overhang regions exhibit a higher surface roughness than layers built directly on to previously solidified material [63]. It follows from this that the upper and lower faces of an inclined build show different levels of surface roughness [23]

Satellite Formation

Satellite formation occurs when particles from the surrounding powder bed are partially molten onto the sides of the built component producing a rough outer surface [23].

Spatter Formation

Spatter is caused when molten material that is splashed out of the melt pool lands on other regions of the printed part [37], [63]. These particles are usually larger than the layer thickness and can therefore impede the deposition of an even powder layer [40]. As this can occur at a random location on the cross section of a part, it can lead to the propagation of LOF defects throughout the centre of the part without these being visible on the surface of the component.

Balling

Balling is when the melt track breaks up in to disconnected beads behind the laser scan track [64]. Similar to spatter, this can increase the surface roughness of the layer as well as affect the subsequent deposition of an even powder layer, leading to LOF defects [64].

The defect manifests due to a variant of the Plateau-Rayleigh instability which causes ripples in the height of the melt track [65]. A smaller melt pool produces a shorter ripple pattern. At lower points in the ripple, the melt temperature is cooler and has a consequently higher surface tension. The Marangoni forces associated with the differences in surface tension lead to the melt track to split up into spherical balls [30], [37], [65].

At a specific power, an increase in velocity produces a narrower, elongated, melt pool that is both lower in temperature and has smaller ripples [64], [65]. This increases the likelihood of balling. Balling is also often observed where the laser energy cannot be conducted easily in to the bulk material such as at overhangs or thin geometries. In this case the melt pool becomes longer which can also lead it to separate into discrete droplets [22], [66].

2.2.4.3 Residual Stress and Cracking

Residual Stress

Components produced by AM usually have high residual stresses which are formed by the localised nature of the AM build process [67]–[69]. Rapid heating of a small region on the surface of a part causes material expansion. This is restricted by the cooler material underneath, and tensile stresses are produced in the surrounding material. If this stress is above the local yield strength of the material, it undergoes plastic deformation. When the material cools, it contracts producing tensile stresses, and becomes restricted by the regions of previously plastically deformed material below it. This causes compressive stresses to form in the underlying bulk [67]. As such, LPBF parts typically show tensile stresses in the top and bottom few layers with a large region of compressive stress in the centre [69]. The magnitude of these stresses in Inconel 718 can be on the order of GPa, and in line with the yield strength of the material [70]–[72].

As well as impacting the mechanical properties of a finished component, parts may warp or crack during manufacture [1], [73]. Warping during a build can affect powder recoating, enabling defect propagation throughout the height of the component, and can also lead to components falling outside required geometric tolerance values. Rotational scanning strategies [74], reduction in hatching lengths [69], reduction in layer thicknesses [75], utilising heated baseplates to reduce thermal gradients in the part [69], and performing post process heat treatments [72], have all been shown to reduce residual stress in AM builds.

Mukherjee et al. [9], [10] define a dimensionless strain parameter, ε*, shown by Equation 4, which describes the maximum thermal strain in an AM part due to the heat input during processing.

$$\boldsymbol{\varepsilon^{*}=\frac{\beta\Delta t}{EI}\frac{t}{F\sqrt{\rho}}H^{\frac{3}{2}}}$$

Equation 4

In this equation, βΔt is a volumetric change in the material due to AM heat transfer and t is the deposition time of the laser. Material constants E and I represent the flexural rigidity of the component printed, and ρ is the material density. The Fourier number, F, is the ratio of heat conduction to storage and a higher Fourier number represents more heat transfer than heat accumulation in the part leading to overall lower part temperatures and in theory, lower strain. In this equation, α is the thermal diffusivity of the material, and L is a characteristic length, in this example, the melt pool length. H is the heat input per unit length and is given by the ratio of laser power (q) to laser velocity (v).

The authors rationalise that as the heat input increases, so does the melt pool volume. The increased shrinkage as compared to a smaller melt pool produces more distortion and hence as the heat input increases, so does the strain. However, the increased distortion experienced by the part acts to reduce the residual stresses [75]. Therefore, by this theory, a higher heat input leads to a reduction in residual stresses.

Cracking

A variety of cracking mechanisms are also common within AM builds. A large body of research focuses on the ability to manufacture crack susceptible materials by AM. However, in order to explore the potential for microstructural control in this thesis, a crack resistant alloy was chosen, and so an in depth analysis of cracking mechanisms will not be discussed here.

2.2.5 In Process Monitoring Methods for LPBF

Whilst the AM process is highly complex, it is fairly simple to produce dense simple shapes with a set combination of process parameters. However, real components have intricate cross sectional geometries which, when processed using static process parameters, result in spatially varying thermal conditions. This leads to local variations in material microstructure and defect populations within a part. Without the use of in-process monitoring methods and techniques that allow process parameter control or variation during a build, the exact locations of these material property differences can only be identified using destructive testing. This is costly, and for a process that prides itself on complete geometric flexibility, it is an issue that requires resolving.

The presence of defects within a material or the formation of these during the LPBF process cause local variations in the melt pool behaviour and stability during lasing. These are referred to as 'Process Signatures' [13], and by monitoring these, more detailed information on the quality of AM parts can be recorded [13], [76] [77]. These process signatures can then be used to determine optimised parameters for different geometries as well as implement self-correcting control strategies that are capable of altering the process parameters *in-situ*.

The main process signatures, shown in Figure 7, are [13]:

- Reflected and/or scattered light from the laser [13].
- Radiation of thermal energy from the melt pool at a specific wavelength; usually corresponding to the melt temperature [78].
- Emission of radiation from the plasma plume generated around the laser due to the vaporisation of metal and ionisation of the inert gas in the build chamber [78]

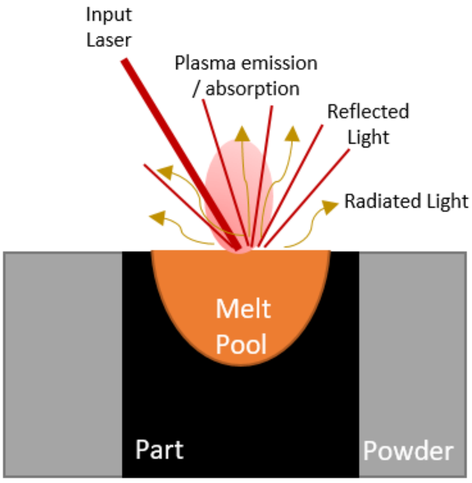

Figure 7: Process Signatures observed in LPBF. Modified from [13] **(Permission for modification not required).**

These process signatures are typically monitored either in line with the laser optics, which allows the melt pool to be followed during lasing, or from a set distance away from the build area, allowing the whole build region to be monitored [13]. The sensors utilised are typically divided in to spatially integrated, where the measured signal is summed to a single value (pyrometer), or spatially resolved, whereby a map of different light intensities can be visualised over a field of view (camera) [13]. Spatially resolved sensors provide a higher level of information than spatially integrated sensors, however, they generate a very large amount of data which is difficult to process quickly.

2.2.5.1 Methods of Monitoring of Process Signatures

This section will focus on the various methods of detecting process instabilities. Good review papers have been published on this topic [13], [15], [79], [80] and only a limited review relevant to this work is presented herein.

Pyrometry and Optical Cameras

Both pyrometers and optical cameras allow for high frequency non-contact data collection of the thermal radiation from the surface of a material [13], [80]. They transform the light emitted off the surface of the melt pool to a voltage signal which is proportional to the relative temperature of the melt pool [81]. Out of all the sensing methods, the use of pyrometers, photodiodes, and optical cameras is the most popular in research studies.

Measurement of Light and Heat Radiated from the Melt Pool

Both the intensity and wavelength of the radiation emitted from an object indicate the temperature of it. A black body is a perfect emitter and absorber of radiation, whilst real objects both radiate and reflect thermal radiation. The radiative performance of real objects is usually given by their emissivity, which is the radiative performance of that object compared to a black body. Emissivity varies between 0 and 1, where 1 is the value given to a black body.

When a sensor detects the radiation coming from an object, it is detecting both radiated and reflected light. In order to determine the amount of radiation directly emitted from the object, the emissivity needs to be known. However, the emissivity of an object changes with material, temperature, material state, and surface finish, and therefore it is very difficult to estimate the emissivity of the melt pool during AM [82].

This means that it is difficult to report results obtained from pyrometry and optical camera set-ups in terms of absolute melt pool temperature values. One method to overcome this issue is to measure the intensity of the emitted radiation at two different, but similar, wavelengths. By taking the ratio of intensities, using an equation detailed by Hooper in [82], it is possible to calculate the absolute temperature [82]. This setup requires double the expense in terms of sensor technology and so the majority of researchers present their results in terms of a ‘relative’ intensity value using a single sensor [81], [83], [84].

Melt Pool Morphology and Temperature Measurements

Since the early 2000s, the team at KU Leuven have been developing their sensing capabilities on a self-built LPBF machine [83]. Their setup, shown in Figure 8, includes two sensors mounted coaxially with the laser; a high speed, near infra-red CMOS camera, and a silicon photodiode [22].

This setup was used to analyse how different factors such as neighbouring scan tracks, overhangs, and acute corners, affected the melt pool area, length and width, and therefore the build quality [22]. Figure 9 shows how the length of the melt pool increases during the lasing of an overhang. Balling due to the increased length to width ratio of the melt pool was found to be the reason for increased roughness at the underside of an overhang region [22]. By comparing the spatially integrated photodiode output with a predetermined set point value, and through the use of a feedback loop with a proportional-integrative controller, the laser power was adjusted *in-situ* to reduce the dross formation on the underside of an overhang structure [85]–[87]. The setup was later integrated with a data processing algorithm that allows the whole build area to be mapped and analysed. This allowed the position of pores in the built part to be visually identified [83] as well as providing a map of overheated regions during the lasing of overhangs [84].

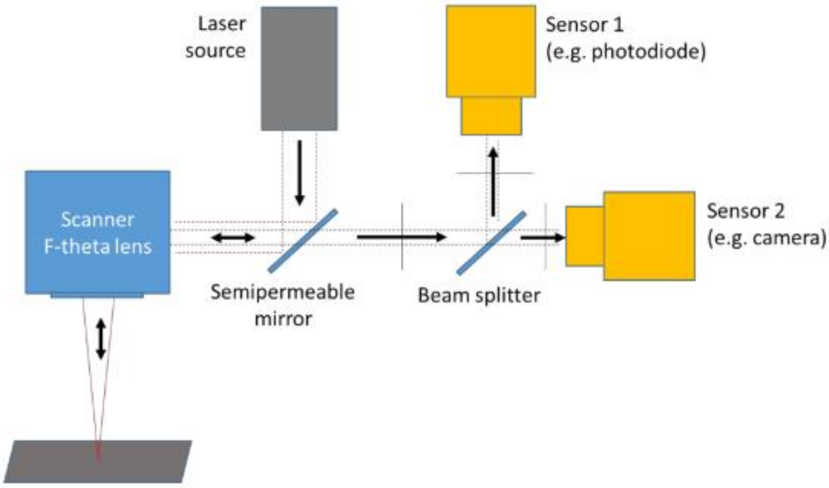

Figure 8: Sensing setup utilised at KU Leuven [15], [88]**. Reproduced with permission from both sources.**

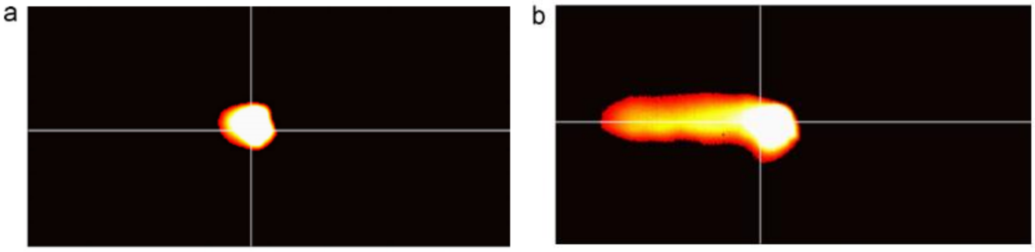

Figure 9: Melt pool images taken a)powder layer supported by solid material, b) powder layer at an overhang (not supported by solid material) [22]**. Reproduced with permission.**

A lot of similar studies were conducted by other groups to analyse the melt pool temperature values [81], [89], observe spatter evolution during lasing [90], [91], infer defect populations [92], [93], and understand the warping and generation of edge effects in built parts [66], [94]. Hooper [82] was able to image the melt pool shape and actual temperature distribution by recording the emitted light at two different wavelengths as shown in Figure 10.

Data analysis using physics based, statistical, and machine learning methods has also been explored in order to detect or predict anomalies such as intentionally placed defects, or regions of overheating at overhang structures [92], [93], [95], [96]. In one case, a correlation between defect volume and material elongation was identified [92]. One interesting use of *in-situ* collected pyrometry data proposed a closed-loop control system on a directed energy deposition AM machine which did not alter laser power or velocity, but instead altered the hatch deposition order in order to prevent the deposition of hatches at a location when the temperature was still above a set point [97]. This led to the production of a more uniform microstructure and hardness over the printed component.

Interestingly, in one report when a predicted defect population was compared to x-ray computed tomography (XCT) data, a large number of false positives were identified. The authors attribute this to defects that were 'healed' by subsequent layer depositions, and therefore no longer visible in the CT scan [93]. This is an important consideration, especially when predicting the presence of defects in a material that has been manufactured in an overlapping layer-wise nature.

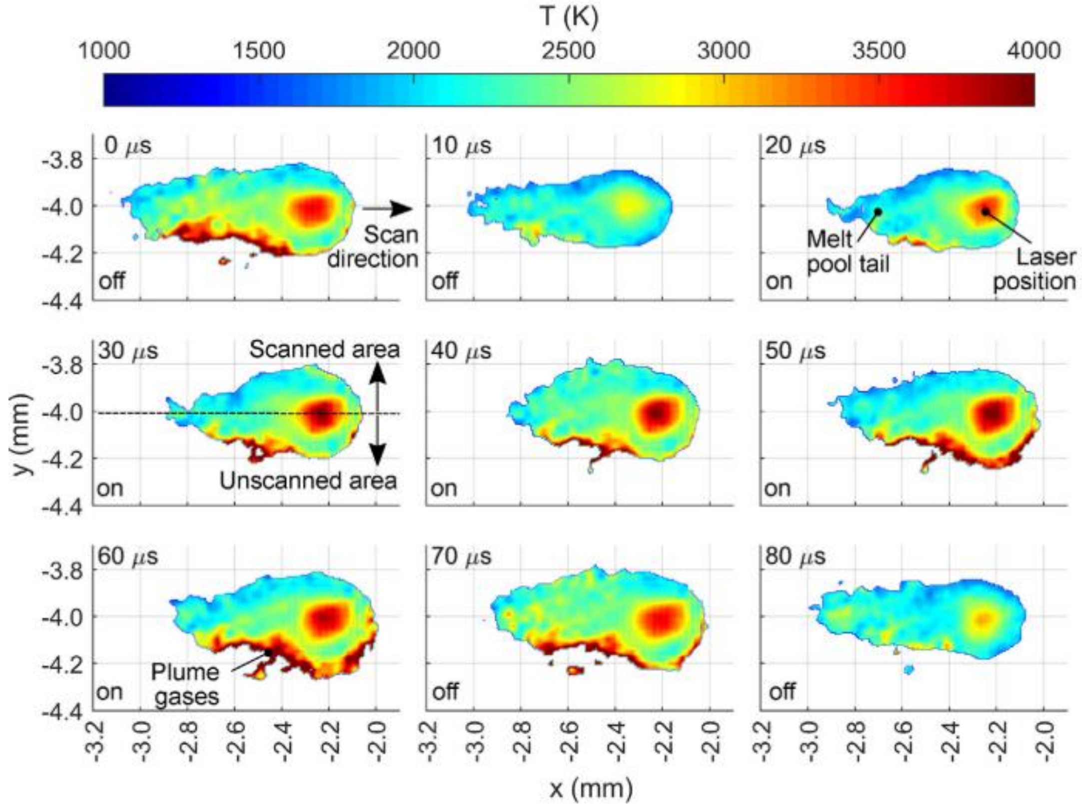

Figure 10: Temperature of melt pool surface during a single laser pulse of a hatch scan (using a pulsed laser). Laser turned on at 13µs and off at 68µs. The "on" and "off" labels show if the laser was on or off [82]**. Permission for reproduction not required.**

Interferometry

Interferometers can be used in LPBF to measure the variation in height of the surface of a part or powder bed by analysing the interference between two light signals that have originated from a single source and split using a beam splitter. One of the beams is reflected using the laser optics to the focal plane of the build, while one beam is used as a reference. The light reflected off the sample is compared to the reference light signal. Any differences between the distance travelled by the first beam and the reference beam causes constructive or destructive interference. This information can be translated to an electrical signal and provides information on the height of the build or powder bed at different locations which is not possible using optical cameras or devices capable of thermal measurement [63], [98]–[100].

Figure 11 shows that the electrical signal derived from the interference between the two light beams allows the height of a region on the built surface to be visualised. The intensity of the reflected beam also provides information on the physical state of the material at that position. This is because powder does not effectively reflect light, whilst molten metal does, producing a difference in the intensity of the reflected light. The powder bed is shown by the low intensity region at beam positions between 0-350µm. The lower height, but high intensity, region at ~450µm shows the denudation zone next to the melt pool. This has a high intensity due to reflection of the light off the solidified metal revealed by the denudated powder. Between 450-1000µm, the imaged material is molten. The interface between the molten and solid material is given by the reduction in intensity at beam imaging position ~1000µm [99]. In this example, the loss of signal at the inclined edge was due to balling. Kanko *et al.* [99] showed the applicability to correlate melt pool stability to that of the solid track, but no closed loop feedback system has been identified for this method.

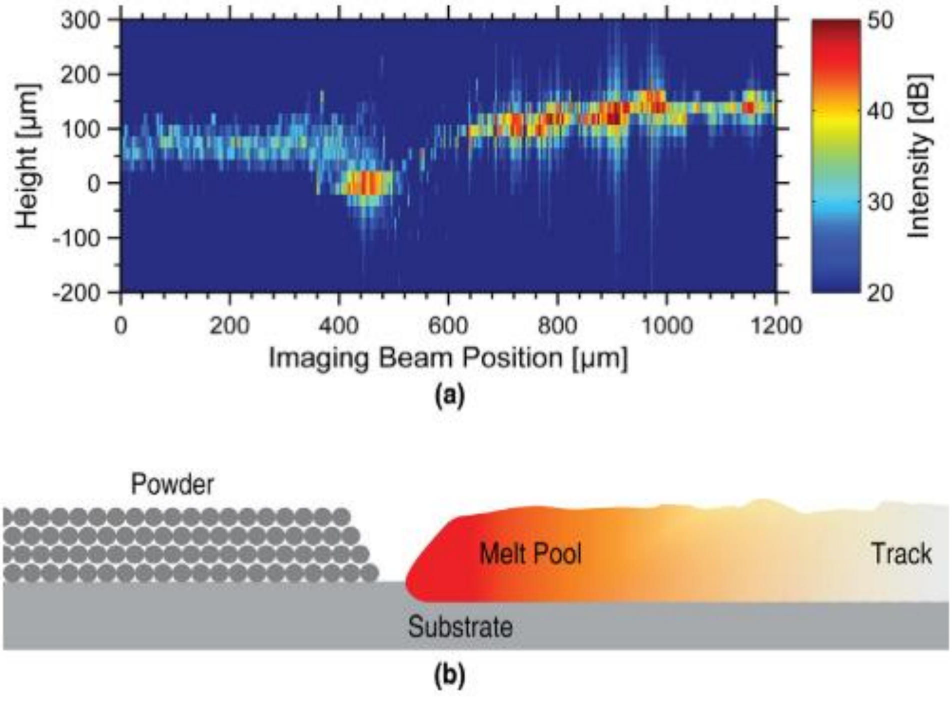

Figure 11: Height map produced as imaging beam is scanned in the opposite direction from the laser scan head; from ahead of the melt track (in the powder bed), through the denudation zone, melt pool, and further through the solidified melt track. Both the phase and intensity of the backscattered light provide valuable information to determine the surface morphology of the melt track [99]**. Reproduced with permission.**

Optical Emissions Spectroscopy

Due to the high power energy input in AM, it is common to vaporise material in the melt pool, producing a gas plume that contains a mixture of electrons and metal ions [101], [102]. Absorption of laser energy by an electron in an ionised metal atom enables it to move to a higher energy orbit in the metal atom. The subsequent movement of the electron back to a lower energy orbit results in the emission of a photon. The wavelength of this photon is given by the difference in energy between the two electron orbitals. By designing a filter capable of collecting only photons of a given wavelength, the amount of ionised material corresponding to a specific element can be captured. From this, the temperature of the material being processed can be inferred. This technique has been used in combination with complex algorithms to understand the location and number of pores in a built part [101], [103]. Like pyrometry and optical cameras, this method has the potential for closed-loop control due to the relative simplicity of the setup.

Summary

The hardware capabilities for all of these sensing technologies are readily available, and have been shown to be capable of detecting process instabilities during a LPBF build. This also means that they may be helpful in the production of components with functionally graded microstructures.

Although some studies report on the use of advanced methods of feature extraction from the collected data as well as machine learning algorithms to predict the location and quantity of defects, the majority of papers published so far only present the possibility of 'viewing' process instabilities using the different sensors. The majority also do not present a method of utilising the set-up for closed loop control. It is clear that while process monitoring systems exist, the current gap in the knowledge is finding methods to extract information from the large data sets quickly enough to allow for *in-situ* corrections to take place.

In addition to this, it is clear from the literature that in general, the long term aims of the use of these monitoring capabilities is to enable closed loop control whereby an algorithm detects process 'flaws' and alters the input parameters on the fly in order to correct these. However, there is currently an insufficient amount of information available about how the process parameters affect the material structure and so only an estimate of the correct parameters can be made for self-correction. In addition to this, allowing an algorithm to alter process parameters may result in otherwise identical positions on identical parts being produced with different laser parameters. In an industrial setting these issues make qualification of parts produced using closed-loop systems very difficult. It would perhaps be smarter to work towards a solution which does not rely on on-the-fly parameter selection, but instead focuses on the off-line combination of monitored signals and physics based calculations in order to produce a set build file that is capable of ensuring minimal defect populations are formed. Repetition of the same build file would then allow for identical geometries to be printed with identical process parameters.

2.3 Superalloys and Inconel 718

Superalloys, initially derived from stainless steels, are a class of nickel, cobalt or iron-based metals which have high creep, fatigue and oxidation resistance at temperatures higher than 60% of their melting points, and often utilise strengthening superlattice precipitates to achieve a remarkable combination of mechanical properties [104]. It is the nickel based superalloys which are now primarily used in the turbine sections of gas turbine engines in order to enable ever increasing engine efficiencies [104], [105].

Inconel 718 is one of the most common superalloys used in industry [106]. While some nickel superalloys with higher weight percentage of Al or Ti are susceptible to strain age cracking during welding, the relatively low fractions of precipitating phases as well as the slow precipitation kinetics of its strengthening phases, leads to good weldability [105], [107], [108]. As such, the material is used in many critical components such as jet engines, nuclear reactors and rocket engines [109].

However, the advantageous mechanical properties of Inconel 718 make them difficult to process by machining as this leads to high tool wear rates. Additionally, due to the large amount of alloying elements present in the material, it undergoes a high level of elemental segregation when cast. These factors provide a case for the use of AM in the production of components manufactured from Inconel 718. In addition to this, due to its high weldability, Inconel 718 is regarded to be a highly 'printable' material and so is often used in additive manufacturing research [108].

2.3.1 Microstructure of Conventionally Manufactured Inconel 718

Inconel 718 has the following nominal composition; 50-55%wt of Ni, 17-21%wt of Cr, 4.75-5.5%wt of Nb and Ta, 2.8-3.3%wt of Mo, 0.65-1.15wt% of Ti, 1wt% of Co, 0.2-0.8wt% of Al, and balanced with Fe [110]. The maximum proportions of other elements are as follows; 0.35wt% of Mn, 0.35wt% of Si, 0.3wt% Cu, 0.08wt% of C, 0.015wt% P, 0.015wt% of S, and 0.006wt% of Boron [110].

The alloy is primarily made up of an FCC γ (austenite)-phase matrix which is solid solution strengthened by Cr, Co, Fe, Mo, and Ta [107]. Cr and Al also enable a stable oxide film to form over the metal, providing the material with good oxidation resistance.

The γ-matrix contains a wide range of precipitates. Depending on the type, these precipitates can either increase or reduce material strength, and careful heat treatment and aging schedules are required to achieve the optimum microstructure.

The main strengthening phases in Inconel 718 are the coherent FCC γ' and the metastable BCT γ'' phases, with the latter being the more dominant strengthening phase in Inconel 718 [111]–[113]. The γ' precipitates have a chemical formula of Ni_3X, where X can either be Al, Ti, or Nb whilst the γ'' phase always has the chemical formula, Ni_3Nb. The formation of either the γ′ or γ′′ depends on the ratio of Al and Nb present in the alloy [113]. Inconel 718 has a defined wt% of these elements, which allows it to precipitate mostly γ′′ precipitates (~20%, compared to ~3% γ′, depending on the heat treatment chosen) [111]–[113]. A modification of Inconel 718 such as Allvac 718Plus contains a higher wt% of Al, enabling the γ‘ phase to dominate [114].

The γ′ phase is coherent with the γ matrix, with its lattice constant being very close to that of the γ matrix (less than 1% difference). This ensures a low interfacial energy between the lattices which means that precipitate growth during high temperature exposure is limited [115]. This lattice constant mismatch also makes it difficult for dislocations to pass through the matrix, enhancing strength [107]. The shape of the γ′ phase depends on the level of mismatch between it and the γ matrix; being spherical at low mismatch values and cuboidal at higher mismatch values. Although the low interfacial energy somewhat prevents extreme coarsening of the γ′ phase, at temperatures above $0.6T_{m,}$ the particles do coarsen, leading to a reduction in strength of the alloy [107].

The metastable γ′′ phase is the main strengthening precipitate in Inconel 718. It is disc shaped, and approximately 10nm in thickness with a diameter of 50nm [105]. Whilst cubic lattices have the same dimension across all edges, BCT crystal structures have one edge that is larger than the others as shown in Figure 12a [116]. Therefore, a larger lattice misfit exists between this phase and the γ matrix [107]. Although this is beneficial for strengthening the alloy, this also increases the interfacial energy, which causes it to coarsen when exposed to elevated temperatures in the range of 650-980^{o}C for extended periods of time. This can either be during service or due to inappropriate post process heat treatment schedules. Coarsening of the γ′′ phase leads to the transformation of it to the stable but incoherent δ phase (Ni_3Nb). Due to a consequential drop in the γ′′ volume, this transformation reduces the strength of the material [105], [107].

The presence of γ′ and γ′′ precipitates can be identified by TEM diffraction analysis as shown in Figure 12b and c. The large bright spots indicate the diffraction pattern from the FCC γ matrix, while the small spots surrounding these indicate the presence of γ′ and γ′′ phase precipitates in different orientations [117].

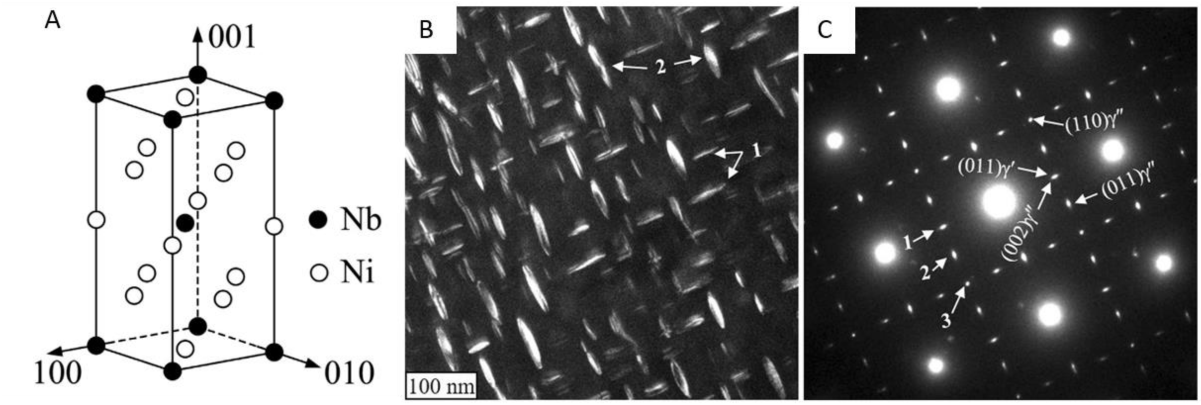

Figure 12: a) Body centered tetragonal (BCT) crystal structure of the γ'' phase [116] **(Reproduced with permission), b) dark field image of γ'' precipitates in the [100] zone axis and c) diffraction pattern from the <100> matrix zone axis** [117]**(Reproduced with permission). The spots indicated by 1, 2, and 3 indicate three different variants of the γ'' precipitates.**

As well as the δ phase, which dissolves at approximately 1000°C [105], other phases such as the Laves, μ and the σ phase can also be present. The Laves phase has a chemical formula of $(Ni,Fe,Cr)_2(Nb, Mo, Ti)$ and is usually introduced during solidification due to segregation of the slower diffusing elements such as Nb. The presence of this phase removes Nb and Cr from the γ matrix, which has knock on effects on the volume of these elements present for the formation of γ'', or a stable and protective oxidation layer [104], [107]. In addition to this, it is a very brittle phase, enabling easy crack propagation through the material. As such, it is detrimental to most mechanical properties of the material [107]. The μ and σ phases are topologically close packed intermetallic phases containing Cr and Mo that precipitate at grain boundaries [111].

Several forms of metal carbides and borides may also be present in the material, some of which take the form of MC, M_6C, $M_{23}C_6$, M_7C_3, and M_7B_2, where the M is the metallic conjugate and can be Nb, Ti, Cr, and Mo [105]. Their formation can be complex and specific to the metal carbide in question. For example, cubic MC carbides are usually formed at high temperatures during solidification from the liquid phase, and so are commonly identified at grain, or sub-grain, boundaries. Comparatively, $M_{23}C_6$ forms on the γ grain boundaries at lower temperatures, usually during extended periods of elevated temperature service, via the breakdown of MC carbides [105]. Ellingham diagrams show that MC carbides are typically the most stable and are made up of a mixture of Ti, Nb, and Ta, with Nb carbides being most typical in Inconel 718 [118]. If long connected chains of carbides are present at grain boundaries they reduce material strength by enabling easy crack propagation routes along grain boundaries.

Generally, all (δ, Laves, μ, σ, and carbide) additional precipitates are generally detrimental to the mechanical properties of the material. However, small amounts along grain boundaries can provide additional strength to the grain boundary region, and reduce grain growth at elevated temperatures [104], [107], [111], [119].

2.3.2 The Structure of Metal Lattices and their Evolution Upon Deformation and Heat Treatment

2.3.2.1 The Structure of Metal Lattices and Grains

Metals are made up of crystal structures which contain repeating units of atoms [120]. In metallic bonding, the electrons in the outer energy shell of each atom are free to roam throughout the material, leaving behind the positively charged ion. These 'free' electrons counteract the repulsive forces between each positively charged ion and as a result, enables the atoms to be bonded together, forming a lattice structure, whereby the smallest repeating unit of the structure is defined as the unit cell [120]. The bond energy between each atom is dependent on several factors including the atom size and charge, and the volume of 'free' electrons available. This factor determines the elastic properties of the lattice. For example, the Young's Modulus.

In a perfect lattice, an equilibrium spacing exists between each atom which is dependent on the magnitude of the local attractive and repulsive forces. However, discontinuities in the lattice structure occur in real materials, leading to either a local increase or decrease in the atomic spacing between atoms. These discontinuities are known as dislocations, and the number of these increases with external plastic deformation. The presence of dislocations have an associated energy cost whereby they prevent the material from exhibiting its lowest energy state.

On a larger length scale, a metallic component is rarely found in which the unit cells of a crystal lattice all observe the same orientation without imperfections. Clusters of unit cells of identical or near identical orientation are typically identified neighbouring clusters of unit cells all orientated in a different direction. If the neighbouring regions are of sufficient misorientation, the region dividing these is called a grain boundary. Grain boundaries are generally categorised in to high angle grain boundaries (HAGB) or low angle grain boundaries (LAGB) depending on the misorientation they accommodate. Usually a misorientation of greater than 10-15^{o} governs a HAGB [121]. These boundaries lead to free space in the material and therefore also contribute to an energy cost in the system.

2.3.2.2 Types of Strain in Metal Lattices

As part of Section 2.2.4 Residual Stress, we discussed the large scale stresses that manifest during the AM process and how these can negatively influence the geometric stability of the part. These stresses are caused by a nearly homogeneous level of strain across the full part in consideration [122].

In reality, a material made up of a crystal lattice is very complex and strain can occur on more than just one length scale. These are defined as Type I, Type II, and Type III strains [122]. The residual stress previously visited is caused by Type I strain. Type II strain occurs on the length scale of individual grains due to differences in the volume of external deformation that can be accommodated by grains of different orientation (defined by the relative orientation of the local lattice slip direction to the loading axis). For example, if one grain experiences deformation, whilst the other grain is not able to deform to a similar extent, this produces strains within the neighbouring grains to accommodate the differences in deformation. Whilst Type I strain occurs homogeneously over the whole part, Type II strain is observed to be inhomogeneous within the material.

As the presence of dislocations causes a local shift of atoms from their equilibrium spacing, this represents a third length scale over which material strain can manifest. This is termed Type III strain [122]. Owen and Jones [122] further define a fourth length scale, Type IV strain which manifests due to a local shift of a single atom from its equilibrium spacing. This type of strain is introduced by solid solution strengthening atoms.

Whilst residual stress as defined earlier is known to lead to part warping, the Type I strain causing this occurs over too large a length scale to aid in the explanation of the fine scale material evolution that occurs during post process HIP and heat treatment procedures of AM parts. Instead, we need to focus on the presence and evolution of the Type II and Type III strains in the AM part, both in the as-built condition and during post processing.

2.3.2.3 Dislocations in a Metal Lattice

The presence of dislocations leads to local regions of positive and negative lattice strain in the material. The lattice is not in its equilibrium position and therefore dislocations represent stored energy in the material. If multiple dislocations are present in close vicinity to each other, the local strain fields may interact. The stored elastic energy in the system due to the presence of the strain fields can cause the movement of dislocations. Depending on the local strain fields present, dislocations can either repel each other, or attract and eliminate each other [120], [123]. This movement typically occurs by slip over the closed packed planes. For the FCC structure, as adopted by Inconel 718, this is the {111} plane, and this plane includes three possible <110> slip directions. Due to the effects of symmetry, there are therefore 12 slip systems available to accommodate this dislocation movement [120]. The higher the volume of dislocations, the more strained the lattice becomes, and the less likely it is for a dislocation to be able to move along these slip planes in order to absorb the effects of external loading. Therefore, it is clear that the presence of dislocations in the lattice provides the material with strength.

When a metallic material is plastically deformed, two main mechanisms of dislocation generation occur within each grain. The first is the generation of more dislocations due to the interaction of a dislocation either with a lattice defect or a neighbouring dislocation. These are called statistically stored dislocations. In the second mechanism, dislocations are produced in order to maintain coherency within regions of the lattice that have undergone an orientation or geometry change in order to accommodate the new shape of the grain. These latter dislocations are called geometrically necessary dislocations (GND) [124]. These dislocations allow the grain to observe large orientation, and strain, gradients across its diameter. Therefore, as opposed to statistically stored dislocations, the GNDs are able to aid in the nucleation of recrystallised grains [125].

As plastic deformation progresses, more of each type of dislocation nucleates in the material, which in turn increases its strength (until material fracture occurs). This is termed work hardening. However, it is clear that this process also produces increasingly elevated levels of Type II and Type III strain in the lattice, leading to high inhomogeneous levels of elastic strain energy in the part [126].

If sufficient thermodynamic conditions are met, these lattice discontinuities can be eliminated, allowing the material to exhibit a lower energy state. The reduction in strain energy can occur by two different mechanisms; recovery and recrystallisation [120], [126]. Both of these are shown schematically in Figure 13. These processes are then typically followed by grain growth as a further means of reducing energy in the system. However, in the case of grain growth, the reduction in energy in the system is associated with a reduction in interfacial energy of the grain boundaries, not a reduction of strain energy in the lattice by the elimination of dislocations [120]. The processes of recovery, recrystallisation and grain growth are discussed in the following sections.

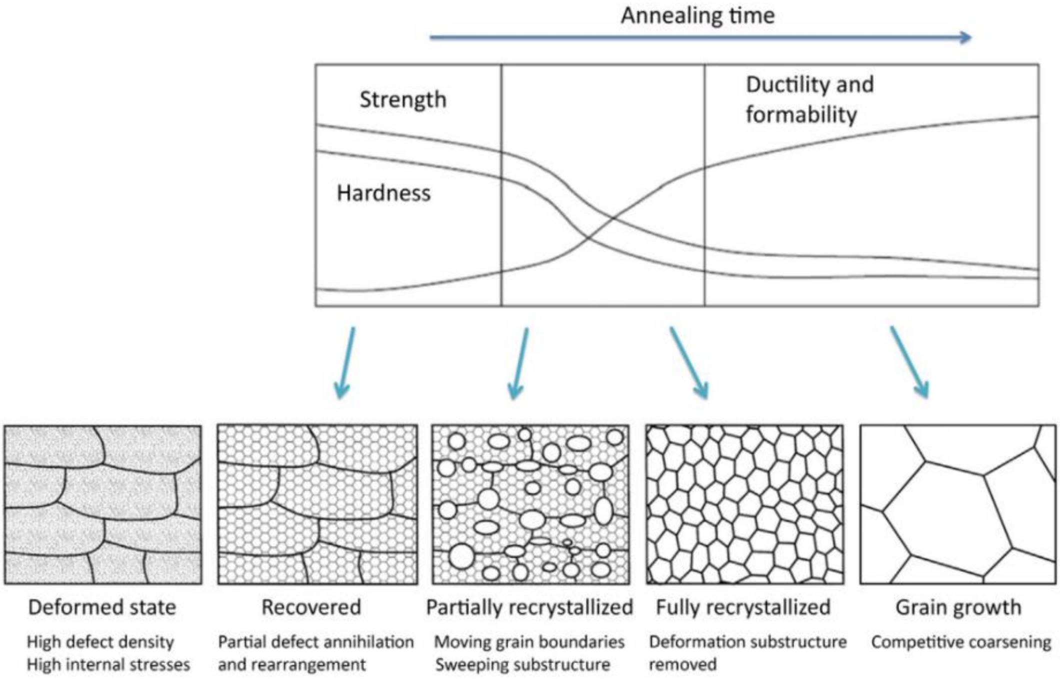

Figure 13: Schematic diagram from [127] **indicating the stages of recovery and recrystallisation, as well as the effects of this on the material strength, hardness and ductility, on a deformed metal. Reproduced with permission.**

2.3.2.4 Recovery

The process of recovery occurs once there is sufficient thermal energy to allow movement of dislocations by climb or cross slip within the lattice structure. Recovery typically requires the presence of elevated temperatures. This is because the movement of dislocations and LAGB without external deformation is dependent on the diffusion of vacancies through the lattice. This process is differentiated from recrystallisation as no movement of HAGB are associated with this process.

If dislocations causing opposing types of lattice strain (compression or tension) combine, they annihilate each other, reducing the lattice distortion and strain energy in the system. Those which are unable to be annihilated may rearrange themselves in an organised manner that reduces the strain energy in the lattice. This typically initially results in the formation of a cellular structure, which then progresses into a well-defined sub-grain structure [121], [127], [128]. In these structures, the cell walls or LAGB, are made up of a high density of dislocations and the inner cell regions contain a low number of dislocations [127]. As the process progresses, the misorientation between neighbouring dislocation free areas increases [126].

The result is the formation of a less distorted crystal lattice which has a lower internal strain energy, and thus lower yield strength. However, the material grains still retain their original orientations and shapes [121]. The material work hardenability is also increased after recovery [121].

Recovery often takes place at temperatures well below the temperatures required for recrystallisation. If the material is subjected to low heating rates or encompasses high dislocation mobility, or a combination of both, sufficient recovery may take place prior to reaching the recrystallisation temperature. In this case, recrystallisation can be supressed as there is insufficient elastic strain energy remaining in the system after recovery to trigger its occurrence [128].

However, dislocation mobility, and therefore the extent of recovery possible, depends on the stacking fault energy of the material, which is unique to every material.

2.3.2.5 Stacking Fault and the Stacking Fault Energy

The closed packed planes of a crystalline material are arranged in different planar stacking orders. The stacking order of an FCC material is ABCABCABC as shown in Figure 14. A stacking fault occurs when one of the planes of atoms does not follow the stacking order. For example, if the stacking sequence were to be altered as follows; ABCBABC, or ABCBCABC. This has an associated energy, which is different for every material [129].

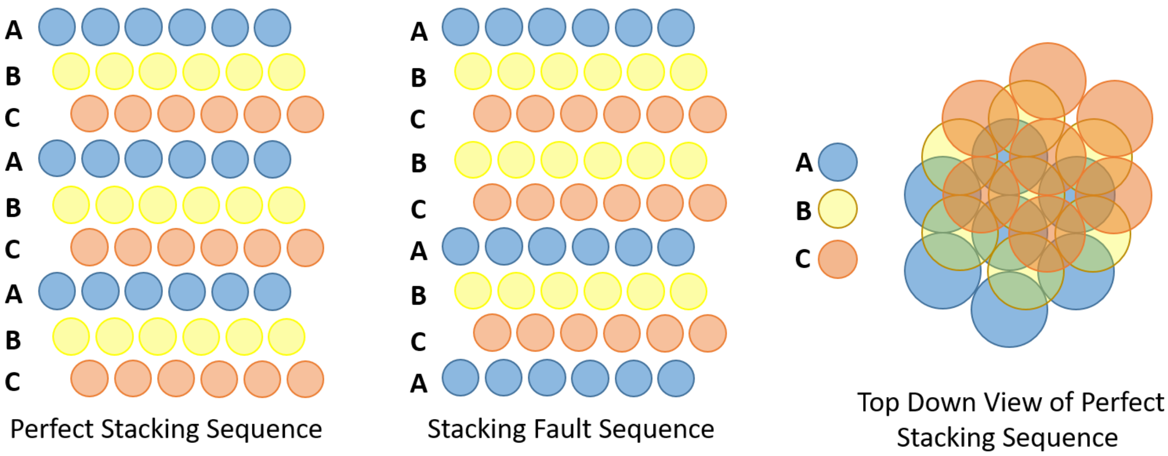

Perfect Stacking Sequence

Stacking Fault Sequence

Top Down View of Perfect Stacking Sequence

Figure 14: Left: perfect stacking sequence for an FCC material, Middle: stacking sequence containing a stacking fault, Right: top down view of stacking sequence in an FCC material.

These stacking faults are created by the movement of dislocations though a lattice. A perfect dislocation moves without altering the crystal structure. However, if it is more energetically favourable for a dislocation to move by splitting in to two partial dislocations, the crystal lattice stacking arrangement is altered, resulting in a stacking fault.

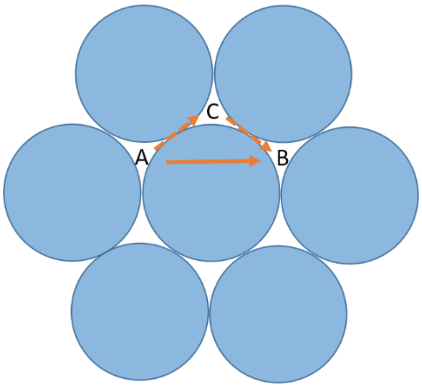

Figure 15: The movement of a perfect dislocation would move the gap labelled A to the point labelled B. This would cause no change to the stacking order of the atoms. However, if the plane of atoms were to move to have the gap at point A now situated over point C the dislocation will have dissociated in to two partial dislocations called Shockley partials.

Figure 15 shows that for a perfect dislocation to move through a lattice, the gap between atoms labelled A, is to move to position B. When this happens, there is no change to the stacking arrangement of the atoms as shown in Figure 16a. However, it may be energetically more favourable for the dislocation to move by dissociating in to partial dislocations and initially moving the plane of atoms from point A to point C, and then another point in the plane from point C to point B. This initial movement from A to C is shown in Figure 16b.

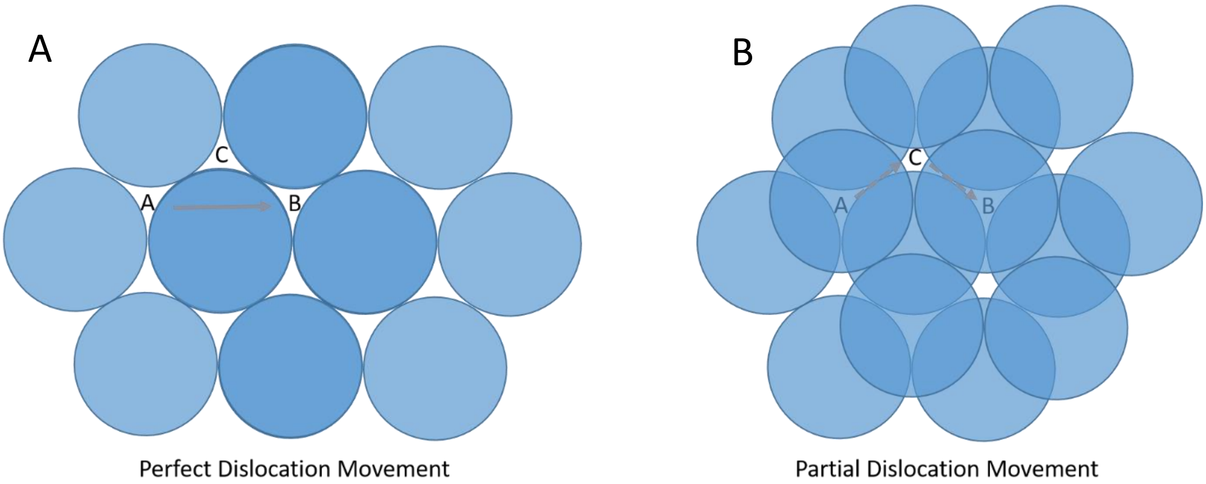

Figure 16: Left: result on the atomic plane of a perfect dislocation moving through a lattice, Right: the result of the moment of atoms along a partial dislocation.

This type of partial dislocation is called a Shockley partial. They are still able to move through the lattice by glide and climb, however remain in pairs due to the energy associated with the stacking fault created between them. The distortion surrounding each partial dislocation repulse each other while an attractive surface tension force, the stacking fault energy, keeps them at an equilibrium distance apart. Physically, this creates a planar gap between the atoms on that plane as shown by the black lines in Figure 17 [130].

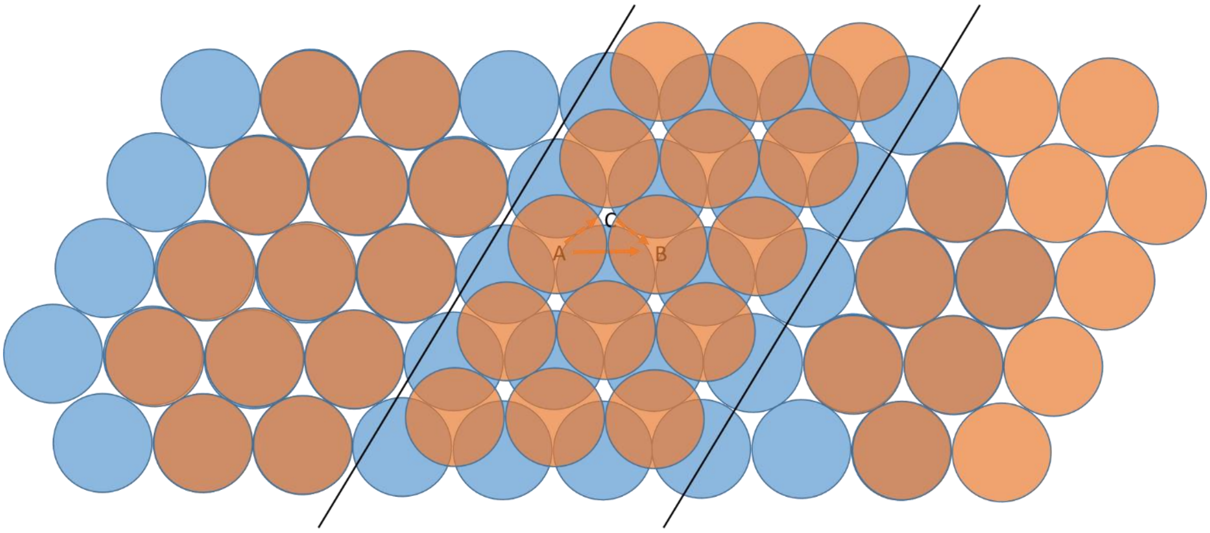

Figure 17: Schematic of a perfect arrangement of atoms shown in blue, and the same atomic plane after being affected by a partial dislocation shown in orange. The two partial dislocations are shown by the black lines.

In order for dislocations to cross slip (as opposed to glide or climb), enhancing recovery, the partial dislocations must first recombine to the perfect dislocation. This requires a sufficient amount of energy; thermal or mechanical.

In a high stacking fault energy material there is a small gap between stacking faults and so a small spacing between Shockley partial dislocations. The energy associated with keeping these partial dislocations close together is high, and so high stacking fault energy materials are more likely to allow movement of dislocations without separation in to partials.

A low stacking fault energy material (large gap between stacking faults) will require more input energy in order to cause recombination of the partials and so will undergo dislocation rearrangement and annihilation (recovery) less readily than a high stacking fault energy material. As Inconel 718 is a low stacking fault energy material above 354^{0}C [131], it is common to only see a very small amount of recovery. Instead, the reduction in lattice energy is typically achieved through recrystallisation.

The stacking fault energy also influences the volume of dislocations that are generated during plastic deformation. As higher stacking fault energy materials enable more dislocation movement, less dislocations are generated. Vice versa, a low stacking fault energy will impede dislocation movement leading to an increase in dislocations, and stored energy, generated [132].

2.3.2.6 Recrystallisation

Recrystallisation is the process in which new, strain free, grains are formed under the application of elevated temperature. In simple terms, the process involves the movement of both LAGB and HAGB from around small individual regions of unstrained material over the deformed microstructure [121].

The process is driven by the difference in elastic strain energy encompassed by the unstrained region and the strained lattice [120], and therefore is directly related to the number of dislocations present in the material [121]. In addition to the number of GNDs, the amount of recrystallisation is known to depend on several other microstructural factors including the solidification structure (and resulting elemental segregation), presence and coherency of second phase precipitates, grain size, grain orientation and residual stress.

Due to the resulting reduction in lattice strain, the process results in a less strong, more ductile material. If the application of elevated temperature is removed prior to the grain growth stage, recrystallisation typically produces a refinement of the material grain structure.

According to the Hall-Petch relationship [133], grain refinement is directly proportional to increased strength in grains larger than 20nm. This is because an increased number of grain boundaries makes the motion of dislocations more difficult [129]. Therefore, in traditionally manufactured materials, stages of deformation and heat treatment, termed annealing, are performed in order to produce progressively finer grain sizes.

Recrystallisation occurs via the ‘nucleation’ of a new grain, followed by its growth. As opposed to the nucleation of a solidification crystal as described in (Section 2.4 - Solidification), the material that makes up the nucleus in the recrystallisation mechanism is already present in the metal as a small strain free region separated from the surrounding deformed material by a HAGB [121], [127], [134]. In order for this small region of material to become a recrystallisation nucleus and grow into the surrounding grains, a sufficient driving force is required in the crystal structure. As such, successful nuclei are typically located near regions of high dislocation density gradient or large inter-crystal misorientations [126]. These can be at grain or twin boundaries, boundaries between different precipitate phases, or regions of high deformation [121], [126]. The movement of dislocations in the lattice also enables discrete regions of strain free crystal lattice to be produced that are energetically capable of becoming recrystallisation nuclei [128]. The different mechanisms of recrystallisation nucleation and growth are discussed in the next section.

Recrystallisation can take place during deformation at elevated temperature, termed dynamic recrystallisation, or during annealing, which is termed static recrystallisation [129]. In this thesis, recrystallisation is achieved during the HIP process (Section 6) whereby the material is understood to undergo a combination of both static and dynamic recrystallisation, with the extent of each depending on the volume fraction of material discontinuities present in each sample.

Within both static and dynamic recrystallisation processes, two more sub-groups can be defined; discontinuous recrystallisation (DRX), and continuous recrystallisation (CRX) [127], [128]. When the recrystallisation process occurs in discrete locations, with well-defined stages of nucleation and growth dependent on the location of the strain energy in the material, it is DRX. CRX occurs homogenously throughout the bulk [129]. The occurrence of either of these largely depends on the amount and distribution of the lattice strain in the part [121].

In addition to the annealing temperature, the kinetics of recrystallisation and the final recrystallised microstructure attained are dependent on the number of recrystallisation nuclei that are able to form, and the kinetics of their growth [121]. This is because the more recrystallisation nuclei formed per unit area, the less they are able to grow before impinging on each other. This results in a finer recrystallised microstructure. Additionally, if only a small volume of recrystallisation nuclei can form, the microstructure may only partially, or in-homogeneously, recrystallise. The speed at which the recrystallisation process occurs, and the extent and grain size of the final recrystallised microstructure depends on the following factors [121], [125], [127]:

- The amount of all types of lattice strain (Types I-III) present – this determines the amount of driving force present
- Heat treatment time
- Grain size
- Grain orientation - due to volume of deformation that can be achieved in grains of different orientation
- Volume of segregated material - reduced elemental segregation during rapid solidification enables a higher fraction of deformation twinning to occur which has been shown to enable recrystallisation nucleation [125]
- Presence of precipitates – these further contribute to Type III lattice strain

A number of conditions, or rules, for the occurrence and kinetics of recrystallisation have been presented by Cahn in [135]. These have been summarised below.

- A minimum threshold driving force for recrystallisation, in terms of material deformation or inherent lattice strain, is required to induce recrystallisation at a given temperature. If the lattice distortion is lower or the annealing time is reduced, higher overall temperatures are required to produce recrystallisation.
- The final recrystallised grain size depends on the amount of lattice strain present, the annealing temperature as well as the initial grain size in the microstructure. A higher level of

deformation, finer initial grain size, and lower annealing temperature produces a finer recrystallised grain size.

- For a set annealing time and temperature, and as the original grain size increases, a higher volume of lattice strain is required to induce recrystallisation.
- Once the recrystallisation process has completed, further exposure to elevated temperatures will cause grain growth.

Methods of Recrystallisation Nucleation

The mechanisms in which a small region of strain free material can become a recrystallisation nucleus and subsequently grow into the neighbouring grains, are not well understood. Several theories have been put forward in the literature, and three of these will be discussed; strain induced grain boundary migration (SIGBM), discontinuous sub-grain growth, and recrystallisation by twin boundary formation.

Strain Induced Grain Boundary Migration

Strain induced grain boundary migration involves the 'bulging' of a HAGB into a neighbouring grain, producing a region of strain free material as shown in Figure 18 [121], [136]. The resulting bulge may either comprise of a number of small sub-grains which have been elongated across the prior HAGB, or a single larger sub-grain. For the former, the process is driven by a difference in dislocation density, or orientation gradient, between the two grains. Due to differences in grain orientation and size, some grains may be able to accumulate a larger number of dislocations than others during deformation, therefore enabling this effect to occur at different regions in the material [121]. During the bulging of a single sub-grain, the process is driven more by the fact that the sub-grain is of sufficient size, and contains sufficient misorientation, to grow into the neighbouring grain [121]. As the difference in dislocation density between the neighbouring grain and the sub-grain increases, the critical size of sub-grain required in order to bulge across the HAGB decreases [121]. The presence of second phase particles is understood to promote the formation of a number of elongated sub-grains, rather than that of a single sub-grain, during grain boundary bulging [121].

The formation of a recrystallisation nucleus from these grain boundary bulges in Ni-alloys has been shown to occur through two different mechanisms; the gradual increase in misorientation of the sub-grain boundary behind the bulge with continual strain [137], or the formation of a twin boundary at the base of the bulged region [138], [139]. This effectively creates a distinct region of strain free material which may then grow. The size of initial bulge regions is thought to be dependent on the misorientation between the grains, mobility of the HAGB, and the local dislocation density between the two grains [137].

This process occurs during static recrystallisation in the presence of well-defined sub-grains [121]. However, this method of recrystallisation nucleation is also often observed during high temperature mechanical testing of Inconel 718 [138], [140], [141] and is therefore also a dynamic recrystallisation mechanism. This is because during deformation, boundaries in the microstructure such as grain boundaries, triple points, or deformation bands, become serrated [137]. This produces regions of misorientated material on either side of a HAGB, and leads to high dislocation density gradients on either side of the boundary, promoting grain boundary bulging.

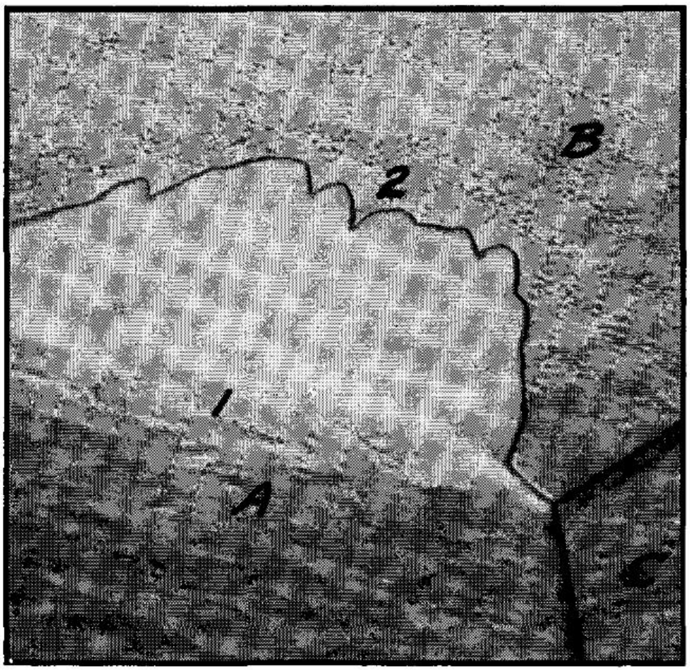

Figure 18: Optical image from [136] **showing the HAGB migration from point A to point B. Number 1 shows the original position of the grain boundary and number 2 shows the new position of the grain boundary. Magnification is 75x, no scale bar provided. Reproduced with permission.**

During dynamic recrystallisation, the process of grain boundary serration, bulging, recrystallisation nucleation, and growth may repeat as a process as long as strain is applied to the material [138], [140]. It has been shown that the formation of a bulged HAGB may cause disruption to the local crystal structure behind the bulge, leading to the formation of several recrystallisation nuclei in the area [137].

Discontinuous Sub-Grain Coarsening

Another method of recrystallisation nucleation is by the inhomogeneous growth of strain free sub-grains, and is called discontinuous sub-grain coarsening [121] [126], [127]. In this case, the resulting recrystallised grains possess an orientation that was already present in the deformed material [134].

In order for a sub-grain to become a recrystallisation nuclei, a sufficient level of misorientation gradient must exist between it and the neighbouring sub-grains to produce a driving force for the migration of LAGB. These regions may evolve during annealing as a continuation of dislocation movement observed via recovery, or may already be present in the material due to high dislocation density gradients present across a number of sub-grains [121].

Sub-grain boundaries have an associated boundary energy and therefore, the growth of the sub-grain occurs as a means to reduce the total energy stored by the system. As the sub-grain grows, a larger misorientation can evolve in the region which may lead to the formation of a new LAGB. As the misorientation between sub-grains increases, so does the mobility of the grain boundary. After a HAGB has formed, there is enough mobility to allow a large strain free grain to grow [134]. In order for a sub-grain to continue growing instead of be grown over (and be eliminated by neighbouring sub-grains), there needs to be an energy advantage for that sub-grain to grow. Therefore, larger sub-grains located in a region of higher long range misorientation gradient, are more likely to grow [136].

The requirement for a high level of or misorientation gradient across a distance larger than approximately 15 sub-grains [121] means discontinuous sub-grain coarsening often occurs in regions of high deformation (stored energy). These are usually observed near shear bands, in material affected by residual stress, in the vicinity of large second phase particles, or at grain boundaries [127]. The high deformation zone surrounding these material inhomogeneities only extend a certain distance from the defect. Therefore the strain free nuclei grow until the amount of lattice strain has reduced to a point where the driving force is no longer sufficient to enable further growth [127]. This is why the mechanism is termed discontinuous.

As dislocation mobility in materials with low stacking fault energy is more difficult, the recovery of the lattice in to sub-grain arrays is also more difficult. Therefore, the material is less likely to undergo recrystallisation by sub-grain coarsening, with this only occurring upon the random presence of a sub-grain with sufficient size and misorientation. However, due to the rapid solidification in AM materials, cellular structures are common (as discussed in Section 2.4.3 Solidification in Laser Additive Manufacturing), and so the random inherent presence of these sub-grains is possible in the as-built condition. In the case of high stacking fault energy materials, this process of recrystallisation requires an incubation time in which the sub-grain structures are produced by recovery. As with grain boundary bulging, the kinetics of the process can be enhanced by increasing the annealing temperature.

Recrystallisation by Twin Formation

As recrystallisation by sub-grain growth is more difficult in materials that exhibit a low stacking fault energy (such as Inconel 718), the nucleation of recrystallised grains during deformation and annealing may take place through twinning.

A twin is a region of the crystal lattice in which the atoms within the twinned region are positioned as a mirror image of those in the original grain along a plane called the twin plane [130]. The process of twin boundary formation typically produces a strain free region which reduces the overall energy of the system. While normal random HAGB occupy a large volume of space, resulting in high associated energy levels, twin boundaries are associated with much lower energy. This is because they contain atoms that are shared by both grains, so take up less space, whilst only being able to form at specific misorientations where the two lattices fit together with little distortion between them [142]. Twin boundary nucleation is therefore more favourable than the formation of new HAGB by recovery processes during recrystallisation in low stacking fault energy materials.

The mechanisms behind twin boundary formation are complex and many theories have been debated in the past. These include formation due to growth accidents on the edge of a growing grain, the coalescence of stacking faults at moving grain boundaries, and the dissociation of the dislocation at a normal HAGB into two partial dislocations and a twin boundary. Schematics of these processes can be found in [143]–[145]. They can form as a result of grain growth, recrystallisation, or deformation. The exact formation pathways of these boundaries are outside the scope of this thesis. Instead, interested readers can find more information at the following references; [121], [143]–[145].

Nevertheless, the formation of a new crystal twin is accompanied by the production of a small region of strain free material. This then acts as a nucleus for recrystallisation. If the grain boundary energy of the twinned boundary is less than the neighbouring grain boundaries, this twinned region will grow [121]. As opposed to that of sub-grain growth, recrystallisation through twinning results in the formation of new grains that are different in orientation from the original material [127].

2.3.2.7 Grain Growth

It is worth at this stage to provide a separation between grain growth during recrystallisation, and grain growth after recrystallisation. These two variations of 'grain growth' occur at different velocities, with the growth during recrystallisation occurring much faster than when a grain grows through already recrystallised, or strain free, material [121]. In this section we discuss grain growth in a strain free material.

As the grain boundary is a defect in the crystal structure, the presence of it means the material is not in the lowest energy state. The elimination of the energy associated with the presence of HAGB boundaries occurs by grain growth. As with recrystallisation, this can occur homogeneously or in-homogeneously throughout the bulk of the material, leading to either normal, or abnormal grain growth. There is currently no complete explanation of the structure of a HAGB, however simplistically, grain growth occurs due to singular atom or groups-of atoms making a jumps across the boundary region [121].

2.3.2.8 Coincident Site Lattice (CSL) and low ∑CSL 'Special' Grain Boundaries

A coincident lattice site between two grains is the position where, if the lattice of each grain was extended to overlap the other, there would be a common point in space occupied by the lattice of each grain. The inverse of the fraction of CSL sites in a lattice is given a parameter, ∑ [146]. As the ∑ value increases, the disorder at the twin boundary increases [147]. Annealing twins in low stacking fault energy materials usually encompass a lot of ∑3 boundaries, and to a lesser extent, ∑9 boundaries [145], [148]. The ∑3 boundaries encompass a wide range of boundary orientations, of which the coherent and incoherent twin boundaries are a part of. Coherent twin boundaries occur when the atoms at the twin boundary fit in the lattice locations of both adjacent grains perfectly. This is associated with the lowest energy. Incoherent twin boundaries occur when the atoms at the boundary do not fit exactly into the lattice locations of both adjacent grains. The energy associated with these is higher, and can be around 20 times the energy of a coherent twin boundary in the same material [142].

The mechanical properties of materials that include low ∑ CSL (∑3-∑29), or 'special' boundaries differ from normal HAGB. They have been shown to possess beneficial engineering properties such as, but not limited to, resistance to sliding, fracture, corrosion, and stress corrosion cracking [121], [147], [149]. As such, materials with extreme operating condition requirements are processed in a specific manner in order to attain a high proportion of low ∑ grain boundaries. This is called grain boundary engineering (GBE) and usually involves several stages of deformation and annealing in order to trigger strain induced grain boundary migration, or twin formation [145].

Once recrystallisation has completed, the driving force in the lattice is such that the recrystallised grains grow in order to reduce the energy associated with grain boundaries. Due to the enhanced mobility of incoherent twin boundaries, grain growth is accompanied by a decrease in the density of these incoherent boundaries [145], [150]. It has also been shown that only very few new twin boundaries are nucleated during grain growth after recrystallisation [151]. Figure 19 shows the resulting twin boundary morphologies in samples of Inconel 718 after grain growth and recrystallisation. It is clear that for a similar grain size, a higher twin boundary density exists in the sample that underwent recrystallisation rather than grain growth. It is therefore also important in the realm of GBE, that grain growth after recrystallisation is prevented [145].

In LPBF, the effects of rapid solidification lead to large numbers of GNDs in the as-built material [125], [152]. This can be further increased by plastic deformation during the HIP process, especially in the presence of internal AM porosities. Therefore, GBE can be enabled in AM samples without the need for repeating stages of plastic deformation and heat treatment, saving time and money.

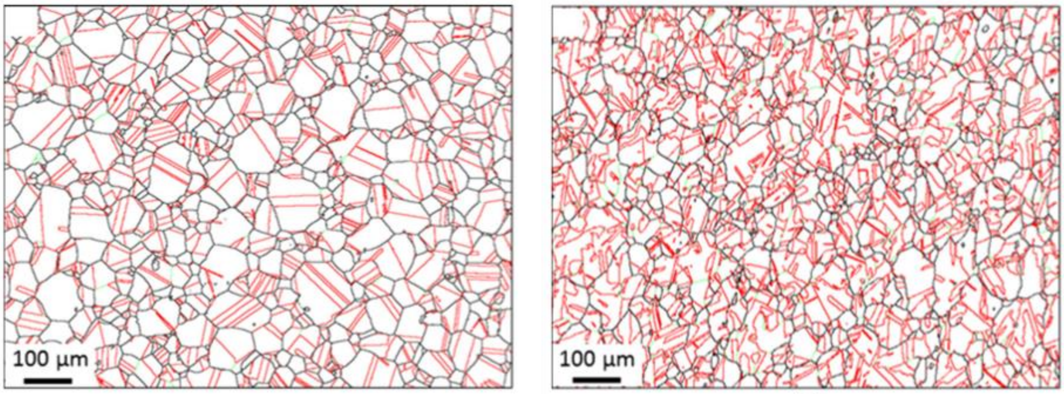

Figure 19: ∑3 boundaries shown in red, ∑9 boundaries shown in green and normal grain boundaries shown in black for a sample of Inconel 718 affected by Left: grain growth only, and right: recrystallisation [145]**. Reproduced with permission.**

2.4 Solidification

2.4.1 Solidification Theory in Metals

The general microstructure of Inconel 718 in solid form has been discussed in the previous section. However, as AM involves the melting and rapid solidification of the material, it is important to introduce the mechanisms of solidification in metals and alloys.

The solidification of a material occurs in order for it to attain a minimum Gibb's free energy. The magnitude of the driving force for this is determined by the difference in Gibb's free energy between the liquid and solid state of the material. Therefore, the further below the equilibrium melting solidification temperature the solid/liquid interface is, the higher the driving force for solidification [153]. A solidification event requires a cluster of atoms to overcome an energy barrier and become a solidification nucleus. The larger the undercooling of the liquid, the more clusters of atoms can form and the more likely it is that these will overcome the energy barrier to become solidification nuclei.

Additionally, solidification in alloys involves the segregation of slow diffusing atoms at the solid / liquid interface. This forms a solute rich boundary layer at the interface. The local increase in solute concentration reduces the solidification temperature of the material. Therefore, solidification becomes retarded as the local temperature of the melt is not low enough to solidify material in the solute rich layer. However, random perturbations may be present on the surface of the solidification front. If these extend to a position outside of the boundary layer, or to a position where the solute concentration is lower, it becomes possible for these perturbations to grow ahead of the solid / liquid interface. This is because in these regions, the melt has a higher solidification temperature, and can therefore solidify successfully at the local temperature of the liquid melt. This phenomena is called constitutional undercooling and allows crystals to nucleate or grow ahead of the solid/liquid interface [154], [155]. A lower thermal gradient in the melt and higher extent of solute segregation during solidification increases the effects of constitutional undercooling. As the constitutional supercooling increases, the growth morphology changes from planar, to cellular, to dendritic, and to equiaxed as shown in Figure 20 [43].

During constitutional undercooling, the region separating the solid growth front and the liquid is called the mushy zone. The characteristics of the microstructure in terms of grain and sub-grain morphology, amount of elemental segregation, and the development of pores, are determined in the mushy zone. This is influenced by the relationship between the temperature gradient in the liquid (G) and the solidification growth rate (R) as shown in Figure 21 [43], [153]. A higher cooling rate and a higher solidification rate (G x R) leads to the formation of finer structures in order to minimise segregation distance between the solidification structures.

Laser manufacturing such as welding, as well as additive manufacturing, both involve the melting and solidification of very small regions at a time. As previously discussed, this produces high thermal gradients in the liquid. The effects of constitutional supercooling are also present as, more often than not, complex alloys are used in engineering applications. Due to the high laser raster speeds involved in these methods, the solidification growth rate is also high. The result is the formation of very fine solidification structures, which may fluctuate between cellular and cellular dendritic.

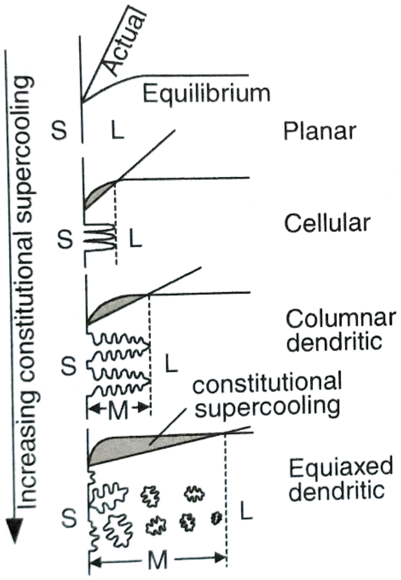

Figure 20: Schematic showing the effects of constitutional supercooling on solidification morphology [43] **(Reproduced with permission). As the level of constitutional supercooling increases, the solidification front becomes increasingly dendritic with the potential for equiaxed grains to be nucleated ahead of the growth front. S = solid, L = liquid, M = mushy zone.**

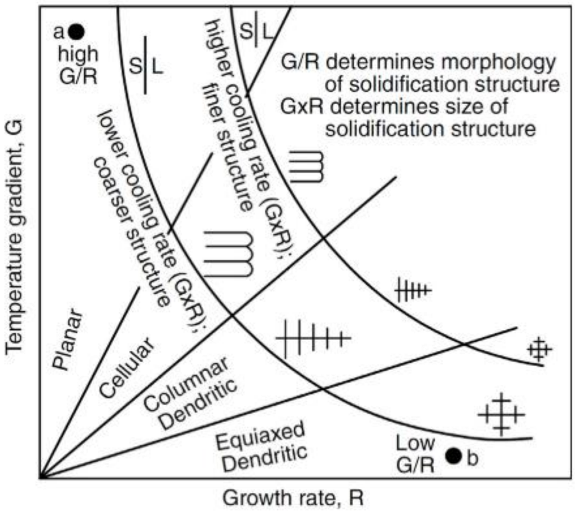

Figure 21: Schematic showing effects of temperature gradient in the melt and growth rate of the solid in the morphology and size of the solidified material microstructure [43]**. Reproduced with permission.**

2.4.2 Solidification in Laser Additive Manufacturing

In real systems, crystals tend to preferentially nucleate and grow on already solidified substrates, termed heterogeneous nucleation. This is because these regions reduce the energy barrier required for solidification nucleation. The extent of the energy barrier reduction depends on the extent to which the solidifying liquid wets the substrate. This is usually measured in terms of the contact angle (θ) between the liquid and solid [156]. If the liquid completely wets the surface, the contact angle is zero and the energy barrier is also zero. This leads to a solidification occurring at very little melt undercooling [155].

During laser additive manufacturing, the molten region is in direct contact with the solid material underneath. This produces a very small contact angle, leading to the epitaxial growth of previously established grains as shown in Figure 22. The newly solidified material observes the same lattice structure and orientation as the grains they grow from. Grain growth is often termed 'competitive' as the grains that are oriented with their easy growth direction perpendicular to the melt isotherms grow more easily at a detriment to the others. As the AM process involves the building up of material in height, and the heat conduction occurs downwards through bulk material, the epitaxial growth occurs upwards through the height of the built component. This results in the production of fine columnar grains that span over several layers. Due to the fast solidification kinetics, these grains typically contain fine cellular or dendritic sub-grain microstructures [108].

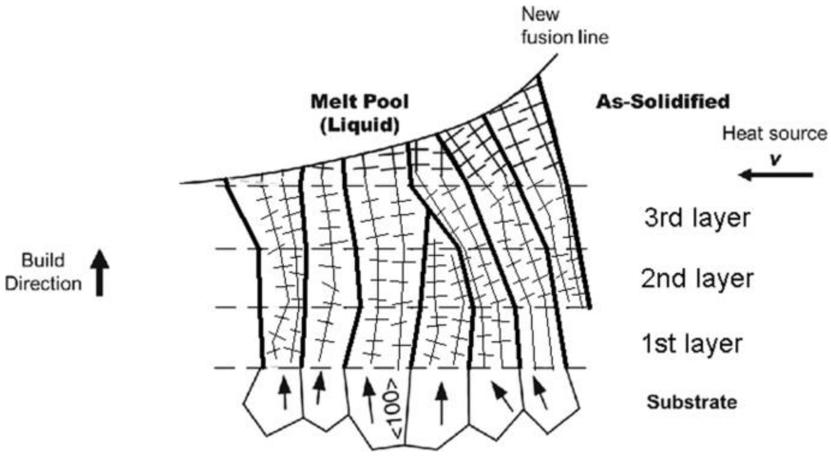

Figure 22: Diagram showing epitaxial competitive growth in additive manufacturing of metals [157]. **Permission not required for reproduction.**

2.5 Laser Powder Bed Fusion of Inconel 718

After the introduction of LPBF, Inconel 718 and its phases, and the theory behind solidification, it is time to bring them all together to look at the LPBF of Inconel 718.

The processing of Inconel 718 by LPBF has been studied by numerous research groups due to the relative ease with which it is printed compared to other nickel-based superalloys. Several in-depth review papers that focus on the microstructures and mechanical properties of LPBF Inconel 718 have been written [20], [158], [159].

2.5.1 Powder Requirements

Laser powder bed fusion utilises particles within the size range of approximately 15-45µm [160]. When the full range of powder sizes are present in a sample, a higher powder bed packing density can be achieved, which has been found to produce printed parts with higher densities [24]. In order to achieve an even coating of powder in the powder bed, powders must have good flowability; this requires them to be spherical without the presence of satellites as shown in Figure 23a [160].

The majority of powders for AM are produced by inert gas atomisation. This is a rapid solidification process which causes the powder particles to exhibit dendritic solidification structures as shown in Figure 23b. As previously discussed, these particles may also contain trapped gas pores which can lead to gas porosity in final printed components [27], [160].

It has been demonstrated that Inconel 718 powder can be sieved and recycled several times without inducing significant detriment to the material properties [161], [162]. If sieving takes place in an argon atmosphere, the powder can be reused up to 50 times and still produce test samples with the required mechanical properties [162].

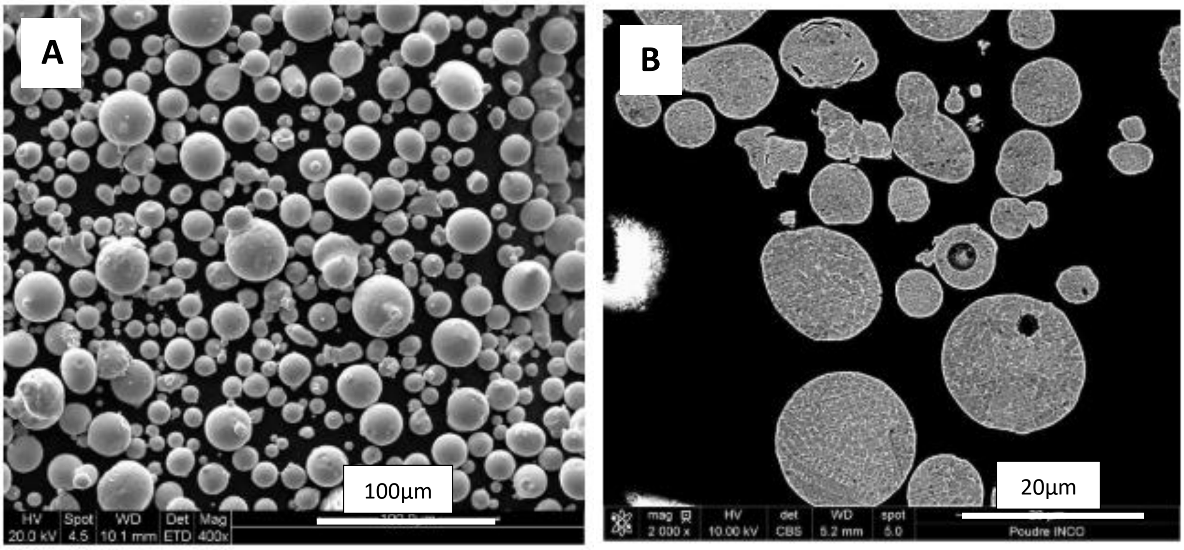

Figure 23: A) Morphology of gas atomised Inconel 718 (powder size below 50µm) [163]**(Reproduced with permission), B) Dendritic structure found within powder particles and example of trapped gas pore within particles**[27] **(Reproduced with permission).**

2.5.2 Build Parameters

Many studies have shown that it is possible to produce fully dense components from Inconel 718 via the LPBF process [17], [27], [164]. Example parameters as well as the machine used for the referenced trials are shown in Table 2. The conditions within the build chamber, such as inert gas flow and inert gas pressure, as well as the operation mode of the laser (continuous or pulsed) also affect the process. Therefore, the parameters shown are highly dependent on the machine utilised. This makes it difficult to translate process parameters between machines, even for identical part geometries.

While it is most common to analyse the effect of changing laser velocity, power, and hatch spacing, on the microstructure of the part, the effects of scan pattern [63], [165]–[167], hatch length (by simulation) [168] and focus offset [169] have also been investigated. As the powder particles in LPBF have a standard size range, usually 15-45µm diameter, this sets the minimum powder layer thickness that is applicable to the process to ensure sufficient coating of the baseplate; approximately 30µm. As the layer thickness is increased, the build productivity increases, however the geometric accuracy typically decreases due to the stair step effect introduced earlier [170].

Table 2: Example of build parameters used to print fully dense samples of Inconel 718 obtained from literature. NR short for 'not recorded'.

	Machine	Laser Spot Size (μm)	Power (W)	Velocity (mm/s)	Hatch Spacing (μm)	Layer Thickness (μm)	Scan Strategy	Additional Information
Wang *et al.* [163]	Self-built	100	170	1500	70	NR	90° rotation	
Amato *et al.* [17]	EOS M270 LPBF	100	NR	800 or 1200	NR	NR	90° rotation	
Cao *et al.* [116]	EOSINT M280 LPBF	70	285	960	NR	40		
Popovich *et al.* [171]	LPBF 280HL	81	275	805	120	50		
Moussaoui *et al.* [27]	DMP PROX300	NR	150-450 (varied)	1000-1800 (varied)	50-90 (varies)	70		
Chlebus *et al.* [131]	LPBF Realiser II 250	180	100	87.5	160	50	90° rotation	
Gao *et al.* [172]	EOSINT M280	100	280	1200	30	30	67° rotation	Preheated substrate 80°C
Aydinöz, *et al.* [173]	LPBF 250 HL	NR	175	620	120	30	NR	Preheated substrate 200°C
Park *et al.*[174]	Concept Laser M2	NR	180	600	NR	NR	Chessboard Pattern	

2.5.3 As Built Microstructure

The as-built microstructure is very distinctive of the AM process. When polished and etched, clear melt pool boundaries are visible as shown in Figure 24a and 24b. The size and shape of these varies with different process parameters. Figure 24a was printed using a laser power, laser velocity, hatch distance, layer thickness, and beam diameter of 950W, 320mm/s, 0.5mm, 100μm, and 100μm (flat top beam profile) respectively. Comparatively, Figure 24b was printed with 250W, 700mm/s, 0.12mm, 50μm, 80μm (Gaussian beam profile) respectively. Both samples were built with the same volumetric energy density of 59.5J/mm^3 however are drastically different in immediate microstructure [9]. In Figure 24b it is also clear that the melt pool depth within a single layer is not consistent. This has also been shown by other researchers and it should be noted that even for constant laser parameters and cross sectional geometries, the heat flow between neighbouring scan tracks can be random and vary greatly [175].

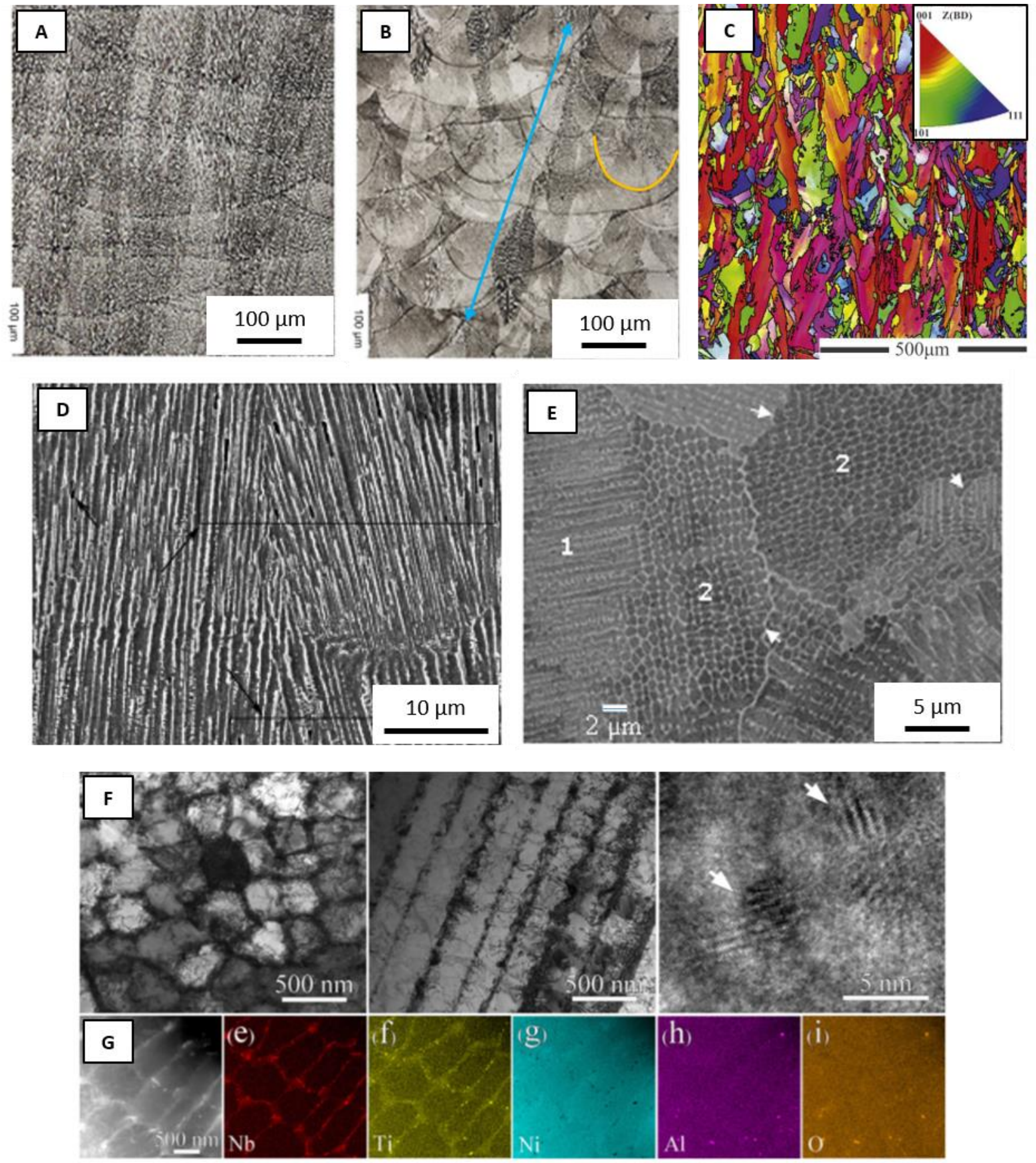

Figure 24: a) shallow, wide, melt pools built with high power, hatch spacing and layer thickness, low speed, b) deep, narrow, melt pools built with lower power, hatch spacing and layer thickness, and high speed. Modified from [9] **(Reproduced with permission). Orange lines show melt pool boundaries and the blue line shows the length of a single grain spanning across several melt pool layers; c) Inverse Pole Figure (IPF) map of LPBF Inconel 718 showing the columnar grains oriented in the build (Z) direction** [176] **(Reproduced with permission); d) cellular solidification structure** [163] **(Reproduced with permission); e) clusters of differently orientated sub grains labelled 1 and 2, separated by grain boundaries indicated by white arrows** [177] **(Reproduced with permission); f) dislocation networks surrounding each growth cell** [178] **(permission for reproduction not required); g) higher magnification image of growth cells and EDS analysis showing segregation of elements in the intercellular regions** [178] **(Permission for reproduction not required).**

Within the melt pools, epitaxial growth opposite to the direction of heat transfer dominates, leading to long thin grains that span over several melt pools [17], [30], [179]. This is shown by the blue line in

Figure 24b. In FCC and BCC materials, as a result of competitive growth, the grains with their <001> easy growth direction parallel to the build direction dominate. This results in most of the columnar grains showing a distinctive orientation in the build direction, as shown in Figure 24c [180]. If sectioned perpendicular to the build direction, these grains would look equiaxed over the surface of the layer [17]. The size of these columnar grains depends on the process parameters and specific AM machine utilised. It has also been shown that the grain aspect ratio increases with increasing processing power [29], [165], [180].

Due to the rapid melt pool cooling in AM, cellular solidification takes place with segregation of slow diffusing elements being deposited at the intercellular regions. Figure 24d shows this cellular as-built AM structure within a single grain in Inconel 718. The dark regions show the γ matrix which forms at 1360^{o}C [107], and the white regions are made up of segregated material at the cell boundaries. The segregated material becomes enriched in Nb, Mo, Ti and C as solidification progresses [17], [68], [161], [173], [176], [181]. Energy Dispersive X-ray Spectroscopy (EDS) maps showing enrichment at cell boundaries is shown in Figure 24g. During solidification, this enrichment can lead to the formation of fine cuboidal or spherical carbide particles ahead of the solid/liquid interface [131], [165], [177], [179]. The reduction in C in the remaining segregated material may then allow final solidification of the Laves phase, alongside carbides and γ phase, at 1250^{o}C [107], [165], [177], [182].

These cellular structures tend to grow in several different, randomly orientated, clusters which can be identified as sub-grains [177]. Therefore, each individual grain contains regions of varying orientation. Figure 24e shows the different orientations of these sub grains (numbered 1 and 2) within a single grain. The grain boundaries are indicated by white arrows.

In the as-built microstructure, the Laves phase is irregularly shaped and brittle, therefore is an easy site for the initiation of cracks [183]. It has been found that processing with a higher power produces an increased amount of Laves formation regardless of the overall energy density applied during printing [9].

Upon even higher magnification using Transmission electron microscopy (TEM), it can be seen that each growth cell is bordered by a dense dislocation network as shown in Figure 24f. During solidification, Ni-Cr alloys have been shown to shrink by 0.9-2% depending on the Cr concentration [184]. Due to the repetitive expansion and shrinkage that takes place during AM, a large volume of plastic deformation is placed on the material. This leads to the generation of a high volume of dislocation networks around each growth cell [130], [177], [183]. The distortion in the crystal lattice caused by these dislocation structures stores a large amount of strain energy.

The scale of these microstructural features changes as the thermal conditions change. This can occur due to a change in component geometry or machine parameters. As an example, in a 6mm tall sample, the width of dendritic solidification structures in the top of a sample have been found to be 50 μm larger than at the bottom. This is due to the baseplate acting as a heat sink leading to faster solidification kinetics at the bottom of the part [185]. Additionally, a decrease in input energy density leads to a higher cooling rate and therefore less segregation [186], smaller volume fraction of Laves phases, smaller carbides, finer cell spacing [187], and less textured, smaller grains [9]. In general, the scale of the growth cells is in the region of 0.2-2 μm [17], [176], [179], [181].

Rapid cooling of the material in LPBF of Inconel 718 leads to limited precipitation of the γ' and γ'' strengthening phases within the cellular γ phase regions in the as-built condition [17], [176]. Although Amato *et al.* [17] resolved these by TEM analysis, showing that they stack along the length of the cell structures, it is always necessary to perform post build heat treatments on AM Inconel 718 to homogenise the material and achieve the required volume fraction of these precipitates.

Ferreri *et al.* [188] created a table of the solvus temperatures for each phase with information sourced from the literature. This information is helpful in the understanding of how the different heat treatments affect the as-built AM microstructure. The table has been reproduced in Table 3.

Table 3: Solvus temperatures for the different precipitate phase in Inconel 718 collated by Ferreri et al. [188]**. Reproduced with permission.**

Phase	**Solvus Temperature (^{0}C)**
γ'	900-970
γ''	910-930
δ	990-1020
MC	1040-1200
Laves	1010

2.5.4 Post Build Heat Treated Microstructure

2.5.4.1 Introduction to Heat Treatments

The high levels of residual stress and sub-grain structures in the as-built microstructure provide high levels of strength. However, the corresponding ductility is very low, which can lead to brittle failures. As previously discussed, part warping due to relaxation of residual stress upon removal from the baseplate is also a common issue.

In order to resolve these issues, as well as release the elements required for the precipitation of the strengthening γ'' precipitates, post build heat treatments are required. These heat treatments can be carried out over a wide range of temperatures, and in order to present a literature review of these in LPBF Inconel 718, they have to be split in to 4 categories; a hot isostatic press treatment (>1100^{o}C at ~100MPa), a lower temperature solution treatment (<1000^{o}C), a high temperature homogenisation treatment (1000-1250^{o}C), and an aging treatment (620-720^{o}C).

The solution treatment is typically applied in order to maintain the as manufactured anisotropic grain structure, while allowing the segregated atoms that make up the strengthening phases to back dissolve into the matrix. Typically, this process involves only recovery. This then allows strengthening precipitates, γ' and γ'', to form in the γ matrix during the aging treatment. This method of post processing is desired in order to preserve the anisotropic grain structure for situations where a directionality in the mechanical properties of the part is required.

The homogenisation treatment is used to remove the effects of rapid solidification during manufacture. In this case, the process of recrystallisation is used to remove the sub-grain structure, as well as the elongated grain morphology. This is why the applied temperatures are higher than for the solution treatments.

The HIP process is applied in order to remove any internal porosity. As previously discussed, it utilises a combination of an external isostatic gas pressure and elevated temperature to force the internal pores to close, densifying the material. This typically takes place at similar temperatures to the homogenisation treatment. Combined with the added plastic deformation produced in the part, this process typically also leads to recrystallisation as a means to remove the as-built AM microstructural characteristics.

Finally, the aging treatment is used in order to precipitate the γ'' phase from the primary γ phase.

The amount of microstructural change that occurs with each of the heat treatments depends on the time and temperature (and pressure for the case of the HIP) of the heat treatments, as well as the amount of stored energy in the material. Due to changes in geometry and processing parameters in AM structures, each have differing levels of stored energy held within them, and so the extent to which microstructural change occurs at a given temperature and time may be different for every part. Additionally, as Inconel 718 is a low stacking fault energy material, it does not readily undergo recovery meaning the internal stored energy is usually released from the matrix through recrystallisation.

2.5.4.2 The Effects of Post Build Heat Treatments on As-Built LPBF Inconel 718

The standard heat treatment according to AMS 5663 for forged Inconel 718 is a solution heat treatment at 980°C for 1 hour (air cool) followed by a double age of 720°C for 8 hours (furnace cool to 620°C), and 620°C for 8 hours (air cool) [159]. Comparatively, the heat treatment applied for AMS 5383 is more suitable for large castings of Inconel 718 and comprises of a homogenisation step of 1080°C for 1.5 hours (air cool) prior to AMS 5663. As the microstructure of AM parts is so different from both forged, and large scale cast structures, several researchers have studied the effects of different variations of these heat treatments on the microstructure of AM parts. A summary of the applied heat treatments is presented in Table 4.

The commonality between most papers was the application of a double age heat treatment similar to that of AMS 5664. It should be noted however, that slight differences in the speed of furnace cool were reported between studies. During the first stage of the double age, 8 hours at 720°C, the strengthening phases γ' and γ'' precipitate. This is followed by 8 hours at 620°C in which the γ matrix further homogenises and the precipitates grow [27]. Deng *et al.* [176] and Brenne *et al.* [180] studied the effect of applying the double age treatment directly to as-built material. No visible changes in microstructure were observed from the as-built condition under SEM analysis as shown in Figure 25. This was primarily due to the temperatures being too low to dissolve the Laves phases and release the precipitating elements into the γ matrix.

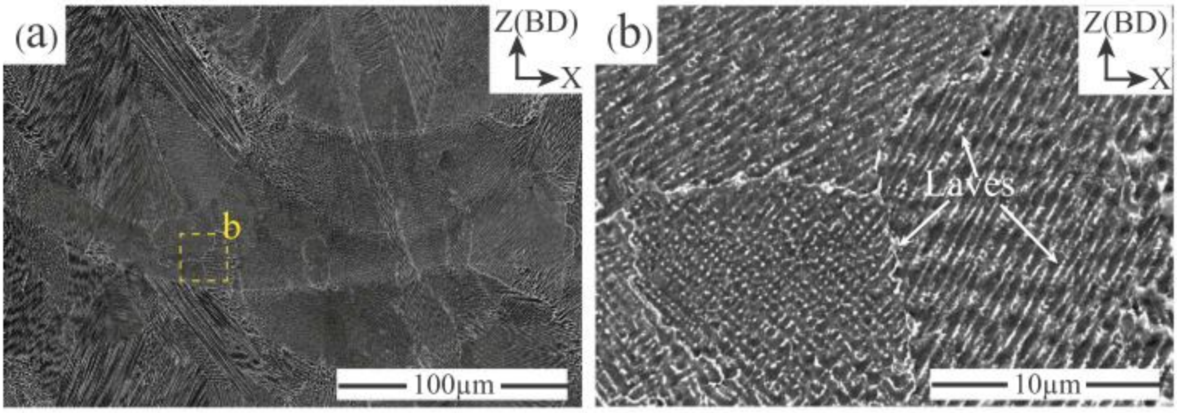

Figure 25: Microstructure of LPBF Inconel 718 after application of a direct age. The sub grains and cellular structures are still visible with large amounts of Laves phase present at cellular interfaces [176]**. Reproduced with permission.**

Table 4: A review of the heat treatments applied to as-built Inconel 718 samples in the literature.

Author	HIP Processing	Homogenisation Treatment	Solution Treatment	Aging Treatment	Notes
Amato [17]	1163°C, 4 hours, 0.1GPa pressure, argon atm		Vacuum anneal: 982°C, 0.5 hours		Anneal performed first, followed by HIP
			Vacuum anneal: 1160°C, 4 hours		Vacuum anneal performed solely for comparison
Wang [163]			980°C, 1 hour, air cool	Double age: 1) 720°C, 8h, (furnace cool) 2) 620°C, 8h, (air cool)	
Moussaoui [27]	1160°C, 3 hours, 0.102GPa, air cool		980°C, 1 hour, air cool	Double age: 1) 720°C, 8h, (furnace cool) 2) 620°C, 8h, (air cool)	
Strößner [181]			980°C, 1 hour, air cool	Double age: 1) 760°C, 10 hours, (Furnace cool for 2 hours) 2) 650°C, 8 hours	Study performed a comparison between HT1: solution treatment and double gaining procedure only, and HT2: performing an additional homogenisation step beforehand.
		1065°C, 1 hour	980°C, 1 hour, air cool	Double age: 1) 760°C, 10 hours, (furnace cool for 2 hours) 2) 650°C, 8 hours	
Deng [176]		1080°C, 1 hour, (water cool)	980°C, 1 hour, (water cool)	Double age: 1) 720°C, 8 hours, (furnace cool at 50°C an hour) 2) 620°C, 8 hours (air cool)	Performed different combination of these three stages in order to understand which would lead to an optimal microstructure
Chlebus *et al.* [131]		1 hour at 980°C OR 1040°C OR 1100°C		Double age: 1) 720°C, 8 hours, (furnace cool at 100°C an hour) 2) 620°C, 8 hours (air cool)	Performed different homogenisation treatments prior to double age
Raghavan *et al.* [179]			1040°C, 2 hours (air cool) OR 1100°C, 2 hours, (air cool) OR 1200°C, 2 hours, (air cool)	Single age: 700°C, 28 hours OR Double age: 1) 720°C, 8 hours, (furnace cool at 100°C an hour) 2) 620°C, 8 hours (air cool)	Compared the microstructures obtained using different combination of homogenisation and aging treatments
Aydinõz *et al.* [173]	1150°C, 4 hours, 1000bar (furnace cool)		1000°C, 1 hour (air cool)	Double age: 1) 720°C, 8 hours, (furnace cool at 50°C an hour) 2) 621°C, 8 hours (air cool)	Performed either solution treatment, solution treatment and age, HIP, or HIP and age
Gao *et al.* [172]			A) 1080°C, 1.5 hours, (furnace cool) OR B) 980°C, 1 hour, (furnace cool)	Double age: 1) 720°C, 8 hours, (furnace cool at 55°C an hour) 2) 621°C, 8 hours (air cool)	Performed A + double age, B+ double age, and A + B + double age
Periane *et al.* [68]	1160°C, 3 hours, 102MPa, rapid cool				

	1160°C, 3 hours, 102MPa, rapid cool			Double age: 1) 720°C, 8h, (furnace cool) 2) 620°C, 8h, (air cool)	
Lesyk *et al.* [189]	1160°C, 3 hours, 160MPa, rapid cool				
Kang *et al.* [190]			980°C, 1 hour, air cool	Double age: 1) 720°C, 8h, (furnace cool) 2) 620°C, 8h, (air cool)	
	1200°C, 4 hours, 103.4MPa, rapid cool			Double age: 1) 720°C, 8h, (furnace cool) 2) 620°C, 8h, (air cool)	
Park *et al.* [174]			980°C, 1 hour, air cool	Double age: 1) 720°C, 8h, (furnace cool) 2) 620°C, 8h, (air cool)	
	1200°C, 4 hours, 103.4MPa, rapid cool			Double age: 1) 720°C, 8h, (furnace cool) 2) 620°C, 8h, (air cool)	
Tucho *et al.* [177]			1100°C for either 1 hour or 7 hours		
			1250°C for either 1 hour or 7 hours		
Brenne *et al.* [180]			550°C, 1 hour, air cool OR, 700°C, 1 hour, air cool OR, 1000°C, 1 hour, air cool	Double age: 1) 720°C, 8h, (furnace cool) 2) 621°C, 8h, (air cool)	
Gruber *et al.* [187]	1150°C, 4 hours, 100MPa		1100°C, 1 hour Or 1065°C, 1 hour	Double age: 1) 720°C, 8h, (furnace cool) 2) 621°C, 8h, (air cool)	Applied a stress relief stage before removal from baseplate: 1150°C, 6 hours or 1065°C, 1.5 hours
Schneider *et al.* [191]	1163°C, 3 hours, no pressure given	1163°C, 1 hour	1010°C, 1 hour	Double age: 1) 720°C, 8h, (furnace cool) 2) 620°C, 10h, (air cool)	Comparison of different combination of all heat treatments. Some had a stress relief treatment of 1066°C for 1.5 hours applied before.
			954°C, 1 hour		

From here, the majority of papers deviated from one another and focused on investigating the effects of various combinations of heat treatments at different temperatures. In general, the solution heat treatment temperatures were clustered around either 980°C for about 1 hour (only one study reported a dwell of 7 hours at this temperature [117]), and the homogenisation heat treatment temperatures were found to be above about 1080°C for approximately 1 hour. Some studied the effects of holding the homogenisation time for an extended period of time, for example 7 hours, and compared this to the effects of a 1-hour dwell. Those who investigated the effects of HIP, tended to perform these first, followed by different homogenisation and solution treatments. The results are detailed below in sections corresponding to the heat treatment temperature cluster they belong to.

Solution Heat Treatment below 1000°C

There is an overlap in temperature between what some authors term a 'solution treatment' and what they deem high enough to call a 'homogenisation treatment'. Therefore, for the purposes of this review, all studies that report a temperature below 1000°C will be discussed in this section, and all other studies will be discussed in the section, 'Homogenisation Heat Treatment above 1000°C'.

The large volume of work that has been reported on this topic has generally come to the same conclusions. After a low temperature solution treatment, the elongated columnar grains and sub grain cellular structures specific to LPBF are still evident. Brenne *et al.* [180] studied the effect of three different solution heat treatments prior to double ageing, 550°C, 700°C and 1000°C for 1 hour, and observed no difference in grain morphology or texture between each sample.

Looking within the grains, heat treatment temperatures around 980°C for 1 hour are generally not sufficient to remove all of the cellular-dendritic microstructural features of AM parts [117], [163], [172], [174], [176], [180], [181], [190], [192]. However, Aydinoz *et al.* [173] report a sharpening of these cellular structures due to a reduction in the amount of dislocations within each cell boundary region (at 1000°C for 1 hour). This is likely due to the process of recovery.

Most studies report only of the partial dissolution of the Laves phase during solution heat treatments [117], [172], [176]. The dissolution of the Laves phase releases Nb atoms. As the precipitation temperature of δ-phase occurs between 780-980°C, the δ phase mops up the released Nb atoms. As such, it is common to observe both Laves and δ-phase in microstructures heat treated to about 980°C for 1 hour [117], [163], [172], [176], [190], [192]. An example of this is shown in Figure 26a and 26b. In this case, the Laves phase is found at cell boundaries, whilst the δ-phase is reported at both cell or grain boundaries, and within the γ matrix [163], [172], [176], [190]. The δ phase has a high aspect ratio, with dimensions in the range of a few hundred nanometres in width, and 1-2µm in length [172], [176]. Because of this, it is described as being needle-like in shape. Tucho *et al.* [117] showed that an increase in the dwell time of the solution heat treatment (970°C) from 1 hour to 7 hours, causes the length of the δ phase precipitates to increase. Figure 26c and 26d show that they can grow to 10µm in length.

It has been suggested that the precipitation of δ phase during these low temperature solution heat treatments prevents grain growth through grain boundary pinning, with this being one of the primary reasons as to why no major microstructural changes are observed during these heat treatments [172].

In addition to this, grain boundary pinning can enhance the strength, crack initiation resistance and creep resistance of a final component. It has been shown by Gao *et al.* [172] that the presence of the δ phase at grain boundaries acts to increase the stress-rupture life and high temperature tensile strength of the material.

However, the presence of a high amount of δ phase within the grains ultimately weakens the material [117]. This is due to its incoherent nature, the fact that it removes Nb from solution (so γ'' precipitation is reduced), and the increased potential for crack initiation due to dislocation pile up surrounding the precipitates [173], [193].

Figure 26e and 26f show two high magnification images displaying the mixture of Laves phase, carbides and δ phase precipitates present between the cell structures after heat treatment at 850^{o}C for 2 hours. As the precipitation of the γ' and γ'' phases occur between 600^{o}C and 900^{o}C, small amounts of these phases may also be present after low temperature solution heat treatments [192]. They are shaped like ellipsoidal discs, and have been measured to be 55 - 59nm in length, and 11nm - 15nm in width after a low temperature heat treatment up to 7 hours [117].

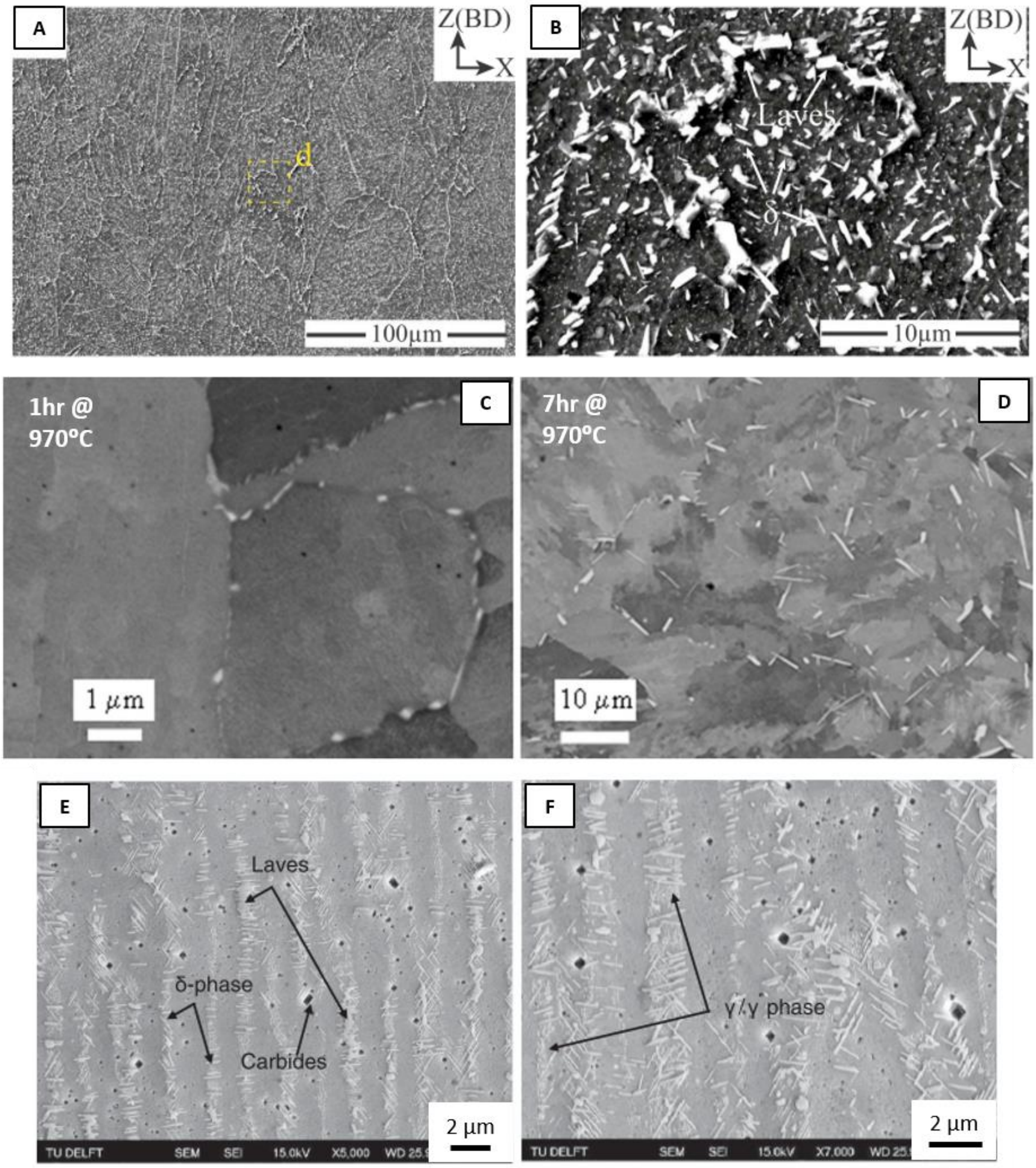

Figure 26: Heat treated microstructures from three different studies; a and b) microstructure of LPBF Inconel 718 after solution treatment of 980°C for 1 hour (water cool) before a double age heat treatment. Both Laves and δ phase precipitates are present, with these being comparatively coarser than after the application of a direct double age heat treatment only shown previously in Figure 25. The Laves phase is primarily found at the grain boundaries while the δ phase is found within the grains [176] **(Reproduced with permission); c and d) shows the comparison of the δ phase precipitates after solution heat treatment at 970°C for c) 1 hour and d) 7 hours** [117] **(Reproduced with permission); e and f) microstructure of Inconel 718 manufactured using a high laser power of 950W after a 2 hour heat treatment at 850°C followed by an air cool. The heat treatment did not trigger recrystallisation and so precipitate structures are observed to be stacked in thin columns associated with the cellular solidification geometry** [192] **(Reproduced with permission).**

Liu *et al.* [194] utilise a heat treatment of 890°C for 12 hours followed by a solution heat treatment at 1020°C between 2 and 240 minutes in order to more quickly reduce the volume of Laves phase present at the intercellular regions of a DED manufactured sample. The initial heat treatment results in the growth of needle like δ phase from the intercellular Laves, effectively cutting the Laves phase in to smaller, disconnected regions. Upon solution heat treatment at the dissolution temperature of the δ phase, the needles are removed, leaving dispersed regions of Laves phase. This reduces the interdendritic Nb concentration and increases the intradendritic Nb concentration in a shorter period of time than if solution heat treatment was applied directly.

Solution Heat Treatment around 980°C + Double Age

Several authors also investigated the effects of applying a double age directly after the low temperature solution treatment of 980°C [181] [190]. In addition to the δ phase, they reported the presence of γ′ and γ′′ within the γ matrix. As the δ phase mops up Nb from the γ matrix, and these precipitates form during the solution heat treatment prior to the double age, there is a depletion of γ′′ phase precipitates immediately surrounding the δ needles. This is shown in Figure 27 [181].

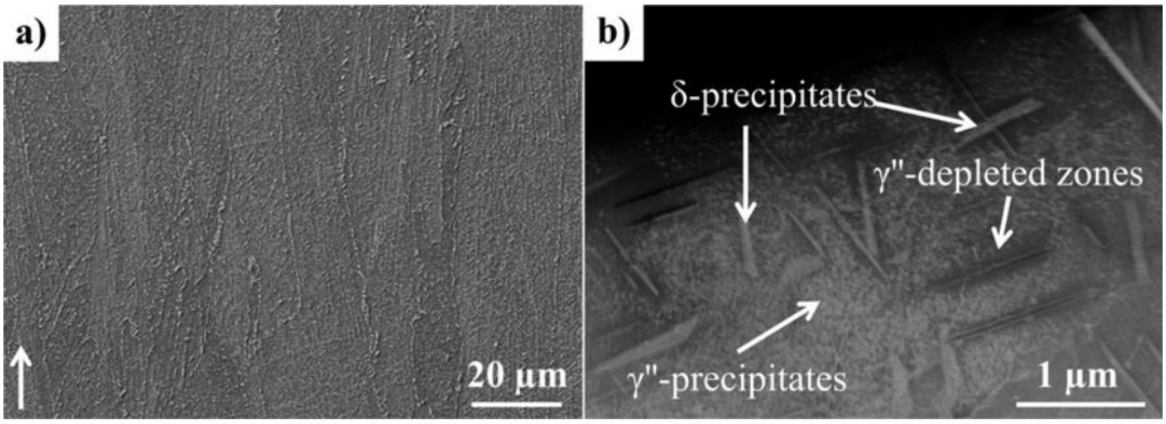

Figure 27: a) STEM micrograph showing in Inconel 718 solution treatment at 980°C and double age, b) higher magnification image showing γ′, γ′′ and δ-phase precipitates [181] **(Reproduced with permission).**

Homogenisation Heat Treatment above 1000°C

Generally, as the homogenisation temperature above 1000°C or dwell time increases, the volume fraction of remaining cellular structures and segregated elements decreases. If the driving force is sufficient, the volume of recrystallised material also increases [117], [176], [179], [187]. This provides the γ matrix with a higher volume of Nb in solution [117]. These temperatures are also near the dissolution temperature of the δ phase [131], [172]–[174], [181], resulting in the reduced ability for this phase to form [172], [176].

The driving force for recrystallisation depends on the stored energy in the material. This is enhanced by the application of external pressure (in the case of HIP). As such, dislocation pile up near precipitates, or plastically deformed voids, can increase the driving force for recrystallisation [179]. As these aspects are so varied between studies, only some authors report the occurrence of recrystallisation in their samples during homogenisation heat treatments. A review of the literature surrounding recrystallisation during HIP and heat treatment is outlined in the next section.

After high temperature homogenisation, several authors report the presence of small amounts of Nb and Ti rich metal carbides, both at grain boundaries and grain interiors [131], [172], [174], [179], [187], [190]. Fine carbides are usually present within the segregated material at cell boundaries in the as-built condition and these can remain in the microstructure after recrystallisation or dissolution of the Laves phase. In one study, in which the material recrystallised during homogenisation, the size and volume fraction of these carbides increased as the homogenisation time increased at a temperature of 1180^{o}C [195]. Conversely, in another study in which the microstructures did not recrystallise, the columnar grain widths were shown to increase as the homogenisation temperature increased from 1040^{o}C and 1200^{o}C. The authors attributed this to a reduction in grain boundary pinning due to the reduction in segregated phases, and MC particles, as the homogenisation temperatures increased [179].

Similar to the effects of δ phase, carbides can aid in pinning grain boundaries, increasing elevated temperature properties. However, they can also result in a detriment to mechanical properties if present in too large a volume, especially when tightly spaced along grain boundaries [27].

Recrystallisation in AM Samples

If the material contains sufficient driving force for recrystallisation, it will recrystallise under the application of a high temperature homogenisation treatment or HIP treatment. The driving force for this has been identified to originate from either high lattice strain and dislocation density gradients [150], [177], [196] or the energy associated with high grain boundary surface areas, both intra-granular [131], [142] and at the edges of discontinuities [56], [197]. Most studies utilise different sample geometries and processing parameters, resulting in different as-built microstructures. Because of this, the majority of studies will deduce differing results as to achieving recrystallisation for a given heat treatment procedure. An as-built part is more likely to attain a recrystallised microstructure after HIP due to the additional plastic deformation introduced into the material by the isostatic pressure applied.

Upon recrystallisation, the resulting microstructure no longer contains cell structures. It is equiaxed, strain free, and contains twin boundaries. Additionally, the preferential alignment of the crystal planes with the build direction (usually observed in as-built AM samples) may reduce, resulting in randomly orientated grains. Each grain contains a homogeneous γ matrix, however, it has been observed that fine carbides can still be present within the γ matrix after recrystallisation. These aspects are demonstrated in Figure 28a and 28B. The size of the recrystallised grains depend on several factors including the time and temperature of the heat treatment, the original grain size, and the amount of stored energy in the material. This was previously discussed in Section 2.3.2.6.

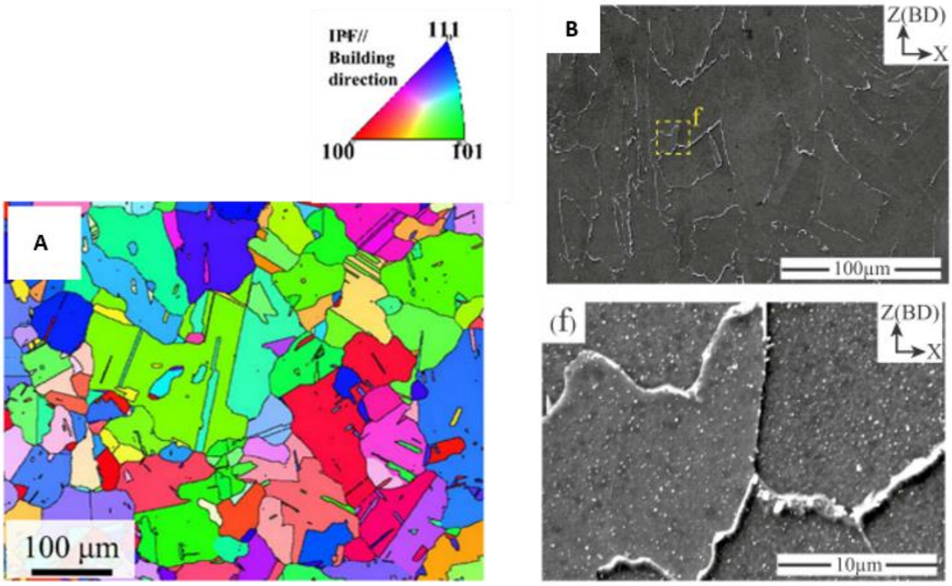

Figure 28: a) EBSD IPF map in the build direction of LPBF Inconel 718 after HIP at 103.42MPa, 1200^{o}C, for 4 hours followed by a standard double age [190] **(Reproduced with permission); b) SEM image of LPBF Inconel 718 after Homogenisation at 1080^{o}C for 1 hour followed by a standard double age** [176] **(Reproduced with permission). Carbide particles can be seen within the grains.**

Generally in the literature, no recrystallisation was observed in samples below 1000^{o}C for any period of time [173], [174], [180], [190]. At temperatures around 1100^{o}C, some studies started to identify either partial or full recrystallisation after an annealing time of above 1 hour. For other studies the annealing time and / or temperature required was higher.

For example, Gao *et al.* [172] report a recrystallised microstructure after homogenisation treatment of 1080^{o}C for 1.5 hours with a furnace cool followed by a double age. However, Deng *et al.* [176] applied the same homogenisation temperature for 1 hour followed by a double age and did not achieve recrystallisation. Nor did Cao *et al.* [116] after a 1 hour homogenisation treatment of 1065^{o}C and double age, or Tucho *et al.* following 1 hour at 1100^{o}C [117]. Tucho *et al.* [150] only achieved full recrystallisation at this temperature (1100^{o}C) after a 7 hour dwell time. Raghavan *et al.* [179] applied a higher temperature solution treatment of 1200^{o}C for 2 hours prior to double ageing and still did not achieve a recrystallized microstructure. Instead, they report on substantial growth of the as-built columnar grains.

However, Tucho *et al.* [177] did achieve full recrystallisation after homogenisation at 1180°C for 30minutes less than Gao *et al.* [172]. In the same study, after the application of a temperature of 1250°C for 1 hour, substantial grain growth was observed. This suggests complete recrystallisation was achieved at the higher temperature. Schneider *et al.* [191] also achieved recrystallisation after what they term a 'stress relief' cycle (1066°C for 1.5 hours) followed by a single aging step (720°C for 8 hours), but do not report the occurrence of recrystallisation after the stress relief cycle only. It is possible that recrystallisation occurred in this sample due to the additional time spent at 720°C, however this is not likely as the authors do not report the occurrence of recrystallisation after a solution treatment (1010°C for 1 hour) followed by a double age. Any heat treatments applied in addition to the stress relief and single age increased the number of visible twins in the material, which is an indication of recrystallisation. This was observed qualitatively from optical micrographs only. This result is supported by the work by Strößner *et al.* [181] who report a partially recrystallised microstructure (with grains still orientated in the build direction, although reduced) after a heat treatment of 1065°C for 1hour, followed by 980°C for 1 hour, and a double age. Additionally, Chelbus *et al.* [131] report patches of recrystallisation after exposure to 1040°C for 1 hour prior to double aging.

The application of HIP increases the likelihood of recrystallisation. In general, the HIP process cycle is longer than that of the homogenisation steps detailed earlier, with many studies applying the HIP temperature and pressure for 3-4 hours instead of just 1. In addition to this, samples are usually exposed to the ramp up and down the HIP temperature and pressure, further extending the time spend at elevated temperature. As opposed to the application of just heat, the HIP exerts pressure on the microstructure which leads to plastic deformation, and an increase in the local misorientation gradients in the microstructure. This increases the driving force for recrystallisation [174], [190]. Because of this, the majority of studies that apply HIP achieve a recrystallised microstructure. Most studies perform a 4-hour HIP, with temperatures between 1100-1200°C, and around 100MPa pressure. [50], [173], [174], [190]. Moussaoui *et al.* [27] performed an additional solution treatment (980°C, 1 hour, air cool) between a three hour HIP (1160°C, 102MPa, air cool), and a double age and achieved full recrystallisation. It is not clear if all of the recrystallisation occurred during the HIP process (note, 3 hours instead of 4 hours), or if the extra hour at 980°C provided the necessary additional time in order to produce a recrystallised microstructure at the end of the full heat treatment process.

Interestingly, Amato *et al.* [17] performed an annealing step (982°C for 0.5 hours) prior to HIP (1163°C, 100Mpa, for 4 hours) and achieved less recrystallisation (5-10% volume fraction) than after direct annealing at 1160°C for 4 hours (>50% volume fraction). This suggests that in this sample, recovery may have taken place during the pre-HIP anneal, reducing the driving force for recrystallisation before the HIP cycle.

This is a good time to indicate that none of the investigations commented on the time required to ramp up to the heat treatment temperature applied. As some recovery is possible during a slow ramp up, it is possible that samples that underwent such a heat treatment had less driving force available for recrystallisation once the correct temperature had been reached. Each study also tested samples of differing dimensions that had been built with different processing parameters. This is why some authors report on recrystallised microstructures after homogenisation treatments only, while some require the additional pressure from the HIP to enable recrystallisation to occur. Therefore, for a set heat treatment temperature and time, the occurrence of recrystallisation in SLM materials is dependent on the geometry and printing parameters utilised.

It is also difficult to state a homogenisation temperature and time that will definitely induce recrystallisation in any sample, as this would cause excessive grain growth in a selection of them, leading to undesirable properties. There exists a trade-off between the microstructural benefits of recrystallisation, and the detriments associated with grain growth, and thus careful consideration of the annealing time and temperature are required.

The literature does suggest that recrystallisation is more likely if medium temperature annealing treatments are prevented prior to those performed at elevated temperatures [177]. It can be implied from this that a faster temperature ramp-up for recrystallisation heat treatments may enable more recrystallisation to occur.

Can an Ideal Heat Treatment Procedure be deduced from these results?

For an ideal material, there should be no δ phase precipitation within the grains before aging. This would enable a high volume fraction of γ' and γ'' to precipitate in this region during aging, with only a small fraction of δ phase precipitating at grain boundaries. Achieving this requires a well-designed homogenisation or HIP treatment prior to aging in order to eliminate the sub-grain dendritic morphology and Laves phase, without enabling the precipitation of δ phase within the grains. The homogenisation or HIP time should be chosen to prevent excessive grain growth as this causes a reduction in strength. It is beneficial to have a small fraction of δ phase at grain boundaries to enhance the strength of the grain boundary region. In order to achieve this, a solution heat treatment should be performed between the homogenisation and aging steps [176].

Figure 29 shows the result of applying different solution treatments (in the range of 900-980^{0}C for 0.5 – 4 hours) to a previously homogenised AM microstructure [193]. δ-phase nucleates at the grain boundaries and grows towards the centre of the grains. This is most evident between 900-920°C. The larger the number of nucleated precipitates, the more they grow towards the centre of the grain. This is because the Nb atoms at grain boundaries will be taken up by other nucleated δ phase particles. As the temperature increases from 940-980°C, the precipitates become smaller and less elongated, precipitating mostly at grain boundaries which is more desirable. It is clear that the applied solution treatment should be kept short, and no temperature drift from 980°C should be allowed to prevent excessive growth of the δ phase.

The precipitation of γ'' phases can then commence after the two step homogenisation and solution heat treatments in the form of the standard double age. However, the duration and temperature of an ideal homogenisation treatment still depends on the amount of strain energy in the part. It has been mentioned numerous times throughout this thesis that the laser parameters, machine utilised, and geometry printed greatly affect the resulting material strain and therefore, the selection of appropriate conditions for the homogenisation treatment remains a difficulty for AM processing.

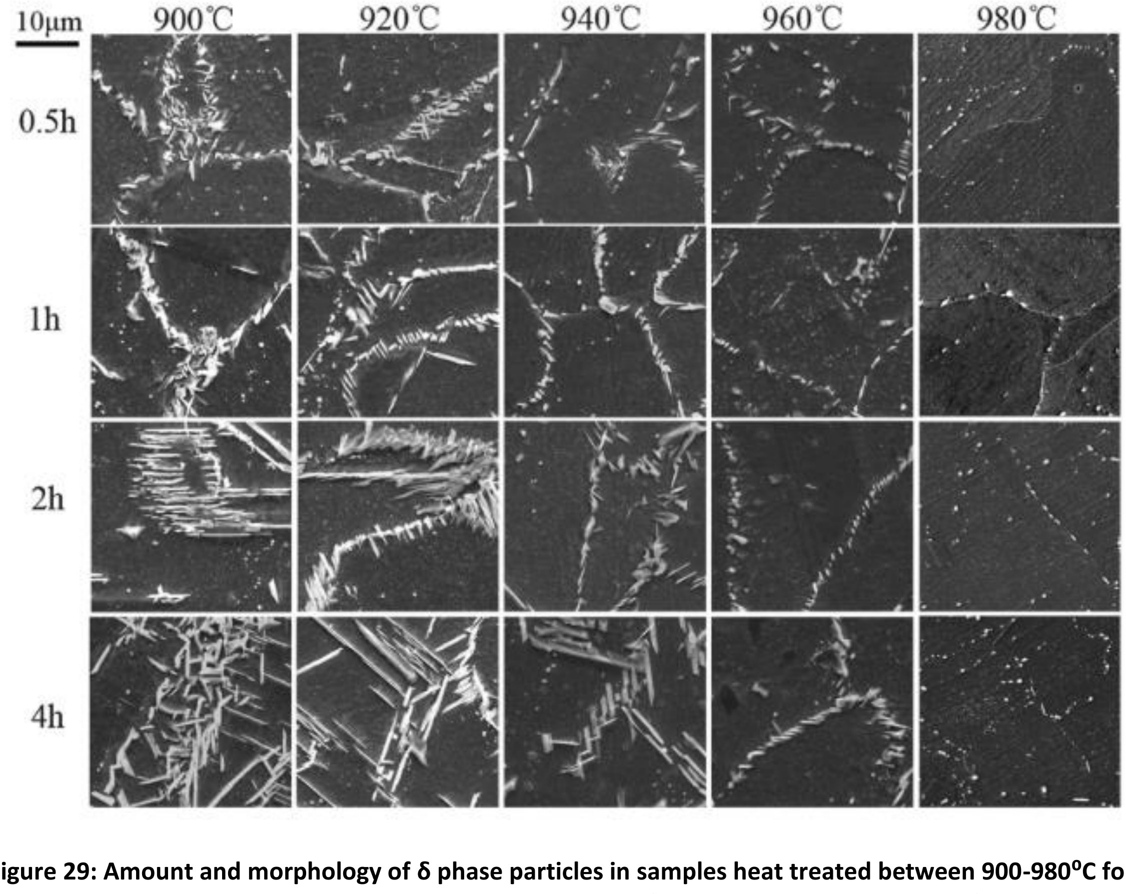

Figure 29: Amount and morphology of δ phase particles in samples heat treated between 900-980°C for 0.5, 1, 2, or 4 hours after initial HIP cycle [193] **(Reproduced with permission).**

2.5.5 Mechanical Properties

2.5.5.1 Hardness

The simplest form of mechanical testing is hardness and therefore, many studies report on this property [173], [176], [192]. Vickers hardness measurements are performed by producing a square based pyramidal indent on the surface of a material. A simple equation linking the applied force and the surface are of the indent allows the material hardness to be determined.

Deng *et al.* [176] observed that the hardness of samples built in the vertical and horizontal directions were approximately similar. In general, the as-built hardness of SLM Inconel 718 samples was in the range of 280-325HV [167], [173], [176], [177], [192]. The minimum hardness achieved by AMS 5662 for Inconel 718 bars is 350Hv, and so as-built samples do not meet this requirement [176]. This is due to the lack of strengthening precipitates present in the as-built state. Independent of heat treatment route, for example, homogenisation and solution temperatures, after a double age, the hardness of samples increased to approximately 490-515Hv [173], [176]. Without the aging step, a homogenisation of 1000^{o}C for 1 hour followed by an air cool leads to lower hardness values (258-280HV), with this value decreasing with increasing homogenisation temperature and time (207Hv for 1250^{o}C/7h) [173], [177]. The application of a HIP treatment with and without subsequent aging leads to hardness values in the range of 440-500Hv, and 230-310HV, respectively [173], [176], [192].

If there is sufficient difference in the height of the hardness measurement along an AM sample in the build direction, a difference in hardness can be obtained. This is due to the differences in cooling rate between material close to the baseplate (heat sink) and material further from this [26].

2.5.5.2 Yield strength, Ultimate Tensile Strength (UTS) and Elongation

Tensile testing provides information on the yield strength, ultimate tensile strength (UTS), Young's Modulus, and ductility of the material by applying a uniaxial tensile force to a sample at a constant strain rate until fracture. Tests can be performed at room temperature or at elevated temperature. The latter would allow a strength value more representative of the material behaviour when in service to be obtained. For Inconel 718, a typical high temperature test condition would be performed at 650^{O}C. According to ASTM E8 for the tensile testing of metals, a strain rate of between 0.05-0.5mm/min is required [198]. In many studies, the LPBF tensile properties are compared to traditionally manufactured Inconel 718, however there is no consistency in the method of manufacture of the control sample between studies.

Due to the preference for grains to orientate with their preferred growth axis along the growth direction, there is directionality in the tensile mechanical properties of samples manufactured (and tested) at different orientations. For example, elongation is higher in samples tested parallel to the build direction whilst yield strength is higher in samples tested perpendicular to the build direction [131], [176], [199]. This is due to differences in thermal history, solidification rate, dislocation accumulation, and number of grain boundaries located perpendicular to the loading direction, between samples manufactured at different orientations [176]. The difference in the mechanical properties of samples built at different orientations decreases with an increase in heat treatment temperature and duration. This is due to progressive homogenisation of the material [176], [181].

Large differences between the mechanical properties in tension occur as the as-built LPBF sample is heat treated. An overview of the measurements identified in the literature are summarised in Table 5. In general, the as-built samples show inferior yield strength and ultimate tensile strength in comparison to wrought Inconel 718, both at room temperature and at 650°C [172], [179], [192]. However, they do achieve higher elongation, 22-33%, versus 12-14% for wrought material at room temperature [172], [191], [192]. Direct aging of the as-built samples in one study lead to an increase in yield strength from 690MPa to 1269MPa [191]. Heat treatment at 1000°C/1hr/AC, leads to a reduction in yield and UTS [173]. This is due to a decrease in dislocation density, the presence of a small number of incoherent precipitates that do not produce strengthening effects, and the dissolution of Laves phase, leading to a primarily single phase γ matrix strengthened only by solid solution strengthening. Comparatively, heat treatment at 850°C/2h/AC lead to a slight increase in yield strength (875MPa) and UTS (1153MPa) and a drop in elongation (17%) as compared to the as-built condition (668MPa, 866MPa, and 22% respectively). This is attributed to the lack of recovery of the as-built microstructure, decrease in laves phase, and increase in volume fraction of δ phase particles at grain boundaries [192]. Above 650°C, however, any γ'' precipitates in the matrix coarsen and transform to δ phase, which reduces the strength of the matrix and limits the strength obtainable by this heat treatment.

The combined application of a higher homogenisation temperature of 1000°C/1hr/AC followed by a double age of 720°C/8h/FC to 620°C/8h/AC enables the Laves phase to dissolve back into the matrix, releasing Nb for γ'' precipitation, suppresses the formation of δ phase, and enables stable coherent γ' and γ'' precipitates to form. The resulting yield strength and UTS are much higher, at approximately 1070-1240MPa, and 1320-1450MPa respectively [131], [172], [173], [179], [191]. A sweet spot in terms of homogenisation temperature seems to be observed; at temperatures above 1100°C and below 1000°C, the strength values are reduced [172], [179]. Indeed, a homogenisation temperature of 1200°C followed by a double age led to a yield strength and UTS of 828MPa and 1330MPa respectively [173]. Additionally, as the application of homogenisation temperatures around 1010 - 1066°C increases in time prior to ageing, the final strength values are also shown to decrease compared to after the application of homogenisation for 1 hour prior to ageing [191]. This is likely due to the loss of strength provided by residual stress and dislocation networks as the material recovers or recrystallises [176].

HIP processing alone on as-built samples generally results in the lowest yield strength values (430-645MPa), these lying below those for the as-built samples [173], [192]. This is due to the material homogenising and softening during recrystallisation, after which the majority of the strength in the material arises from solid solution strengthening. A corresponding increase in elongation to 38% was recorded, and UTS values in the range of 875-1025MPa were achieved. This shows that the material allows a much larger amount of work hardening after HIP. Even after adding an aging treatment, yield and UTS strengths in the range of 1100-1145MPa and 1376-1315MPa were observed respectively [173], [192]. This is still below the values attained after homogenisation and ageing.

When tested at elevated temperatures, for example at 650^{o}C, LPBF samples heat treated with an optimised schedule have been shown to observe similar or higher yield and UTS than wrought material [172], [192].

Each of the samples in these studies were built with differing process parameters, in different machines, and had different geometries. Therefore, the thermal history and microstructure in each of the parts will have been different, and so the effects of a similar heat treatment will have had different effects on the material in each study. This has knock-on effects on the mechanical properties, proving the difficulty in understanding the performance of even a single material produced by AM.

Table 5: Mechanical properties obtained from tensile tests on SLM and heat treated Inconel 718 samples. Samples in [179] **were printed at 0°, 15°, 30°, 45°, 60°, 75°, 90° to the build platform in order to obtain average values of properties. Other samples were built at 90° to the built platform. All 'age' treatments performed were at or very near to 750°C/8hr/furnace cool to 620°C/8hr/air cool unless otherwise stated** [173], [179], [192]**.**

	Test Temperature	**Heat Treatment**	**Yield Strength (MPa)**	**Young's Modulus (GPa)**	**Elongation (%)**	**UTS (MPa)**	**Hardness (HV)**
Raghavan *et al.* [179]	Room Temp	As-Built	621		29	967	
	Room Temp	1040°C/2h/AC + age	1210		18	1400	
	Room Temp	1040°C/2h/AC + 700°C/28hr	1210		19	1410	
	Room Temp	1100°C/2h/AC + age	1140		18	1320	
	Room Temp	1200°C/2h/AC + age	828		22	1130	
	Room Temp	Rolled + HT	1093		20	1330	
Aydinöz *et al.* [173]	Room Temp	As-Built	580			845	320
	Room Temp	1000°C/1hr/AC	535			870	280
	Room Temp	HIP-1150°C/1000bar/4h/FC	430			875	230
	Room Temp	1000°C/1hr/AC + age	1240			1400	515
	Room Temp	HIP + age	1100			1315	440
Popovich *et al.* [192]	Room Temp	As-Built	668	173	22	866	287
	Room Temp	850°C/2h/AC	875	190	17	1153	360
	Room Temp	HIP 1180°C/150MPa/3h/FC	645	188	38	1025	310
	Room Temp	HIP + 1065°C/1hr/AC + 760°C/10h/FC/650°C/8h/AC	1145	190	19	1376	468
	Room Temp	Wrought	916	200	17	1055	353
	650°C	As-Built	650		28	845	
	650°C	HIP 1180°C/150MPa/3h/FC	626		29	857	
	650°C	HIP + 1065°C/1hr/AC + 760°C/10h/FC/650°C/8h.AC	942		20	1078	

	650°C	Wrought	955		14	1061	
Schneider *et al.* [191]	Room Temp	As-Built + age	1269		15	1739	
	Room Temp	As-Built	698		33	995	
	Room Temp	As-built + 1066/1.5hr/WC	859		34	1171	
	Room Temp	1010°C/1h + age	1238		19	1379	
	Room Temp	1066°C/2h +1010°C/1h +age	1203		22	1390	
	Room Temp	1066°C/2h +HIP 1163/3h/no pressure given + 954°C/1h +age	1087		23	1385	
Trosch *et al.* [199]	Room Temp	980°C/1hr +age(718,621)	1180/1185*		20.4/18.6*	1400/1380*	
	450°C	980°C/1hr +age(718,621)	1026/1046*		15.9/13.7*	1160/1210*	
	650°C	980°C/1hr +age(718,621)	860/862*		14.2/7.9*	992/1026*	
	Room Temp	Forged Control	1192		19.1	1380	
Gao *et al.* [172]	Room Temp	As-Built	848		22.8	1126	
	Room Temp	1080°C/1.5hr/FC + age	1173		13.5	1450	
	Room Temp	980°C/1hr/FC + age	1084		10.1	1370	
	Room Temp	1080°C/1.5hr/FC + 980°C/1hr/FC + age	1046		12.3	1371	
	Room Temp	wrought AMS 5662	1030		12	1280	
	650°C	As-Built	677		40	914	
	650°C	1080°C/1.5hr/FC + age	914		22	1091	
	650°C	980°C/1hr/FC + age	773		18	992	
	650°C	1080°C/1.5hr/FC + 980°C/1hr/FC + age	965		21	1126	
	650°C	wrought AMS 5662	862		12	1000	
Chlebus *et al.* [131]	Room Temp	As-Built + age	572	162	19	904	
	Room Temp	1100°C/1hr/WC + age	1074	163	19	1320	

2.5.5.3 Creep Behaviour

Creep is plastic deformation that occurs when a part is loaded for long periods of time at a stress level below its yield point. This can result in component geometries that are no longer within tolerance as well as lead to failure by material rupture. In the case of turbine blades, progressive elongation can cause contact with the engine housing, resulting in considerable damage to the engine. The process is accelerated by elevated temperatures and so reducing the creep rate and increasing the creep life of a material intended for use in high temperature engineering applications is imperative [200].

Depending on the applied temperature and stress, creep can occur due to different mechanisms. These mechanisms can loosely be divided into diffusion related or dislocation related [200]. At very high temperatures and low stresses, deformation can occur by vacancy diffusion within grains, or at grain boundaries. In most engineering applications, the working temperatures are lower and stresses are higher. In these cases, creep depends mostly on dislocation movements such as dislocation glide and climb [200].

Creep damage occurs by the formation of voids on the micron scale at grain boundaries (usually those perpendicular to the applied stress [112]), or at grain boundary precipitates. As these grow and combine, the effective load carrying area of the material is reduced, leading to a loss of strength [201]–[204].

Where creep is dislocation driven, is it imperative to strengthen the material against the movement of these. This can be achieved through a combination of solid solution strengthening, and the precipitation of second phase particles both within the grains, and to a certain extent, at grain boundaries [202], [203], [205]. However, care must be taken as coarsening of the δ phase at grain boundaries during high temperature exposure may lead to cracks appearing, quickly reducing the strength of the part [112], [206], [207].

The grain boundary also plays an important role in creep. A wider grain boundary area provides a higher potential for cavity formation [202]. Therefore, the engineering of a material with a high proportion of low CSL boundaries (∑3 and ∑9) is important for creep resistance. In addition, stress concentrations resulting from dislocation pile up at grain boundaries has been shown to cause crack formation [206]. Therefore, minimisation of the volume fraction of grain boundaries is beneficial for creep life. This is the notion behind the manufacture of single crystal turbine blades.

Despite its importance, few studies have investigated the creep behaviour of LPBF Inconel 718, potentially due to the elevated temperature testing equipment, and time, required for testing. Those who have, have performed a variety of different tests including, compression creep [179], [203], [204], stress rupture creep [202], [209] and two bar specimen creep [205], [210], making comparison between the studies difficult. Some looked at the aspects of heat treatment [179], [202], [204] while others investigated the effects of loading orientation [121], [203], [211] and scan strategy [121]. Additionally, although the test temperature was similar between studies at 650^{o}C, the stress applied in each study differed between 650-900MPa. Some studies observed a superior creep response [204] compared to traditionally manufactured wrought material while some observed inferior properties [205], [209], [211], [212].

2.5.5.4 Oxidation Behaviour

Oxidation is a chemical reaction between a metal surface, and oxygen in the air, whereby some of the metal atoms in the alloy transfer electrons to the oxygen atoms in contact with them. The oxygen atom then forms an oxide nucleus on the surface of the metal which grows to form the oxide scale. Once the oxide layer has developed, further growth occurs by the diffusion of oxygen inwards, or metal atoms outwards, through this [208], [209]. Diffusion increases with temperature, and so the rate at which oxidation occurs also increases with temperature [210].

The oxidation behaviour of metallic samples can be investigated by exposing them to elevated temperatures for a specific amount of time and measuring the weight gain per unit area (Δm) using Equation 5, where W_t is the mass of the sample at time t, W_0 is the starting mass of the sample, and S_0 is the surface area of the sample [190], [211].

$$\Delta \boldsymbol{m} = \frac{\boldsymbol{W_t} - \boldsymbol{W_0}}{\boldsymbol{S_0}}$$

Equation 5

In the presence of a dense and protective oxidation layer, further oxidation of a metal alloy usually takes place with a continuous reduction in rate [28]. Therefore, when the mass gain is plotted against time, it forms a parabolic shape, whereby the mass gain per unit of time decreases as the oxide scale grows in thickness [208], [209]. This is the basis of how high temperature materials operate, by forming a protective oxide layer, further oxidation can be reduced. As the scale can only grow via the diffusion of elements through both the base material and the oxide, the oxidation rate depends on the amount of defects, including grain boundaries, present in the material.

The growth of the oxide scale is accompanied by an increase in stress within the layer [208]. Unless the thermal expansion coefficient of the oxide scale is the same as the metal substrate, the stress may become too large, and cause the oxide layer to crack and spall. This results in the exposure of the base metal to the atmosphere, leading to increased oxidation of the base metal.

Alloys for high temperature applications contain elements specifically selected for their ability to form protective oxide layers. Inconel 718 contains 17-21wt% Chromium, which allows the formation of a stable and protective chromia-based oxide layer, Cr_2O_3, at temperatures between 550-850^oC [208], [210], [212], [213]. A stable Cr_2O_3 layer slows down the inward diffusion of oxygen ions to a point where there is no longer sufficient oxygen available for the formation of Cr_2O_3. At this point it is possible to form TiO_2 or Al_2O_3 at higher temperatures [213], [214]. It is important to note that at temperatures above 900-950^oC, these chromia-based oxides break down [208].

If the diffusion of Cr atoms in the material is slow, large scale segregation is present in the material (such as for large castings), or a Cr depleted layer is produced at the metal/oxide interface due to rapid Cr_2O_3 formation, it can lead to these atoms being unavailable for continued growth of the oxide scale. In this case, if other oxide forming atoms are present, either as part of the metal matrix, or within a γ', γ'', δ, or MC, precipitate, it is possible to form other oxidation products such as Ni, Ti, Al, Fe, or Nb based oxides [28], [215]–[218]. The oxidation of NbC and TiC can lead to a sudden change in shape of the carbide as oxidation progresses. This may cause cracks to form leading to oxide ingress along grain boundaries into the base metal [190], [215], [219].

Diffusion occurs more readily through grain boundaries than through bulk material [28], [215]. It has been shown that the increased number of interdendritic cell boundaries in as-built LPBF Inconel 718 leads to the faster formation of a stable oxide film than in both cast and forged Inconel 718. This is because cast and forged materials have larger grain sizes and elemental segregation distances [215], [217]. Similarly, the slower solidification rates in electron beam AM (EBM) samples produce a comparatively larger dendritic solidification structure than in LPBF, leading to slower oxide formation [214]. Additionally, a coarser dendritic structure leads to the formation of a coarser oxide layer while a finer microstructure enables a more fine grained oxide layer to form, which provides enhanced strength [28].

As-built Inconel 718 contains a high level of interconnected grain boundaries, few of which are special boundaries, which can lead to an increased penetration depth of the oxide along these boundaries compared to in recrystallised material [214]. As the volume of oxygen that is able to penetrate along grain boundaries is lower than that available on the surface of the component, Cr_2O_3 may not be able to form. In these cases, elements with a higher affinity to oxygen from oxides. Therefore, it is common to form TiO_2 or Al_2O_3 along grain boundaries [214].

The anisotropic microstructure observed in as-built LPBF materials is also reflected in the oxide thickness formed on different faces of a component [220], or at different printing orientations [218]. In the presence of defects such as pores, the diffusion of oxygen into the material is faster, leading to an inhomogeneous oxide scale. This leads to the production of varying stresses across the oxide scale which may increase the likelihood of oxide cracking and spallation [28]. After spallation, it is common for non-protective Ni, Nb or Fe oxides to form. This is due to the lack of Cr still present at the metal/oxide interface as they have already been consumed by the original oxide film [28].

Many studies investigate the oxidation behaviour of LPBF Inconel 718 at tempeartures of 800^{o}C and above [210], [214], [218]. This can potentially release harmful oxidation products and may not necessarily be representative of the oxidation kinetics at the maximum working temperature of Inconel 781; 650^{o}C. In addition to the Cr_2O_3 scale, the oxides reported to have formed in Inconel 718 at these temperatures are: $TiNbO_4$ [214], $NiCr_2O_4$ and $NiFe_2O_4$ [28], [210], and SiO_2 [210]. At lower oxidation temperatures such as 650^{o}C, a small number of Nb_2O_5, $NiCr_2O_4$, or a mixture of NiO and Cr_2O_3 particles, have been shown to form within the stable Cr_2O_3 scale [221], [222].

2.5.5.5 Fatigue Behaviour

Most often, components in operational machines fail due to fatigue. This is the repetitive loading of the component at stress or strain levels below the yield strength of the material [223]. The process of fatigue begins by the formation of small cracks at stress concentrations. In bulk samples, as the crack length increases, plastic deformation occurs at the crack tip and the crack slowly orientates perpendicularly to the applied stress axis [223]. Further loading cycles cause the crack to grow until the material is no longer strong enough to hold the applied load, and fracture occurs. Crack initiation and small crack growth may occur in several places at once within the material.

Several different types of fatigue tests have been performed on Inconel 718 samples manufactured by AM. These are four point bend [68], [224], tensile [225], [226], in plane bending [227], and rotational [57], fatigue tests. Any defects on the sample surface produce stress concentrations which accelerate the formation of slip bands. Therefore, the majority of fatigue fractures start on the surface of a sample [223] and in the literature, samples with polished or machined surfaces obtained increased fatigue lives compared to those with an as-built surface finish [224], [228] [23]. This shows the importance of removing the as-built AM surface prior to allowing a component to go in to service.

A finer grain size and corresponding larger number of grain boundaries increase material strength which decreases the ease at which small cracks can grow [26]. The directional nature of AM parts therefore also results in differences in the fatigue properties of a part printed at different orientations [227].

In comparison to the as-built material, the application of a HIP and double aging heat treatment, leads to a higher fatigue life in a test piece. This is due to a decrease in the amount of brittle phases present, as well as an increase in the amount of strengthening phases in the material [68]. However, in comparison to applying just a HIP (recrystallisation) heat treatment, the application of a short solution heat treatment (1000°C/1h) and double age, which is not sufficient to remove the presence of sub-grains, also produces a longer fatigue life [173]. This shows that the material in which dislocation motion is more impeded, aids fatigue life in Inconel 718.

All studies that investigated the fracture surface of fatigued samples found that cracks initiated at pores in, or on the surface of, the material. Across all studies, this porosity is believed to be the reason for the reduced fatigue life, and increased test scatter, in LPBF materials [23], [26], [68], [159], [224]–[227]. Therefore, any method of manufacture which reduces surface roughness or eliminates internal porosity is believed to increase the fatigue performance.

2.5.5.6 Summary

The microstructure of LPBF Inconel 718 has been heavily detailed in the literature. However, the mechanical properties other than those in static tension have been under reported. In addition to this, as the mechanical properties of AM parts are so sensitive to the cooling conditions and build orientations of the part, standard test coupons may not actually be representative of the performance of a complex component with varying geometries. This is an issue that needs resolving in order to enable more straightforward qualification processes for industrial components.

In general, it can be concluded that for optimal performance, parts are to be void of internal porosity. This is to avoid the formation of stress concentrations as well as preventing unnecessary reductions in strength, fatigue life, oxidation resistance, and creep resistance. Parts would ideally contain a controlled volume of strengthening precipitates within the grains, and a small volume of secondary precipitates at grain boundaries to prevent grain boundary sliding. Grain boundaries should be as coherent as possible to reduce the possibility of grain boundary sliding or oxide ingress. Components which are not required to have anisotropic properties require heat treatments in order to homogenise the grain structure.

2.6 Grain Structure Control and Functional Grading in AM

All of the above literature culminates to this chapter. The aim of this thesis is to utilise the information gathered on manipulating laser parameters on the AM machines, metal solidification, the phenomena of recrystallisation, and the way Inconel 718 operates as a material system when printed via LPBF, in order to manufacture components with distinct microstructures within the same part. This section details the ways in which AM parts have already been functionally graded and outlines the gap in the literature as to how we contribute to the research in Inconel 718.

Functional grading is the spatial altering of material composition or structure to produce corresponding changes in mechanical properties. The technique can be utilised in the design of advanced engineering components in order to reduce assembly time, cost, and complexity, as well as increase functionality; whereby certain regions of a component are tailored specifically to their required in-service demands.

2.6.1 Functional Grading by Material Composition

The gradual variation of material composition from one alloy to another has been studied for a range of materials [4], [229]. Through the use of additive manufacturing, abrupt changes in material properties that arise by multi-material joining operations, such as thermal conductivity and thermal expansion mismatches, can be eliminated. This may lead to a reduction in stress concentrations present in the component during use [230]. Additionally, in applications where the direct transition between two alloys may produce undesirable phases, the alloying freedom brought about by AM may enable an alternative alloying route, allowing these phases to be side-stepped [231].

Due to the method in which metal powder is delivered to the molten region in directed energy deposition (DED) AM, the progressive alloying of powder is simpler to perform using this technique than on LPBF machines. As such, a lot of the research on functional grading via compositional changes has been performed within the DED context [4]. For example, the DED technique was used to manufacture low coefficient of thermal expansion (CTE) radially graded insets for spacecraft panels as shown in Figure 30. Spacecraft panels, usually manufactured from an aluminium or carbon fibre face and an aluminium honeycomb centre, have a lower CTE than the inserts used to secure equipment to the panels. In order to overcome this issue, a linear gradient between 304L stainless steel (with a similar CTE to the A286 steel bolt) and Invar 36 (with a similar CTE to the carbon fibre panels) was printed radially on to the A286 steel bolt. The graded inserts resisted a higher pull out load than the inserts made fully of A286 and Invar 36 [4].

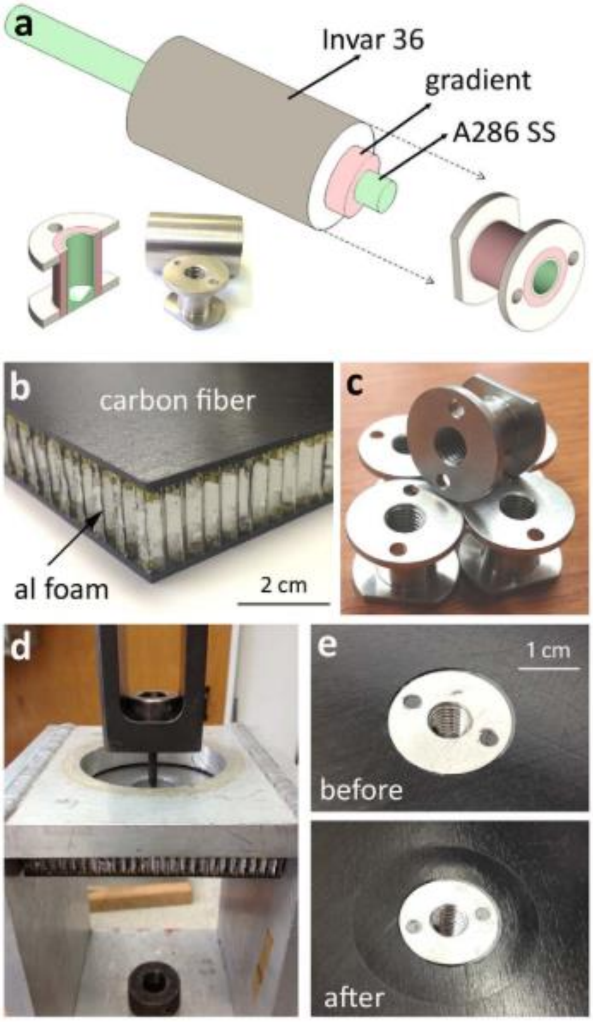

Figure 30: A graded spacecraft panel insert that reduces the mismatch of CTE between the insert and the panel in which it sits. The figure shows the design of spacecraft panels and the positioning of inserts within them for clarity of the discussion [4] **(Permission for reproduction not required).**

Although machine structure makes compositional functional grading easier using DED, Mumtaz *et al.* [232] achieved a compositionally graded joint between the nickel-superalloy, Waspalloy, and a ceramic material used in thermal barrier coatings, Zirconia, using the LPBF technique. The graded joint was sought after in order to reduce the difference in thermal expansion coefficient between the two materials and so, reduce delamination. In order to achieve the compositional grading, 4 layers containing waspalloy and different wt% of zirconia were stacked on top of each other within the powder bed. The human aspect of this layer stacking method makes it difficult, potentially messy, and open to errors in terms of achieving an even grading. Nonetheless, it demonstrated the possibility to achieve compositionally graded structures using LPBF.

2.6.2 Functional Grading by Microstructural Variation

Another method of functionally grading a material is by structural change, either in the form of spatially altering defect populations, or by producing variations in bulk microstructure. In LPBF, the microstructure is manufactured at the same time as the component geometry. This is variable due to the cooling rate differences observed by different geometries during solidification. As the LPBF technique contains a large volume of controllable parameters, each capable of affecting the cooling rate of the molten material, there are theoretically many different methods in which the solidified microstructure can be tailored.

Esmaeilizadeh *et al.* [233] investigated the microstructural effects of varying the laser scanning speed in the LPBF of Hastelloy X. They found that higher scanning speeds led to a refinement of the microstructure through the presence of partially melted powder particles, which locally terminated epitaxial growth and introduced a random grain structure. This is shown in Figure 31. In contrast, a low scanning speed led to the generation of more textured and larger grains elongated in the build direction. These differences led to the generation of variations in strength and elongation across each sample.

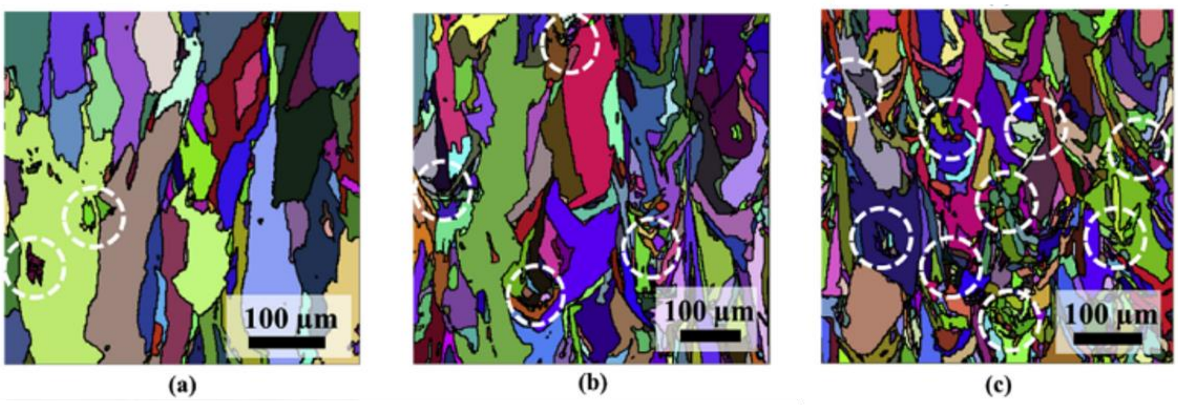

(a) (b) (c)

Figure 31: Effect of increasing scanning speed on grain morphology in LPBF of Hastelloy X. a) shows the effects of 850mm/s, b) shows the effect of 1150mm/s and c) shows the comparative effect of 1300mm/s laser scanning speed [233] **(Reproduced with permission).**

Another group, utilised laser power to produce microstructurally distinct regions in LPBF Inconel 718 whilst keeping the overall volumetric energy density applied equal [9], [26], [171], [192], [234], [235]. Using this method, they were able to produce regions with large elongated grains and high texture, using a 950W laser power, as well as fine equiaxed grained regions with minimal texture, using a 250W laser power as shown in Figure 32. Using digital image correlation (DIC), different levels of strain were observed in the two regions during tensile testing [9].

Although after heat treatment the coarse grained region observed overall better creep properties than the fine grained region, a high amount of scatter was present in the data due to the coarse grained region containing four times the amount of porosity as the fine grained region. This also resulted in poor thermomechanical fatigue life in this region. However, when combined, the multi-modal sample was found to alter the normal mode 1 crack propagation method within the material, with the interface between the microstructurally distinct regions arresting or deflecting crack propagation. This resulted in a longer fatigue life after heat treatment than a sample made from each of the different microstructures alone [235].

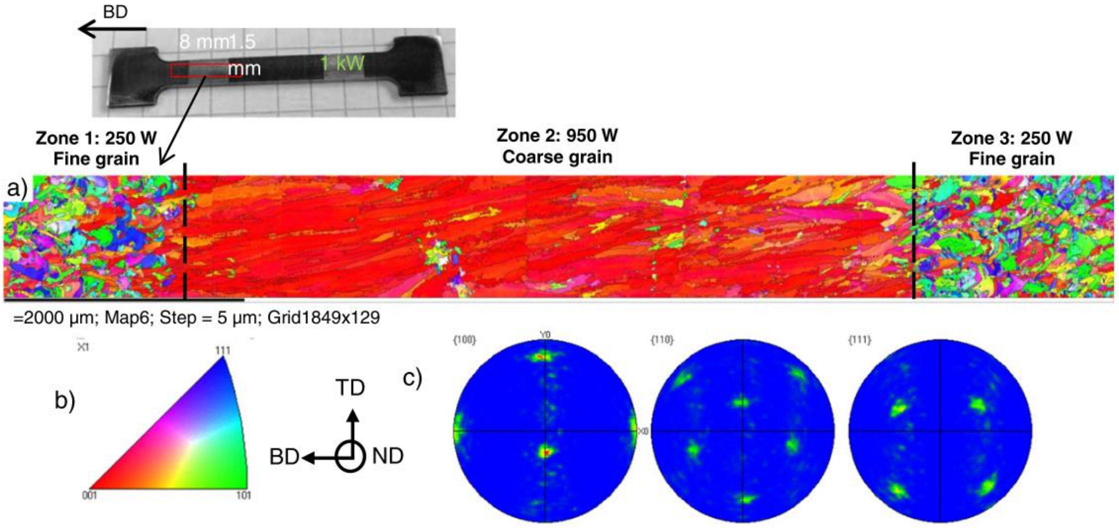

Figure 32: Distinct microstructural regions within a tensile bar produced by Popovich et al. [9] **(Reproduced with permission). The coarse grained region was produced using a 950W laser power and shows a high degree of texture in the <001> direction which is aligned with the build direction. The fine grained region was produced using a 250W laser power and displays a more equiaxed nature with random orientation.**

The researchers also found that altering the printing orientation of samples between vertical and horizontal elicited variations of each microstructural region, along with a change in stress intensity range for fatigue crack growth [26].

Also utilising the ability in AM to alter the input energy density, Sun *et al.* [236] were able to create controlled neighbouring regions of different crystallographic texture in steel. This was achieved by printing with a low enough energy density that would enable the central region of each melt pool to grow parallel to the build direction, whilst the outer edges of the melt pool grew at a 45^{o} angle from this. They found that a higher energy density led to larger melt pools in which all the material grew at a 45^{o} angle from the outer edge of the melt pool towards the centre. Sofinowski *et al.* [175] also achieved spatially tailored textures in 316L stainless steel by modifying the scan angle between layers as shown schematically in Figure 33. Whilst the majority of the grains followed the desired texture in specific regions, a high area fraction of deviant grains always accompanied this. These may have different properties to the grains that did achieve the desired texture. In addition to this, the transition between different textures was not sharp. Nevertheless, an alteration to the grain texture in a crystalline material has the potential to produce spatially varying mechanical properties.

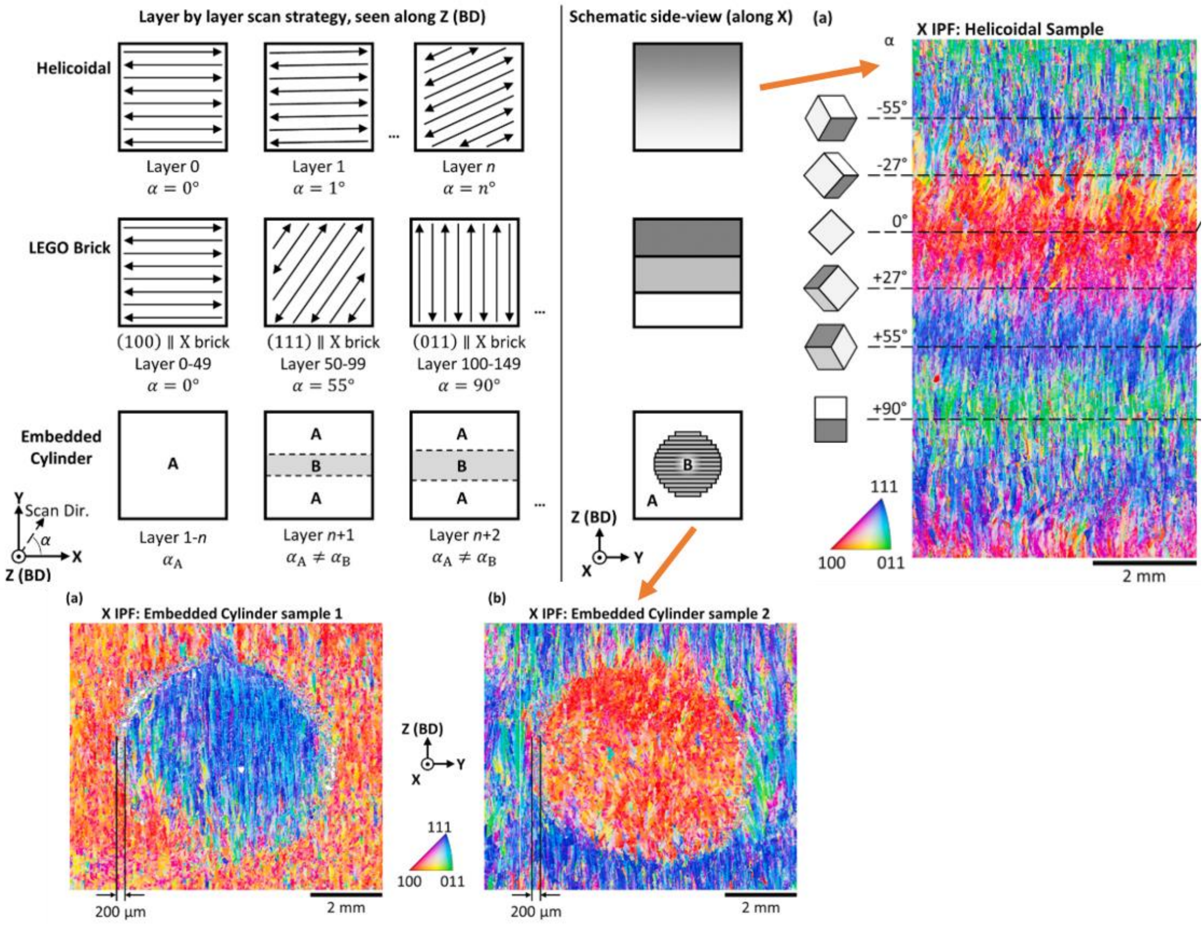

Figure 33: Method of engineering grain texture in to AM parts by altering the meander scan angle between layers [175] **(permission not required for reproduction). Grey schematic shows three different methods of altering the scanning angle between each layer. The helicoidal method involves a 1^0 rotation between each layer. This produces a microstructure in which the grain texture alters throughout the build height. In another cuboidal sample the authors embedded an internal cylinder which was printed at a different scan angle than the shell material.**

Another method of altering microstructure in LPBF is by utilising post process heat treatments. Although not achieved using a LPBF machine, Gao *et al.* [237] utilised CNC capabilities to mechanically deform the solidified surface of a 316L stainless steel DED printed part in specific locations. Upon post process heat treatment, the additional deformation induced by the machining tool triggers recrystallisation leading to twin formation and grain refinement in these specific regions. This is an interesting method of achieving site specific properties and increasing twin boundary density which is of interest in GBE. However, this is currently not possible on LPBF machines. In addition, as the machine tool leads to a gradient of deformation from the surface of the material in to the bulk, the transition between normal AM grain structures and the recrystallised refined grain sizes is transient which may not be beneficial if a more precise location for grain refinement is required.

Engineering components manufactured by AM are usually consolidated by the hot isostatic press (HIP) process in order to remove internal porosity. Due to the high levels of residual stress and lattice strain in AM parts, this process has been shown to alter the as-built microstructure through recrystallisation. This effect has been harnessed by a number of authors.

Using the DED additive manufacturing method, Liu *et al.* [238] identified bands of coarse and finely recrystallised regions in their samples after heat treatment for an hour which was found to be caused by variations in residual stress, and therefore driving force for recrystallisation, between the overlapping regions of neighbouring hatches, and central regions of these areas. Overlapping regions were subjected to remelting and rapid solidification, leading to high residual stress whilst internal regions were only heat treated, leading to a reduction in residual stress. Although not used in order to manufacture functionally graded components in this study, the printing of parts with a varying hatch spacing has the potential to enable regions of varying recrystallised grain size to be produced.

During the time frame of this PhD thesis, several papers have been published with the purpose of altering the grain structure in different AM alloys through the use of HIP. Using electron beam melting and HIP, Hernandez-Nava *et al.* [239] generated titanium parts that comprised of precision located variations in grain size. The authors demonstrated this by enclosing an electron beam melted outline of a beetle within a circular cylinder. The material located between the outer shell and the printed beetle was either loose, or lightly sintered, powder which fully densified after HIP. The differences in microstructure were found to affect the mechanical properties however, insufficient testing was performed to confidently state which microstructure showed the best performance.

Kaletsch *et al.* [57] utilised the aspect of HIP induced densification to produce a bimodal microstructure in LPBF Inconel 718 as shown in Figure 34. By increasing the hatch spacing over a grid lasing pattern, regions of dense material were printed surrounding pillars of unmelted powder which were subsequently densified by HIP. The densified regions in this study were very small, on the scale of 50µm, however HIP densification of powder encapsulated in a 2mm diameter sphere has also been shown for Ti-6Al-4V [51]. Although both projects were initially motivated by an increase in productivity as well as to obtain a deeper understanding of the pore closure capabilities of HIP, it provides an example of another method in which microstructure could be tailored.

Interestingly, the microstructure of Inconel 718 powder densified by HIP is prone to the presence of alumina (Al_2O_3), shown by dark regions in Figure 34, and other brittle Al and Ti rich particles that reside between the former powder particles [57], [240]. In the study by Kaletsch *et al.* this led to weak bonding between the two microstructures which led to fracture during rotation bending fatigue testing.

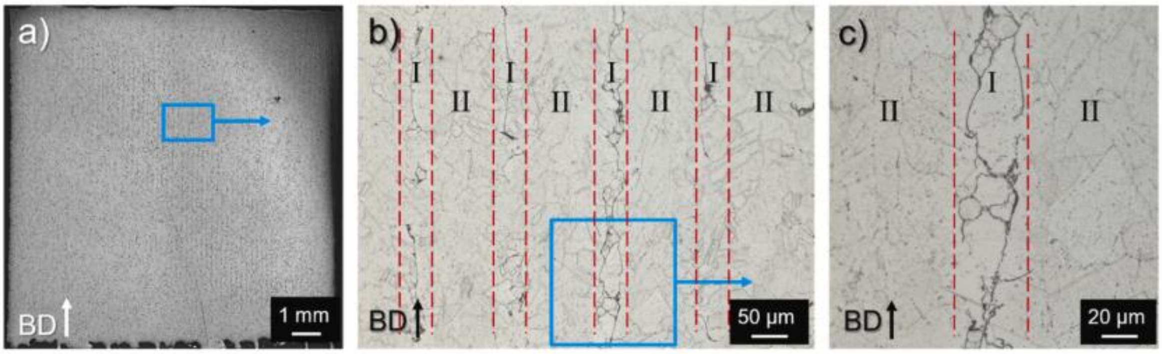

Figure 34: Work produced by Kaletsch at al. [57] **(Reproduced with permission) in which a large hatch spacing, which resulted in rows of unmelted powder residing between each laser scan line, was used to produce a bi-modal microstructure after HIP processing. Image a) shows the grid pattern printed with distinct holes present due to the lack of overlap of the laser scan path, b) shows densified microstructure obtained after HIP processing the full sample with c) showing a closer view of b). Dark regions in b) and c) are regions of Al and Ti rich particles such as alumina.**

Another interesting method of microstructural manipulation can be identified by performing research on microstructures that were previously avoided. Lack of fusion defects, due to their large and often unpredictable size, as well as their sharp internal edges, are highly detrimental to the mechanical properties of any engineering component. As such, they are strongly avoided in research. Bustillos *et al.* [56] utilised this defect structure, with a porosity of 42%, in order to obtain a duplex microstructure in Ti-6Al-4V after HIP. The authors attribute the closure of lack of fusion defects during HIP to be driven by the reduction of high energy surfaces as well as the recrystallisation driven by a high dislocation gradient at the sharp edges of the LOF defects. By changing the HIP temperature from below the beta transus temperature to above it, the average size of the duplex microstructure was also shown to be altered. The LOF samples showed an increase in failure strain of 90% compared to a fully dense control sample that was also post processed by HIP, while retaining the same yield strength. Jiang *et al.* [241], with the initial motivation of increasing build productivity instead of grain size control, also exploited extensive (up to 73%) LOF defects in Hasteloy X. The post HIP microstructure in their samples comprised of fine equiaxed grains, with the grain size dependent on the amount of as-built LOF porosity. The obtained grain sizes led to significantly distinct tensile properties.

The potential for multi-modal microstructures to be produced from internal porosities under the application of pressure and temperature has also been shown in a paper by Xin *et al.* [242], where recrystallisation driven crack healing was investigated in very large 30Cr2Ni4MoV steel ingots. The authors attribute the crack healing to be due to a combination of high strain energy in the lattice, as well as a high surface energy caused by the presence of a crack.

3 Materials and Methods

This chapter contains information on the experimental methods and data analysis protocols used across several chapters. Within each chapter, slight modifications may be made to each of these methods, however this will be stated within the chapter. Any methods that are specific to a chapter will be outlined within the chapter.

3.1 Powder Analysis

Gas atomised Inconel 718 powder (LPW-718-AACJ - Lot Number UK83045 and Powder Range – Lot number not known), size range 15-45µm, was used in this study. The composition of the LPW powder was; 0.52t% Al, 0.002wt% B, 0.03wt% C, <0.01wt% Ca, 0.01wt% Co, 18.96wt% Cr, <0.1wt% Cu, <0.01wt% Mg, 0.01wt% Mn, 3.0wt% Mo, 0.01wt% N, 5.07wt% Ni and Ta, 53.18wt% Ni, 0.02wt% O, <0.005wt% P, 0.004wt% S, <0.001wt% Se, 0.03wt% Si and 0.94wt% Ti. Recycled powder was used after being passed through a 45µm powder sieve (chapters 4, 5, 6, and 7) or a 90µm powder sieve (chapter 8).

3.1.1 Powder Particle Size Analysis

A Malvern Mastersizer 3000 PSA particle size analyser was used to analyse the particle size, and particle size distribution, of the Inconel 718 powder. The technique involves passing a laser though a dispersed particulate sample and measuring the intensity of the scattered light for both red and blue wavelengths over a range of angles. The blue light increases the measurement accuracy of particles below 1µm in size. As not many particles are expected below 1µm in size, this is not expected to significantly alter the results obtained. To perform the analysis, a small quantity of Inconel 718 powder, refractive index 1.960 [160], was dispersed in isopropan-2-ol (IPA), refractive index 1.378 [243]. 30 consecutive readings were taken by the analyser in order to achieve a statistically significant number of results. The particles were designated as non-spherical as it was not known if the particles would be perfectly spherical after the atomisation process.

Results are usually displayed in terms of the powder size under which 10%, 50% and 90% of the total sample volume is covered. This is given by the labels D_v10, D_v50, and D_v90.

It is common to monitor laser obscuration and weighted residual. The weighted residual indicates how well the measurement data fit the calculated data; a value below 1% indicates a good fit. The laser obscuration shows the amount of laser light that is lost due to the sample passing through the analyser beam. This should remain approximately constant and between the values of 3% - 20% for the duration of the experiment. Any fluctuation in the laser obscuration could indicate particle clumping or dissolution of the sample.

3.2 Laser Powder Bed Fusion

3.2.1 Build File Creation

All trials were designed on NetFabb Ultimate (Autodesk). This includes geometry creation and layout within the build space, and the allocation of all process parameters and laser toolpath settings to each geometry. The Boolean logic algorithm was utilised to create internal voids within different samples. Build files were exported in the '.ilt' file format and uploaded to the Aconity software connected to the machine.

3.2.2 Machine Setup

An Aconity Mini (Aconity 3D, Germany), with a continuous 200W ytterbium-doped laser (wavelength of 1070nm) and focused spot diameter of 70µm was used in all trials reported. Specimen building was performed under an argon atmosphere and 50mbar pressure, and a recirculation intensity of 60%; this corresponded to an oxygen content of less than 500ppm. During machine operation, a continuous supply of compressed air (1 bar pressure) was used to cool the laser glass.

The majority of samples printed as part of this thesis utilised a meander scan pattern with a rotation strategy of 90^o between each layer. The initial orientation was generally set to 45^o in order to prevent any excessively long hatches from being lased when printing longer parts. In Figure 35, a 90^o initial deposition orientation corresponds to the direction of layer 1 if viewed from the front of the Aconity Mini machine.

All parts were removed from the AM baseplate by electrical discharge machining (EDM).

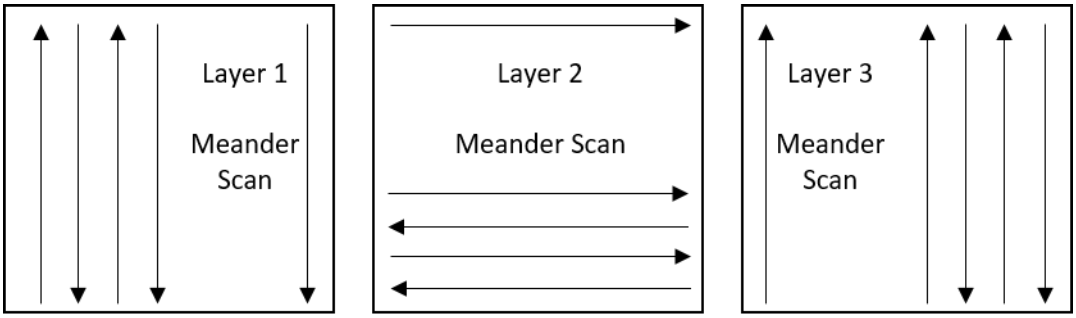

Figure 35: 90^o rotation in laser meander strategy between layers.

3.3 Pyrometry Data Collection and Processing

A Kleiber KG 740-LO spatially integrating pyrometer (operating over wavelengths of 1580-1800 nm) was used to measure the thermal radiation emitted by the material in the vicinity of the laser. The pyrometer was situated in-line with the laser optics, and observed a field of view (FOV) of 1mm in diameter. Pyrometry data was automatically recorded with a sampling frequency of 100kHz during each build detailed in chapters 4-7. Output intensity values were measured in mV.

As the melt pool is orders of magnitude smaller in size than the pyrometer FOV, it is to be noted that recorded data is not solely of the melt pool, but contains regions of cooler, solidified, material as well. This poses issues whereby the differentiation between a small, hot melt pool, and a large, cooler, melt pool is not possible. The pyrometer is currently used on its own, and as discussed in Section 2.2.5 In Process Monitoring Methods for LPBF, would require a secondary pyrometer in order to be able to calculate an absolute temperature value for the material under the laser spot. Therefore, pyrometry measurements detailed in this thesis are not calibrated to provide an absolute temperature value.

As material emissivity changes non-linearly with temperature and surface structure, the pyrometry values detailed in this work can only be used as an approximation of the relative temperature differences observed between each sample. For example, one sample can be regarded as 'hotter' than the other, but no quantification of exact difference is possible. Nevertheless, it provides valuable insight into the build process when viewed quantitatively.

Work is ongoing in order to identify a manner in which the pyrometry intensity values can be correlated to real temperature values, and as such, the values and analysis presented in this thesis will enable valuable insight into real temperature values in the future.

Pyrometry data can be collected either 'by part' or 'by layer'. If the pyrometry data is collected 'by part', all pyrometry data for a specific part is stored within a separate folder for that part only. This allows for easier post processing of the average part temperature using Matlab. If pyrometry data is collected 'by layer', each data file contains the pyrometry data for every part at a specific layer. This allows for fast comparison between different parts on the build plate.

Pyrometry data was processed in Matlab using modifications of an original code written by Lova Chechik (PhD Student, University of Sheffield). It operates as follows;

1) Removal of noise:
    a. Data is smoothed using a kernel smoothing function.
    b. Pyrometer intensities below a given threshold, determined by the frequency of appearance, are considered to be 'noise' and are removed.
2) Data averaging by position - all pyrometer intensity measurements taken at the same X and Y position are averaged.
3) A conversion factor is applied to the X and Y positions to transform the electrical position signals from the pyrometer to physical positions on the Aconity Mini baseplate.

Pyrometer intensity values were either averaged over the layer to provide a single tabulated value, or presented graphically in order to analyse variations in intensity values over a single layer.

3.4 Post Processing Treatments

3.4.1 Hot Isostatic Pressing

Hot isostatic pressing (HIP) was performed (by Vahid Nekouie, Richard Pears, Will Pulfrey, and Jorge Elkin at the Royce Translational Centre, Sheffield) using an AIP8-45H (AIP). The cycle parameters were as follows; 1160°C, 102MPa, for 3 hours, followed by an air cool. The temperature ramp-up rate was 10°C/min.

3.4.2 Furnace Heat Treatments

Heat treatments were performed (by Neil Hind, University of Sheffield) under an argon atmosphere using a muffle furnace (Carbolite). A solution treatment was performed at 980°C for 1 hour followed by an air cool. A double age treatment followed this. The double age procedure was as follows; 720°C for 8 hours, followed by a furnace cool to 620°C for 8 hours, and an air cool to room temperature. For these heat treatments, the samples were put in the furnace at temperature to limit the effect of ramp up rates on the microstructure as much as practicably possible.

3.5 Sample Analysis and Data Collection

3.5.1 Sample Preparation

Where required, samples were sectioned using a 50A20 aluminium oxide cut-off wheel at 2000rpm in a Secotom-50 precision cutting machine, or machined using wire-electro discharge machining (EDM), by the Mechanical Engineering Workshop at the University of Sheffield. Samples were hot mounted in Bakelite using a Simplimet 1000 with a temperature and pressure of 180°C and 29MPa respectively (heat and cool times of 2 and 4 minutes respectively). Samples were ground using a variety of grinding papers and polished for 13 minutes using OPS Colloidal Silica (0.25µm). In order to remove all traces of colloidal silica from the samples, they were rinsed using water on a rotating polishing cloth for 5-9 minutes.

In order to reduce the size of the mounted samples such that they would fit inside the chamber of the SEM used to perform EBSD analysis, the bakelite was subsequently ground down around the samples. The reduced size samples were secured to an aluminium stub using silver paint.

3.5.2 Sample Etching

All samples in this study were electrolytically etched using a 10% by volume phosphoric acid and water solution. A piece of steel, functioning as the cathode, was partially submerged in the phosphoric acid held in a low sided beaker. A 5V voltage was applied across the steel sheet and a conductive wire, functioning as the anode. The wire was touched to the sample surface for approximately 5 seconds or until the surface dulled. Samples were then dipped into two separate water beakers to dilute the acid prior to cleaning with IPA.

3.5.3 Optical Microscopy

All samples were analysed using an Olympus BX51 optical microscope with an automated image analysis system (Clemex).

3.5.4 Density Analysis

Sample densities were analysed by performing an automatic thresholding technique using ImageJ on images acquired by optical microscopy. As pores appear dark on microscopy images, the ratio of solid material to porous material can be determined. In order to understand the bulk porosity across a full sample, images for density analysis were taken at low magnifications, and a mosaic of the whole sample surface was acquired. While this may not provide wholly accurate measurements of density (as finer pores may not be resolvable at this scale), it does give enough evidence of the build quality required for this stage in the research.

3.5.5 Hardness Tests

Vickers hardness information was gathered from fully polished samples using the Durascan automatic hardness testing machine using a 15s dwell time and HV1 load which corresponds to a load of 1kg/f.

3.5.6 Scanning Electron Microscopy

Scanning electron microscopy imaging was performed with an Inspect F50 at the Sorby Centre for Electron Microscopy, University of Sheffield, with an accelerating voltage of 20kV and a spot size of between 3 – 3.5 µm. Secondary electron images were captured in order to show sample surface details while backscattered electron images were used for obtaining images more representative of the bulk of the sample and identifying potential precipitates.

3.5.7 Electron Backscattered Diffraction Analysis

Electron backscattered diffraction (EBSD) was performed in a JEOL 7900 SEM with a focus depth of 21, a probe current of 14 (controlled by spot size, 'large'), an accelerating voltage of 20kV, a specimen tilt of 70^{o}, and step size of between 0.5 and 1.5µm, to analyse the grain orientations within each sample. Some scans were kindly performed by Dr Le Ma (Sorby Centre for Electron Microscopy, University of Sheffield). Grain image and orientation analysis was performed on Matlab using the MTex toolbox and a threshold orientation of $>10^{o}$ to define the high angle boundaries, and $<3^{o}$ to define the low angle grain boundaries. Grains smaller than 3 pixels in size were removed before grain reconstruction and the resulting grains smoothed. Samples with high levels of porosity warranted a slightly different approach; following the removal of grains smaller than 3 pixels, the grains were reconstructed and all non-indexed locations removed. Inverse Pole Figure (IPF) maps were produced with respect to the build direction in order to show the grain growth direction.

4 Printability Studies in Inconel 718

4.1 Introduction

Many studies have been performed in order to observe the effects of different process parameters on the build quality of Inconel 718 parts. The majority of these focus on the application of a volume or linear energy density (produced by a specific combination of laser parameters) and state that defect free parts can be produced within the bounds of two values of input energy. However, many different combinations of parameters can give a similar energy density, and there have not been many studies published which aim to understand differences in grain morphology, if any, obtained whilst printing with different parameters, but remaining under the same energy density. Bertoli *et al.* [25] found that significant differences in the morphology of single scan tracks were obtained in 316L stainless steel after printing with different laser power and velocity values, but the same volumetric energy density. As the power and velocity increased, the scan tracks became more irregular and balling occurred. This work was not extended to bulk parts, and therefore the performance of specific laser parameter sets (constant volumetric energy density) as the cross sectional area of a sample increased, is also not understood.

Additionally, the effects of printing with a defocused laser beam has not seen a great volume of research. As a defocused laser effectively leads to a wider spread of the input laser power, it is proposed that significant variations in build quality can be expected as the beam is moved through focus. This input parameter has largely been ignored in the AM community, however has the potential to enable another level of control over the build process. In addition, if the laser spot diameter is larger than the hatch spacing, this may enable a local heat treatment to be induced in the material surrounding the melt pool, potentially reducing the thermal gradient, and the formation of residual stresses.

All of the above may allow for variations in microstructure within a fully dense print, therefore enabling the production of more functional components. The overarching aims of this section are to:

- Find a set of processing parameters (laser power, velocity, hatch spacing, and layer thickness) that will allow fully dense parts, of varying geometry, to be produced in Inconel 718 using an Aconity Mini.
- Form an understanding of how the individual process parameters affect the density, grain shape, grain orientation, and pyrometry intensity values, across a range of different build conditions.

4.2 Initial Process Parameter Selection

4.2.1 Experimental Rationale and Method

In order to find successful printing parameters for Inconel 718, a Box-Behnken surface response design of experiments (DOE) was performed using Minitab. The power, velocity and hatch spacing was varied between 70-190W, 400-1300mm/s, and 20-130µm respectively. A layer thickness of 30µm was chosen for this work as the powder utilised had a quoted size range of 15-45µm. This was internally verified with results presented herein. All parameter sets in the DOE are displayed in Table 6. Sample numbering begins at 11, as 10 additional samples, not relevant to this experiment, were also included on the baseplate. Samples 12, 16, 24, 25, 29, and 30 were all produced with the same laser parameters to understand the repeatability of identical parameters.

Each sample is a 5x5x10mm cuboid, manufactured with a meander scan strategy, and a 67^o hatch rotation between each layer. The normalised equivalent energy density of each combination of process parameters trialled as part of this DOE have been calculated using Equation 1 (detailed in section 2.2.3), where A is 0.5 [32], ρ is 8100 kg/m^3 [244], C_p is 600 J/kgK [245], T_0 is 297 K [212], and T_m is 1533 K [212]. These are superimposed on the process map by Thomas *et al.* [32] in Figure 36. Average part pyrometry intensity values have been calculated for each part. Within each figure, these are referred to as 'Pyrometry Temperatures' to aid in the understanding of their relevance.

The sensitivity of three of the build parameters, namely those labelled 12, 14, and 15, in Table 7, to different geometries and component sizes was investigated in order to allow confidence in the selection of process parameters that are, within practicable limits, resistant to geometrical effects.

Table 6: Design of Experiments used to identify AM parameter sets that enable high density Inconel 718 to be prepared.

Part Label	Laser spot diameter (µm)	Power (W)	Laser Velocity (mm/s)	Hatch Spacing (µm)	Layer Thickness (µm)	Normalised Equivalent Energy Density, E_0*
11	70	166	1118	108	30	1.91
12	70	130	850	75	30	2.83
13	70	94	1118	42	30	2.77
14	70	166	582	42	30	9.33
15	70	166	582	108	30	3.66
16	70	130	850	75	30	2.83
17	70	130	1300	75	30	1.85
18	70	130	850	130	30	1.63
19	70	94	582	108	30	2.09
20	70	130	400	75	30	6.01
21	70	190	850	75	30	4.13
22	70	130	850	20	30	10.61
23	70	70	850	75	30	1.52
24	70	130	850	75	30	2.83
25	70	130	850	75	30	2.83
26	70	94	582	42	30	5.31
27	70	166	1118	42	30	4.86
28	70	94	1118	108	30	1.09
29	70	130	850	75	30	2.83
30	70	130	850	75	30	2.83

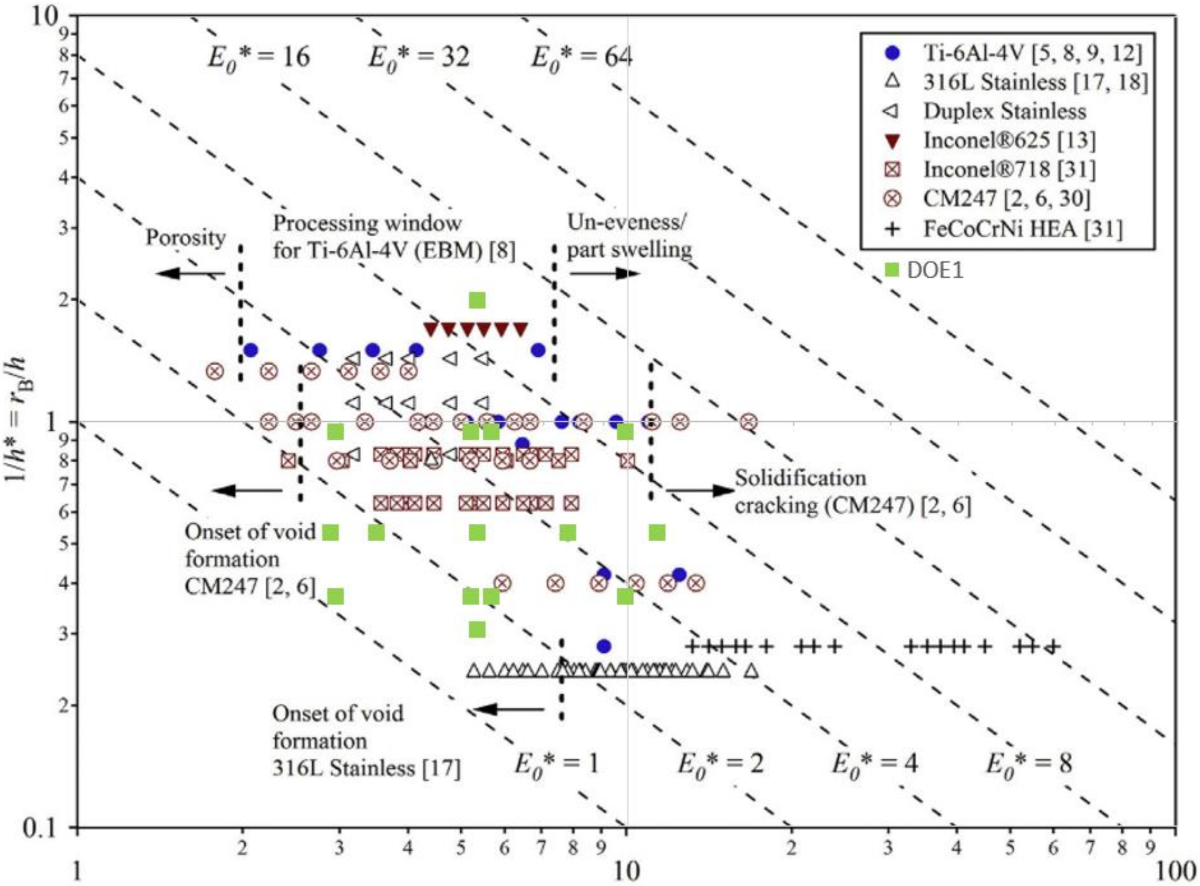

Figure 36: Green squares show the spread of the DOE on the processing map produced by Thomas et al. [32]**. Permission not required for reproduction.**

4.2.2 Results

4.2.2.1 Powder Size Analysis

The average results for the D_{10}, D_{50}, and D_{90} are shown in Table 7. The largest value of weighted residual and laser obscuration are also shown in the table to show that the correct refractive index and absorption values were used in the test set-up. Minimal differences were obtained between the measurements taken using different light sources. This was as expected as blue light is used to increase measurement accuracy for particles below 1μm in size. A weighted residual over 1% would signify the incorrect input of values for the refractive index of the IPA and absorption coefficient of the powder. A laser obscuration that does not lie between 3-20% would signify clumping of the powder leading to inaccurate results. These remained stable throughout the experiment with maximum values as displayed in Table 7.

A D_{10} of 19.6μm signifies that 10% of the sample volume has a particle size below 19.6μm. A D_{90} of 40.3μm signifies that 90% of the sample has a particle size below 40.3μm. This is in good agreement with the powder size distribution of 15-45μm, as stated in the manufacturers documentation.

Table 7: Particle size distribution of Inconel 718. Errors shown as coefficient of variance.

Material	**Number of Measurements**	**Medium**	$D_{10}(\mu m)$	$D_{50}(\mu m)$	$D_{90}(\mu m)$	Maximum Weighted Residual (%)	Maximum Laser Obscuration
Inconel 718	30	IPA	19.6±0.6%	28.4±0.5%	40.3±1.0%	0.29	4.75
Inconel 718	30	IPA – Blue light only	19.6±0.2%	28.4±0.2%	40.6±0.6%	0.3	4.12

4.2.2.2 Initial Printing Parameter Selection

Printed samples are shown in Figure 37. An O_2 sensor error caused the laser to stop firing at layer 36 during the build while the powder delivery system remained operational for 4 layers. LOF defects are visible on some of the parts at this layer height. The average part pyrometry intensity was calculated from layers 41 onwards to omit the erroneous data. This is shown for the relevant cubes (11-30) in Table 8, with errors presented as the coefficient of variance of each data set. Figure 38 shows the average part pyrometry intensity for cubes 11-30 superimposed on the process map along with optical micrographs of the cross sections of a selection of the parts.

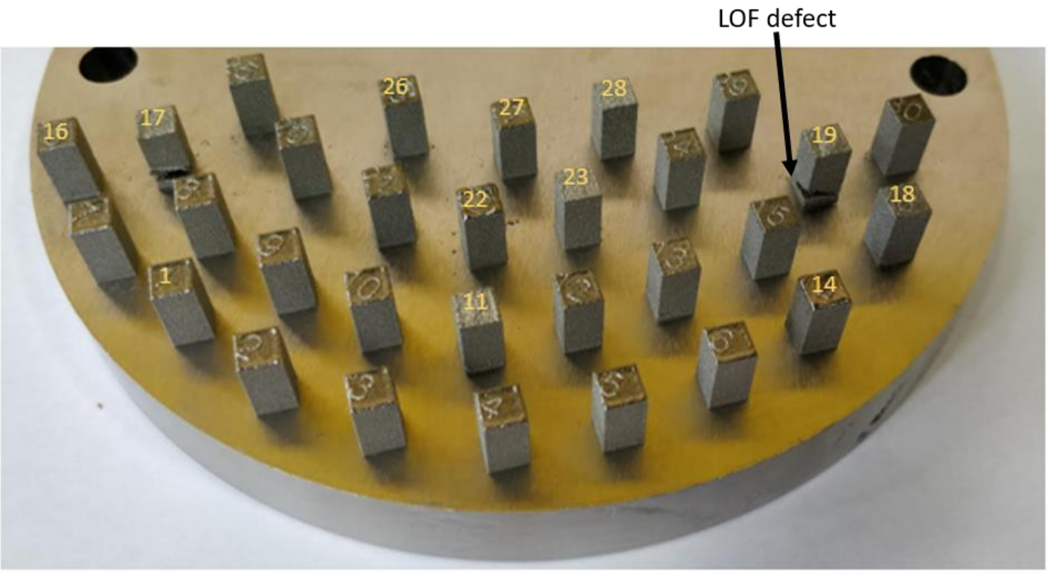

Figure 37: 30 5x5x10mm cuboids printed for DOE1, all labelled on top by a unique identifier. Cubes 1-10 printed as part of a different trial, cubes 11-30 printed as part of this trial with unique combinations of laser power, velocity and hatch spacing. Dimensional accuracy and surface quality noticeably differs as process parameters changes.

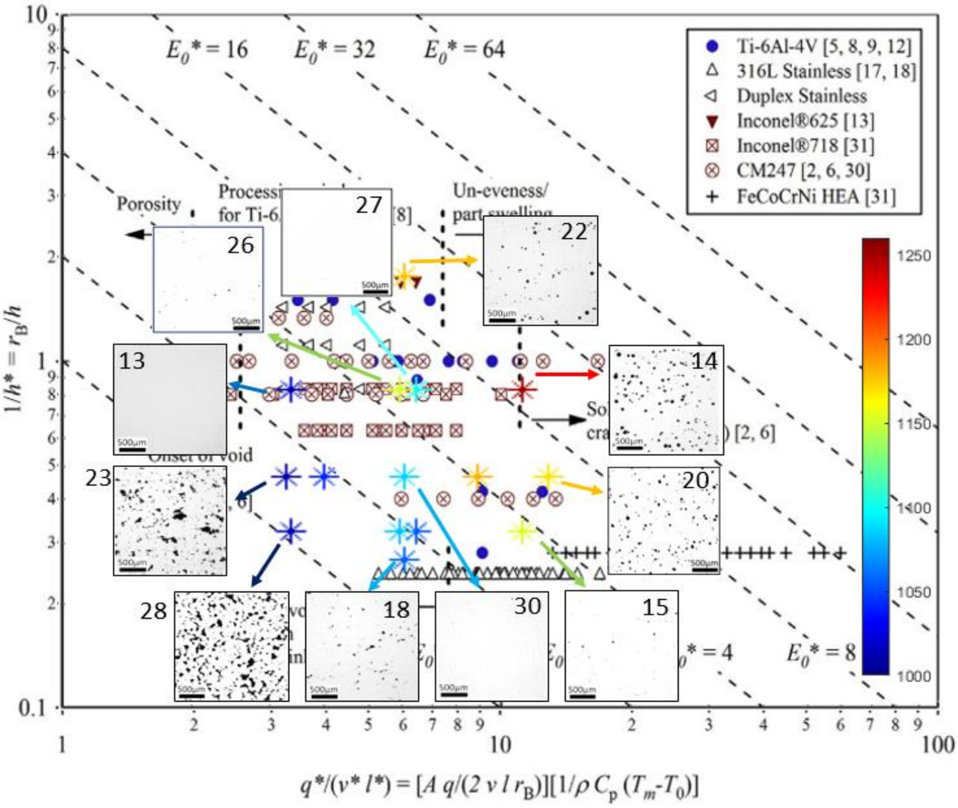

Figure 38: Average part pyrometry intensity in mV (temperature) for cubes 11-30 superimposed on the process map according to the process parameters used to produce each part. Micrographs show defect population and type corresponding to the indicated build. All scale bars are 500µm.

Initially it is clear that samples 12, 16, 24, 25, 29, and 30, all printed with a laser power, velocity and hatch spacing of 130W, 850mm/s, and 75µm, respectively, achieved similar densities and average pyrometry intensity values.

As the normalised equivalent energy density increases, the average part pyrometry intensity increases from about 1000mV to about 2250mV with a corresponding change in defect population from LOF to keyhole porosity. Cubes 26 and 27, which are placed very close together on the process map, show very different average pyrometry intensities and densities. Although they have both been printed with a similar energy density, they are not similar in part quality. Cube 26 utilises a low power and low speed, while cube 27 utilises a higher power and high velocity. Therefore, it is clear that the correct choice of individual parameters is important, and presenting data in terms of energy density alone is inadequate.

Figure 39 shows the difference between linear velocity and hatch velocity. While linear velocity is the laser scanning velocity, hatch velocity can be introduced as the speed at which an area of the cube is printed. Although the builds in this experiment were printed using a 67^{o} hatch rotation between layers, the hatch velocity (displayed in Table 8) was calculated for each parameter with the assumption of a 90^{o} hatch rotation. Figure 40 shows three plots; average pyrometry intensity versus 1) linear velocity, 2) hatch velocity, and 3) laser power. There is no obvious trend between pyrometry intensity and linear velocity, however, as the hatch velocity increases, the pyrometry intensity of each part decreases. The notion of hatch velocity has not yet been identified in the literature, however, this experiment has proven its importance in the selection of process parameters for LPBF. Lastly, a correlation between laser power and average part pyrometry intensity was identified in Figure 40.

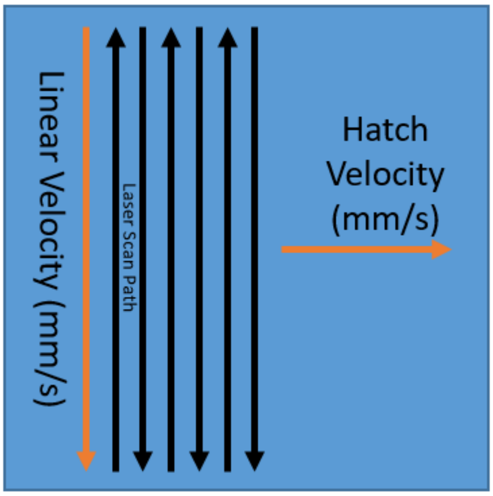

Figure 39: Schematic showing difference between linear velocity and hatch velocity.

Table 8: Density and average pyrometry intensity for printed cubes. Pyrometry intensity errors shown as coefficient of variance. Density values were taken from a single threholded image for each sample and so do not have an associated error. These values are only to provide a rough indication of part density and more analysis is to be done if a more accurate value is required.

Cube Number	Normalised Energy Density, E_0*	Density (%)	Average Part Pyrometry Intensity (mV)	Hatch Velocity (mm/s)
11	1.91	99.64	1082 ± 2%	24
12	2.83	99.94	1082 ± 1%	13
13	2.77	99.95	1012 ± 1%	9
14	9.33	94.90	1251 ± 2%	5
15	3.66	99.70	1153 ± 3%	13
16	2.83	99.97	1076 ± 1%	13
17	1.85	99.69	1040 ± 3%	20
18	1.63	98.94	1056 ± 1%	22
19	2.09	99.45	1053 ± 2%	13
20	6.01	97.18	1169 ± 1%	6
21	4.13	100.00	1181 ± 2%	13
22	10.61	99.59	1178 ± 3%	3
23	1.52	86.60	1011 ± 4%	13
24	2.83	99.98	1085 ± 1%	13
25	2.83	99.91	1080 ± 1%	13
26	5.31	99.87	1096 ± 1%	5
27	4.86	99.99	1153 ± 3%	9
28	1.09	83.66	1011 ± 1%	24
29	2.83	99.95	1086 ± 1%	13
30	2.83	99.97	1086 ± 1%	13

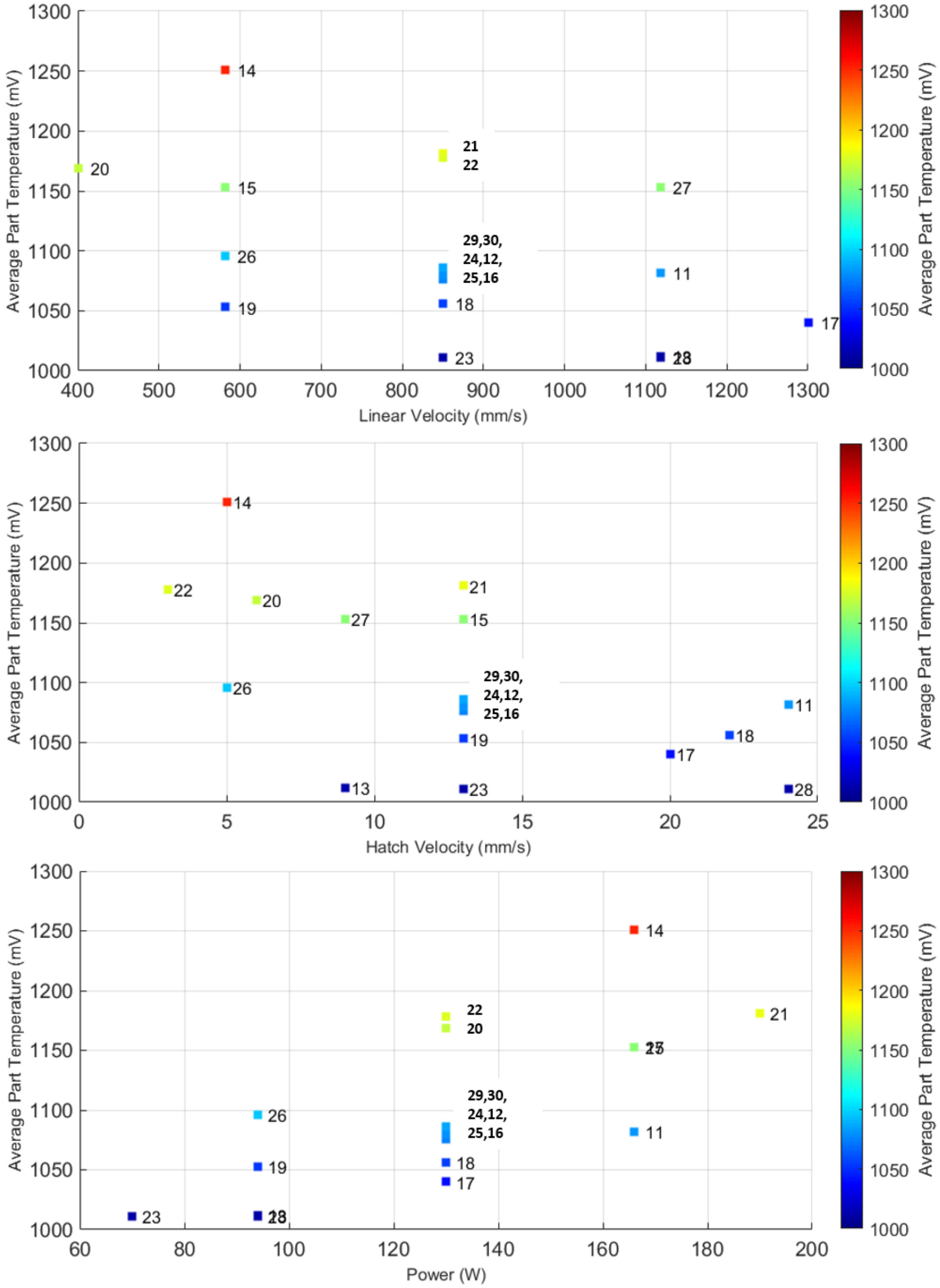

Figure 40: Plots showing the variation in average pyrometry intensity (temperature) versus linear velocity (top), hatch velocity (middle) and laser power (bottom). Colour of points provides visual representation of the pyrometry intensity to ease in comparison. Number labels indicate cube numbers.

Parameter sets 12 (duplicates given by 16, 24, 25, 29 and 30), 14, and 15 were used to build larger shapes (10x10x10mm) and (20x20x20mm) as shown in Figure 41. Parameter set 12 continuously produced highly dense 5x5x10mm cubes and so the stability of this parameter set against larger geometries was to be investigated.

As the printing of larger parts leads to increased laser return times per hatch, and therefore increased part cooling, it was hypothesised that as the part size increased, a higher volumetric energy density would be required to produce a fully dense component. Therefore, parameter sets 14 and 15 were chosen for the build shown in Figure 41. Compared to set 12, parameter set 15 observed a slight increase in normalised equivalent energy density, with an equal hatch velocity, whilst parameter set 14 observed a large increase in normalised equivalent energy density, and a reduced hatch velocity. Only the parts printed with parameter set 14 were unsuccessful due to overheating, and cancelled mid-build. All other shapes printed with high dimensional accuracy and surface finish, proving the stability of the process parameters over a wider range of geometries.

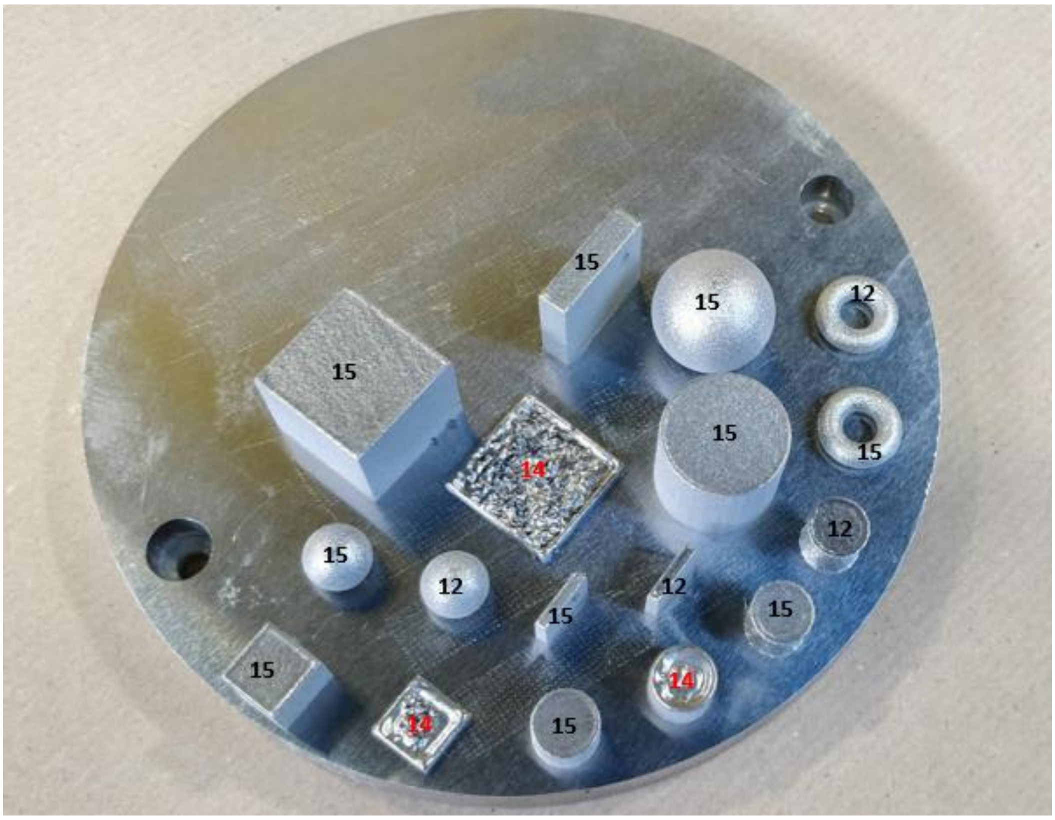

Figure 41: Larger parts printed using parameter sets 12, 14 and 15.

As a result of this work, two parameter sets were identified as appropriate for building Inconel 718 on the Aconity Mini; 1) 130W power, 850mm/s velocity, and 75µm hatch spacing, and 2) 166W power, 582mm/s velocity, and 108µm hatch spacing. It is acknowledged that several other parameter sets detailed in Table 6 may have also produced good results, however in order to remain consistent throughout this thesis, one main standard parameter set was chosen. All builds performed as part of chapters 5, 6, 7, and 8, utilise the parameter set comprising of 130W power, 850mm/s velocity, and 75µm hatch spacing.

4.3 Testing the Limitations of Equivalent Energy Density Part 1

4.3.1 Experimental Rationale and Method

Many authors report that successful printing occurs at specific values of volumetric energy density (VED). However, within the designation of any form of energy density, the process parameters can theoretically take any value, and it is not understood how sensitive to changes in individual laser parameters this overarching statement is. As previously discussed, Bertoli *et al.* [25] identified large differences in the molten shape of single tracks manufactured with different laser parameters, but at a constant VED. This shows that there may be limitations to utilising only VED to describe build parameters.

To elucidate these effects further, three different cube sizes were printed with 8 different parameter combinations outlined in Table 9, all with the same normalised equivalent energy density, $E_0{}^*$ (2.83-2.87) [32]. Cube sizes were 5x5mm, 15x15mm, and 30x30mm, all at 10mm tall. In four of the combinations (set A), the velocity remained constant whilst the hatch spacing was reduced, and vice versa for the remaining four combinations (set B). As the 'changing' parameter was reduced, so too was the power in order to retain the same energy density. In order to achieve consistency between the sets, the power was reduced as follows for both sets; 190W, 140W, 75W, 51W. The time taken to print each layer is shown in Table 9 to highlight the productivity differences between each parameter set.

A 90^{o} hatch rotation was used between each layer. Pyrometry intensity data was collected by layer and the average part pyrometry intensity (labelled as pyrometer temperature) was calculated based on the average intensity of 7 layers (layers taken at approximately 1, 2, 4, 4.5, 6, 7.8, and 8mm in height). The pyrometry data was recoded 'by layer' in order to visualise differences in the pyrometry intensity value between each cube size and parameter set. However, this meant that the calculation of average pyrometry intensity values for each sample required a computationally expensive clustering algorithm to separate the data points to each individual sample. Hence, the average was calculated using 7 layers spaced throughout the height of the parts.

Table 9: Process parameters selected for DOE3 and corresponding time taken to print one layer of each part

						Time to print 1 layer		
ID	**Power (W)**	**Velocity (mm/s)**	**Hatch Spacing (µm)**	**Layer Thickness (µm)**	E_0^*	**5x5mm (s)**	**15x15mm (s)**	**30x30mm (s)**
A-1	190	850	109	30	2.84	0.27	2.43	9.71
A-2	140	850	80	30	2.86	0.37	3.31	13.24
A-3	75	850	43	30	2.85	0.68	6.16	24.62
A-4	51	850	29	30	2.87	1.01	9.13	36.51
B-5	190	1550	60	30	2.83	0.27	2.42	9.68
B-6	137	1120	60	30	2.83	0.37	3.35	13.39
B-7	74	600	60	30	2.85	0.69	6.25	25.00
B-8	49	400	60	30	2.83	1.04	9.38	37.50

The experiment was designed to observe:

- The sensitivity of each parameter combination to a change in cube size.
- The sensitivity of the part pyrometry intensity to different parameter combinations (same normalised equivalent energy density) for a constant cube size.

All medium and large samples were sectioned in two perpendicular planes along the build direction while all small cubes were sectioned just once along the build direction. Density measurements were acquired three times for each section plane, and an average value calculated.

4.3.2 Results

Average part pyrometry intensity and densities for each build condition are shown in Table 10. Errors in average part pyrometry intensity are shown as the coefficient of variance of layer averages. Part A-4, 30x30mm cube, only has an approximate pyrometry intensity value listed in the table as this part was cancelled mid build, and limited data was recorded for it. Errors in the averaged density values were found to be very small. As the human error in performing manual image thresholding was deemed much higher, these have not been quoted in the table. These values therefore only provide a rough indication of part density and a more accurate density analysis is required if a more accurate value is desired.

Table 10: Average pyrometry intensity, density, and layer process speed for all samples printed in DOE3.

	5x5mm			15x15mm			30x30mm		
	Layer Process Speed (mm/s)	Average Pyrometry Intensity (mV)	Density (%)	Layer Process Speed (mm/s)	Average Pyrometry Intensity (mV)	Density (%)	Layer Process Speed (mm/s)	Average Pyrometry Intensity (mV)	Density (%)
A-1	18.5	1115±0.2%	99.96	6.2	1090±0.2%	99.97	3.1	1068±0.9%	99.97
A-2	13.6	1064±0.4%	99.97	4.5	1059±0.1%	99.97	2.3	1035±2.3%	99.97
A-3	7.3	1041±0.7%	98.68	2.4	1027±1.3%	92.28	1.2	1028±1.7%	85.01
A-4	4.9	1017±2.3%	84.59	1.6	1034±3.7%	80.14	0.8	~1003	74.22
B-5	18.6	1063±3.3%	99.99	6.2	1044±1.8%	99.96	3.1	1035±2.6%	99.96
B-6	13.4	1047±5.0%	99.99	4.5	1033±4.3%	99.98	2.2	1004±7.8%	99.98
B-7	7.2	1050±4.7%	99.46	2.4	1036±2.5%	97.08	1.2	1021±9.4%	90.62
B-8	4.8	1029±1.1%	98.23	1.6	994±1.1%	94.33	0.8	990±1.0%	82.73

4.3.2.1 Part Temperature

Average part pyrometry intensities for a single layer (6.02mm) are shown in Figure 42 in order to aid visualisation of the data in Table 10. At higher laser velocities, less pyrometer data points are available for analysis. At lower velocities, a higher proportion of 'edge' position data points were recorded. The pyrometer spot size is larger than the melt pool, so the measured pyrometry intensities will be lower due to imaging of the cold powder bed. Additionally, quicker builds will have a proportionately larger number of data points recorded when the laser is off and the data processing method may not completely remove all 'cold' points. This induces an error in overall part pyrometry intensity when comparing cubes scanned at different velocities [81]. However due to the high sampling frequency of the pyrometer, this effect is deemed negligible and has not been taken in to account in this analysis.

Figure 43 shows that as the part increases in size, the pyrometry intensity reduces. Generally, as the power reduces, the average part pyrometry intensity for all cube sizes also reduces.

Parameter set A-4 utilises a very small hatch spacing, 29µm. The pyrometry intensity of the 15x15mm cube is higher than the pyrometry intensity of the 5x5mm cube printed with this parameter set. It is possible that at very small hatch spacing, unusual effects are observed in the in the way heat is distributed within the part which has manifested in the results obtained. It is also possible that at one length scale, linear velocity is dominant, and at another length scale, hatch velocity is dominant.

For each cube size, the variation in pyrometry intensity across builds printed within parameter set A (varying hatch spacing) is larger than the variation in pyrometry intensity across builds printed within parameter set B (varying laser velocity). This is shown in Figure 44. This suggests that the process is more sensitive to hatch spacing than to the laser velocity. Pavlov *et al.* [81] as well as Doubenskaia *et al.* [89] state that the hatch spacing is the most significant parameter affecting the quality of a LPBF build. This is likely to be due to the effects of how much contact the melt track has with the solid bulk and therefore, the level of heat conduction possible away from the heat source. This effect is not generated when altering the velocity, so following this logic, the pyrometry intensity variation within set B is expected to be less.

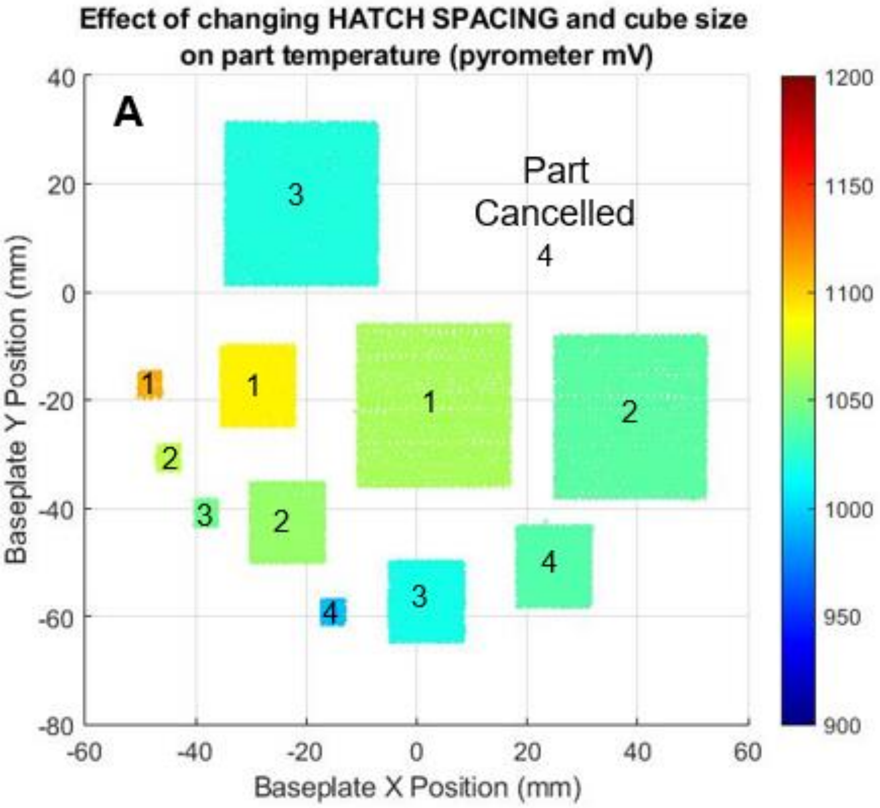

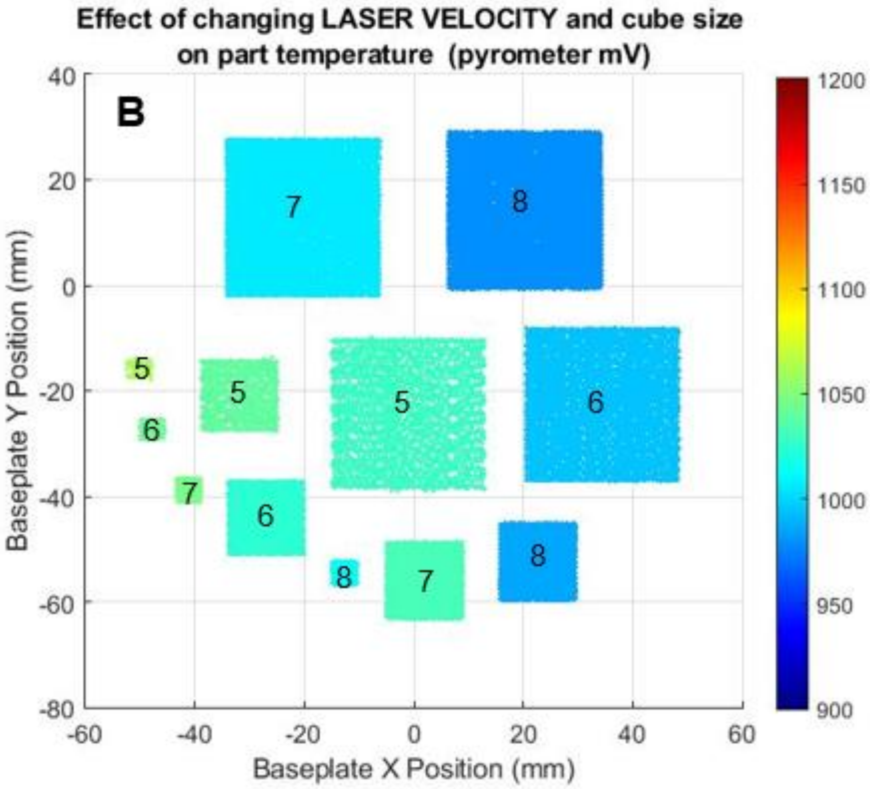

Figure 42: Pyrometer data showing variation in pyrometry intensity (temperature) between built parts for (A) group A and (B) group B (showing layer at 6.02mm height)

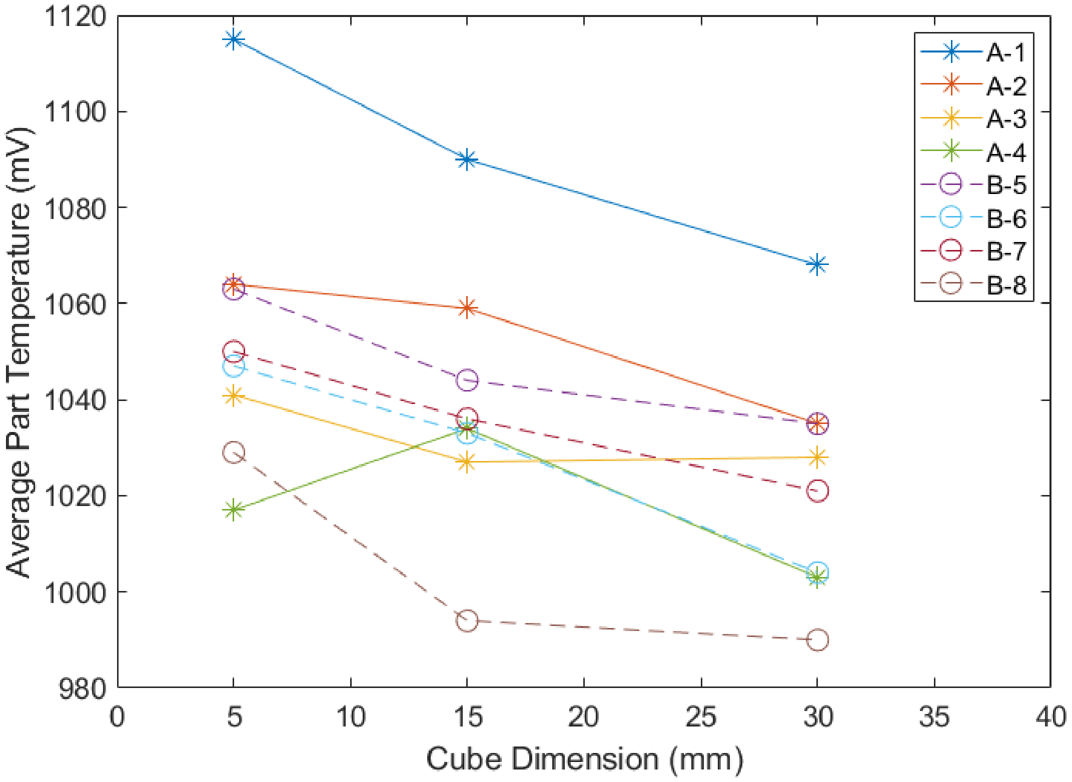

Figure 43: Part pyrometry intensity (temperature) vs cube size for each parameter set 1-9.

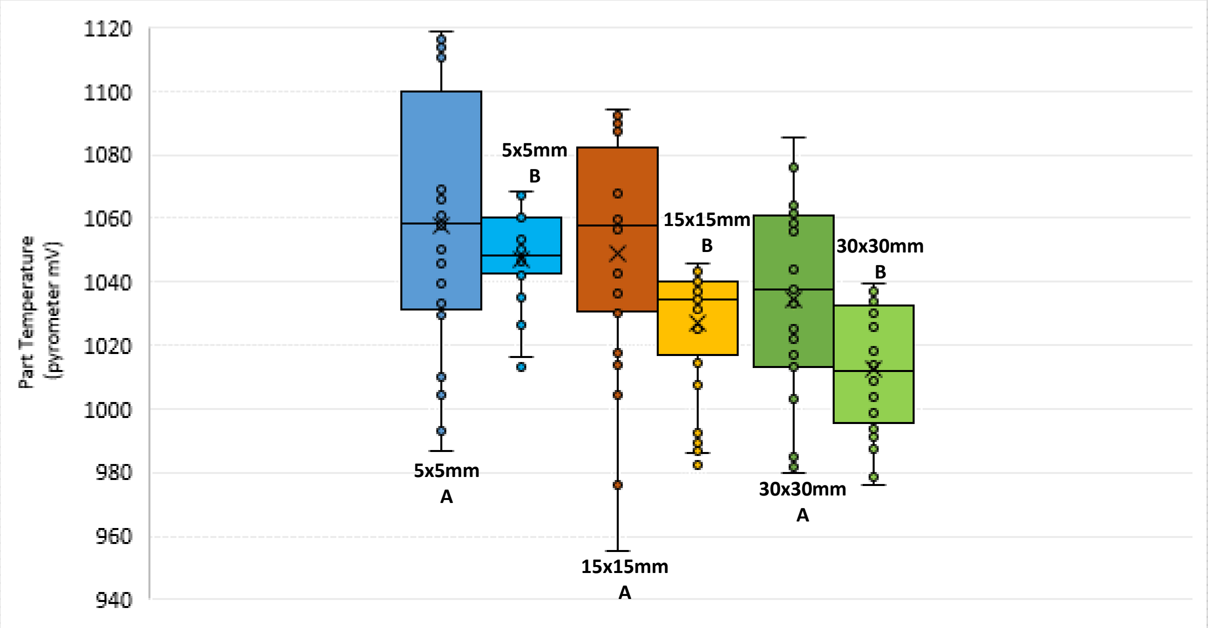

Figure 44: Effect of changing hatch spacing (A parameter sets) and laser velocity (B parameter sets) on pyrometry intensity (temperature) for constant normalised energy density. Repeated for three cube sizes, 5x5mm, 15x15mm, 30x30mm.

Figure 45 shows the average pyrometry intensity of each cube plotted on a 3D graph with power, hatch velocity and linear velocity. It is possible that a trend exists between part pyrometry intensity and hatch velocity, however, this could also be an artefact of the FOV of the pyrometer. Further investigation is a topic of ongoing research.

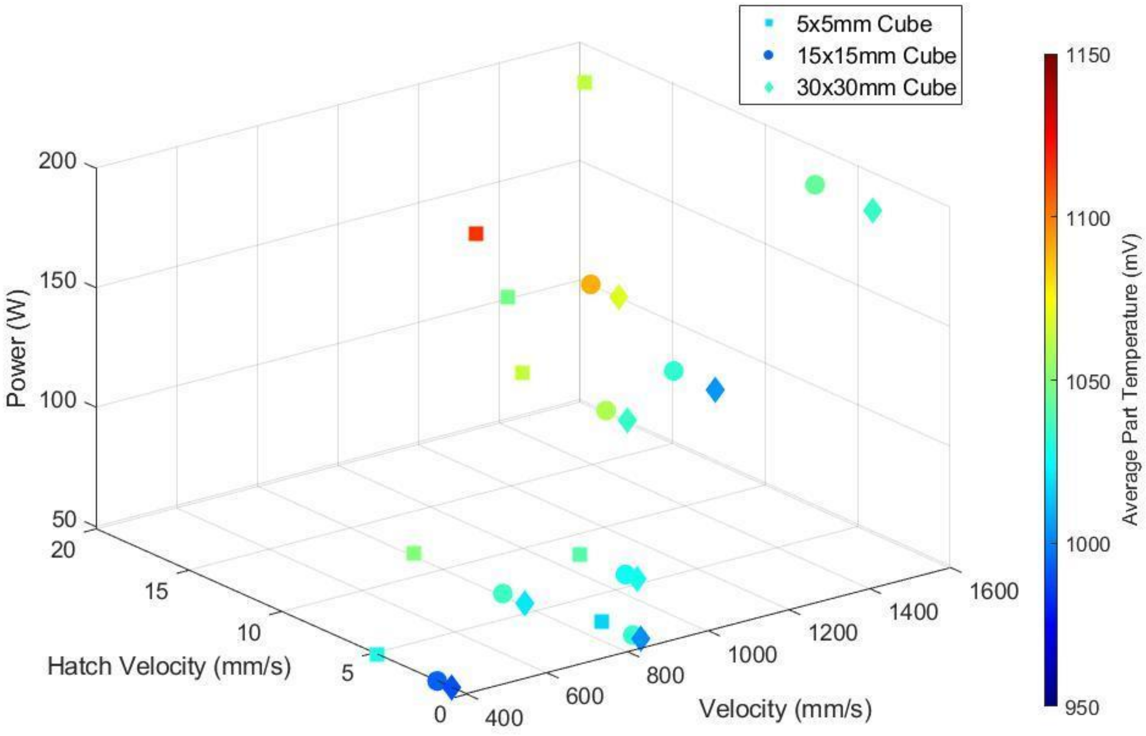

Figure 45: 3D representation of the variation in part pyrometry intensity (temperature) of 5x5mm, 15x15mm, and 30x30mm cubes with power, hatch velocity and linear velocity.

4.3.2.2 Part Density

Parameter sets 1-A, 2-A, 5-B and 6-B all produced fully dense samples across the different cube sizes as shown in Figure 46a. Parameter sets 3-A, 4-A, 7-B and 8-B all show decreasing density with part size. All defects observed in these samples were LOF type. All four of these parameter sets used a power of 75W or lower suggesting that this is the minimum power for a successful build at this energy density on the Acconity Mini. Sample 4-A displays a significantly higher level of porosity than all other samples for all cube sizes.

Figure 46b shows the average part pyrometry intensity against the density. It is clear that fully dense parts can be printed over a wide range of intensities and that part densities are not guaranteed based purely on maintaining a specific pyrometry intensity value. This suggests that employing 'temperature' control alone may not be the optimum method of process control to ensure high quality parts.

In the B-6 30x30mm cube, although the majority of the cube was fully dense, the cross section exhibited large LOF defects as shown in Figure 47. The top surface of this sample, shown in Figure 48c, showed significant levels of spatter. This rough surface likely prevented an even layer of powder from being spread across the build platform in this region, leading to the propagation of LOF defects through the thickness of the part. The region of LOF was found to widen with increasing part height, demonstrating the effect of defect propagation from small to larger areas. As the 15x15mm and 5x5mm cubes printed with the same parameter set (shown in Figure 48b) did not result in these defects, the spatter is unlikely to be caused directly by the parameters chosen. Some evidence of spatter was also observed on the surface of sample 2-A, which had an identical position on the second baseplate, however, no LOF was observed in this sample. It is possible that the position of these samples directly in front of the argon inlet affected the build process, as a variation in part quality with build plate position has previously been observed in the literature [21].

A larger range of pyrometry intensity values was observed across the category A parameter sets. This also resulted in a larger variation in final part density than those printed using parameter set B (Figure 46).

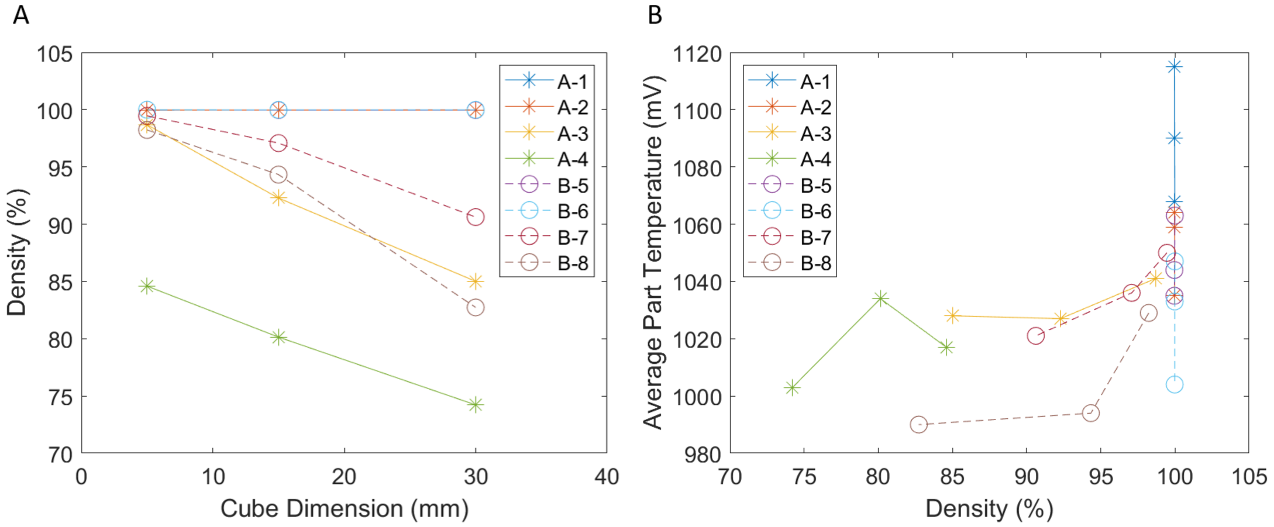

Figure 46: a) Cube density against part size for each parameter set, b) Cube density against temperature for each parameter set.

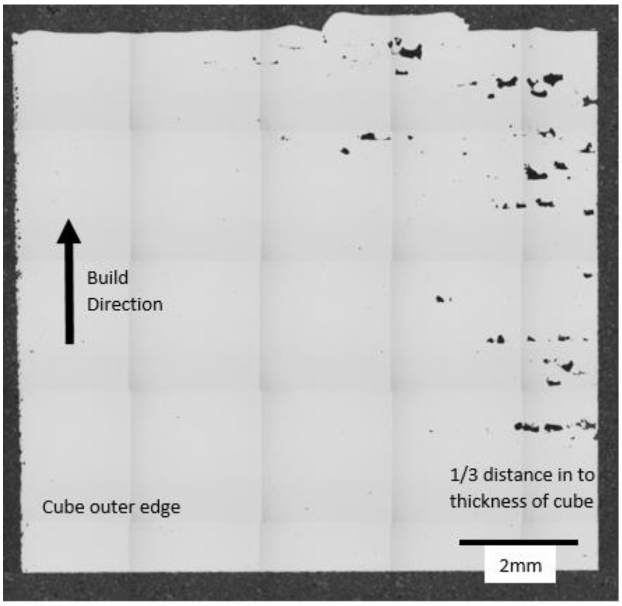

Figure 47: Lack of fusion defects shown through the thickness of the built part 6-B 30x30mm cube

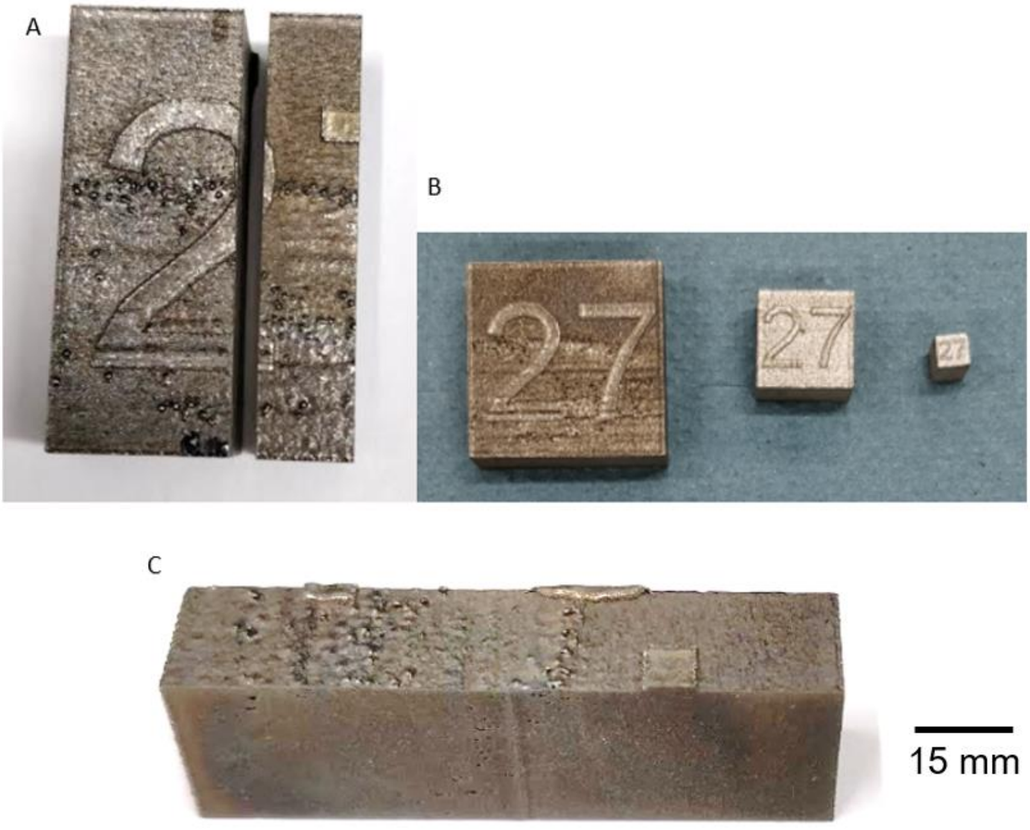

Figure 48: a) top surface of sample 6-B 30x30mm cube (labelled 27) showing balling defects, b) Top surface of all cubes printed with parameter set 6-B – only the large cubes shows surface defects, c) top surface with view of cross section showing that position of surface spatter is coincidental with a string of lack of fusion defects through the bulk of the sample.

4.4 Testing the Limitations of Equivalent Energy Density Part 2

4.4.1 Experimental Rationale and Method

In the above set of experiments, the hatch spacing and velocity were altered, however it was found that laser power values below approximately 75W were not high enough to produce fully dense parts. Therefore, the effects of Equivalent Energy Density on LPBF of Inconel 718 parts was mostly investigated in terms of sample size.

In the next set of experiments, 10 combinations of laser power (75-190W), velocity (500-1600mm/s) and hatch spacing (43-109µm) were selected to build 4x4x6mm tall samples. All parameters are displayed in Table 11. A 90^0 hatch rotation strategy, with an initial rotation of 45^0, was again implemented. Pyrometer intensity data was collected and average intensity values calculated for each part. Samples were sectioned along the build direction and the surface was prepared for optical density analysis and EBSD analysis. For EBSD data acquisition a step size of 1µm and an exposure time of 1ms was utilised. Lastly, hardness measurements were taken for each sample.

A second set of 4x4x4 mm cubes were printed with their initial rotation set to 90^0 so that the printing direction was parallel to the cube edges. Printing of the top layer was stopped mid-way to allow for melt pool dimension data to be extracted from the part after polishing, and etching with Kalling's reagent. This method was chosen as it provides a more accurate representation of the melt pool dimensions as they would form within a bulk material compared to performing single melt tracks on to a single large heat sink.

The samples were compared in terms of melt pool geometry, defect density, grain shape, grain orientation, grain area, grain average misorientation (GAM), pyrometry intensity, and hardness, in order to understand the effectiveness of the use of the term equivalent normalised energy density to describe LPBF processing parameters.

Table 11: Laser power, velocity and hatch spacing used to build equivalent energy density cubes. Layer thickness remained constant at 30 µm for each sample.

	Sample Number									
	1	**2**	**3**	**4**	**5**	**6**	**7**	**8**	**9**	**10**
Power (W)	190	165	130	130	190	137	162	100	190	75
Velocity (mm/s)	850	740	585	850	1240	1120	1300	500	1600	850
Hatch Spacing (µm)	109	109	109	75	75	60	61	98	58	43
$\boldsymbol{E_0}^*$	2.84	2.84	2.83	2.83	2.83	2.83	2.83	2.83	2.84	2.85

4.4.2 Results

All experimental results are tabulated in Table 12. A high level of porosity in sample 10 meant it was not imaged using optical or EBSD analysis and so no experimentally derived values are available for it.

Table 12: Tabulated data for each parameter set. Errors given as a coefficient of variation. Density values were taken from a single thresholded image for each sample and so do not have an associated error. These values are only to provide a rough indication of part density.

	Sample Number									
	1	**2**	**3**	**4**	**5**	**6**	**7**	**8**	**9**	**10**
Density (%)	99.99	99.99	99.99	99.99	99.98	99.96	99.96	99.97	99.99	93.55
Average Pyrometry Intensity (mV)	1110.6 ± 0.8%	1090.5 ± 0.8%	1089.0 ± 0.9%	1079.5 ± 0.8%	1074.9 ± 1.0%	1070.1 ± 0.8%	1063.4 ± 1.2%	1071.7 ± 1.1%	1077.8 ± 1.4%	1074.2 ± 1.4%
Melt Pool Depth (µm)	137.7 ± 1.7%	174.2 ± 0.3%	134.0 ± 0.5%	109.4 ± 0.8%	96.8 ± 0.5%	80.5 ± 0.6%	95.4 ± 0.7%	131.4 ± 0.2%	84.7 ± 0.6%	-
Melt Pool Width (µm)	159.8 ± 1.8%	186.1 ± 0.4%	136.2 ± 0.6%	134.0 ± 0.8%	112.8 ± 1.9%	115.8± 0.9%	135.2 ± 1.9%	124.4 ± 2.0%	104.1 ± 0.5%	-
Layer Process Speed (mm/s)	23.2	20.2	15.9	15.9	23.3	16.8	19.8	12.3	23.2	9.1
Mean GAM $(^{o})$	0.0130 ± 61%	0.0111 ± 57%	0.0091 ± 49%	0.0132 ± 66%	0.0129 ± 63%	0.0123 ± 61%	0.0136 ± 77%	0.0117 ± 73%	0.0135 ± 70%	-
Hardness (Hv)	318 ± 0.5%	323 ± 1.5%	330 ± 1.3%	329 ± 2.4%	335 ± 1.3%	330 ± 0.1%	327 ± 1.4%	328 ± 0.4%	330 ± 1.7%	

4.4.2.1 Part Pyrometry Intensity and Density

The density of all cubes, apart from number 10, was above 99.9%. Cube number 10 was printed with a power of 75W and contained a large volume of LOF porosity. This agrees with the results obtained in Section 4.3, providing further evidence of there being a lower limit under which the laser power is not high enough to produce full melting. The pyrometer intensity values all lay between 1063mV and 1110mV, however there is an absence of a strong correlation between part density and the recorded part temperature value.

4.4.2.2 Melt Pool Cross Sections

Optical images of the etched melt pools are shown in Figure 49 (Images taken by Rob Hillier, Masters Student) with red arrows indicating the points at which melt pool width and depth measurements were taken. Measurements were taken three times and an average value calculated.

It is clear that the melt pool dimensions are not equal for each parameter set and therefore it can be stated that the melt pool size and shape is not constant if varying parameters are chosen for AM processing, even if an equivalent energy density is used.

Sample 2 (P, V, H - 165 W, 740 mm/s, 109 µm) attained the widest and deepest melt pool. The melt pool shape shows that the processing conditions are close to becoming keyhole mode melting. Interestingly, Sample 1, which had a higher power of 180W, had a lower melt pool depth and width than sample 2. This must be due to the 100 mm/s increase in laser velocity compared to sample 2, as both had the same hatch spacing. The smallest melt pool depth recorded was 80.5 µm, for sample 6 (P, V, H – 137 W, 1120 mm/s, and 60 µm), which was closely followed by sample 9, 84.7 µm (P, V, H – 190 W, 1600 mm/s, and 58 µm). Both of these samples observe a higher laser velocity and low hatch spacing values. The reduced hatch spacing produces an increased level of overlap with the previous melt track which theoretically results in an increased level of heat conduction away from the melt region, enabling a smaller melt pool to form. This is then exacerbated by the high laser velocity as less energy is imparted to the material per unit time. Sample 9 also recorded the smallest width, at 104 µm. While sample 5 also displayed a low width, 112.8 µm (P, V, H – 190 W, 1240 mm/s, and 60 µm), it had a higher depth of 96.8 µm, which is due to the reduction in laser speed as compared to that of sample 9.

All of the parts printed in this trial were of equal geometry, and no significant spatter, balling, or powder layer recoating defects were observed during the build. Therefore, they were all produced under optimum process conditions. However, had undesirable in-process issues occurred, the differences in melt pool dimensions shown in Figure 49 may have meant that some parameter sets would be more robust against these issues than others. For example, if significant spatter had formed on the surface of a part, as demonstrated in Figure 48, process parameters that produced deeper melt tracks may have still enabled fully dense parts to be formed, whilst this might not be the case using parameter sets that produced shallower melt pools.

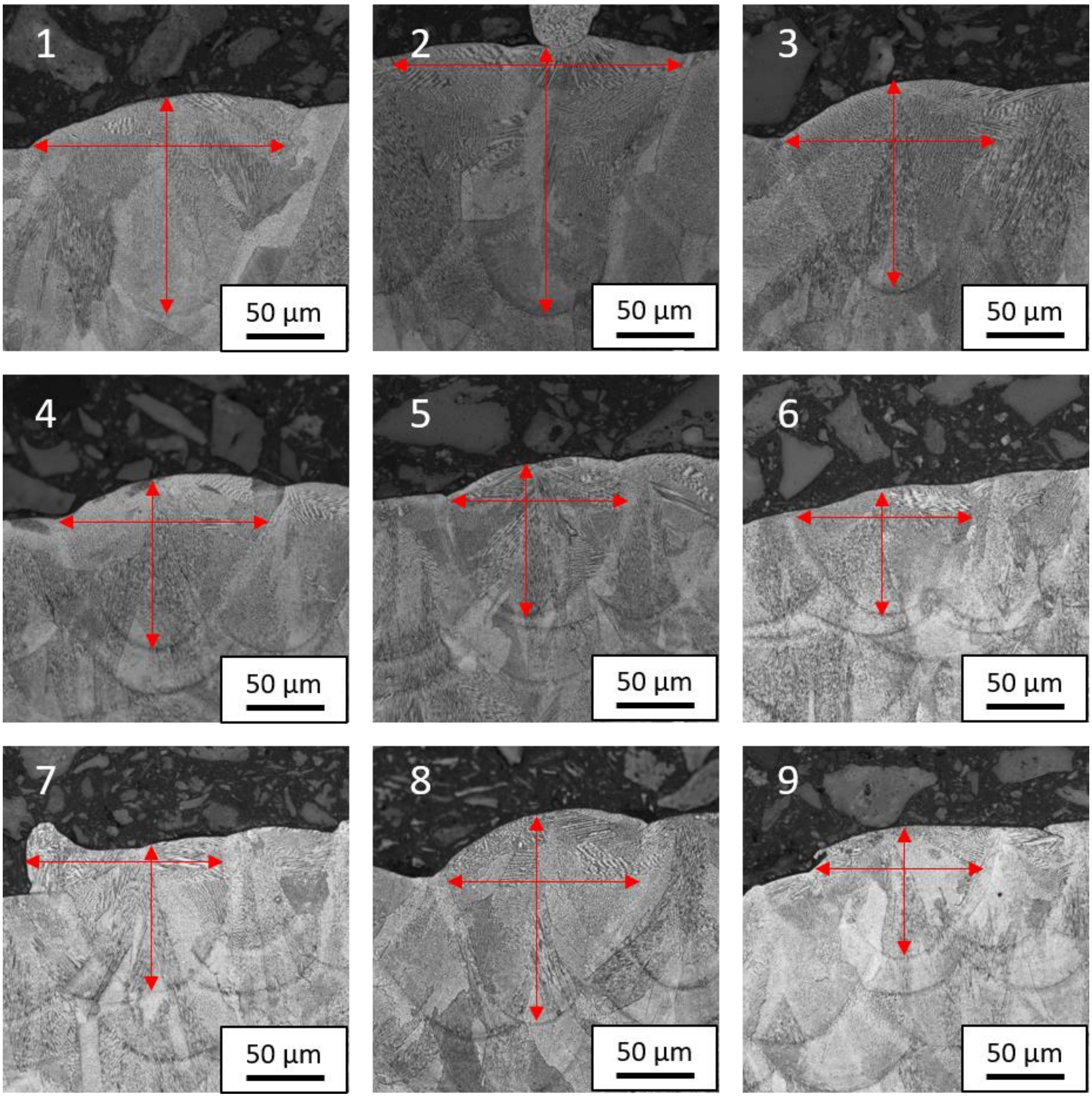

Figure 49: Melt pool cross sections showing the approximate locations of width and depth measurements

4.4.2.3 Grain Structure Analysis

Inverse Pole Figure (IPF) maps with respect to the Y (build direction) for each sample (1-9) are shown in Figure 50. All samples exhibit long elongated grains in the build direction which is expected from epitaxial growth. The majority of the grains are orientated with their easy growth direction, [001], aligned with the build direction. This texture is further shown by the pole figure maps in Figure 51, which display the direction of the (100) plane of each grain as viewed from the build direction for each sample. It is clear that the grains in samples 1, 3, and 8 all exhibit a slightly reduced alignment with the build direction. However, this effect cannot be correlated to the build parameters used to process them and the cause is behind this effect is currently not known.

A rainbow effect can be seen in the colour of the EBSD maps within the majority of the grains in each sample. This represents a change in orientation within each grain and is enabled by the presence of GNDs. GAM values can be used to quantify the magnitude of these orientation changes within each grain. These are tabulated in Table 12. It is clear that these values all lie within error for each sample. This leads to the conclusion that despite printing with a different combination of laser parameters, which leads to differences melt pool shape, if an equivalent normalised energy density is utilised, approximately similar values of inter-grain misorientation can be achieved.

As GND density and grain size is believed to correlate to recrystallisation kinetics [125], these results show that it may be difficult to induce differences in recrystallisation kinetics by varying laser parameters alone, whilst remaining at an equivalent normalised energy density.

Figure 52 shows a histogram of grain sizes present in each sample. The 100 bin histogram has been modified to reflect the area of the grains in each bin. This is because a very large number of fine grains saturate the lower end of the histogram. However, the majority of the microstructure area is taken up by large grains, and these largely determine the properties of the overall material. All of the histograms show grain sizes between 0 to 40000 μm^2, except cube 7 which shows that a high proportion of the microstructure is taken up by very large grain area (>80000 μm^2). The EBSD imaging of cube 7 is believed to have been taken too close to the left hand edge of the sample and so this large grain may be an artefact of this and not fully representative of the processing parameters used in this analysis. This is further evidenced by the fact that this sample also displays a string of fine equiaxed grains along the left sample edge, which is likely due to heterogeneous nucleation of solidification nuclei from the external powder bed.

Samples 1, 3, and 8 observe a microstructure that is dominated by a proportionately smaller overall grain size than observed in samples, 2, 4, 5, 6, and 9. As with the differences observed in the pole figures, these differences are very slight and do not correlate to the smallest melt pool width and depth values discussed previously.

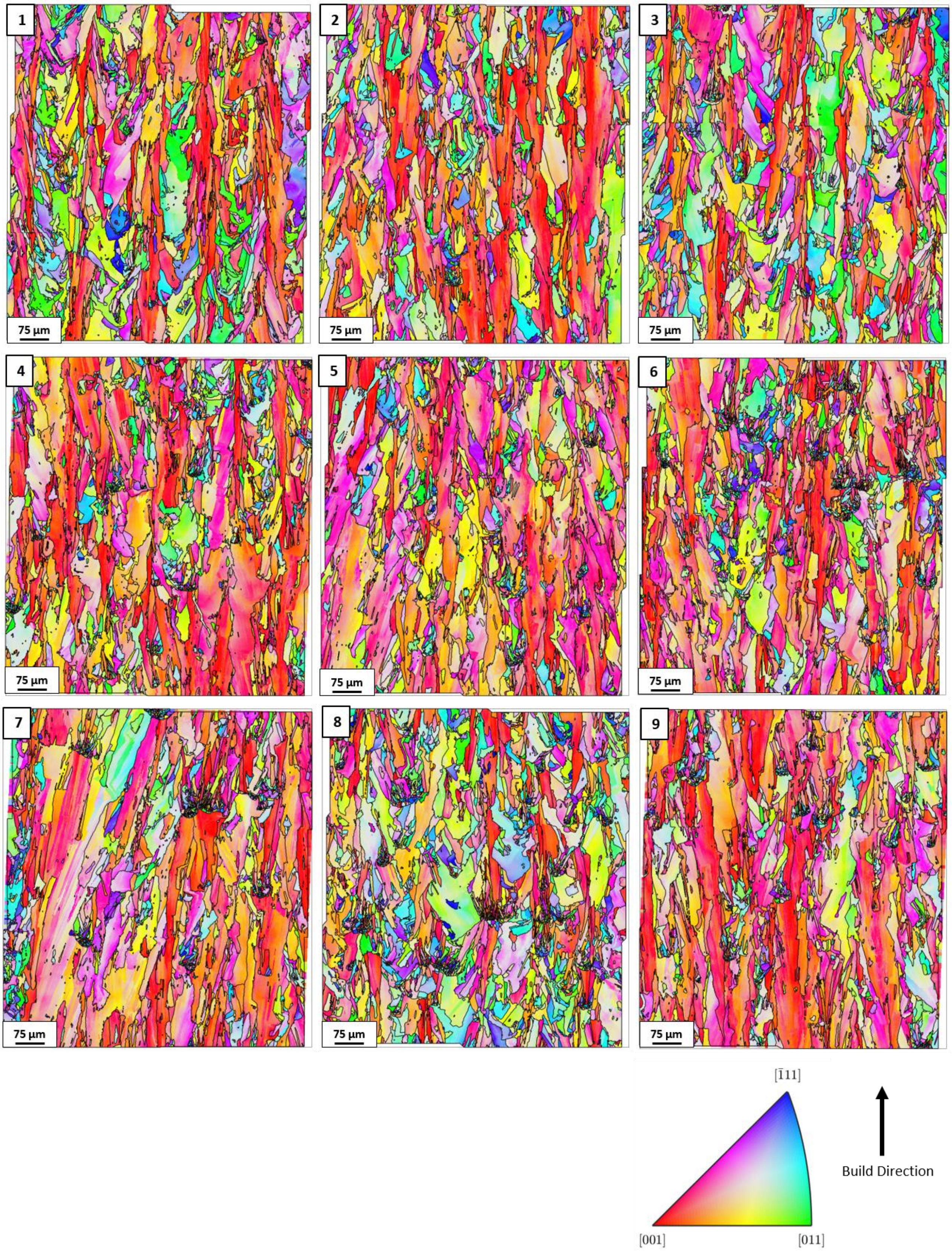

Figure 50: IPF maps with respect to the building direction for all cubes 1-9. All samples display evidence of epitaxial growth with the majority of grains displaying an alignment between the easy growth direction for Inconel 718 and the build direction.

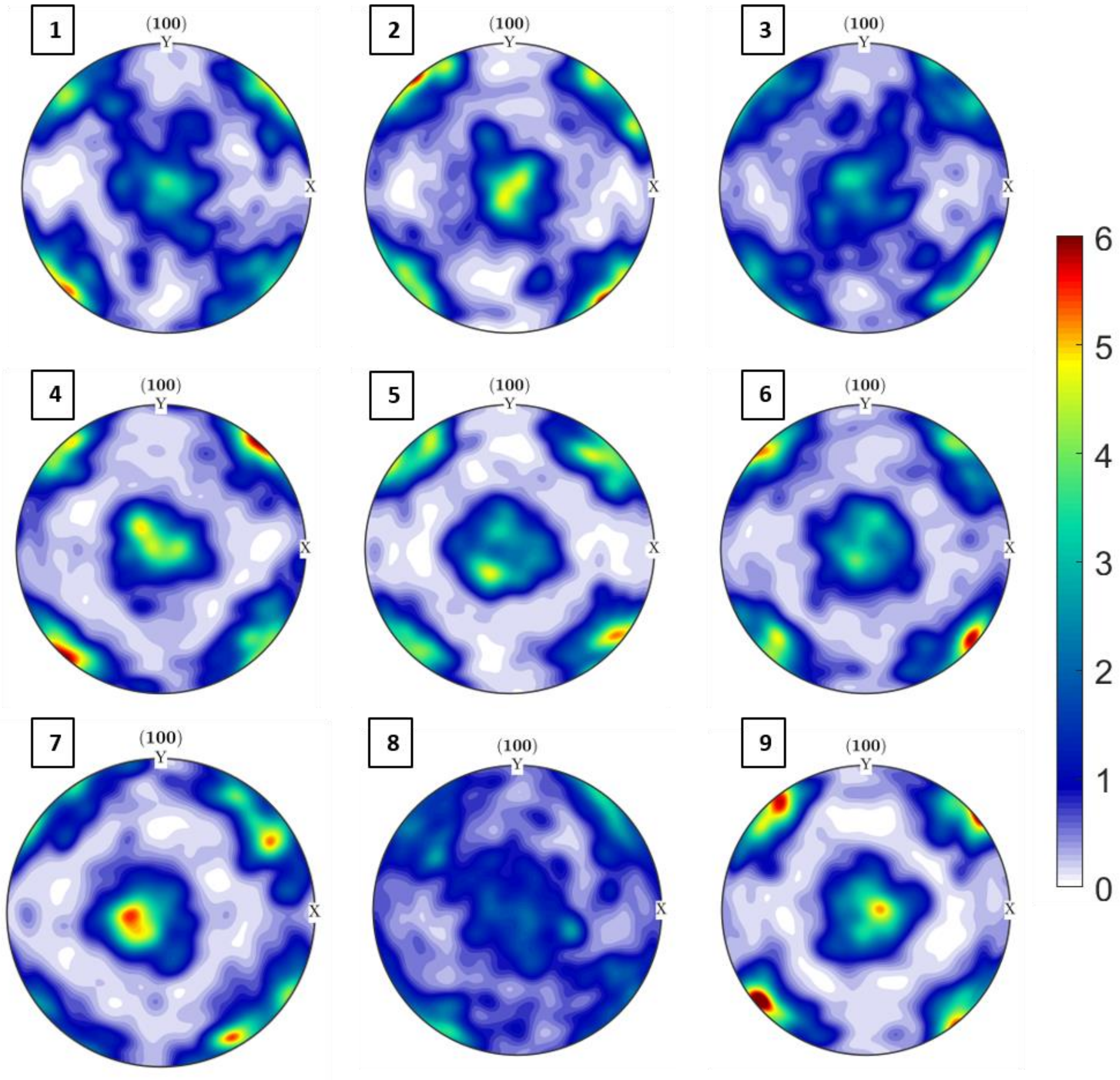

Figure 51: Pole Figures for each sample 1 – 9 showing the orientation of the (100) plane of each grain from the perspective of the build direction. All samples show a high degree of alignment of the (100) crystal

planes with the build direction, with samples 2, 4, 5 6, 7, and 9 showing this to a higher degree. Sample 8 shows the weakest texture.

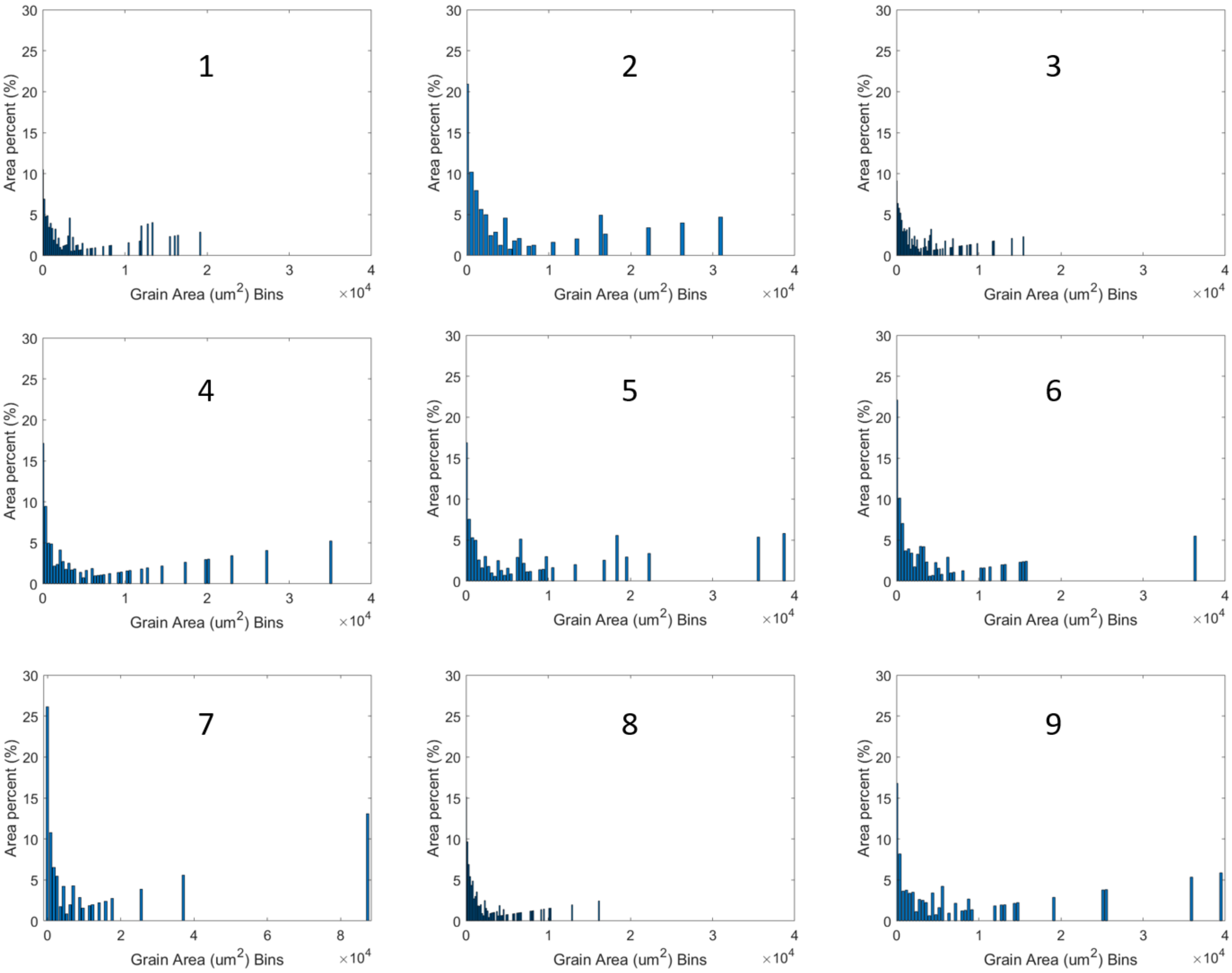

Figure 52: Histograms of grain area for each sample normalised by the percentage area of grains within each bin. Samples 1, 3, and 8 are dominated by smaller grain sizes than those observed in samples 2, 4, 5, 6, and 9.

4.4.2.4 Hardness

The harness measurements in Figure 53 showed variation between 318 ± 1.7 HV (Cube 1) and 335 ± 4.5 HV (Cube 5). Most hardness values lay within error of one another and so the difference in hardness obtained by printing at different parameter sets within the same energy density is minimal. This result is consistent with the minimal differences in grain size and grain misorientation (from the GAM measurements) observed from the EBSD data, and suggests that any secondary phase precipitation, which was not investigated, will also be similar.

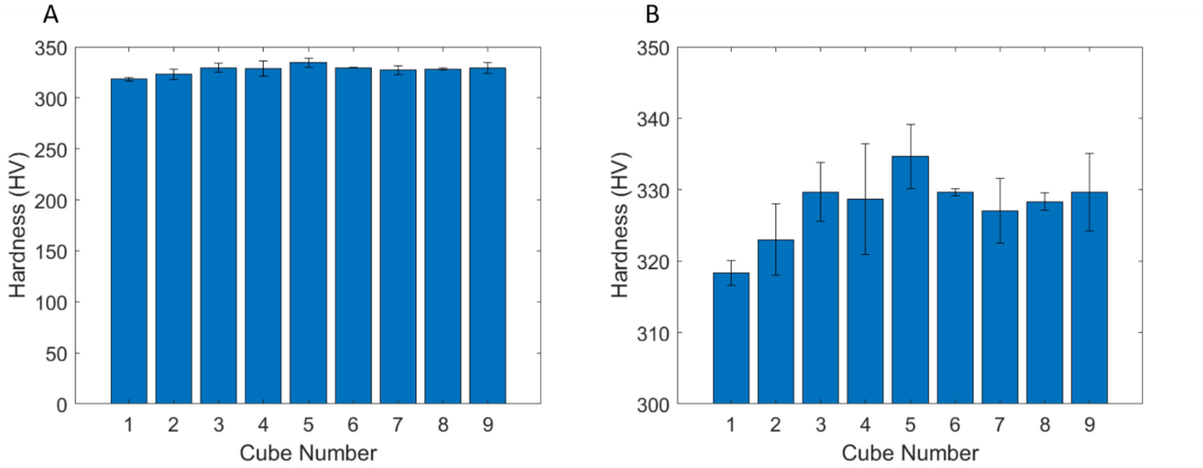

Figure 53: Average hardness measurements calculated from four indents on the cross sectional surface of each cube, 1-9. Figures a) and b) show the same graph, but b) only shows the hardness values between 300 and 350Hv in order to more clearly see the differences between each sample. Error bars show standard deviation of all measured points.

4.5 Laser Focus Offset

4.5.1 Experimental Rationale and Method

A defocused laser beam produces a larger spot radius on the processing plane, leading to a lower power density. This poses a potential method of altering the heat input to the part during the production of complex geometries or as a means of producing graded components. In literature, the effects of laser focus offset on defect population was not found to be perfectly mirrored across the laser focal point [169], [246], [247]. Metelkova *et al.* [246] attributed this to the fact that when defocused, the laser beam is either diverging or converging as it reaches the build plane. This will have different effects on the melt pool. Correlation between laser focus and average part temperature has not yet been performed; this might provide insight to the varying build quality observed in the referenced study.

Nine cylinders (6mm diameter, 7mm height) were each built with a different focus offset, initially to a maximum defocus of +/-4mm, as shown in Table 13. The laser power, velocity, hatch spacing and layer thickness were all held constant at, 130W, 850mm/s, 75µm, and 30µm respectively. The laser spot size was calculated by interpolation of data provided in the manufacturers machine laser quality measurement report, and have not been checked [248]. Power density was calculated as shown in [169]. A positive defocus moves the laser focal point above the working plane, leading to a diverging laser on the build surface, and a negative defocus moves the laser focal point below the working plane, leading to a converging laser on the build surface as shown in Figure 54. Pyrometry data was collected by layer. It was predicted that the negative defocus would produce samples with increased density due to the converging nature of the laser beam at negative defocus.

Table 13: Build parameters used in Laser Focus Offset Study 1

ID	Laser Focus Offset (mm)	Laser Spot Size (µm)	Power Density (kW/mm^2)[20]
1.1	+4	135	9.1
2.1	3	111	13.4
3.1	+2	87	21.8
4.1	+1	77	27.8
5.1	0	67	36.7
6.1	-1	80	25.7
7.1	-2	93	19.0
8.1	-3	120	11.5
9.1	-4	146	7.8

Upon analysis of the results, and to ensure confidence in the initial results obtained, the defocus range was extended to +/-8mm and the trial was repeated with slightly altered geometries of 6x6x6mm, or 4x4x6mm cubes. Details are shown in Table 14.

Table 14: Build parameters used in Laser Focus Offset Study 2. Note difference in cube sizes.

ID	Sample Size (mm^3)	Laser Focus Offset (mm)	Laser Spot Size (µm)	Power Density (kW/mm^2)[20]
1.2_6	6x6x6	8	259	2.5
2.2_4	4x4x6	7	227	3.2
3.2_6	6x6x6	6	195	4.3
4.2_4	4x4x6	5	165	6.1
5.2_6	6x6x6	4	135	9.1
6.2_6	6x6x6	3	111	13.4
7.2_4	4x4x6	3	111	13.4
8.2_6	6x6x6	2	87	21.8
9.2_6	6x6x6	1	77	27.8
10.2_4	4x4x6	1	77	27.8
11.2_6	6x6x6	0	67	36.7
12.2_4	4x4x6	0	67	36.7
13.2_6	6x6x6	-1	80	25.7
14.2_4	4x4x6	-1	80	25.7
15.2_6	6x6x6	-2	93	19.0
16.2_4	4x4x6	-2	93	19.0
17.2_6	6x6x6	-3	120	11.5
18.2_4	4x4x6	-3	120	11.5
19.2_6	6x6x6	-4	146	7.8
20.2_4	4x4x6	-5	177	5.3
21.2_6	6x6x6	-6	207	3.9
22.2_4	4x4x6	-7	238	2.9
23.2_6	6x6x6	-8	269	2.3

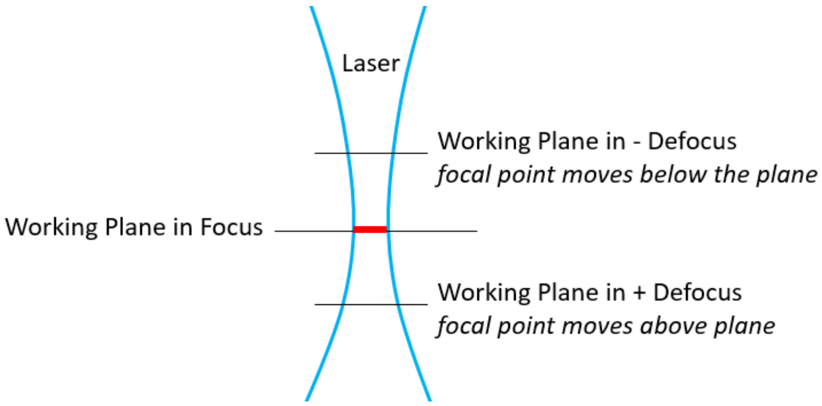

Figure 54: Schematic of build plane with respect to +ve or – ve focus offsets.

4.5.2 Results

Figure 55 shows how the beam diameter and power density vary with focus offset and Figure 56 shows the variation of part density and pyrometry intensity with focus offset. The part density and pyrometry intensity from all samples in Tables 13 and 14 are displayed in Table 15. The beam diameter is not completely mirrored across the focal spot with negative focus offsets producing a slightly wider beam. The hatch spacing was not altered as the beam diameter increased, leading to a larger hatch overlap with increasing defocus.

The part pyrometry intensities increase from the maximum negative defocus to the maximum positive defocus for all trials as shown in Figure 56. The introduction of porosity begins at defocus values less than -6mm or greater than +3mm. It is clear that this effect is not even across the focal point. In 316L stainless steel, Metelkova *et al.* [246] identified a similar phenomenon. In their study, when the laser is focused above the build plate (-ve defocus), the process is less efficient but more stable, and therefore less sensitive to changes in the thermal input.

Figure 57 shows the etched melt pool cross sections for the 4x4x6 mm cubes at various defocus levels. Clear differences in the melt pool depth can be observed as a result of the reducing power density and increasing laser spot size. At higher positive and negative focus offsets, the melt pool becomes very shallow. Upon defocusing in the positive direction from 0, the flattening of the melt pool occurs very quickly, however in the negative direction, the melt pools initially become deeper before beginning to flatten out. In Inconel 718, published after the work in this thesis had been started, McLouth *et al.* [247] identified that an increased defocus level (-3 vs 0) produced wider, flatter, and more overlapping melt pools. The corresponding microstructure was coarser and more grains were orientated in the build direction. It is unclear from the etched cross sections in Figure 57 if this is also the case in this study, and further EBSD analysis is required to verify this.

A more recent report on the effects of the laser focus shift on the microstructure and mechanical properties of LPBF Inconel 718 has found that the reduced power density, resulting from a higher focus shift in the +ve direction, leads to a number of interesting solidification phenomena in samples with near full density. As the power density reduces, the material observes a higher cooling rate. This leads to a finer solidification cell structure. The maximum melt pool temperature is also reduced, leading to a smaller difference in surface temperature between the centre and the edge of the melt pool, and a correspondingly lower Marangoni flow. A strong Marangoni flow has the ability to break off newly solidified grains, leading to the nucleation and growth of new grains and resulting in a microstructure with patches of a more refined grain structure. Therefore, as the laser focus is increased, the homogeneity and average equivalent grain size of the microstructure is increased [249].

It is clear from the results presented herein, and the recent published reports, that altering the laser focus provides another potential method in which the microstructure of the material can be controlled.

In order to understand the potential for laser defocus to enable locally distinct mechanical properties in a single part, analysis of the sub grain cell size, grain shape morphology, and intra-grain misorientation of all samples in this section, is required and a topic of ongoing research. As the lattice misorientation gradient in a part dictates the recrystallisation kinetics, the utilisation of laser focus offset during the production of fully dense parts may enable them to achieve a variation in grain size and mechanical properties after heat treatment.

Table 15: Tabulated data for each sample. Density values were taken from a single thresholded image for each sample and so do not have an associated error. These values are only to provide a rough indication of part density and more analysis is to be done if a more accurate value is required. Pyrometry intensity errors provided as COV.

ID	Sample Size	Laser Focus Offset (mm)	Laser Spot Size (µm)	Power Density (kW/mm^2)[20]	Density (%)	Average Part pyrometry intensity (mV)
1.1	Dia:6, H:7	+4	135	9.1	99.71	1116±2.2%
2.1	Dia:6, H:7	3	111	13.4	99.95	1084±1.9%
3.1	Dia:6, H:7	+2	87	21.8	99.96	1070±1.6%
4.1	Dia:6, H:7	+1	77	27.8	99.98	1065±1.6%
5.1	Dia:6, H:7	0	67	36.7	99.97	1057±1.4%
6.1	Dia:6, H:7	-1	80	25.7	99.99	1048±1.1%
7.1	Dia:6, H:7	-2	93	19.0	99.97	1044±1.3%
8.1	Dia:6, H:7	-3	120	11.5	99.97	1040±1.4%
9.1	Dia:6, H:7	-4	146	7.8	99.93	1040±1.3%
1.2_6	6x6x6	8	259	2.5	90.46	1045± 1.5%
2.2_4	4x4x6	7	227	3.2	90.20	1159 ± 2.5%
3.2_6	6x6x6	6	195	4.3	94.83	1045± 1.4%
4.2_4	4x4x6	5	165	6.1	96.45	1135± 1.7%
5.2_6	6x6x6	4	135	9.1	98.52	1039± 1.3%
6.2_6	6x6x6	3	111	13.4	99.86	1047± 1.5%
7.2_4	4x4x6	3	111	13.4	99.16	1123 ± 1.5%
8.2_6	6x6x6	2	87	21.8	99.85	1050± 1.3%
9.2_6	6x6x6	1	77	27.8	99.96	1059± 1.2%
10.2_4	4x4x6	1	77	27.8	99.98	1106± 1.3%
11.2_6	6x6x6	0	67	36.7	99.97	1065± 1.3%
12.2_4	4x4x6	0	67	36.7	99.98	1100± 1.4%
13.2_6	6x6x6	-1	80	25.7	99.97	1076± 1.7%
14.2_4	4x4x6	-1	80	25.7	99.94	1071± 1.0%
15.2_6	6x6x6	-2	93	19.0	99.97	1114± 2.4%
16.2_4	4x4x6	-2	93	19.0	99.98	1042 ± 1.3%
17.2_6	6x6x6	-3	120	11.5	99.96	1122± 2.4%
18.2_4	4x4x6	-3	120	11.5	99.99	1054 ± 0.9%
19.2_6	6x6x6	-4	146	7.8	99.96	1141± 2.0%
20.2_4	4x4x6	-5	177	5.3	99.99	1046 ± 1.0%
21.2_6	6x6x6	-6	207	3.9	99.76	1158± 2.1%
22.2_4	4x4x6	-7	238	2.9	99.98	1033 ± 0.7%
23.2_6	6x6x6	-8	269	2.3	97.71	1171± 2.8%

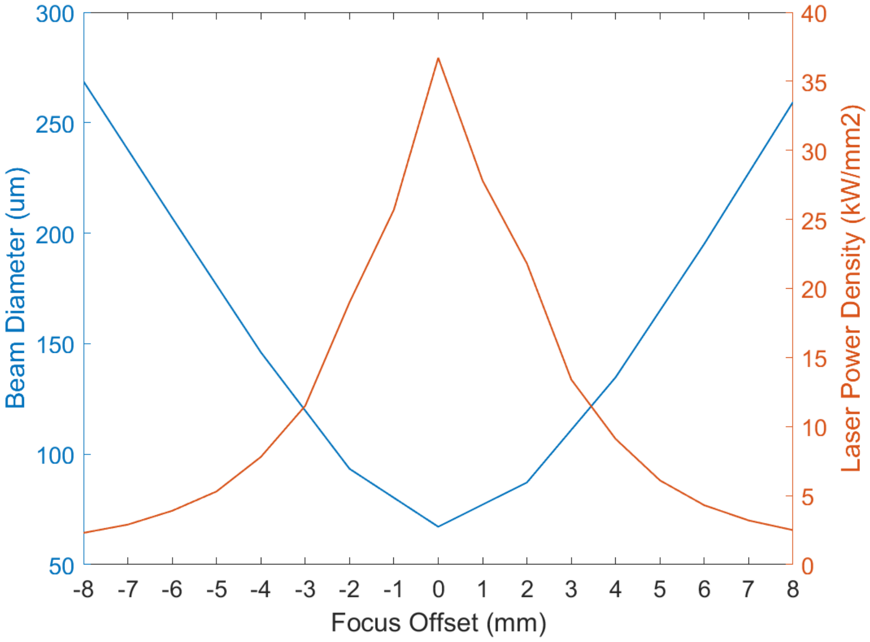

Figure 55: Laser beam diameter and laser power density variation with laser focus offset.

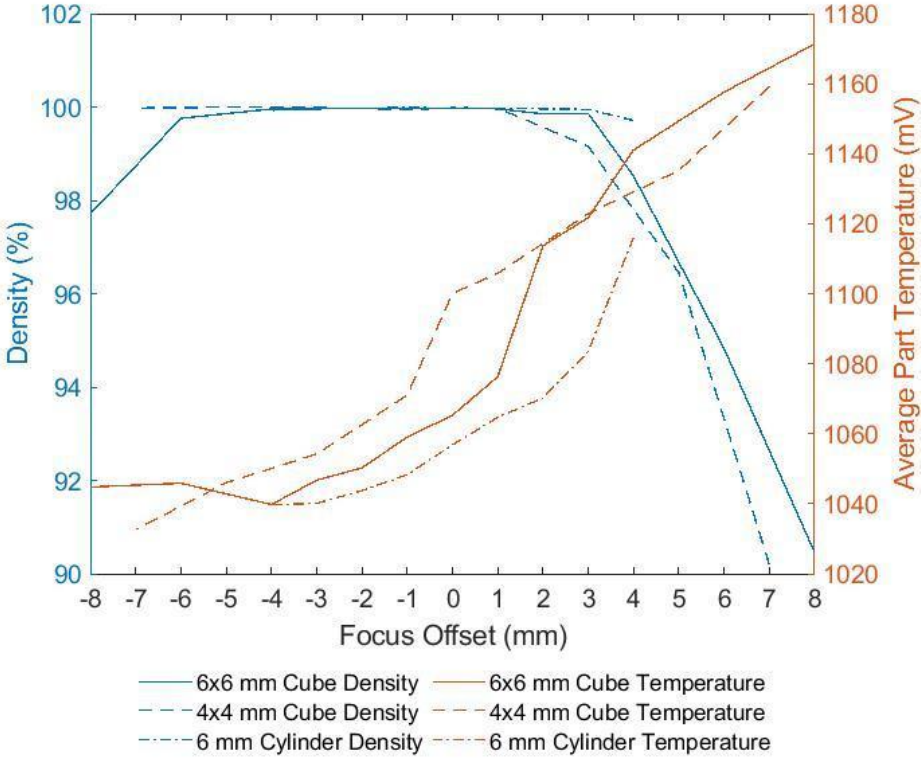

Figure 56: Part Density and average part pyrometry intensity (temperature) variation with laser focus offset for three different experiments; 6x6x6mm cubes, 4x4x6mm cubes, and 6mm diameter cylinders.

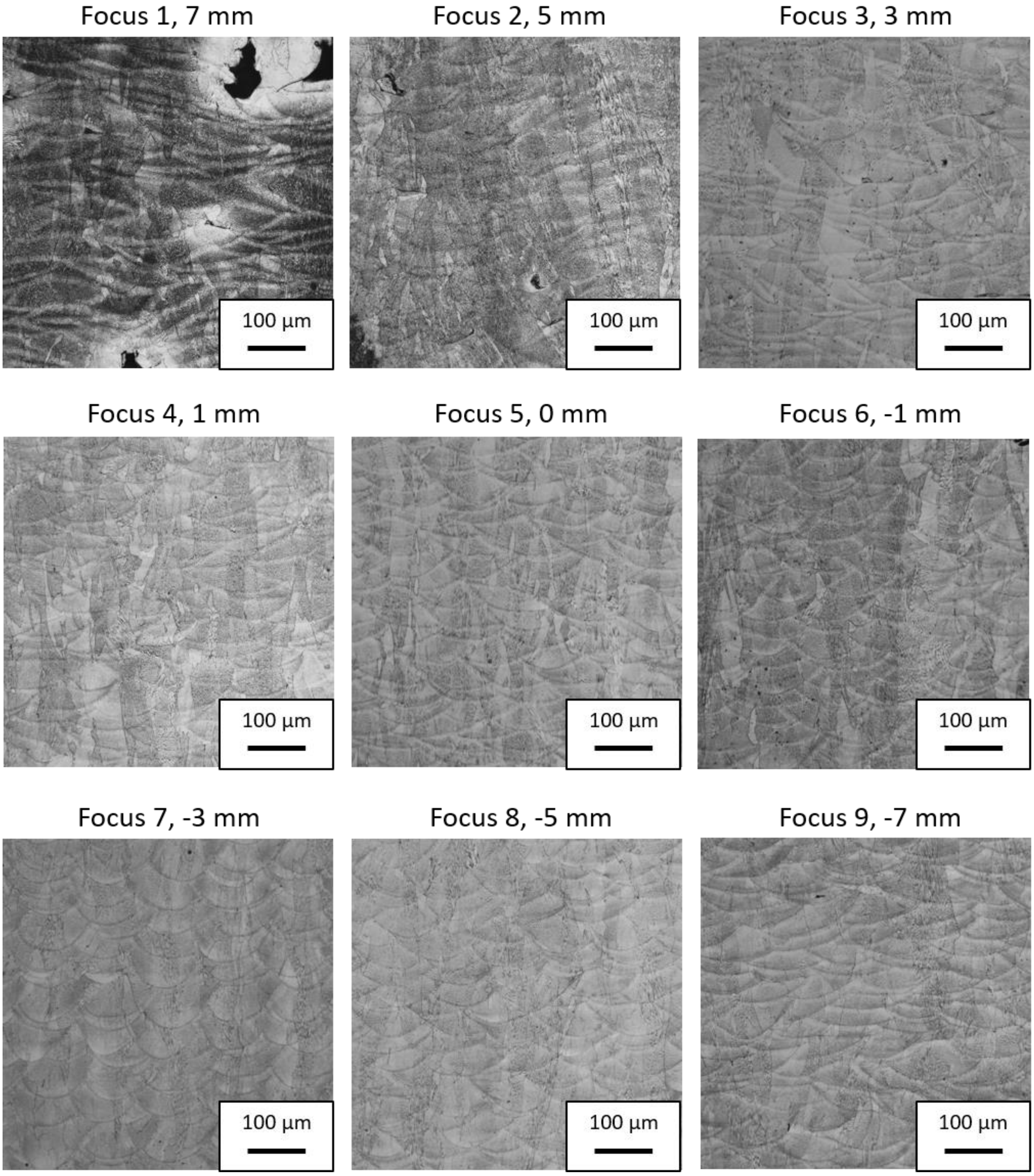

Focus 1, 7 mm

Focus 2, 5 mm

Focus 3, 3 mm

Focus 4, 1 mm

Focus 5, 0 mm

Focus 6, -1 mm

Focus 7, -3 mm

Focus 8, -5 mm

Focus 9, -7 mm

Figure 57: Etched cross sectional images of 4x4x6mm samples printed at different focus offsets revealing melt pool shape.

4.6 Chapter Summary

In this chapter, laser parameters have been identified that are capable of printing parts with minimal defect density over a range of geometries. These are a laser power, velocity, hatch spacing, and layer thickness of 130W, 850mm/s, 75µm, and 30µm respectively. These parameters will be used in all of the following experiments. This chapter also enabled understanding as to which parameters would allow the production of material inclusive of LOF and keyhole defects, therefore, providing the basis for the introduction of deliberately placed defects utilised in the following chapters.

It has been shown that altering the hatch spacing within the realm of an equivalent energy density potentially has more of an impact on the pyrometry intensity of the part and resulting part density, than altering the laser velocity. In addition, the notion of 'hatch velocity', which has not been identified in the literature, was introduced and shown to affect the pyrometry intensity of each part.

For Inconel 718, various ranges of input process parameters which all culminated in the same normalised equivalent energy density, lead to approximately similar grain morphologies in terms of grain shape, area, growth orientation, and intra-grain misorientation. This also lead to similar hardness values. For applications where closed loop control is desired, it is therefore plausible that an algorithm created to select corrective process parameters is able to maintain a fully dense component, provided an equal normalised equivalent energy density for each parameter combination is maintained.

Leading on from this, it is unlikely that significant differences in the recrystallisation kinetics, required for functional grading applications and GBE, can be achieved in fully dense samples of Inconel 718 using changes in laser parameters alone.

Utilising laser defocus allows the incident laser power to be spread over a larger area. This reduces the power density leading to flatter and more shallow melt pools. In the Aconity mini this was not found to happen uniformly across the focal point. Recent literature has suggested that laser defocus can enable regions of varying grain structure to be obtained in a single sample. Closer investigation into the solidification structures and grain morphologies of the samples printed as part of the defocus trials should be performed in order to understand if this printing technique can be used to print functionally graded microstructures. Similarly, the recrystallisation kinetics of these samples should investigated with the same end goal in mind.

5 Part Temperature Control for Additive Manufacturing

5.1 Introduction

Process monitoring in AM is a highly researched topic at the moment. This is because it has become clear that in order to produce high quality complex parts that can be qualified for use in advanced engineering structures, it is not possible to select a single set of laser parameters for the whole complex geometry. Rather, as the geometry of the part layer changes, the process parameters need to change accordingly to prevent both under and over-heating of the local material, and the subsequent introduction of defects.

Prior to the start of this PhD programme, a Master’s student in the research group produced a closed loop feedback control system capable of altering the laser power and velocity of each subsequent layer of a cuboid. The system works as follows; on-axis pyrometry intensity signals are recorded during lasing of the full layer, after which the build is paused as the data is uploaded to a high performance computer. Here the data is segmented into a desired number of sections across the layer, an average value for these regions calculated, and the power and velocity values for the next layer are calculated based on the minimisation of the variation between each area segment as well as the proximity of each value to a set point pyrometry intensity value. In order to help refine the decision process, the control system required the production of a number of ‘learning’ cubes. It used these in order to learn what the effects of each parameter change was on the subsequent layer. This was then also used to inform the selection of the correcting parameters for the ‘real’ part. These process parameters are returned to the AM machine, and the build is resumed for the next layer of the component.

This system was only capable of altering the laser parameters between layers and only for a simple cube geometry. This process also required the build to be paused between each layer, resulting in a longer build time which is costly to a manufacturer. The next logical step would be to introduce a system capable of adjusting laser parameters for any given geometry and location within each cross section.

In order to do this, it is important to understand the limitations of current methods of AM control. Advanced melt pool data collection systems are reliant on high cost sensing equipment and generate a large amount of data. These sensors are usually not built in to the AM machines and so need to be retrofitted, which poses challenges in terms of access and mounting points for sensing equipment, interfacing with the AM machine control, and requiring engineers that have an in depth knowledge of the physics behind each sensing system.

In addition to this, for complex geometries, different locations on the build have different local thermal environments. Therefore, numerous calculations would be required per layer in order to generate a set of correcting process parameters for each unique thermal environment. In general, the selection of a new set of process parameters requires a mathematical algorithm to operate freely on the collected data. It then may select a combination of process parameters for the next location/layer/hatch in the build. It is unlikely that the material response to all of these parameter possibilities will have been previously tested, making the suitability of the output risky if used in safety critical components. In addition, in a build where six or seven identical parts are produced, it cannot be said for certain that each location on each part has been produced with identical laser parameters. This makes part qualification for industrial components nearly impossible, and these issues currently prevent uptake of the various control systems in industrial applications.

This chapter focuses on the introduction of a new method of controlling laser parameters in AM parts that does not focus on closed loop on-the-fly control but instead focuses on the generation of a build file with parameters optimised for every location on the part prior to the start of the build process. This shift should make the qualification of parts manufactured using future iterations of this process, easier.

5.2 Experimental Rationale and Method

It is clear that a new system of generating identical, but complex, and thermally homogeneous parts is required in the AM industry to further promote the introduction of the technology into manufacturing lines. Easier part qualification is also required for this.

Stepping back to basics, AM systems control laser parameters using a list of X and Y coordinates with accompanying laser power and speed constants. The X and Y coordinates are passed to the galvanometer which adjust a series of mirrors so to focus the laser at a specific region on the build plate. All of this information is contained within a .cli file format.

It is theoretically possible to edit the .cli file and generate a new list of X and Y coordinates, along with accompanying power and velocity values. This makes it possible to not only alter laser parameters for complex geometries, but also enables the laser power and velocity to be altered mid hatch. Following from this logic, each hatch can be divided in to lengths of any value enabling very specific regions of the build to be processed using different parameters. It has been shown in previous chapters that some sets of laser parameters that are capable of producing dense components in small parts, are not able to produce dense parts if the geometry cross sectional area is increased. Tight corners, very thin sections, and overhangs were not discussed, however are also known to require different processing conditions to bulk sections. By editing the .cli file for a build based on prior information, the laser power and velocity can be altered to any resolution required so as to prevent excessively hot or cold regions to manifest during each build. This solution would negate the use of on-line closed-loop sensing systems as the build file would be prepared prior to building. The method also ensures that if multiple identical parts are to be produced, they will all be processed with the same conditions at each location, making them mechanically identical.

In order to achieve this, several steps need to be met:

- Understand the effects of cross sectional geometry and scan strategy on the local temperature of each part.
- Understand the effects of through-height cross sectional geometry changes on the local temperature of each part.
- Create an algorithm which splits each hatch line from each layer in to small hatches a few microns in length, and analyses the temperature of each micro hatch. If this is above or below the ‘set point’, or desired, temperature as determined from previous experimental conditions, the laser power and velocity are scaled up or down by an algorithm determined by the difference between the actual and ‘set point’ temperature in order to remove the effect of the hot or cold spot in the pyrometry data.
- A new .cli file is generated from the previous calculations in which all mini hatch lines have their own unique, but fixed, power and velocity values. This file can then be used to build as many identical parts as desired.

An initial build comprising of six different complex shapes, with six repeats of each, was printed using a constant laser power, velocity and hatch spacing set to 130W, 850 mm/s, and 75 µm respectively. For the first four shapes, triangular and square cross sections were chosen. These contained a change in cross sectional area throughout the height of the part in order to identify the effect of this on part temperature; a smaller cross section will see a shorter laser return time and theoretically a larger heat build-up across the layer. Triangular cross sections were chosen in order to replicate the lasing of a part where the return time of the laser reduces with each subsequent pass within the same layer. The change in laser return time within a single layer may lead to localised hot and cold spots on the layer.

A part with a star-shaped cross section was also printed to observe this effect to different extents within each layer. Lastly, a part produced from an artefact provided by Solar Turbines containing overhang structures, internal holes and thin walls was printed in order to observe the effects of differing layer geometries on the layer temperature distribution.

It became clear early on in this work, in 2020, that the AM machine, Aconity Mini, used in this study was unable to read .cli files that contained a change in power or velocity over a single main hatch line. The newly generated file was not registered by the Mini software interface. It was not until 2023 that this was possible due to a software update on an Aconity Midi at Nottingham University, with a subsequent update on the Aconity Mini at the University of Sheffield underway at the time of writing. This Chapter will contain the thermal analysis from the initial builds which was originally to be used as a comparison to identical builds printed using the advanced micro-hatch, power and velocity variant, .cli build file.

5.3 Results

Figure 58 shows the completed build as a top down view and side on. The different part geometries have been labelled A-F, with each duplicate in the set being given a number identifier from 1 – 6. The surface finish on all parts is good and the change in cross sectional area with height is clearly visible. Slight overbuilding can be seen along the edges of each sample. This is due to the edge effect and is hopefully an artefact that can be eliminated using more intelligent build control.

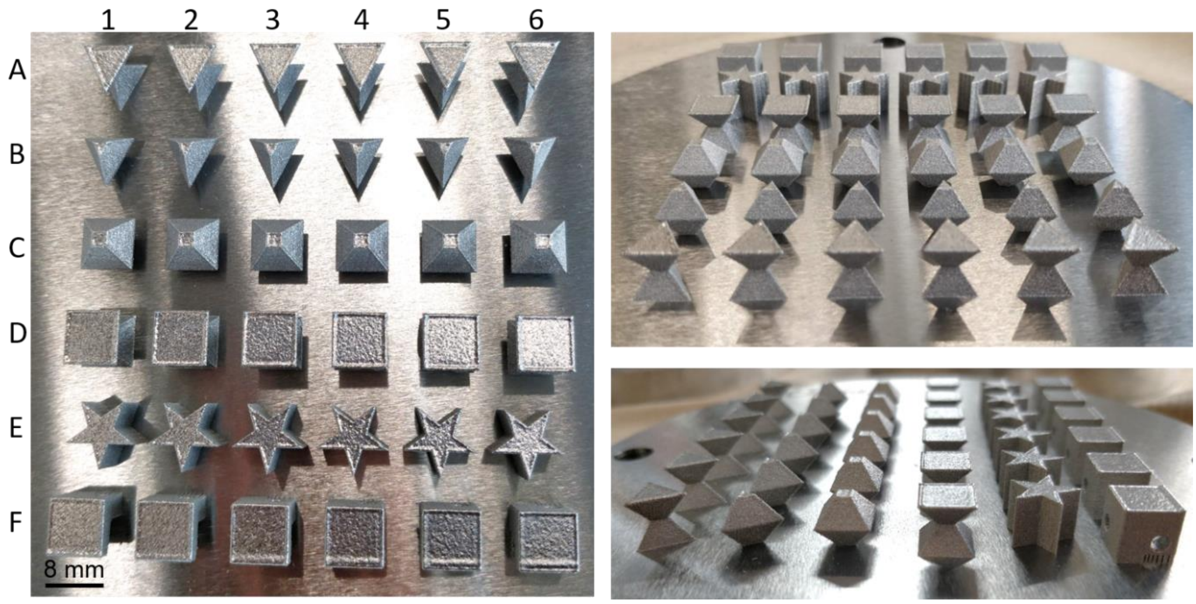

Figure 58: Image of the build plate used to understand the trends in layer pyrometry intensity of different shapes as the cross sectional area increased and decreased with layer height.

5.3.1 Pyrometry Intensity Data

In this section, all discussion will involve the data collected from the pyrometer. As previously, this measurement is an intensity value. However, to make reading of the section easier, the intensity value will be referred to as ‘temperature’. Emissivity changes based on temperature and state of the material, whilst the pyrometer assumes a constant emissivity. It is understood that once a suitable method of transforming intensity values to a real temperature is established, more variation will be observed in the data, enabling correcting strategies to be implemented.

The average layer temperature of part types A - D were produced to understand how the average layer temperature changes with build height, as the cross sectional area is reduced and enlarged. The results of this analysis are presented in Figure 59. The first image shows the average layer temperature data for every layer and the second graph shows the same data after Gaussian noise reduction.

The noise on the data is believed to be due to the 90° hatch rotation scanning strategy used. If the pyrometer is not perfectly aligned with the machine optics, depending on the direction of travel of the laser, a cooler or hotter temperature is recorded (Information from the Aconity Users Online Portal – no reference publicly available). Therefore, the average layer temperature data looks to continuously jump between a 'slightly hotter' and slightly colder' temperature. This is visually demonstrated in Figure 60 which shows part type A (sample 3) over five consecutive layers, 5.34 – 5.46. Layers 5.34, 5.40, and 5.46 show an overall warmer temperature. In these layers, the laser is lasing in a different direction to layers 5.37 and 5.43. This is an artefact of the pyrometer and so proper alignment should be performed prior to setting up the control system on a new machine.

Parts A and B have a triangular base and parts C and D have a square base. Parts A and D initially have a large surface area. This reduces with build height before increasing again. Parts B and C have the opposite trend. These trends are reflected in the average layer temperatures observed in Figure 59. Parts A and D show an increase in layer temperature as the cross sectional area reduces, however this only occurs after a certain point, approximately 125 layers in. Below this, the average layer temperatures are approximately equal. Although the temperatures do decrease again once the cross sectional areas increase past the restriction, they do not decrease to the same level as before. Additionally, no further decrease in temperature occurs after approximately layer 180.

The initial layers of parts B and C are the hottest layers over the whole part. This is likely due to the short laser return time. The temperature decreases steadily until the largest cross sectional area is reached. The increase in average layer temperature from the mid-point to the full part height is more marked in the triangular based parts. Comparatively, the square based parts do not show a clear enough trend to confirm a steady increase in temperature after the mid-point layer height has been reached. This is likely due to the increased probability of forming a hot spot in a sharp triangular shape, where the geometry tapers off during hatching, compared to on a square shape. The final layer temperature of the B and C parts is cooler than the starting temperature. The reasoning behind this is not fully understood.

It is clear from these results that the part geometry plays a large role in the layer temperature of a component. It is important to eliminate this temperature increase with layer height as the temperature difference may alter the solidification kinetics and microstructure obtained in the part.

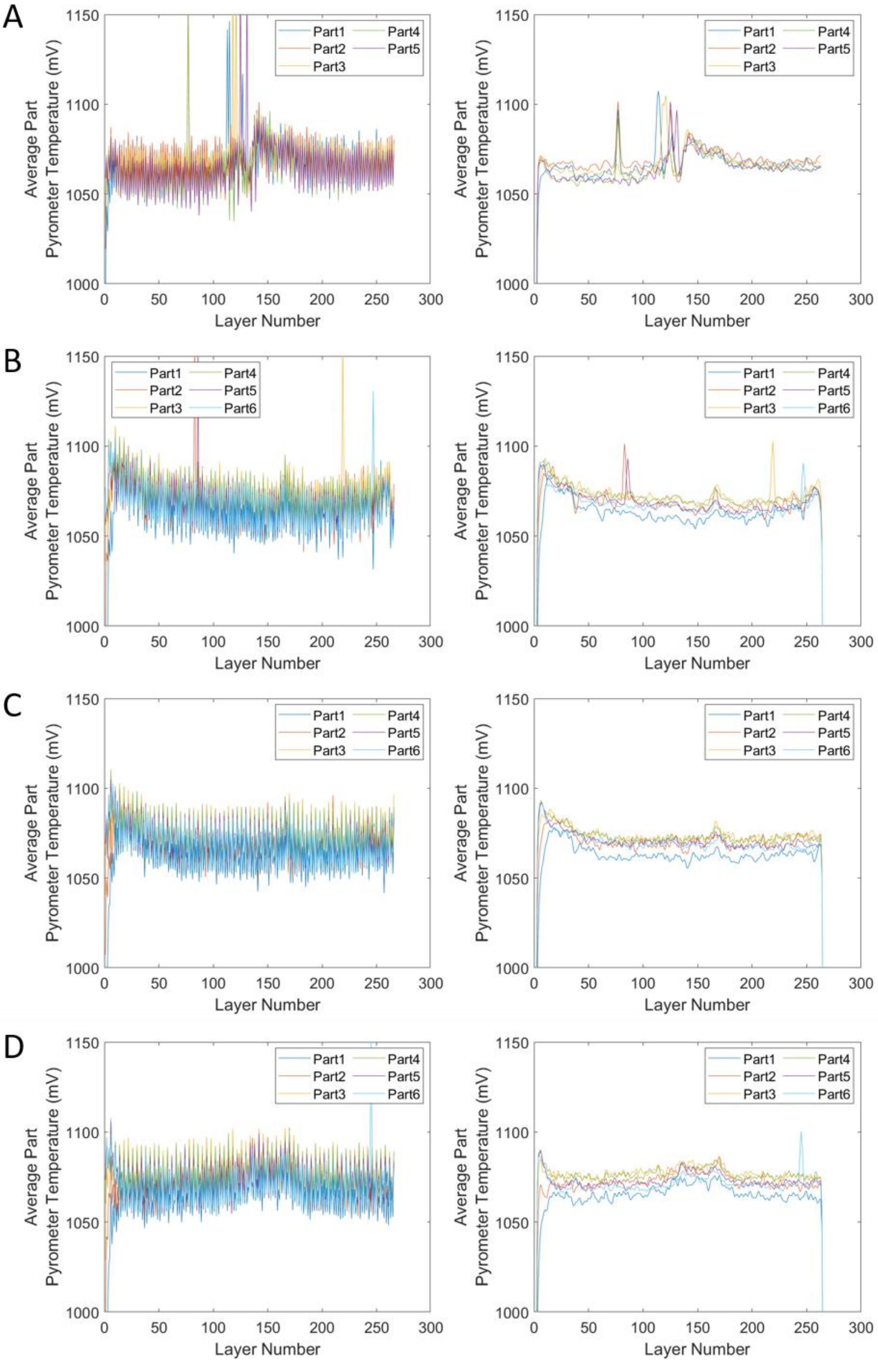

Figure 59: Average layer temperature in millivolts for each part type and part number. Left hand graph shows all the layer temperature values and right hand graph shows the data smoothed by a Gaussian filter allowing the trends to be more easily identified.

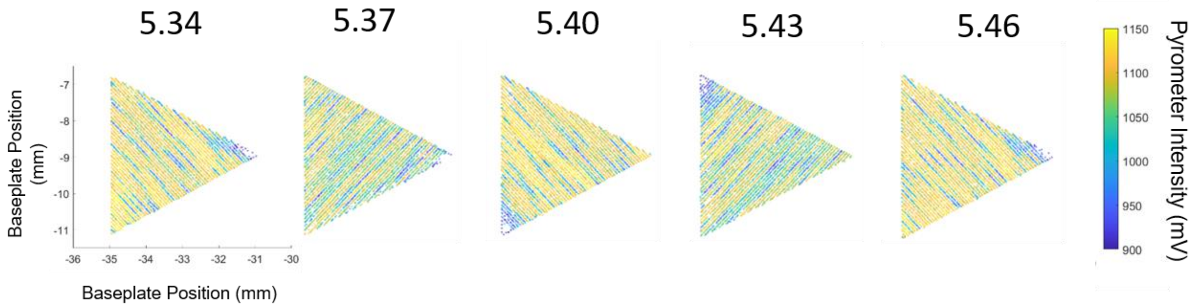

Figure 60: Pyrometry layer data for five consecutive layers of part type A, sample 3, showing the alternating nature of average temperature in each layer. As the laser scans back and forth between the top left and bottom right, a higher temperature is recorded than when the laser scans from bottom left to top right. X and Y axis show baseplate position in mm. This is approximately equal for each layer displayed.

Part types E (Figure 61) and F (Figure 62), were printed in order to understand the extent to which the local temperature within each layer changes depending on the cross sectional area. Shape E is a star shape that was designed to envisage temperature variations in tapered sections. Shape F is a simplified model of a test piece used by the sponsor company Solar Turbines Inc. in order to test their process parameters. The component has thin fins built in the vertical and horizontal directions, thick sections and overhang regions. It is clear that large temperature variations occur across each layer and that the locations of these regions are not the same from layer to layer.

Of importance to note, is that the pyrometer continues to collect data when the laser is off. As discussed in section 3.3 of the Methods chapter, a clustering based algorithm was utilised on the data in order to remove as many cold spots (data where the laser is off) as possible. It is clear in Figures 61 and 62, that it was not able to remove all cold spots in complex geometries. Because of this, low level laser intensity data is present on the Figures between regions where the part cross section is lased. At the time of writing, the Aconity Mini is being updated. In the future, pyrometry data will be saved with a time stamp and so it will be possible to eliminate all captured data points where the laser is off. This will enable a more accurate understanding of the pyrometry intensity values at part edges.

Discounting also the temperature variation brought about by the misalignment of the pyrometer with the laser optics, it is clear that the current laser hatching method is a cause of cooler regions in the build. The laser scans in a meander pattern across the full area of the build which means that for complex shapes, the laser turns on to scan one section, turns off to travel the distance between sections, and turns back on again to lase another section. As the laser turns on and off, it requires a period of ramping up and down the power which may affect the part homogeneity and surface quality. If the laser skips across a number of very fine features, the laser is on for a short period of time, making it more difficult to generate sufficient heat in that portion of the part. In Figure 61 it is clear that cold spots are present at some of the star tips and in Figure 62 cold spots can be seen at thin sections and in the regions surrounding the open circles at the bottom left hand side of the part. Since this work was started, several researchers have investigated the effect of altering the hatching pattern in order to more efficiently lase a complex part without having the laser jump across several thin sections [250], [251]. This is achieved by simulating the temperature field around a laser as it moves though a cross section and creating an algorithm capable of determining the best scan direction in order to reduce the thermal variation across the part. Infrared analysis of very simple two-layer experimental builds show a more homogeneous layer temperature than normal meander scanning methods and this is translated into a reduction in part warping after a build. Therefore the solution reduces residual stress in the part [250]. However, this method increases the build time and as time savings are very important for industrial applications, this poses a disadvantage of the proposed method [250]. Additionally, this method does not enable process parameters such as laser power or velocity to be altered as the scanning geometry changes both with height and across a single layer. Because of this, complex parts will still experience regions of over and under-heating.

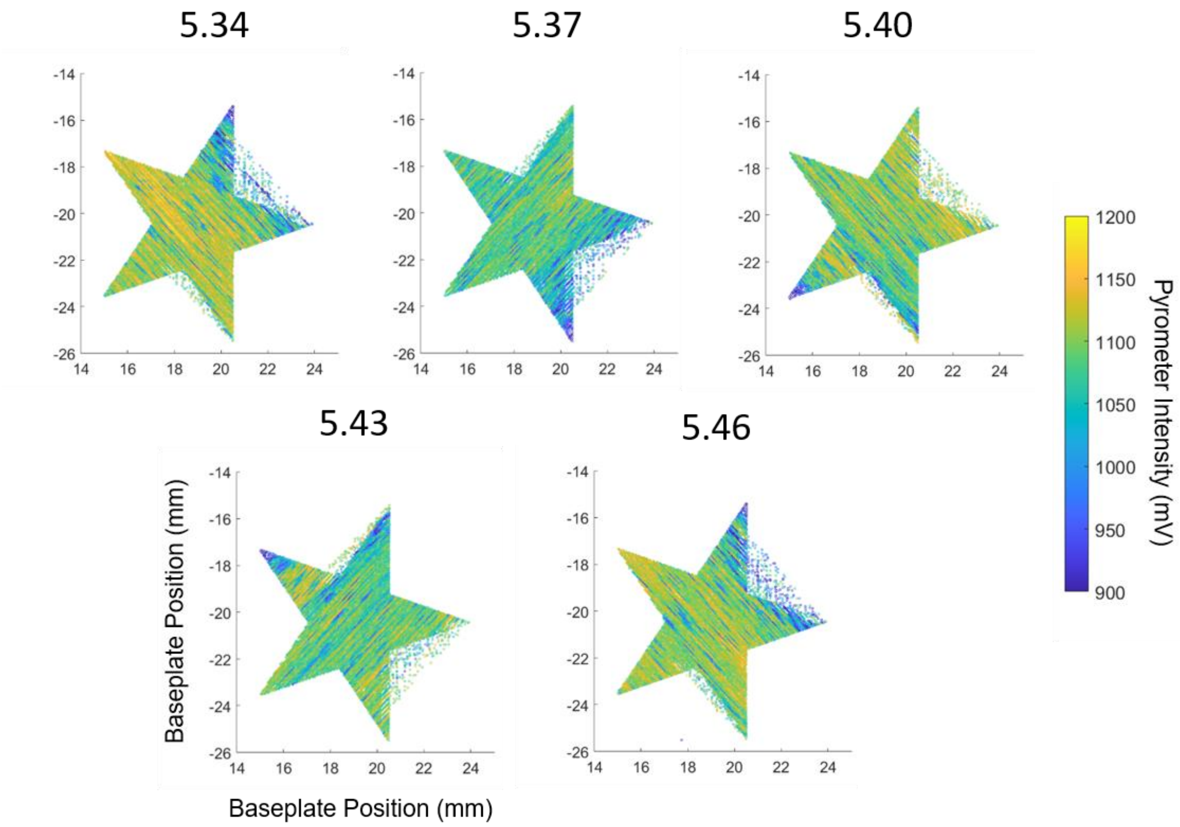

Figure 61: Five consecutive layers of part type E showing the cold spots generated in some of the star shape tips. X and Y axis show baseplate position in mm.

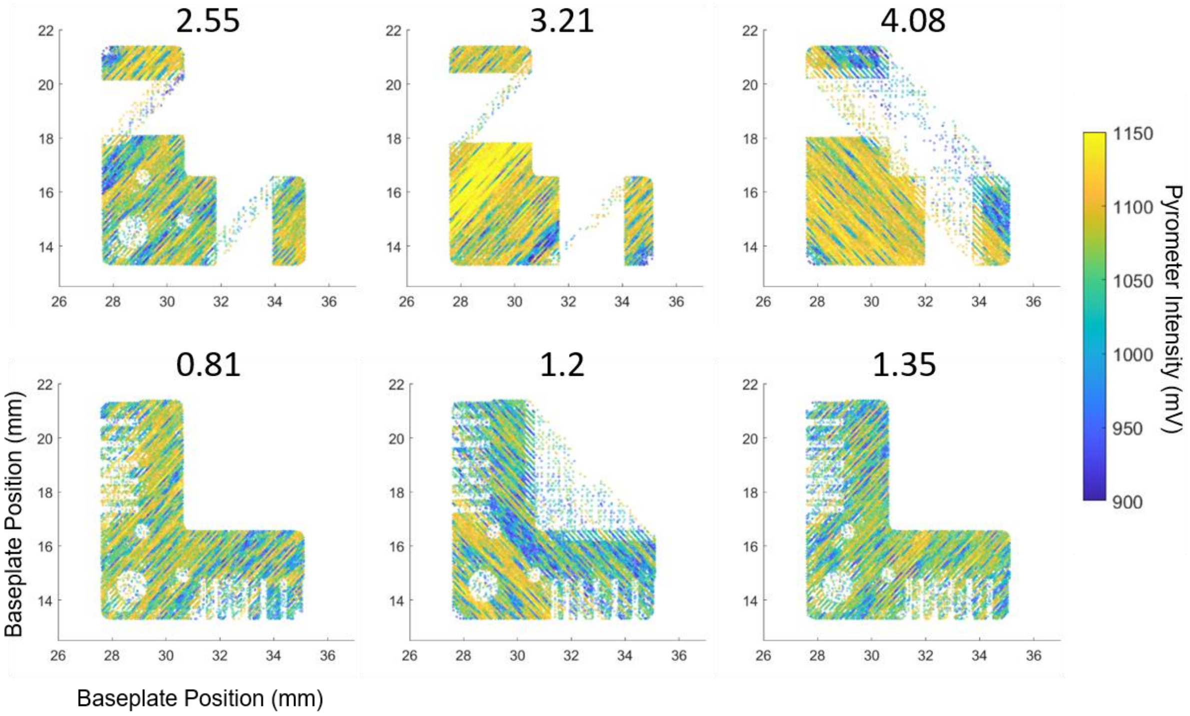

Figure 62: Six different layers of part type F showing hot and cold regions across the layer area. X and Y axis show baseplate position in mm.

5.4 Chapter Summary

When using a single set of processing parameters, as well as standard hatching toolpaths, to print a geometry of varying cross section, temperature variations will occur within and between layers. In this work parts were produced using ‘optimised’ parameters, however these parameters were optimised for simple cuboidal parts and therefore when used to build more complex parts, these lead to the temperature variations displayed in Figures 59-62. It is important to understand that Inconel 718 is a very weldable material with a large processing window and therefore if this experiment were to be repeated for difficult to print metals, the observed temperature variation may have more extreme effects on the part density, surface finish, and microstructure. Therefore, this reinforces the fact that in order to confidently print any complex geometry from any material, as AM was intended for, the ability to keep all regions of a build at the same temperature is required.

Whilst closed loop control systems are able to adjust laser parameters during a build, it has been explained that producing parts in this manner makes them difficult to qualify in advanced engineering situations. Additionally, it has been shown that inter layer temperature variations can be minimised by altering the laser toolpath, however this method has been shown to have disadvantages.

A method of control which splits all hatch lines in to mini segments that are all capable of producing a different laser power has been proposed. This method would utilise the pyrometry data from a previously built part in order to produce, and lock down, an optimised .cli file for a particular component. This would ensure a homogeneous temperature to be obtained at all regions of the build and ensure all parts printed using the file were identical.

Unfortunately, the adoption of a new control method was not possible within the time-frame of this thesis due to software constraints on the LPBF system at the University. It is not until after the submission of this thesis that the machine will have the required upgrades. However, in the meantime plans had been made to investigate how this new method of control could be developed and how it would work.

This chapter provides a start to this work package by generating a baseline to which the eventual ‘control’ builds are to be compared. Although not shown here, as well as visual analysis of the overall layer temperature variation, specific locations within these shapes will be monitored layer by layer and compared to a ‘control’ build.

Initially the effect of altering the laser power mid hatch on the local temperature was to be observed. From the experimental results discussed in Chapter 4, the pyrometry signal that corresponds to the production of an optimised and fully dense microstructure was ~1070mV. This is called the ‘set point’ pyrometry value. By tuning the power in each sub-hatch based on a weighting factor determined by the difference in mV between the ‘set point’ and the ‘real’ case as displayed in this chapter, it is believed that a more homogeneous part temperature can be achieved.

Based on the information learnt from Chapters 4 and 5, as well as the limitations on *in-situ* control that were available on the instrument at the time, the direction of the project shifted emphasis towards microstructural control and functional grading utilising defect distributions. The subsequent chapter will emphasize this in greater detail.

6 Functional Grading via Intentionally Placed Defect Populations

6.1 Introduction

A major untapped potential of laser powder bed fusion is the ability to additively manufacture parts with site-specific properties. However, robust methods of improving performance and manufacturing efficiency via spatial variations in microstructure are underexplored.

Previous chapters have demonstrated the ability to produce microstructures with varied and characteristic LPBF defect structures by altering the applied processing parameters. However, although the use of process parameters can be an effective tool towards spatial microstructural variation, it is also clear from the preceding chapters that the large uncertainties associated with layer temperatures as well as the complexity of geometries can lead to reduced confidence in utilising build parameters alone for microstructural control. This work introduces a hybrid method of manufacture for the creation of multi-modal microstructures in Inconel 718 by performing a Hot Isostatic Pressing (HIP) procedure on characteristic LPBF discontinuities such as keyhole and lack of fusion porosity, as well as large powder filled voids.

The method of producing functionally graded microstructures by relying solely on the build phase of component manufacture has been explored by Popovich *et al.*[9]. Although their approach was successful in generating a bi-modal microstructure, the parameters used were extreme, resulting in increased levels of porosity in one of the microstructures generated. This led to poor fatigue properties [235]. Additionally, in the previously discussed work by Sofinowski *et al.* [175], it was shown that although variations in texture can be achieved in AM parts by altering the scan angle between layers, this did not alter the grain structure and so the produced parts will still likely have anisotropic mechanical properties. In their work, the transition between two different grain textures was also not instantaneous, which limits the use of this method in achieving precise microstructural differences within complex samples. Work using electron beam additive manufacturing has shown the potential for precise differences in grain structure to be achieved in titanium samples after HIP however [239].

HIP is regularly utilised in the post processing of AM materials in order to reduce porosity, and has been shown to be able to eliminate both keyhole and LOF pores [51]. HIP densifies material by the collapse and healing of pore walls by microscopic plastic deformation and atomic diffusion under the effects of elevated temperatures and isostatic pressure [25]. Operational temperatures, in the region of 1100-1200^{o}C, often provide sufficient additional driving force for recrystallisation to occur in the material. The combination of the above processes was believed to prove useful in the generation of a novel method to produce multi-modal microstructures in Inconel 718.

Observed using electron backscattered diffraction, this approach enables the formation of site-specific variations in microstructure and extreme bi-modal microstructures in which grains differ in area by 194%. Additionally, as opposed to the typical anisotropic AM microstructures, this method facilitates the production of equiaxed and strain free materials culminating in a 62% energy saving, and 47% time saving per layer. Although trialled using Inconel 718, this method has the potential to enable more difficult to additively manufacture materials, such as nickel superalloys with high γ' fractions, to be produced into components without cracks. This presents a large benefit for the AM industry.

6.2 Material and Methods

6.2.1 Material Processing

Four sets of 6 identical cylindrical samples, as shown in Figure 63, were printed on the Aconity Mini. Each cylinder measured 8mm in diameter and 10mm high. A fully dense outer shell contained a 6x6mm internal region in which the printing parameters were altered to produce either, a) fully dense material, b) keyhole discontinuities, c) LOF discontinuities, or d) 3 internal spherical cavities, 2mm in diameter, holding unmelted powder. The process was performed under an Argon atmosphere and printing parameters are detailed in Table 16. The parameters used to print the Dense were previously optimised for Inconel 718, as discussed in Chapter 4. Pyrometry intensity data for the Dense, Keyhole, LOF and Dense samples was recorded 'by layer' during building. In order to process the pyrometry layer data to sections corresponding to the individual defect regions, all data points belonging to a single part were clustered using a density based spatial clustering algorithm (DBSCAN) developed by Ester *et al.*[252]. Once clustered, the average pyrometry intensity of each cluster was calculated.

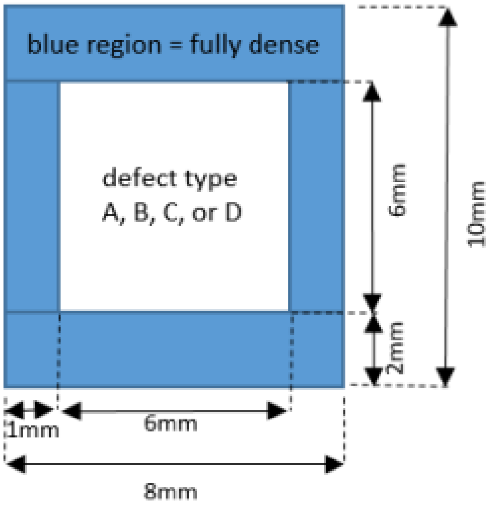

Figure 63: Cross sectional diagram of the cylindrical samples manufactured. Blue outer shell printed with optimised parameters for Inconel 718 with the internal region printed with laser parameters intended to produce b) Keyhole and c) LOF porosity or d) spherical voids. Control samples were printed with a fully dense centre region; defect type a).

Two additional sets of cylinders were retrospectively built on a different baseplate, one in which the central region was produced using a -8mm laser defocus, and one where a higher laser power and lower laser velocity than the original Keyhole discontinuity sample, was used. These additional samples were printed with a 90^{0} layer rotation strategy as compared to the 67^{0} rotation strategy used for all other samples in this section. These additional samples were also only subject to HIP as detailed below, and not additional post HIP heat treatment.

The samples are designated as follows: Dense, Keyhole, LOF, Sphere, Defocus and High Power Keyhole. When the bulk region of the Sphere sample is discussed, it is referred to as Sphere Bulk. When the densified powder region of the Sphere sample is discussed, it is referred to as Sphere Void.

Table 16: Laser process parameters used to manufacture the discontinuity cylinders

	Laser Power (W)	Laser Velocity (mms^{-1})	Hatch Spacing (μm)	Layer Thickness (μm)	Focus Offset (mm)
Dense	130	850	75	30	0
Keyhole	166	582	42	30	0
LOF	94	1118	108	30	0
Defocus	130	850	75	30	-8
High Power Keyhole	170	500	42	30	0

6.2.2 Heat Treatment

Four samples in each set underwent HIP (1160^{o}C / 102MPa / 3 hours / air cool) with a temperature ramp up rate of 10°C/min. Of these, two samples in each set underwent post HIP solution treatment (980^{o}C / 1 hour / air cool) and a double age heat treatment (HT) (720^{o}C / 8 hour / furnace cool to / 620^{o}C / 8 hour / air cool). The first stage of the HT performed was designed to allow a small fraction of δ phase to precipitate at grain boundaries, preventing grain growth, while the second, two-step, stage was designed to enable the hardening precipitates to form. Two of each sample type were printed to ensure sufficient data availability in this study. Samples are referred to as as-built if they did not undergo any heat treatments, and HIP, or HIP + HT if they underwent only HIP or both HIP and Heat Treatment respectively.

6.2.3 Sample Analysis

Samples were cross sectioned parallel to the build direction in the as-built, HIP only, and HIP + HT states by wire electrical discharge machining (EDM), and polished to a mirror finish using standard metallographic preparation techniques culminating in a polishing step utilising colloidal silica suspension of 0.25µm.

Observation of the internal discontinuity structures across the whole sample cross section was performed using an optical microscope fitted with a Clemex Vision camera and Image Analysis Software. Information on the sample density and discontinuity shape characteristics was obtained from the optical images using an automatic thresholding technique in Fiji ImageJ [253]. As a single image was taken for each sample, no associated errors are presented.

Electron backscattered diffraction (EBSD) was performed in a JEOL 7900 SEM with an accelerating voltage of 20kV, and a step size of between 1-1.5um, to analyse the grain orientations within each sample. Image reconstruction and analysis was performed on MATLAB2021b using the MTEX toolbox using the protocol discussed in section 3.5.7 of the Methods section.

Maps showing grain orientations, Σ3 boundaries, Grain Orientation Spread (GOS), and Kernel Average Misorientation (KAM) were produced from the reconstructed EBSD data for all discontinuity samples in the as-built, HIP only and HIP and HT states. The GOS indicates the amount of intergranular misorientation present and is calculated by taking the ratio of the average of the deviation of all points in the grain from the grain mean orientation and the grain mean orientation. This information can be supplemented with KAM maps, which show the location and extent of this misorientation. Pole figure diagrams for the Dense, Keyhole and LOF samples were also plotted from the EBSD data for the as-built and HIP + HT conditions.

Histograms of the area weighted grain area were produced for each sample in all conditions. All grain size data such as grain area, grain diameter, and aspect ratio did not follow a normal distribution and therefore the calculation of mean and standard deviation data was not possible. As a result, all analysis of the resulting microstructures in this chapter will be performed qualitatively using the figures presented.

Lastly, hardness information was gathered on the Dense, Keyhole, LOF and Sphere samples in the as-built, HIP and HIP+HT states using the Durascan automatic hardness testing machine as described in section 3.5.5 of the Methods section.

6.3 Results

6.3.1 Pyrometry Intensity Data

Pyrometry intensity data for the defect regions of each cylinder are shown in Table 17. For the Sphere sample, the average layer temperature for the full sample was calculated. This is because the sample did not include an ‘outer cylinder’, rather included large inner voids. Each value shows the mean average layer intensity signal with an error given as the coefficient of variation.

The Dense and Sphere samples both had an average part intensity of approximately 1040mV which is expected as they were both processed with the same laser parameters. The Keyhole sample recorded a higher value, whilst the LOF sample recorded a lower value. This is representative of the laser parameters utilised in each respective sample type as they resulted in an equivalent energy density of 9.33 and 1.09 respectively (with the Dense parameters providing an equivalent energy density of 2.83).

Table 17: Pyrometry values of the mean average layer intensity of each part in millivolts. Error given as coefficient of variance.

	Mean Average Layer Intensity (mV)			
	Dense	**Keyhole**	**LOF**	**Sphere**
Part 1	1027.7 ± 1.3%	1157.8 ± 7.0%	1006.7 ± 1.5%	1051.8 ± 1.0%
Part 2	1049.9 ± 1.5%	1183.1 ± 7.0%	1015.7 ± 1.8%	1050.1 ± 1.1%
Part 3	1025.4 ± 1.3%	1144.3 ± 7.4%	1017.4 ± 1.9%	1045.4 ± 1.3%
Part 4	1035.3 ± 1.9%	1176.0 ± 6.6%	1013.5 ± 1.2%	1047.7 ± 1.1%
Part 5	1050.6 ± 2.2%	1163.4 ± 6.8%	1011.0 ± 1.4%	1049.7 ± 1.5%
Part 6	1045.9 ± 1.0%	1194.6 ± 5.6%	1016.7 ± 1.5%	1048.4 ± 1.0%
Average	1039.1 ± 0.6%	1169.9 ± 2.8%	1013.5 ± 0.6%	1048.9 ± 0.5%

Although all the internal defect regions had constant cross sectional areas, that of the sphere sample decreased and increased in order to accommodate the internal spheres. This resulted in a change in average layer temperature during the course of the build as shown in Figure 64. The initial layers required lasing of the full cross sectional area of the part, leading to a specific average intensity. As the internal voids appeared, the cross sectional area reduced, with the laser turning on to lase the cylinder edge, turning off to skip over the central region, and turning back on to lase the far edge of the cylinder. No skywriting parameters were utilised in the building of these parts and therefore there will have been a laser ramp up and down time in the lasing of each edge (before it skipped over the central void region). In addition to the reduced build area in these regions, this effect will have led to reduced heat build-up in these respective layers, resulting in a lower average layer intensity. This effect was previously also demonstrated in Section 5. As the layer increased in cross sectional area during the processing of the second half of each internal void, lasing of a slight overhang was required in each subsequent layer until the inner sphere was fully formed. In this case, the inverse of the discussed effect took place, a larger build up in heat occurred in each subsequent layer, producing an increase in overall layer intensity. This is also accelerated by the lasing of an overhang as powder has a reduced heat conduction capability than solidified material. The increase in layer area also leads to a larger region of material that is able to produce a constraining effect during cooling, potentially leading to a higher level of residual stress at these locations.

It is clear that the Keyhole sample contains very large spikes in average layer intensity. This is accompanied by a larger coefficient of variation between average layer temperatures. These spikes seem to occur in a semi-regular manner. The pyrometry data was recorded by 'layer' for the whole build. This means that in order to separate out the data points that belonged to each 'defect' section for analysis, a k-means clustering algorithm was used to identify the mid-point of the data points for each cylinder. From here, all data points that lay within a circle of radius 2.8mm was extracted in order to calculate the layer intensity for each part. Figure 65 shows the region of each cylinder covered by this circle. It is clear that the laser path taken produced a slight ellipse in the built part. This is likely due to effects pertaining to the laser beam being directed by galvanometer controlled mirror system, however identifying exact reasons for this are out of the scope of this work.

The Keyhole sample was produced with a lower laser velocity. As the data recording frequency of the pyrometer is constant, this results in more data points being produced per unit area in the Keyhole sample. In addition to this, the keyhole sample was produced using a higher input energy density, leading to a steeper increase in temperature as the hatch lines reduced in length near the edge of the circular cross section. This is exacerbated by the fact that the Keyhole sample was designed to produce keyhole porosities, which requires material to vaporise and induces turbulent melt pool activity. This is likely to have impacted the intensity collected by the pyrometer.

Therefore, due to the elliptical shape of the built part and the circular space from which data points were utilised, as well as the 67^{o} layer rotation used to build the parts, the data extracted per layer for the keyhole sample will periodically exclude the regions where an increase in temperature is expected. Combined with the stochastic turbulence exhibited during printing of the Keyhole sample, these phenomena are believed to produce the effects observed in Figure 64. The Dense and LOF samples are not expected to undergo such a large increase in temperature near the edges of the sample, so, although these traces still show peaks and troughs in the average layer temperature, this effect is not as prominent as in the Keyhole sample.

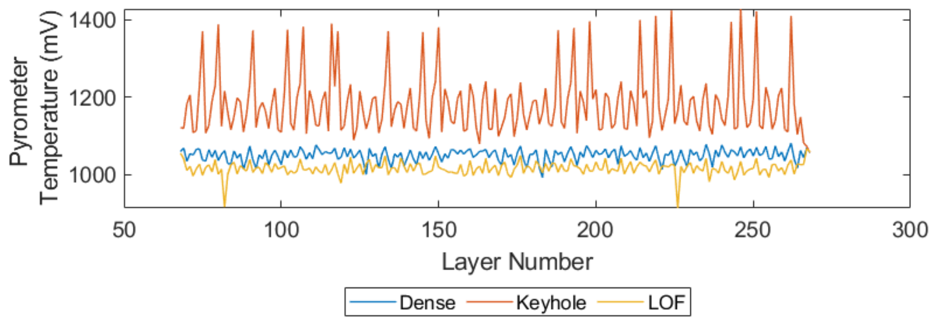

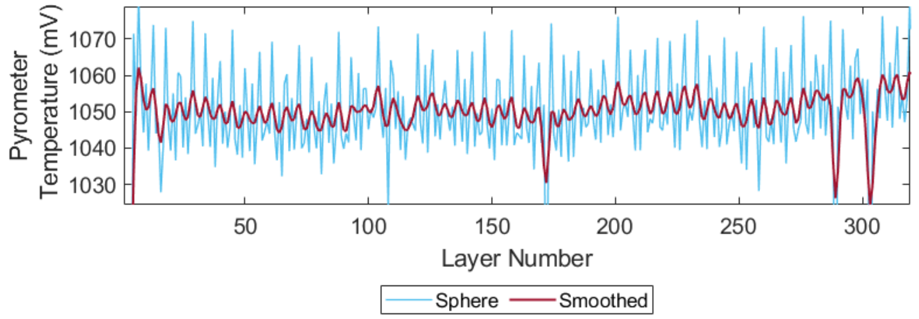

Figure 64: Average layer pyrometer intensity measured in millivolts for each sample, Dense, Keyhole, LOF, and Sphere. The Sphere sample is shown on the bottom subplot in order to highlight the waviness of the average layer intensity pattern due to the variation in internal geometry lased. The Keyhole sample shows a number of intensity spikes in a regular pattern which is believed to be an artefact of the combination of the data processing method utilised as well as distortion in the built part.

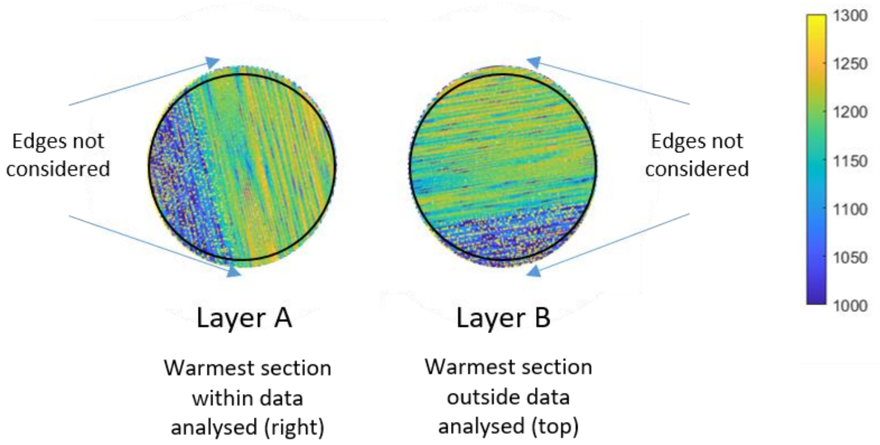

Figure 65: Pyrometry data for two layers of the 'defect' section of the Keyhole sample along with the data included in the calculation of average layer temperature shown inside the black line. Due to slight inaccuracies between the intended laser scanning coordinates and the actual laser scanning coordinates, as well as the method utilised to extract the required data from the pyrometry file, some temperature information from each layer is not considered in the average temperature measurement. In some layers, for example A, the warmest part of the layer lies within the data capture area, while for other layers, B, the warmest part of the layer lies outside the data capture area. Due to the set layer rotation of 67^{o}, this produces a periodic effect in the average layer pyrometry intensity calculated.

6.3.2 Morphology of Defect Structures

A laser power of 130W, velocity of 850mm/s and hatch spacing of 75µm, enables fully dense outer shells to be produced with a density of 99.98%, as shown in Figure 66. Although these parameters have been optimised for fully dense microstructures, defect analysis in Figure 67, shows that a few small and circular gas pores are still present in the central region of the Dense cylinder. As discussed in section 2.2.4 Defects in LPBF, these pores are known to originate from the metal powder or can become incorporated in to the material by entrapment of the process gas during printing.

An intentional increase in power, and decrease in velocity and hatch spacing to 166W, 582mm/s, and 42µm respectively, leads to the formation of keyhole porosity (99.66% density). Figure 67 shows that the Keyhole porosity is less homogeneous in size than the gas pores identified in the Dense sample. In Figure 66, the keyhole pore size is observed to increase nearer the shell region indicating that the increased heat generated during the laser turn function in the meander scan strategy was required to initiate keyhole pore formation.

The increased levels of keyhole formation at cylinder edges is also observed in the High Power Keyhole sample which was produced with a higher laser power (170W) and lower laser velocity (500mm/s). Although the sample achieved a similar density to that of the Keyhole sample at 99.71%, from the defect distribution shown in Figure 67, these pores are more circular and overall larger.

A power, velocity and hatch spacing of 94W, 1118mm/s, 108µm respectively leads to extensive lack of fusion (LOF) porosity with a density of 91.50%. These pores are highly irregular in shape and a proportionately small number of very large pore lengths (200-470µm) indicate a high level of pore connectivity.

The defocus sample shown in Figure 66 is approximately 2/3 the height of the other cylinders. This was due to an error in the build file for that sample in which the height of all parts on the baseplate were reduced in size. This will have affected the number of counts of pores identified in Figure 67, but should not affect the distribution of discontinuities obtained. The Defocus sample achieved the lowest density, 89.00%. The average feret length and average pore area are larger than those observed in the LOF sample indicating the presence of larger LOF pores and a higher level of pore connectivity.

A line of discontinuities can be observed between the cylinder shell and internal region in the Dense sample. These are due to insufficient overlap between the two surfaces. As they are assumed to be present in each sample, all grain structure analysis post heat treatment was performed in the central region of the defect area so as to not include these discontinuities in concluding analysis.

Densities of the Dense, Keyhole, LOF and Sphere samples after HIP + HT were 99.94%, 99.85%, 99.94% and 99.95% respectively. Depressions are observed in the top and bottom of the Sphere sample as a result of plastic deformation by the isostatic pressure on the hollow spherical regions.

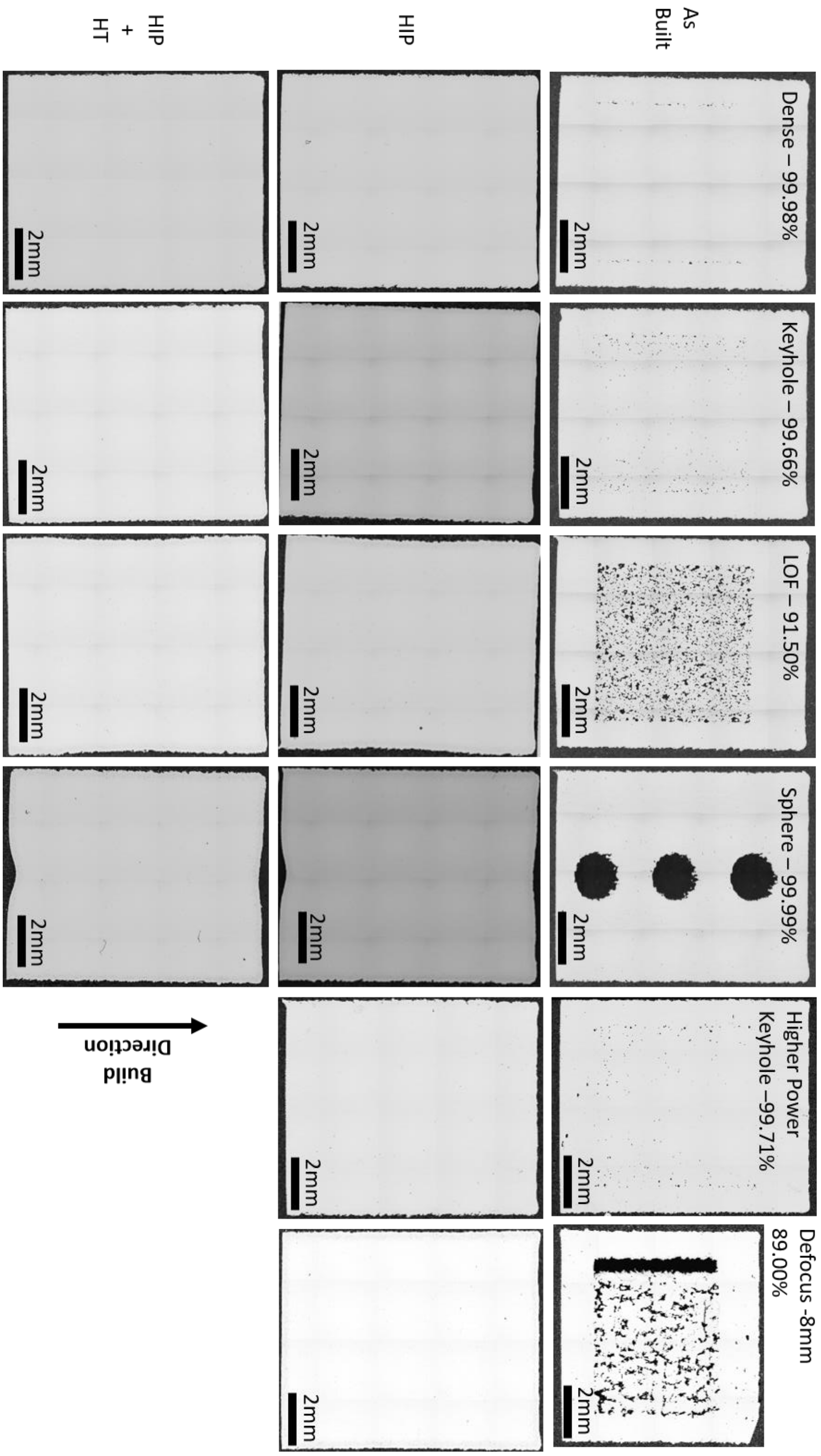

Figure 66: Optical micrographs of the cross section of each cylindrical sample. The top row shows the as-built samples containing the associated internal discontinuity structures, the middle row shows the samples after HIP only, and the bottom row shows the samples after HIP + HT. All samples observed full densification by the heat treatments performed.

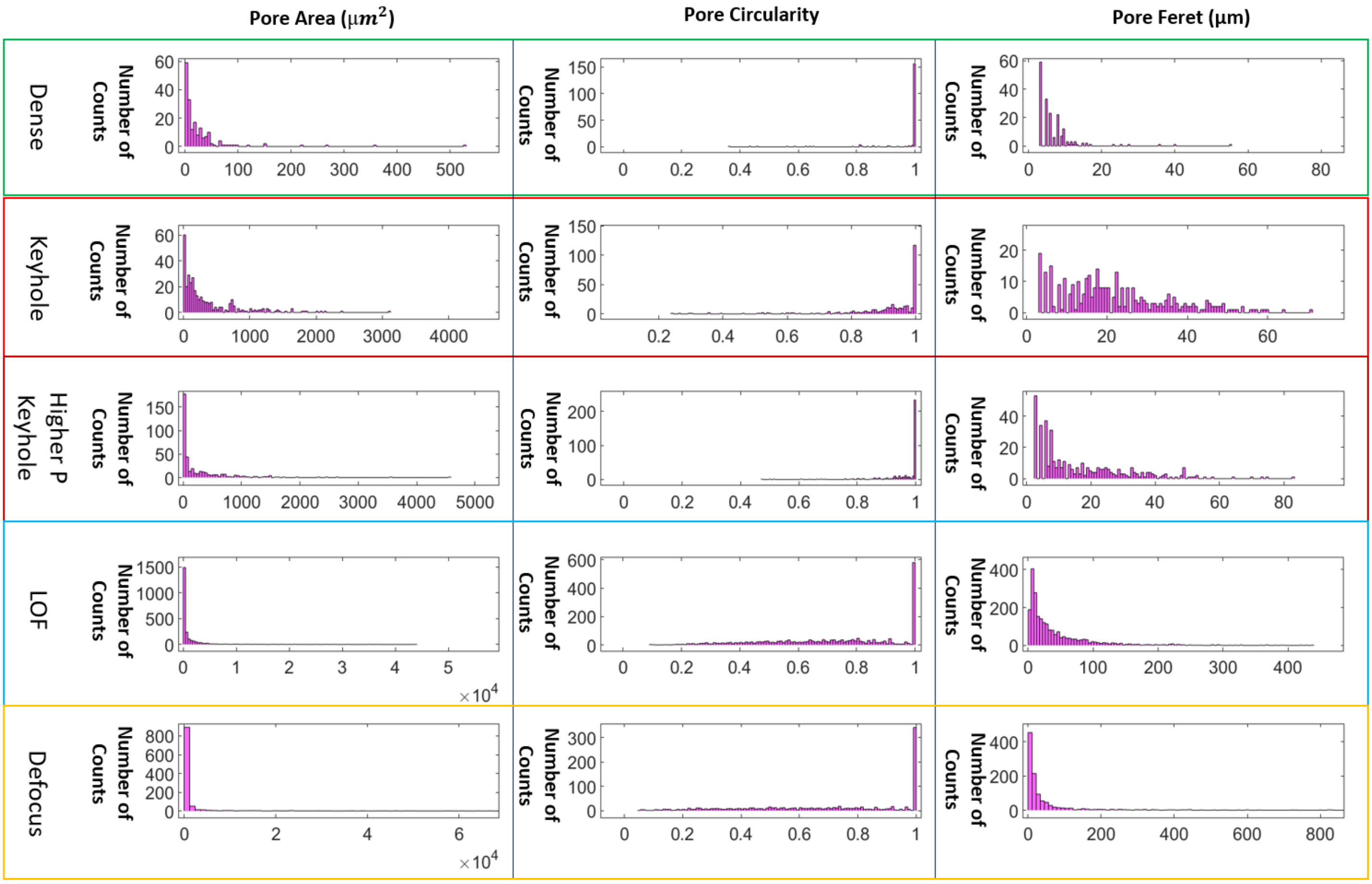

Figure 67: Analysis of the as-built discontinuity structures for the Dense, Keyhole, LOF, Defocus and High Power Keyhole samples. Note the change in scale for LOF. The top row shows details for the Dense sample (green outline), second row shows details for the Keyhole sample (red outline) and bottom row shows details for the LOF sample (blue outline). The first column shows a comparison of the pore area for each sample, the second column shows a comparison in pore circularity between each sample, and the third column shows the ferret length of discontinuities s in each sample.

6.4 Microstructural Morphologies of the As-Built, HIP and HIP + HT Samples

6.4.1 As-Built State

Inverse pole figure (IPF) maps with respect to the building direction of the as-built samples are shown in Figure 68. All samples observe elongated grains as a result of epitaxial growth from the melt pool. Figures 69 and 70 show data for the grain area measurements for each sample.

In the as-built state, the higher energy processing parameters enabled the Keyhole sample to obtain a higher grain area than the Dense, LOF, and Sphere Bulk samples. As only a narrow region of the Sphere Bulk sample could be analysed in the as-built state, it is acknowledged that these results may not be representative of the full sample. The Defocus sample attained a larger grain area than the LOF sample. This could be due to the larger laser spot size used in this sample which enabled a larger area of the material to remain above the solidification temperature for a longer period of time. This sample was also printed using an overall higher normalised equivalent energy density. The High Power Keyhole sample contains the largest grain areas and exhibits a grain structure in which the grains have a 'zigzag' shape. All samples apart from the High Power Keyhole and the Defocus samples were printed using a 67^{o} layer rotation, however the latter two were printed using a 90^{o} rotation which is believed to have caused this microstructural difference.

Pole figure maps in Figure 71 confirm a higher degree of preferential alignment of the [001] grain direction with the build direction in Keyhole and High Power Keyhole samples compared to the LOF and Dense samples. This is to be expected as they were produced with a higher energy density [9]. The Dense and Defocus samples also show preferential alignment, however, the LOF sample shows the absence of any particular preferential grain orientation. Figure 68 includes a closer image of the LOF sample in which a large amount of very fine grains can be seen. The lack of epitaxial growth in this sample is believed to the reasoning behind the lack of preferential grain orientation.

Clusters of finer grain sizes are observed within the Keyhole sample in Figure 68, some of which are accompanied by keyhole pores. These are believed to have been caused by high levels of turbulence in the melt pool, consequently preventing local epitaxial growth [233].

While evidence of epitaxial growth is visible in regions far from voids in the LOF and Defocus samples, the presence of large voids resulted in locally reduced epitaxial growth, resulting in a bimodal distribution of grain sizes. The LOF and Defocus samples therefore contain a high volume of small, more randomly orientated, grains surrounding the irregular void regions. Closer inspection of the boxed region in the LOF sample (Figure 68) shows that partially melted powder particles, which have retained their fine grain morphology, reside within the void regions. In all samples that contained deliberately placed voids, such as the Keyhole, High Power Keyhole, Defocus and LOF samples, the reduction in epitaxial growth led to an increase in grain boundary area as well as an associated increase in surface energy [197].

Elevated levels of GOS and KAM in each sample, shown in Figure 72, suggest regions of increased long range misorientation across each grain due to the presence of GNDs [254], [255]. Quantification of these requires higher magnification EBSD analysis and is out of the scope of this thesis. Instead, the relative reduction in KAM and GOS will be used as an indicator of recrystallisation having occurred. Elevated levels of KAM were identified at regions immediately surrounding voids in both the LOF and Keyhole samples as shown in Figure 73. As material voids hinder heat conduction, it is proposed that regions near a void remained warmer for longer, enabling the formation of dislocation walls. It has also been demonstrated that keyhole and LOF voids have angular internal shapes which may act as stress concentrators, leading to the accumulation of dislocations during subsequent laser passes, during the relaxation of residual stresses, or during external plastic deformation [33].

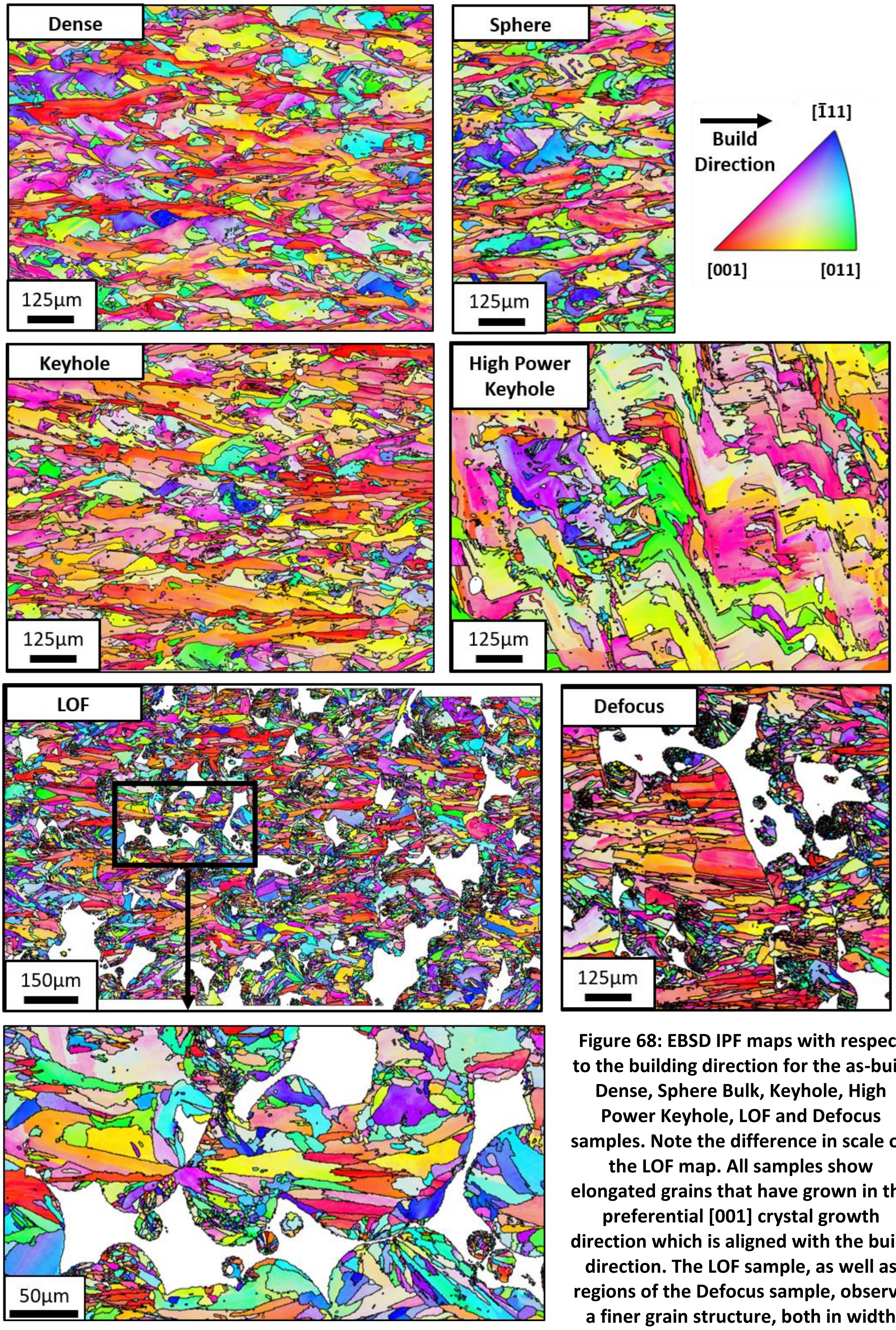

Figure 68: EBSD IPF maps with respect to the building direction for the as-built Dense, Sphere Bulk, Keyhole, High Power Keyhole, LOF and Defocus samples. Note the difference in scale on the LOF map. All samples show elongated grains that have grown in the preferential [001] crystal growth direction which is aligned with the build direction. The LOF sample, as well as regions of the Defocus sample, observe a finer grain structure, both in width and length of the grains, as compared to the other samples. The inset shows that regions surrounding voids in the LOF sample have a more random selection of orientations. Unmelted

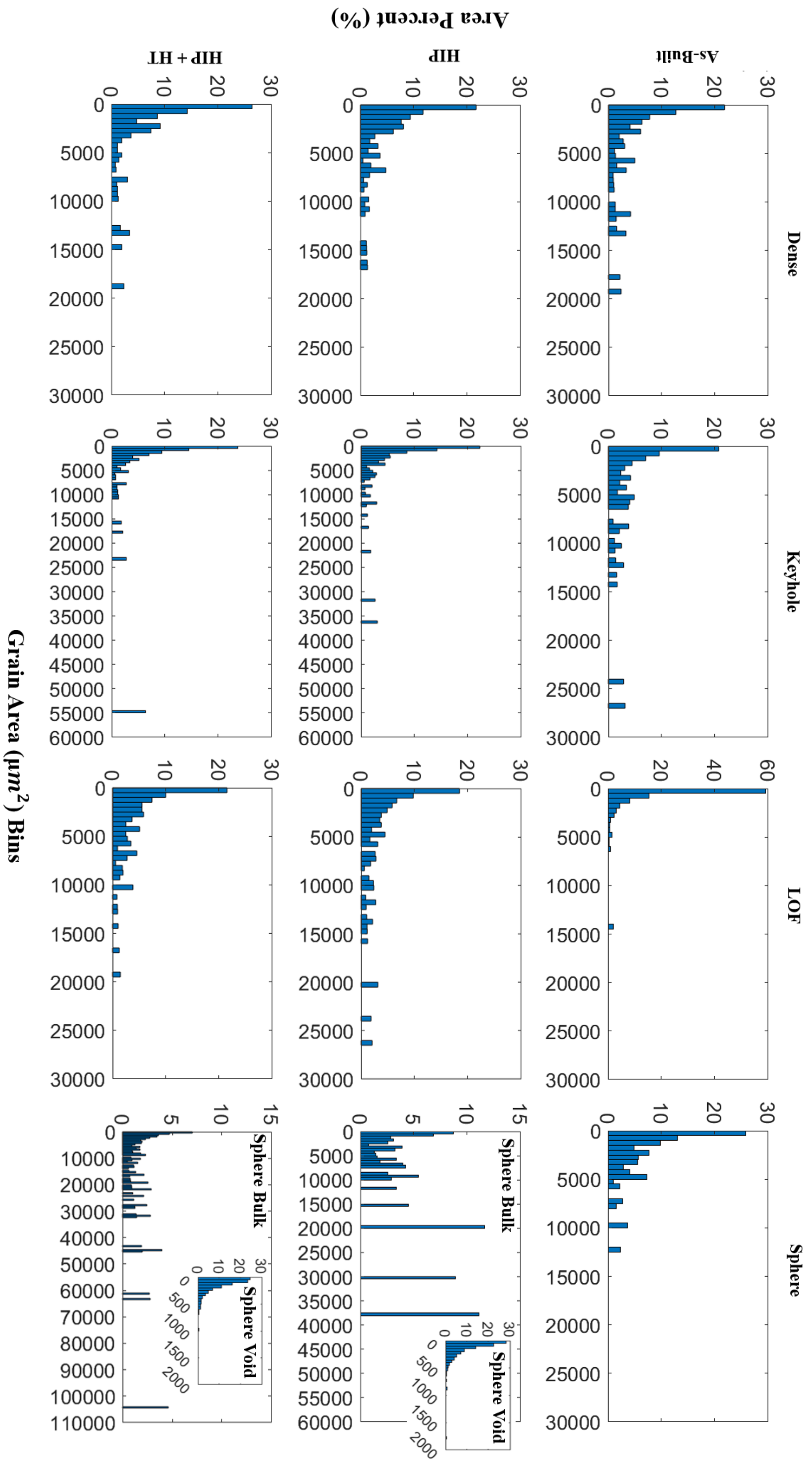

Figure 69: Grain area plots for the Dense, Keyhole, LOF and Sphere samples in the as-built, HIP and HIP+HT states.

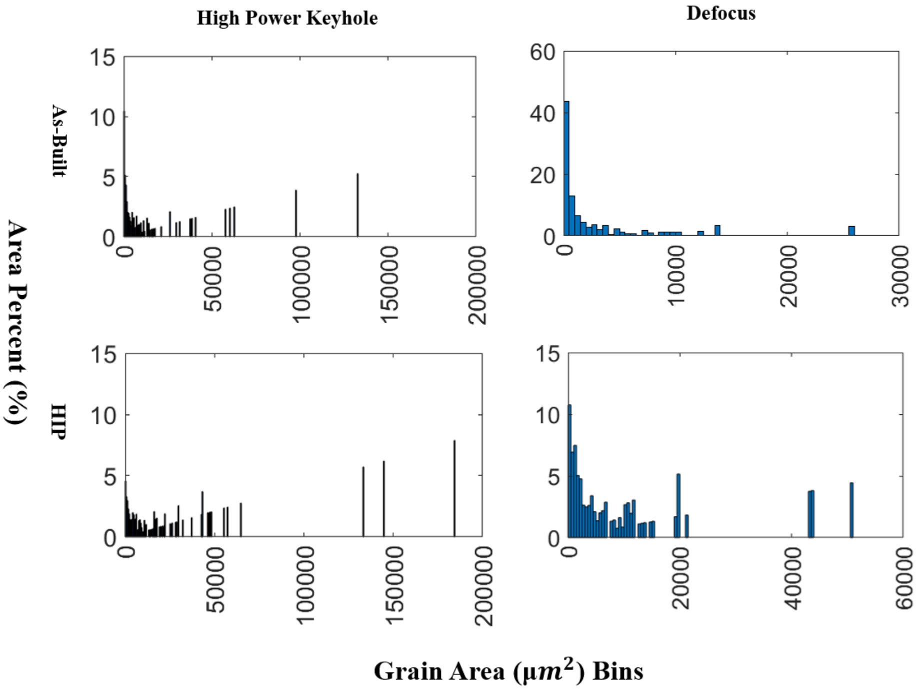

Figure 70: Grain area plots for the High Power Keyhole and Defocus samples in the as-built and HIP states.

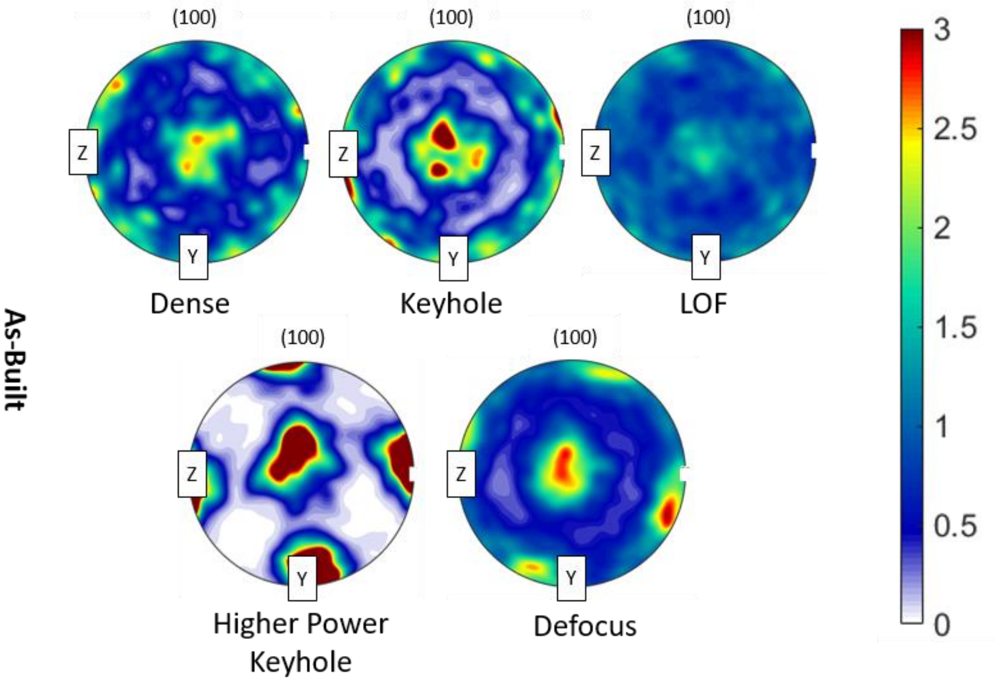

Figure 71: Pole figure maps of each sample in the as-built state in the X, or build, direction. The Dense, Keyhole, Higher Power Keyhole, and Defocus samples all observe grains with their easy growth direction

parallel to the building direction whilst the LOF sample shows an absence of specific grain growth orientations.

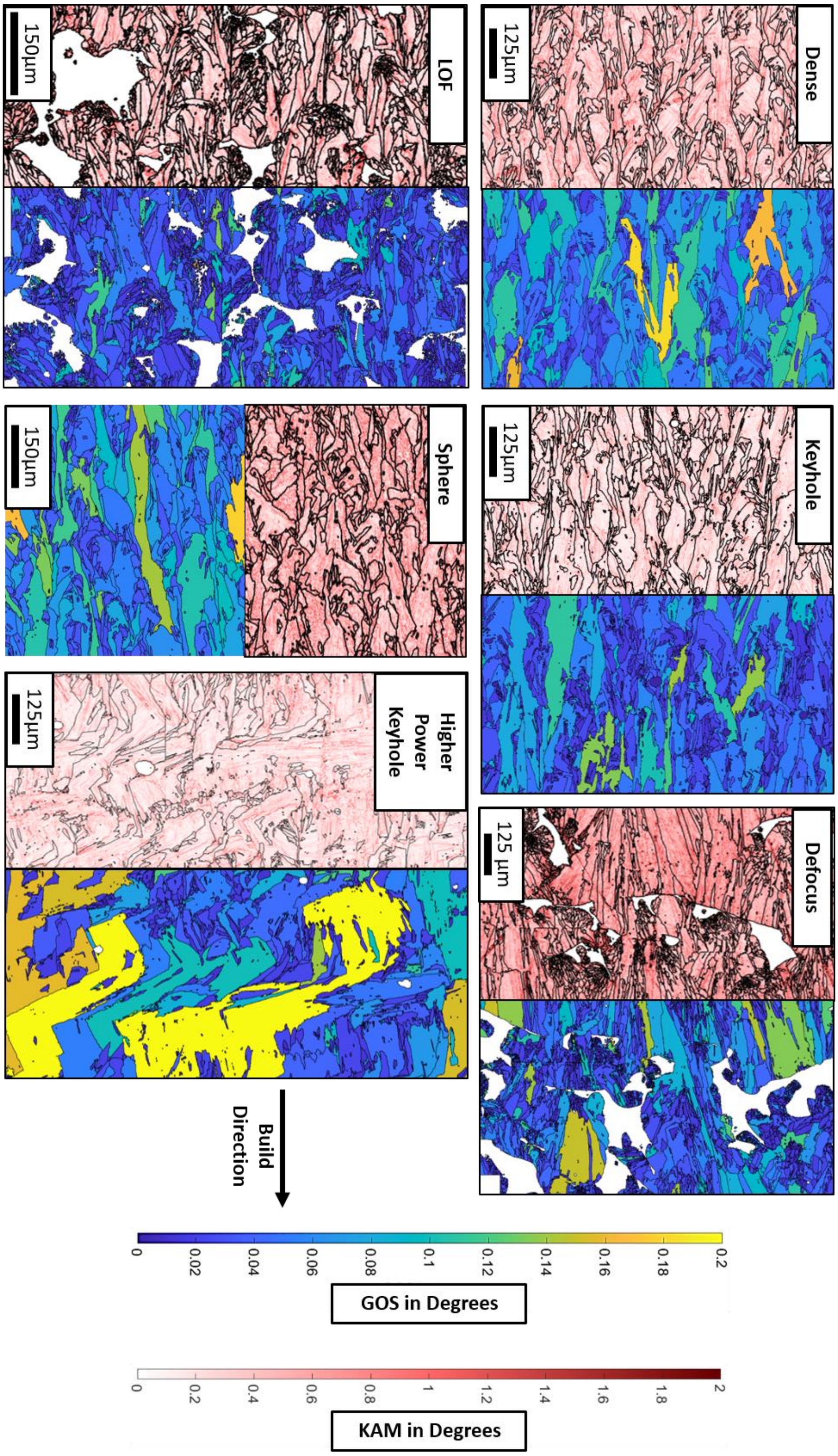

Figure 72: KAM and GOS maps of each as-built sample. Keyhole pores in the Keyhole sample are shown with a GOS of 0. Pores in all other samples have been eliminated from the map, showing up as white space.

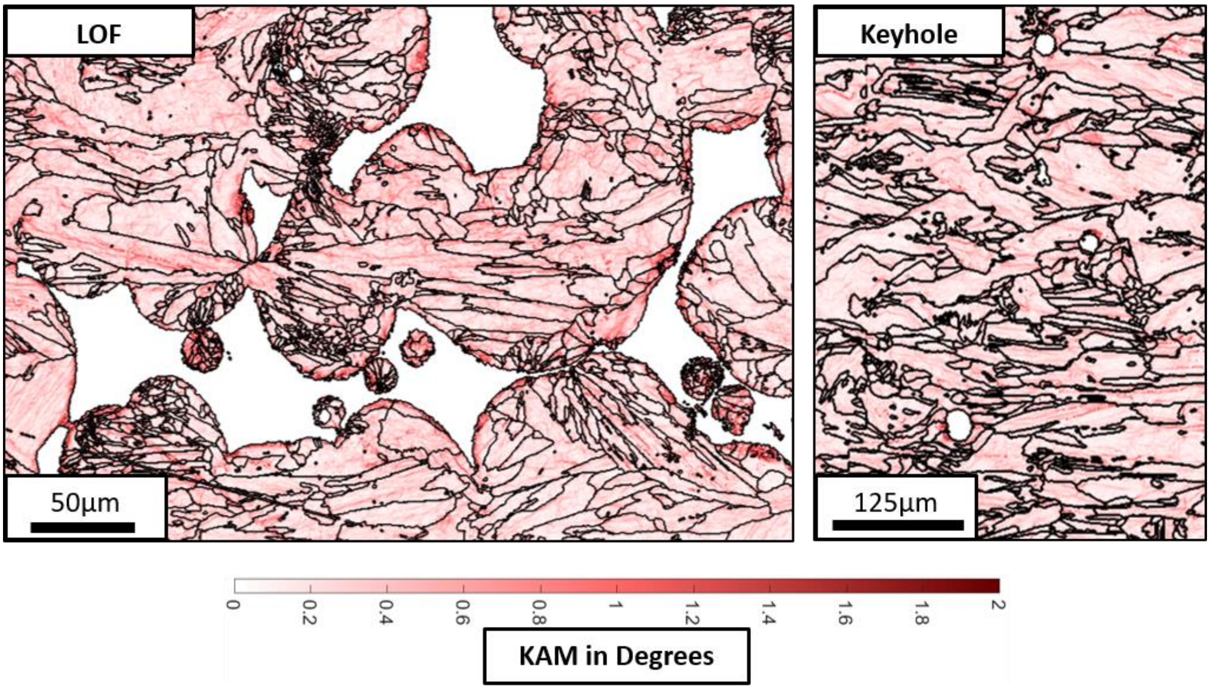

Figure 73: Higher magnification KAM map of the LOF and Keyhole samples. Elevated regions of KAM are observed surrounding internal voids indicating a high dislocation density gradient in these regions.

6.4.2 HIP and HIP + HT Processed States

IPF maps with respect to the building direction for each sample after HIP and HIP+HT are shown in Figures 74 and 75 respectively. The IPF key from Figure 68 should be used to interpret these. Note, the High Power Keyhole and Defocus samples were not subjected to additional heat treatment and are presented in the as-HIP state only. The GOS and KAM maps for the HIP and HIP + HT conditions are shown in Figure 76, and a figure highlighting all the twin boundaries is shown in Figure 77. Table 18 displays the ∑3 boundary percentage for each sample.

The Dense sample did not undergo a significant change in grain morphology after HIP or after further heat treatment. It did however, contain very small patches (10-100μm in length) of recrystallised microstructure as indicated by the localised presence of twin boundaries (Figure 77), as well as a local reduction in KAM and GOS in these regions (Figure 76). As different samples were imaged in the as-built and HIP states, these patches could not be directly correlated to any particular region, such as a pore or region of elevated lattice strain, in the as-built microstructure. However, as gas pores were observed in this sample in the as-built state, it is likely that these recrystallised regions neighbour a gas pore, densified by the HIP process.

The Keyhole sample generally also retained the elongated columnar grain structure observed in the as-built condition, however, with patches of very large recrystallised grains. These also contain a number of twin boundaries. These large grains observe visually lower KAM and GOS values than the rest of the microstructure. Both of these observations indicate the occurrence of localised, or discontinuous, recrystallisation. These grains are located near the edge of the inner cylinders, where the return time of the laser was lowest, and keyhole defects were present in the as-built state.

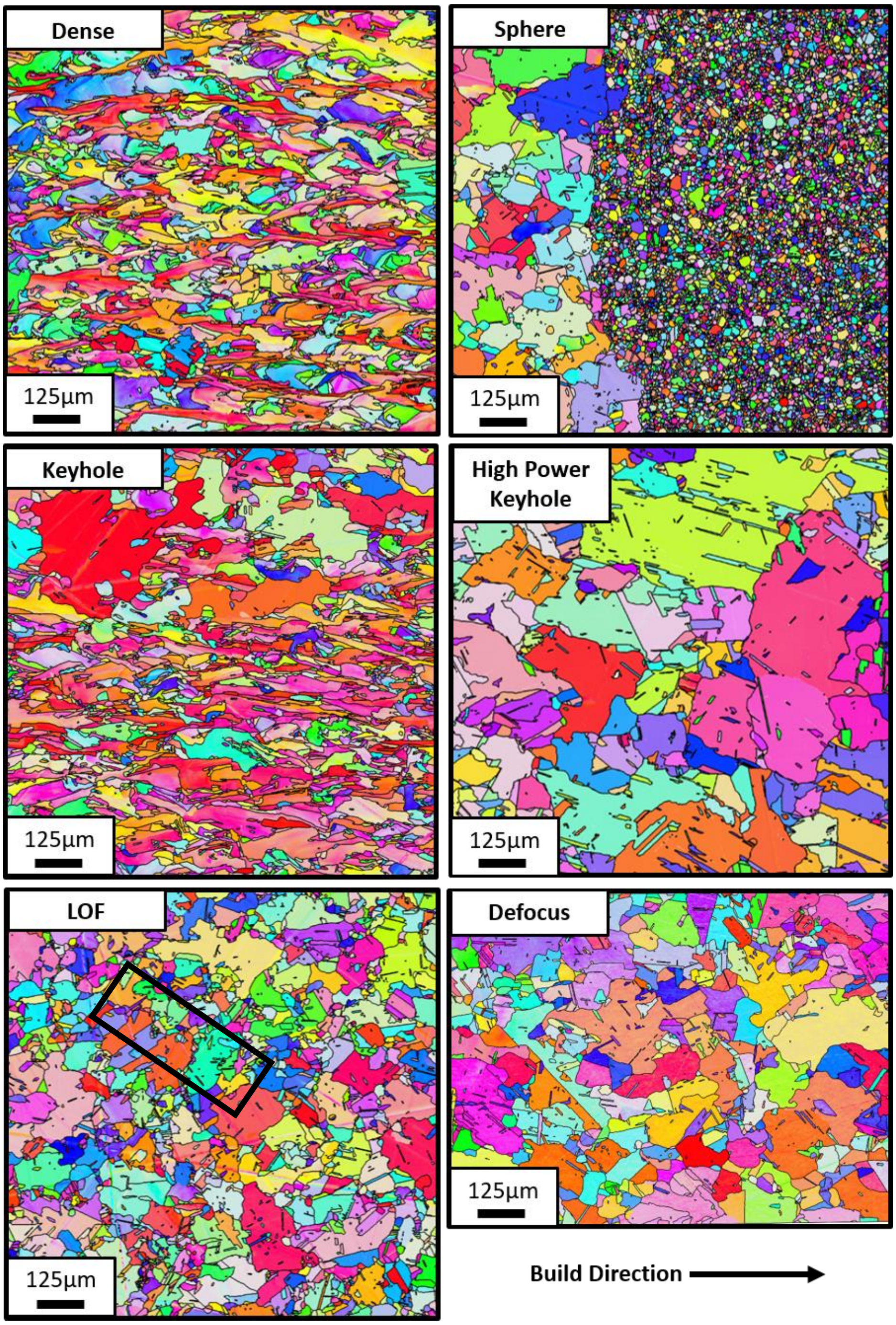

Figure 74: EBSD IPF maps with respect to the building direction for the Dense, Sphere, Keyhole, High Power Keyhole, LOF and Defocus samples subject to HIP only. Note the difference in scale on the Sphere map. The Dense and Keyhole samples still show the elongated nature of as-built AM grain structures with a general orientation in the [001] direction. Large recrystallised grains are visible in the Keyhole sample. The LOF, Defocus, Sphere, and Higher Power Keyhole samples have fully recrystallised. The Sphere sample contains an extreme bi-modal grain size whilst the LOF and Defocus samples show this in a more subtle manner. See Figure 68 for the IPF key.

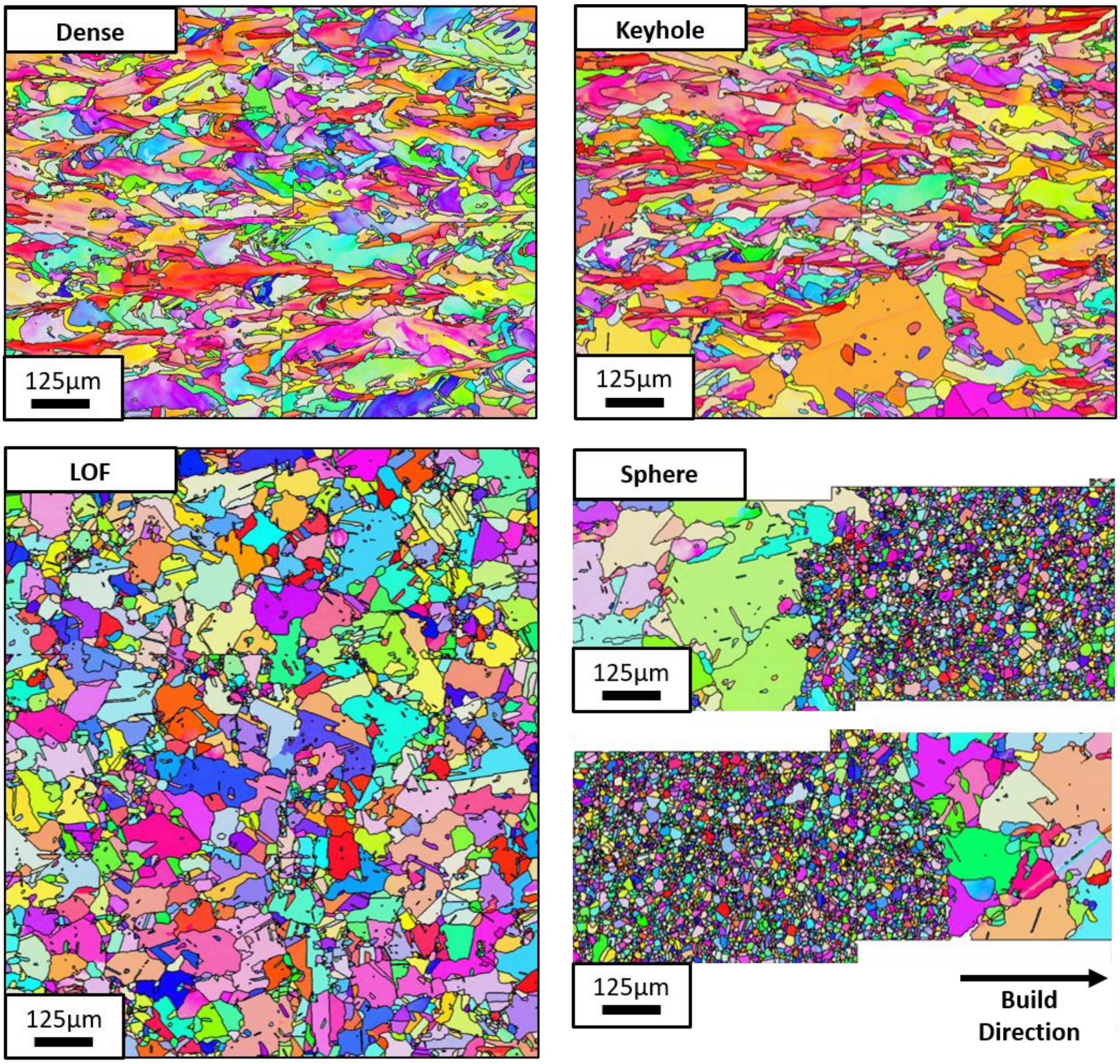

Figure 75: EBSD IPF maps with respect to the building direction for the Dense, Keyhole, LOF and Sphere samples subject to HIP and Heat Treatment. The Higher Power Keyhole and Defocus samples were not further heat treated beyond HIP. Note the difference in scale on the Sphere map. Generally, all samples are visibly unchanged from the HIP state. See Figure 68 for the IPF key.

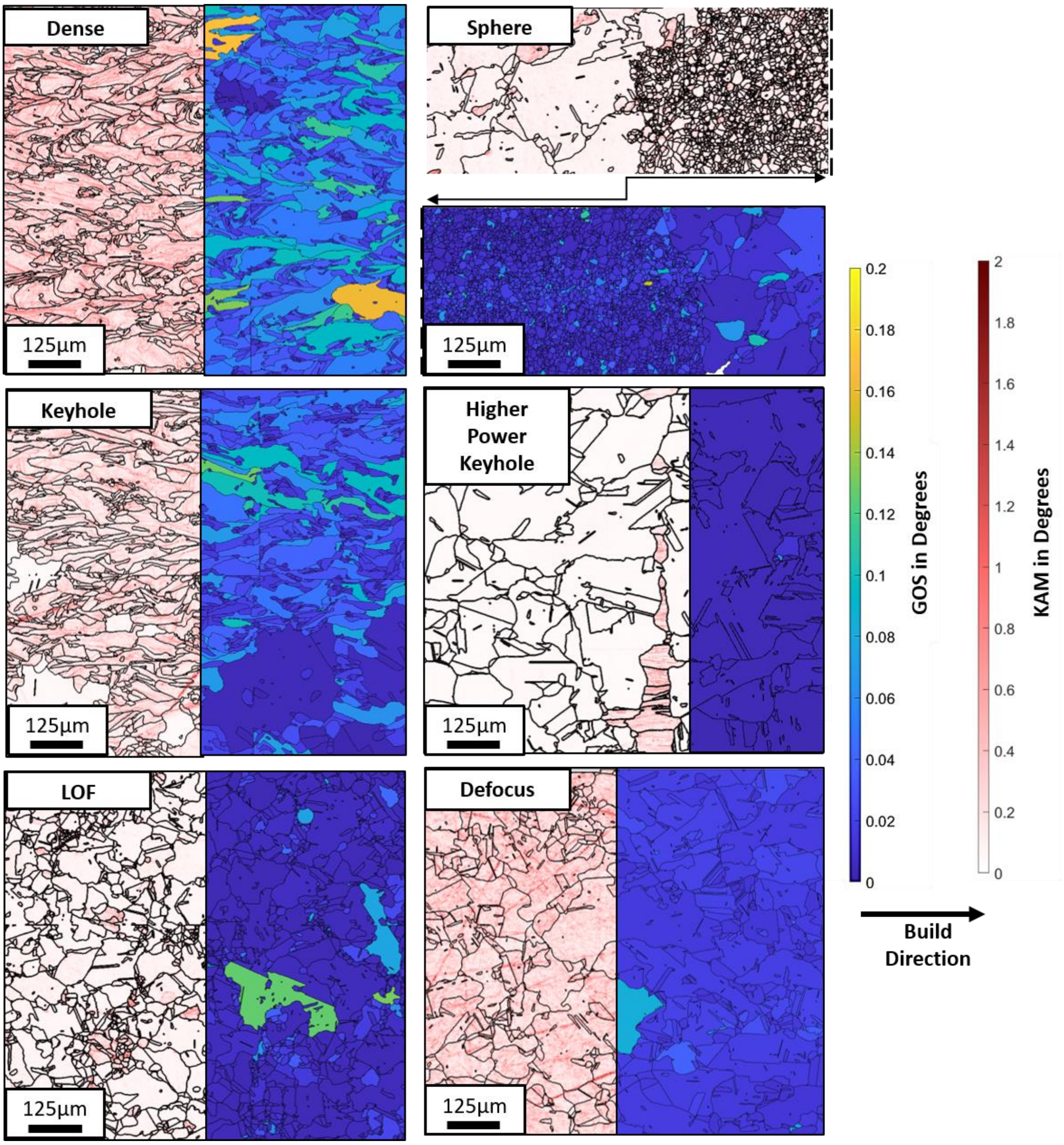

Figure 76: KAM and GOS maps of each sample in the HIP + HT states (Dense, Sphere, Keyhole, and LOF), or HIP only states (Higher Power Keyhole and Defocus). The Dense and Keyhole samples still show elevated levels of KAM and GOS after HIP + HT with the exception of pockets of recrystallisation located stochastically throughout the Dense sample and the presence of large recrystallised grains on the edge of the imaged area in the Keyhole sample. Comparatively, the Sphere, Higher Power Keyhole, LOF and Defocus samples show overall lower KAM and GOS values which is indicative of a reduction in the volume and size of sub-grain misorientations within each grain. A few regions of these samples still observe regions of elevated KAM and GOS. This could be due to incomplete recrystallisation. The Defocus sample, although showing reduced KAM and GOS values compared to the as-built state, still observe higher values than those seen in the Higher Power Keyhole Sample, which also underwent complete recrystallisation. This could be an artefact of insufficient surface preparation for EBSD misorientation measurements.

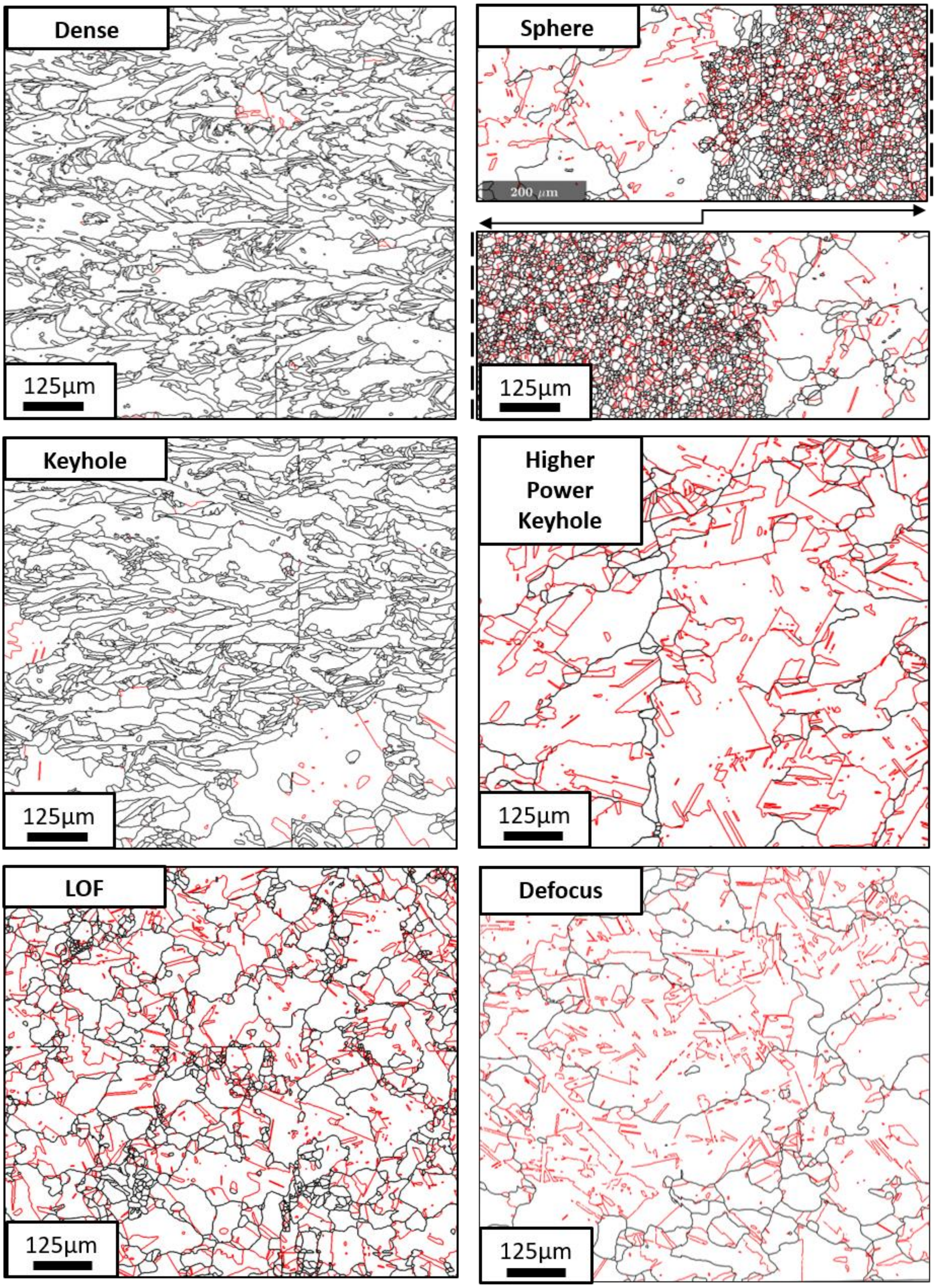

Figure 77: Grain boundaries for each sample in the HIP + HT state (Dense, Keyhole, LOF and Sphere samples), or HIP only state (Higher Power Keyhole and Defocus). All ∑3 Boundaries indicated by red lines. 'Pockets' of twinning can be observed in the Dense and Keyhole samples. The LOF, Defocus, Higher Power Keyhole, and Sphere samples contain evenly distributed twinning throughout the sample.

Table 18: ∑3 boundary fraction for each sample in the as-built, HIP and HIP+HT states.

		Length Fraction ∑3 (%)
As-Built	Dense	0
	Keyhole	0
	LOF	0
	Sphere	0
	High Power Keyhole	0
	Defocus	0
HIP	Dense	2
	Keyhole	2
	LOF	42
	Sphere Bulk	52
	Sphere Void	27
	High Power Keyhole	68
	Defocus	53
HIP+HT	Dense	1
	Keyhole	3
	LOF	41
	Sphere Bulk	44
	Sphere Void	22
	High Power Keyhole	-
	Defocus	-

The Sphere, Higher Power Keyhole, LOF and Defocus samples all show a large change in grain morphology after HIP, with the as-built elongated grain morphology no longer present. This is instead replaced by a more equiaxed grain shape. All also observed a large proportion of ∑3 twin boundaries which is indicative of large scale recrystallisation having taken place in each sample [256]. Compared to the Dense and Keyhole samples, which retained their original grain area, the Sphere Bulk, Higher Power Keyhole, LOF and Defocus samples, all observed large increases in grain area. With the exception of the Defocus sample, all of these also observed a visible reduction in KAM and GOS after HIP or HIP + HT. Interestingly the Defocus sample still shows an elevated level of GOS after HIP, whilst the Higher Power Keyhole sample (which was also only heat treated to the HIP stage) shows a much lower GOS. The reason for this is currently not understood and both samples visually indicate the occurrence of recrystallisation. It is important to note here that the Defocus sample contained a higher level of surface effects from sample preparation which may have influenced the KAM maps to a small extent. Despite this however, the map still does show underlying misorientation structure and so not all of the elevated KAM is due to the effects of surface defects.

Further heat treatment after HIP did not significantly alter the grain structure morphology of any of the samples. The Dense, Sphere Bulk, and Sphere Void samples further increased in grain area between the HIP and HIP + HT states. The recrystallised grains observed in the keyhole sample were larger in the HIP+HT state, however this could be an artefact of imaging different samples for each heat treatment state. Similarly, the LOF sample looks to have a fewer number of larger grains after HIP + HT compared to just HIP. The first post HIP heat treatment stage of 980^{o}C for 1 hour was designed to precipitate some δ phase at grain boundaries in order to reduce grain growth between HIP and HT states [165], [190], [257]. Therefore, had this stage not been performed, it is believed that the grain growth between HIP and HIP + HT would be greater for all samples. Additional characterisation of the microstructure resulting from these treatments will be presented in Section 7.

Pole figures in Figure 78 show that the preferential grain orientation in the build direction (X) in all samples reduced between the as-built and HIP (Higher Power Keyhole and Defocus) state and HIP + HT (Dense, Keyhole and LOF) state. In samples where no recrystallisation occurred, this may be indicative of recovery, enhanced by the dissolution of cell structures and segregated elements. The Keyhole sample, however, still observes some preferential alignment in the final heat treated state.

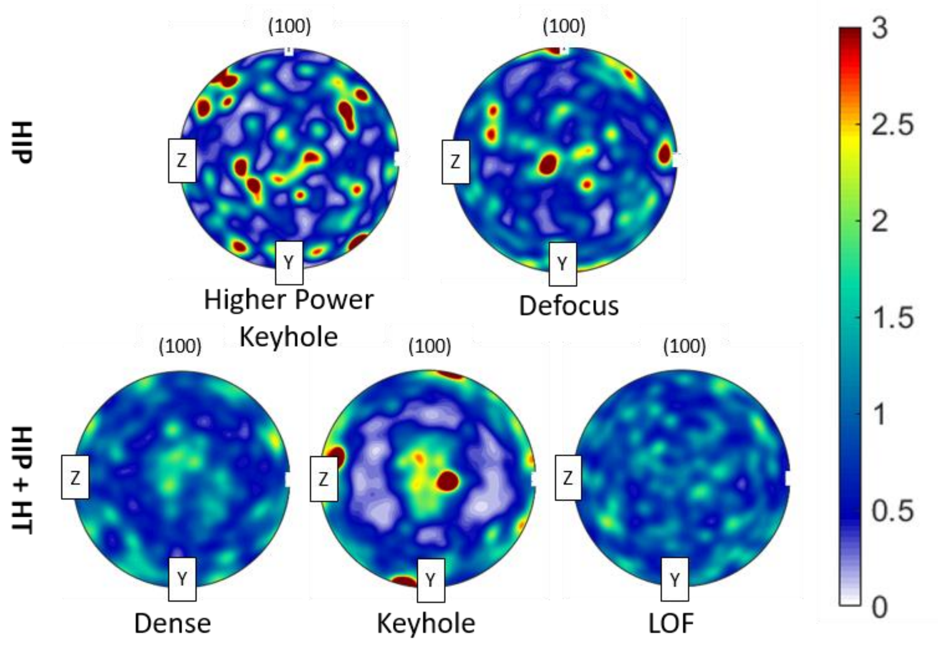

Figure 78: Pole figure maps of each sample in the HIP+HT state (Dense, Keyhole, LOF), and HIP only state (Higher Power Keyhole and Defocus) in the X, or build, direction. All of the samples show a decrease in preferential orientation between the as-built and HIP or HIP + HT states. The Keyhole sample still shows the largest amount of grains with their easy growth direction oriented with the AM build direction. Although the Higher Power Keyhole and Defocus samples show a more random rain orientation, there are definite hot spots visible in the pole figures.

6.4.3 Discussion of Morphological Changes after both HIP and HIP + HT

Due to the fast solidification conditions in AM, all samples observed directional solidification encompassing of long columnar grains with cellular sub-grains in the as-built state. Each sample is understood to have a different level of inherent lattice strain. This is due to a number of factors including the differences in the LPBF process parameters used to build them, the introduction of different characteristic AM voids, and differences in the sample geometry. The rainbow effect in the IPF maps in Figure 68 as well as the misorientation data displayed in the KAM maps in Figure 72 both exhibit the presence of GNDs and local misorientation gradients. The introduction of characteristic AM porosity also acted to hinder epitaxial growth leading to a local refinement of the microstructure (increasing the local grain boundary energy [197]). This is especially evident in the LOF and Defocus samples. Sharp internal features within these void regions, likely led to stress concentrations during subsequent heating and cooling cycles, enabling the accumulation of GNDs, further locally enhancing the local lattice strain in the Keyhole and LOF parts [258].

All samples underwent a HIP procedure in which plastic deformation and diffusion occurred in order to form a strong bond between previous void interfaces [259]. Differences in the internal densities and spatial location of each defect type within each sample in the as-built state led to differences in the volume, spatial location, and speed of plastic deformation. Therefore, the corresponding strain accumulation, and driving force for recrystallisation for each sample also differed in magnitude and spatial location [260]. As a result, each sample attained a very different grain morphology after the HIP process. Simplistically, this result shows that the presence of deliberately placed pores, and the structure and distribution of these pores, can be used to design and tailor the final microstructure obtained after the HIP process in AM parts.

The Dense sample, as well as large dense regions located centrally in the Keyhole sample, did not contain sufficient inherent lattice strain to enable the driving force for recrystallisation to be met during the HIP or heat treatment cycles. As each sample in this trial displayed similar levels of GOS and KAM in the as-built state, and the other samples did recrystallise, it is likely that the plastic deformation during HIP was necessary in order to transform the microstructure at the applied temperature.

Whilst the alignment of grains in the build direction reduced after HIP and HT for all samples, this was qualitatively observed to have occurred to a lesser extent in the Keyhole sample. In Directed Energy Deposition of Inconel 718, Parimi *et al.* found that an increase in laser power led to the formation of larger sized Laves phase with inclusions of carbides and needle like δ-phase within the Laves distribution. Although the heat input to DED is higher, leading to generally slower cooling rates, it is possible that the Keyhole sample in this study also observed larger fractions of Laves phase and carbides compared to the Dense sample. This will be further investigated in Chapter 7. As all samples were heat treated to the same heating profile, it is possible that this sample retained a larger volume fraction of secondary phases than the Dense sample, the only other sample that did not undergo recrystallisation. These may have pinned the grain boundaries, reducing the potential for recovery to occur during heat treatment. According to the theory presented by Mukherjee *et al.* [75], discussed in section 2.2.4.3 Residual Stress, a higher heat input leads to less residual stress accumulation in the part. As relaxation of residual stresses may produce GNDs, it is possible that this sample contained fewer GNDs than the Dense sample, and so exhibited less driving force for recovery.

Before the effects of different discontinuity distributions on the HIP microstructure is discussed, it is important to discuss the fine, stochastic, patches of recrystallisation that were observed in the Dense sample. These are believed to have occurred due to compression of small gas pores. However, the rearrangement of dislocations to stochastic regions of elevated dislocation density gradients is also feasible due to recovery. This result shows the potential for localised or inhomogeneous recrystallisation to take place in components printed with optimum parameters. Consequently, critical changes in the mechanical properties of a part may occur, with their location impossible to detect from the part surface. As this effect may be exacerbated by increasing the geometric complexity of a build, care must be taken when selecting the post build HIP and HT procedures.

The Sphere Bulk sample underwent considerable deformation during HIP, enabling full recrystallisation to occur within the dense regions of this sample. This is shown by the dimples in the top and bottom of the sample in Figure 66. It should be noted that if HIP is used in order to densify powder encapsulated by an AM structure, such deformation should be considered in the initial component design stage.

Densification of the powder filled region of the Sphere sample initially occurred through pressure induced particle sintering at the elevated temperatures applied during HIP [259], [261]. The added effects of high grain boundary area from the powder, and HIP induced plastic deformation on the sintered powder, enabled recrystallisation to readily occur. The finer the original grain size, the more recrystallisation nuclei form, and the less they are able to grow before impinging on one another [127]. As a result of the gas atomisation process, the powder particles contained a large fraction of fine grain sizes, leading to a very fine recrystallised microstructure which is on average smaller than the maximum powder size of 45µm. Because of this, the Sphere sample comprised of two distinct and intentionally placed regions that differed in grain area by 194% after HIP + HT. This is shown more clearly in Figure 79. This sample reinforces the finding that large spherical voids up to 2mm in diameter containing unmelted powder can be successfully densified during HIP processing [51], which opens up the design space to create bimodal microstructures in more complex components.

Although fully recrystallised, the LOF sample contained elongated strings of finer grain sizes randomly distributed within the sample (black box in Figure 74) resulting in the formation of a slightly bi-modal microstructure. The variation in recrystallisation kinetics within this sample is expected to originate from a combination of higher dislocation density gradients present at the edges of the voids (exhibited in Figure 73) [150], [196], a variation in the volume of grain boundaries at different locations in the sample, and a variation in the effects of the deformation induced by the HIP at different locations in the sample [56]. This is similar to the formation of recrystallisation necklace structures along deformation planes in hot deformed samples of Inconel 718 [262], and also to the mechanisms of pressure and temperature assisted crack healing shown in low carbon steel ingots [259]. Bi-modal microstructures have been shown to exhibit a combination of both high strength and ductility, making this a valuable method of AM microstructure manipulation [263].

The Defocus sample contained a larger initial grain size at locations far from a LOF void. It is believed that this enabled the recrystallised grain structure to be overall larger than in the LOF sample. The slight bi-modal effect observed in the LOF sample due to proximity of recrystallised grains to prior void edges, is also observed in the Defocus sample. However, all grain sizes in the bi-modal distribution are larger than in the LOF sample.

The Higher Power Keyhole sample contained the largest grain area after HIP of all the samples tested. This is expected as it also observed one of the largest initial grain sizes. The large initial grain size compared to the standard Keyhole sample is assumed to be due to several different factors; one is the larger normalised equivalent laser energy density imparted to the material, 11.15 compared to 9.33, the difference in rotation strategy used to build the samples (67^o layer rotation in the Keyhole sample compared to the 90^o rotation in the Higher Power Keyhole sample), and the fact that both samples were printed on different baseplates next to other parts with differing geometries. This affects the overall heat retention in the material and therefore, the extent of epitaxial growth that occurs during solidification. It is therefore not easy to compare the starting and final grain structures of the Keyhole and Higher Power Keyhole samples directly in terms of laser parameters alone. The sample did, however contain a larger volume of larger keyhole pores compared to the standard Keyhole sample. These also extended further in to the centre of the defect region. The increased capacity for pore compression by the HIP cycle is believed to have enabled the recrystallisation of the whole ‘defect’ region in the Higher Power Keyhole sample as compared to the localised region in the Keyhole sample. The larger initial grain size also resulted in a large final grain structure with a lot of twin boundaries.

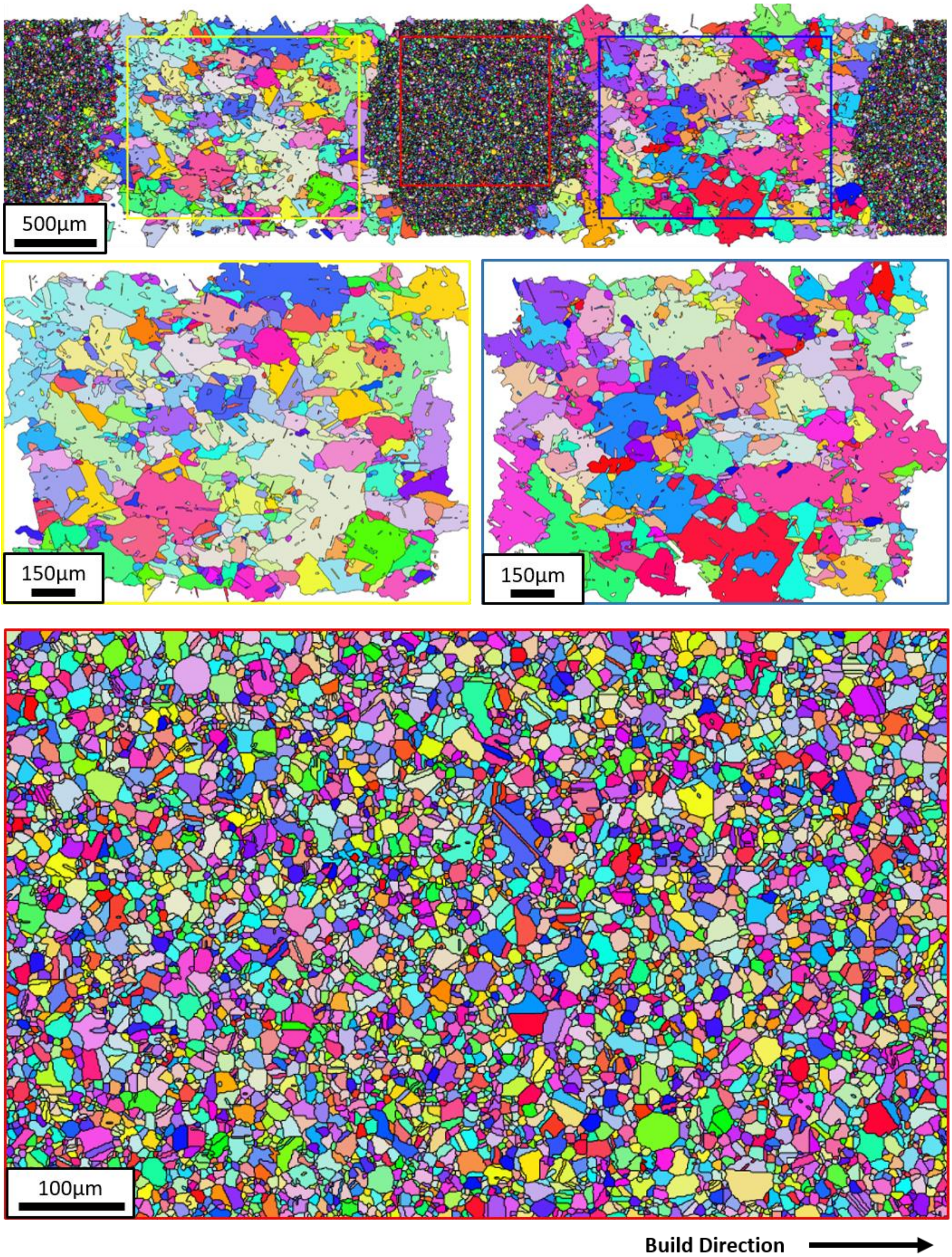

Figure 79: Enlarged IPF maps in the building direction of the Sphere sample after HIP + HT. Internal spheres are observed to have lost their sphericity. The large difference in grain size observed in the Sphere Bulk and Sphere Void regions is clearly shown. See Figure 68 for the IPF key.

6.5 Twin Structures

Grain boundary engineering (GBE) involves the refinement of grain boundaries in a material in order to enhance the mechanical properties of a given component [147], [256]. Low coincidence site lattice (CSL) boundaries, of which the ∑3 twin boundaries are part of, have been shown to provide increased resistance to stress corrosion cracking, fatigue, and creep in nickel superalloys [147], [214]. Therefore, the volume of these retained in each sample after a given heat treatment procedure, as well as their connectivity, is imperative to GBE [256].

The exact formation mechanisms of recrystallisation twin boundaries are not fully understood [146]. However, it has been agreed upon that the driving force for migration of a new HAGB in a recrystallisation nucleus is proportional to the number of twins produced [131]. Therefore, the twin boundary density increases with an increase in the number density of recrystallised grains [264]. Once the driving force for recrystallisation has been exhausted, and the grain growth mechanism dominates, further twin formation is reduced and existing twin boundaries may be eliminated by the movement of the surrounding grains [145], [202].

The length fraction of the ∑3 boundaries in the LOF, Sphere Bulk, Sphere Void, Higher Power Keyhole, and Defocus samples were 42%, 52%, 27%, 68% and 53% respectively after HIP. These values were calculated by taking the ratio of the total length of ∑3 boundaries to the total length of all grain boundaries in the sample. For the LOF, Sphere Bulk and Sphere Void samples, these reduced to 41%, 44% and 22% respectively after further HT. The number of twin boundaries present in the Dense and Keyhole samples were negligible both after HIP and after HIP + HT (2%).

The largest decreases in the length fraction of ∑3 boundaries occurred in the Sphere Bulk and Void samples after HT, which is in agreement with the increase in grain size in each of these samples [202]. The ∑3 length fraction of the LOF sample remained stable after HT, while fewer larger grains were observed in the imaged sample after HIP+HT. This suggests that recrystallisation had not yet completed during HIP. However, as different regions of material were analysed for each sample, it is also possible that these values are not significant and within error.

As external deformation, traditionally used to achieve low CLS boundaries in GBE, is not required in LPBF components, and it has been shown that large variations in ∑3 length fraction can be achieved through the introduction of different AM discontinuities, the method outlined in this work to achieve graded microstructures also shows promise for GBE.

6.6 Hardness Measurements

Hardness measurements for the Dense, Keyhole, LOF and Sphere samples in the as-built, HIP and HIP+HT states are shown in Figure 80. In order to prevent damage to the indenter tip from large voids, the hardness of the as-built LOF sample was not measured.

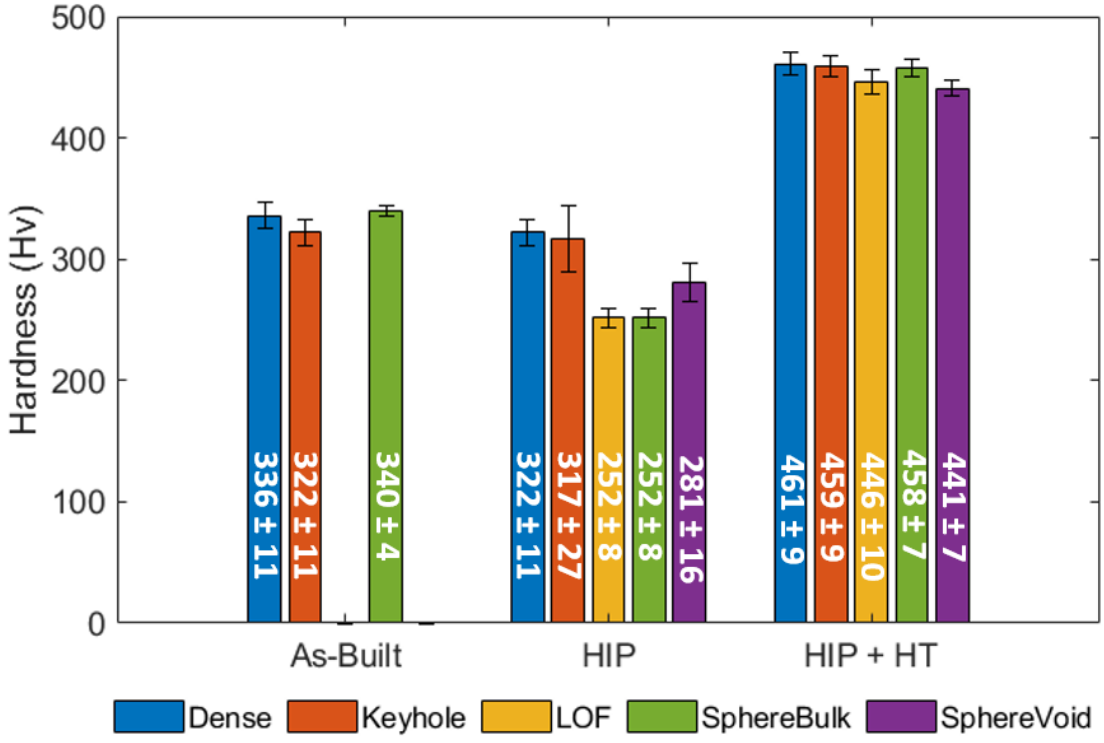

Figure 80: Hardness measurements for each sample in the as-built, HIP and HIP+HT states.

The Dense, Keyhole and Sphere Bulk samples observed an as-built hardness of 336±11HV, 322±11HV, and 340±4HV respectively. Elevated pyrometry intensities observed in the Keyhole sample during building may have enabled the sample to remain at an elevated temperature for longer than the Dense and Sphere samples (built with identical parameters). The associated decrease in cooling rate may have enabled more recovery to take place during solidification, leading to a reduction in the volume of dislocation densities present, and a corresponding lower hardness value.

The Dense and Keyhole samples maintained the majority of their strength during HIP due to the retention of their sub-grain cell structures and dislocations. These were eliminated in the Sphere sample leading to a corresponding drop in hardness. Grain refinement in the Sphere Void region rationalises the slight increase in hardness as compared to the other recrystallised samples.

After HT, the Dense, Keyhole, and Sphere Bulk samples observed similar hardness measurements, 461±9, 459±9, and 458±7 respectively while the LOF and Sphere Void samples observed a hardness of

446±10 and 441±7 respectively. The samples with the finer grain sizes, LOF and Sphere Void, achieved a lower hardness than the grains with a larger grain size which is unexpected if the Hall-Petch relationship is considered.

Overall, all of the hardness values obtained after HIP+HT are very similar. This is also an unexpected finding considering the large differences in grain sizes observed across the different samples. In addition, the recrystallisation process should have enabled Nb, the element required for precipitation of the strengthening phase, to homogenise throughout the γ matrix, enabling the formation of γ'' during heat treatment, and leading to an increase in material strength. Comparatively, the retained fine solidification structures are still assumed to be present in the Dense and Keyhole samples.

It is likely that the hardness results obtained across these samples is due to the underlying grain structure. This will be discussed in Chapter 7.

The HIP + HT hardness values for all samples are in line with those found in other studies given the subtle changes that will be observed between studies due to differences in build parameters, extent of recrystallisation, retained dislocations and residual stress [68], [150], [176], [181].

6.7 Combination of Microstructures in to a Single Part

This section shows only a proof of concept for the combination of different microstructures within a single AM part using the technique discussed in this chapter. Therefore, extensive analysis was not performed, rather, simple EBSD measurements were taken to highlight the effectiveness of the methodology in selectively achieving grain structures.

Figure 81 shows a single HIPed part containing previous regions of Keyhole defects, LOF defects, dense material and loose powder. It is clear that after HIP all four types of initial material were able to recrystallise and produce their characteristic post HIP grain morphologies. This provides evidence that the combination of different microstructures within a single part is possible. All layers of the cylinder initially had the same dimensions so it is clear that varying extents of deformation of must have occurred in order to allow the part to densify. This should be taken in to consideration when designing parts using this technique.

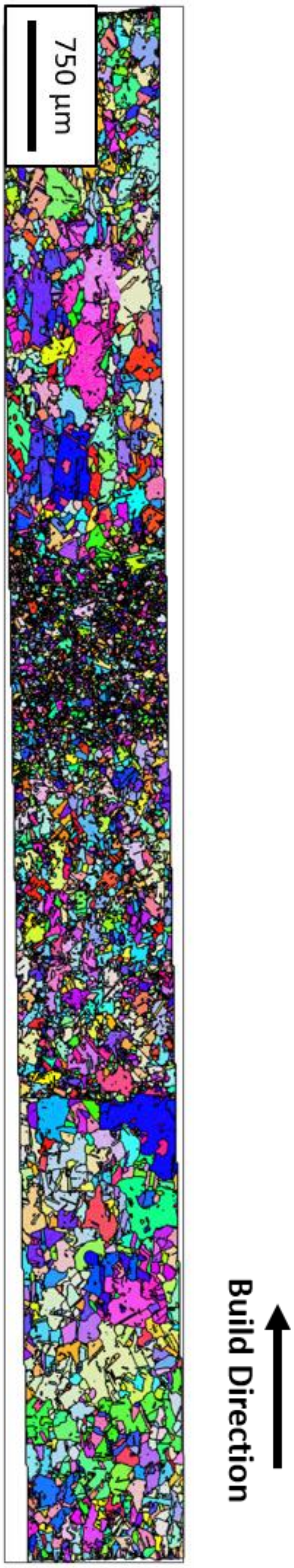

Figure 81: IPF (build direction), map of a HIP sample containing layers of, in the as-built state, from top to bottom, Keyhole defects, loose powder, LOF defects, and fully dense material. See Figure 68 for the IPF key.

6.8 Chapter Summary

This chapter introduces a method in which microstructural control can be achieved in Inconel 718 manufactured by additive manufacturing. The approach utilises easily repeatable processes by requiring only the necessity to induce Keyhole or LOF porosity or encapsulating loose powder within a component. These discontinuities occur readily when printing at the limits of the processing window for a particular alloy, which is generally well understood for a given material and machine.

These different intentionally placed characteristic AM defects can enable the production of differing grain, and grain boundary, morphologies after HIP within the same part. This is due to inherent differences in as-built lattice strain concentrations and grain boundary densities produced when printing at the edge of the material processing window, and is further enabled by differences in the volume and distribution of plastic deformation made possible in samples with a different distribution of voids during the HIP process.

As a result, a variety of grain structures were obtained; coarse grained equiaxed, fine grained equiaxed, and bi-modal. A high length fraction of beneficial ∑3 boundaries were also produced, increasing properties such as stress corrosion cracking and fatigue which are highly desired properties in components designed for advanced engineering applications. It is believed that further optimisation of the spatial distribution of these defects can enable further control over the microstructure.

It has also been demonstrated that it is possible to retard the recrystallisation process of AM parts if regions of anisotropic mechanical properties are desired. In terms of productivity, this method enables AM parts to be produced with a 47% time saving and 62% energy saving per layer, compared to printing a fully dense AM part, whilst also enabling more isotropic properties to be attained.

In comparison, a Dense as-built microstructure may require a longer HIP or HT procedure to achieve full recrystallisation which requires more energy. It has also been shown that the use of HIP to consolidate fully dense microstructures has the potential to induce inhomogeneous recrystallisation, altering the properties of the material in unintentional locations. This is believed to be exacerbated for complex LPBF geometries.

As the hardness was found to be relatively similar for each sample after HIP and heat treatment while the grain structures differ vastly, it is assumed that the precipitate structures within each sample also play a large role in the mechanical properties of each sample. This will be explored in Chapter 7.

As the HIP process is used as standard for most AM parts intended for aerospace applications, this method may be expanded to other material systems in order to enable the production of parts produced from otherwise difficult to AM materials. Examples of these may be high γ' nickel superalloys which tend to crack during manufacture, or materials with a very fine processing window.

7 Microstructural Analysis of Functionally Graded Parts

7.1 Introduction

The samples produced in Chapter 6 exploited discontinuities towards grain structure control. They were analysed using optical microscopy to obtain the density, as well as through large scale EBSD, to elucidate the grain structure. Although each sample displayed the typical columnar grain structure in the as-built state, large differences in the grain structures of each sample were obtained after HIP. Interestingly, despite the large grain morphology differences, all samples displayed relatively similar hardness values after HIP + HT. This was an unexpected result owing to the marked differences obtained in grain sizes within these samples, as it is well understood that a more refined grain size should ultimately lead to a stronger material following the Hall-Petch relationship [133].

Therefore, it is believed that differences in the underlying microstructures are likely the cause of the similarities in hardness obtained. This chapter aims to understand the differences between the precipitate structures within the Dense, Keyhole, LOF and Sphere samples through the analysis of Scanning Electron Microscopy (SEM), Energy Dispersive X-ray Spectroscopy (EDS) and Transmission Electron Microscopy (TEM) data.

SEM and EDS data was collected for the Dense, Keyhole, LOF and Sphere samples in all three states; as-built, HIP and HIP + HT and the microstructures discussed qualitatively. Higher magnification SEM data for the HIP + HT state of each sample was collected in order to quantitatively analyse the differences between the intergranular precipitate distributions. Data analysis was performed using an ImageJ thresholding technique.

Further to this, TEM data was collected for each sample type in the HIP + HT condition in order to resolve some unanswered questions that arose from the SEM investigations.

7.2 Material and Methods

7.2.1 Sample Etching for SEM

In order to reveal the precipitate colonies within each sample introduced in Chapter 6, electrolytic etching was performed using a 10% by volume phosphoric acid solution. The etching step is described in section 3.5.2 Sample Etching for SEM.

7.2.2 Precipitate Size Analysis

Manual thresholding was performed in ImageJ on secondary electron micrographs of the Keyhole and Sphere samples in the HIP + HT state to determine the average area percent, and diameter, of the precipitates identified. Precipitates in the LOF sample were too fine to resolve with sufficient contrast for image thresholding, and the Dense sample had not undergone sufficient homogenisation to image individual precipitates without also imaging the material segregated to cell walls. At least 8 images were taken for each sample type to ensure an adequate sample of the data was collected for analysis. The ImageJ process was as follows:

1. All images to be analysed for each sample were opened to an ImageJ stack and a common scale set to all.
2. Brightness and contrast was edited to enhance precipitate structures.
3. Images were black/white thresholded.
4. Images were despeckled to smooth the image, then outliers were removed using a radius of 2 pixels.
5. All particles, excluding those touching image edges, were analysed.
6. All data points with a circularity of exactly 1 were removed prior to analysis as these were likely single pixel outliers.

7.2.3 Focused Ion Beam (FIB) Sample Extraction for TEM

TEM samples were extracted from the HIP + HT cylinder samples using focussed ion beam (FIB) machining by Dr Geoff West (University of Warwick) using a gallium ion source. Samples were extracted from grains orientated with one of their {100} planes perpendicular to the sample surface in order to make the identification of precipitates from the electron diffraction patterns easier.

Transmission electron microscopy of the FIB samples was performed at Cambridge University by James Miller using an FEI Tecnai Osiris. The presence of the strengthening precipitates, γ' and γ'', was investigated and chemical mapping of several regions of each sample was performed in order to identify the fine features in each microstructure.

7.3 Results

7.3.1 SEM analysis on As-Built Samples

Figures 82-85 show SEM micrographs of the Dense, Keyhole, LOF and Sphere samples in the as-built state. Each sample observes the typical AM sub-grain cellular structure. This is demonstrated in Figure 82 for the Sphere Bulk and Dense samples. Clusters of cellular growth with varying orientations are present within each grain, with each different cluster of cells making up a different sub-grain. The red arrows indicate the melt pool boundaries.

The colour contrast distinguishes the segregated solute rich region (light) which formed during solidification, from the γ matrix (dark). According to published sources, the segregated regions are comprised of mixture of fine metal carbides, dispersed metal oxides and Laves phase in the as-built condition [131], [176], [178]. This was not extensively inestigated in the work herein. Figure 83 shows the segregation of Nb, required for the precipitation of the strengthening γ'' phase, to these cellular boundary regions.

Figure 84 shows these cell structures at a higher magnification for each sample. The diameter of each cell is approximately 0.5-1 µm, however the cell size and thickness of the segregated material in the keyhole sample appears larger than in the other samples. Although this could be an artefact of the location at which the image was taken, it is possible that the higher energy density associated with this sample resulted in slower solidification and consequently, a coarser cellular structure with a higher level of intercellular segregation [186], [187]. In addition to a coarser segregation pattern, the keyhole sample contains larger white specks than other samples within the segregated material. These are believed to be small carbides that formed ahead of the growth front during solidification. The presence of an increased level of segregation at cell boundaries was discussed as a potential cause for the reduced homogenisation of the grain orientations (pole figure in Figure 78) observed between the Keyhole sample and the Dense sample in Section 6.

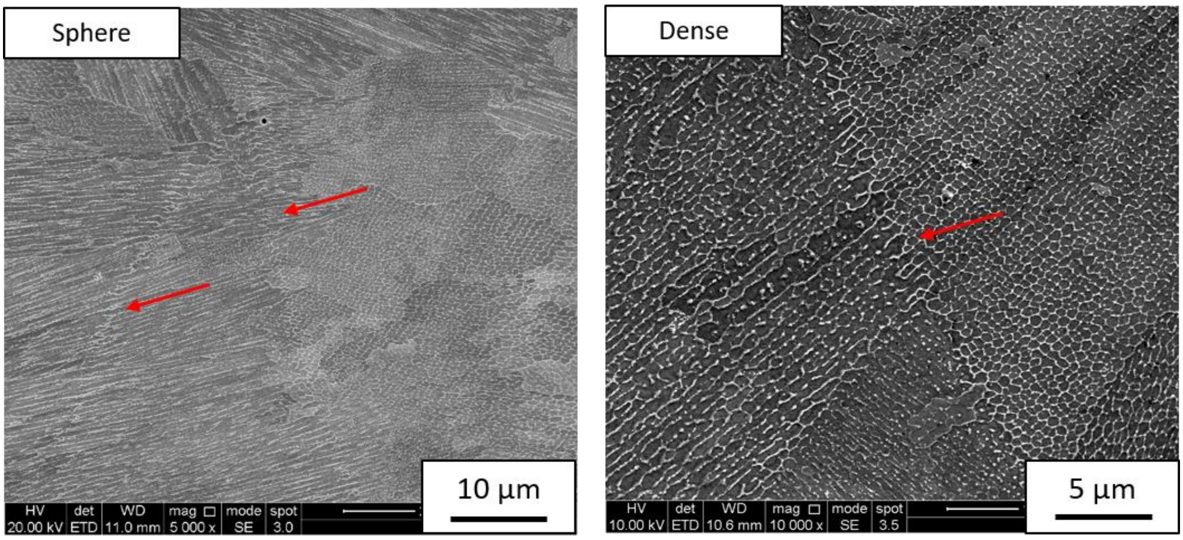

Figure 82: SEM micrograph showing the cellular nature of the solidification in the Sphere Bulk and Dense sample. The red arrows indicate the melt pool boundaries.

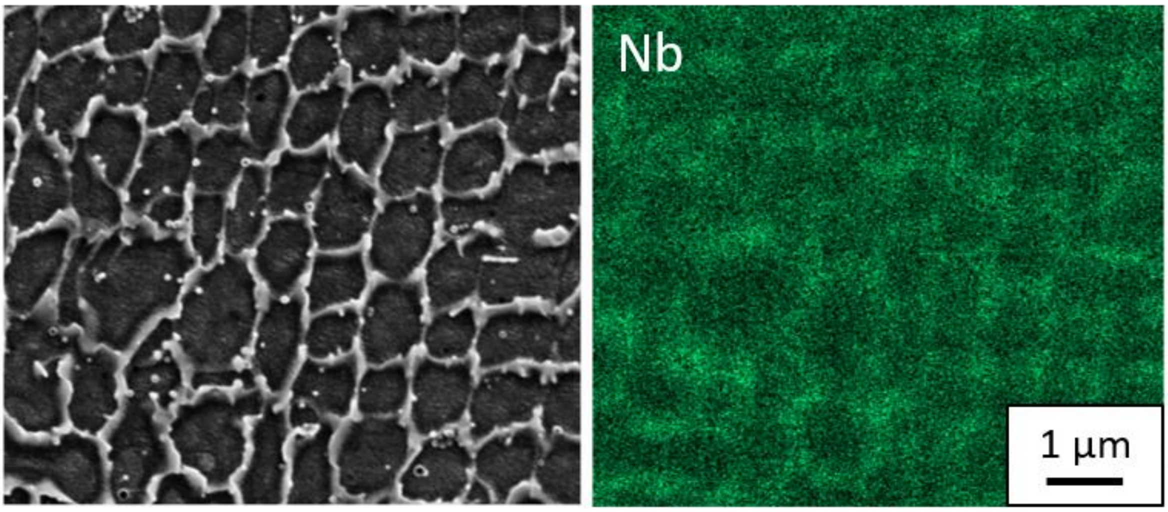

Figure 83: SEM micrograph of the cellular sub-grain structure in the Dense sample with accompanying EDS data showing the partitioning of Nb, which is required for the γ'' strengthening phase, to the inter-dendritic region.

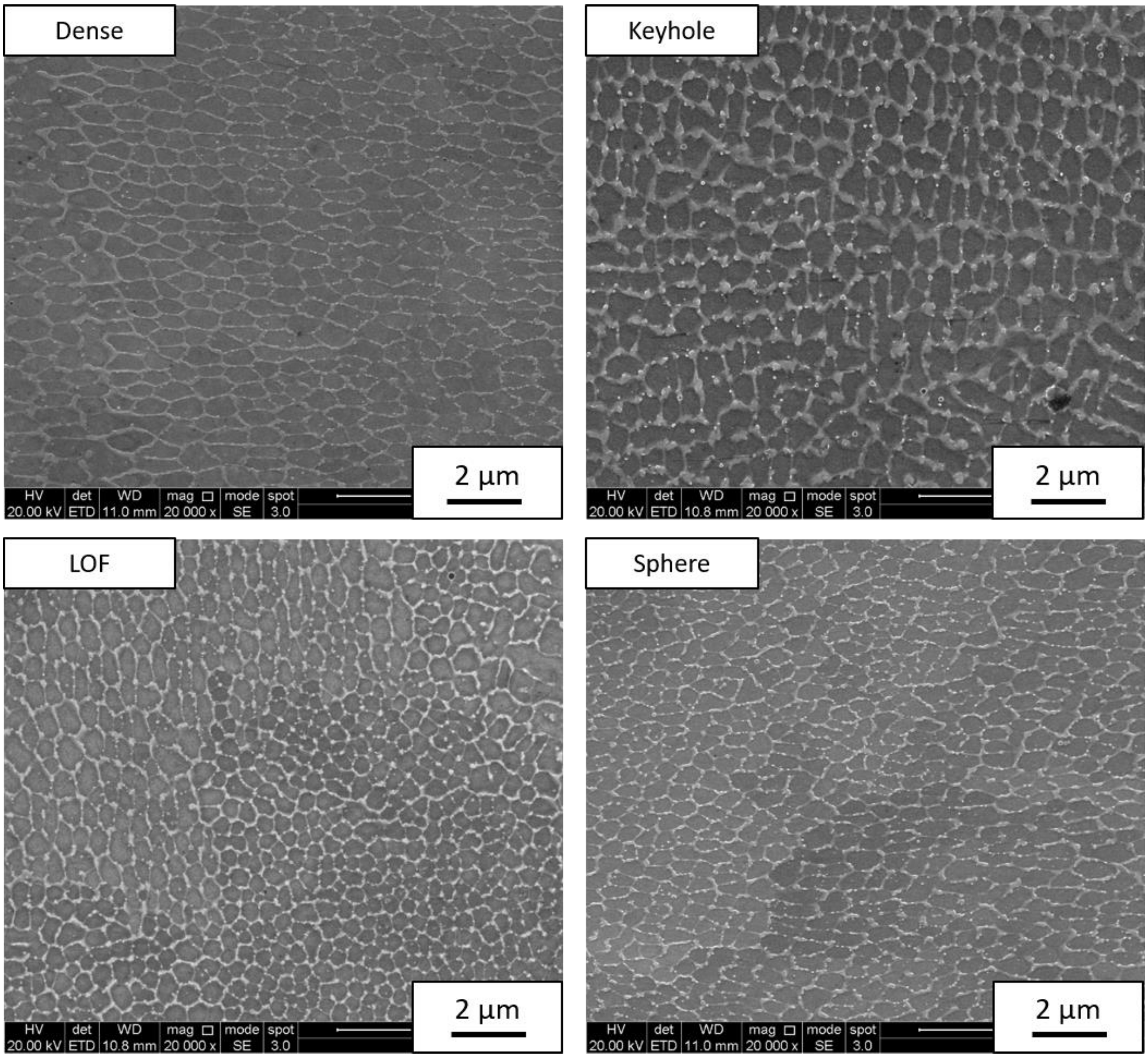

Figure 84: Etched SEM micrograph of the growth cells in each sample. The cells in the Keyhole sample look larger than the cells in the other samples. They are also accompanied by a thicker inter-dendritic region containing white specks, which are less visible in the other samples.

Figure 85 shows SEM images of the keyhole and LOF defects present within the cylinders. The Keyhole sample contains large circular pores of varying dimensions. The bottom left image of the LOF sample shows a LOF interface between a previously molten region and an unmelted powder particle. A clear difference in the size of the solidification structures is observed between the unmelted powder particle and the bulk LOF sample. Additionally, the bottom right image shows a LOF void at the bottom of the image and a long thin line separating two different growth orientations. Although these regions touch, no epitaxial growth occurred across the boundary.

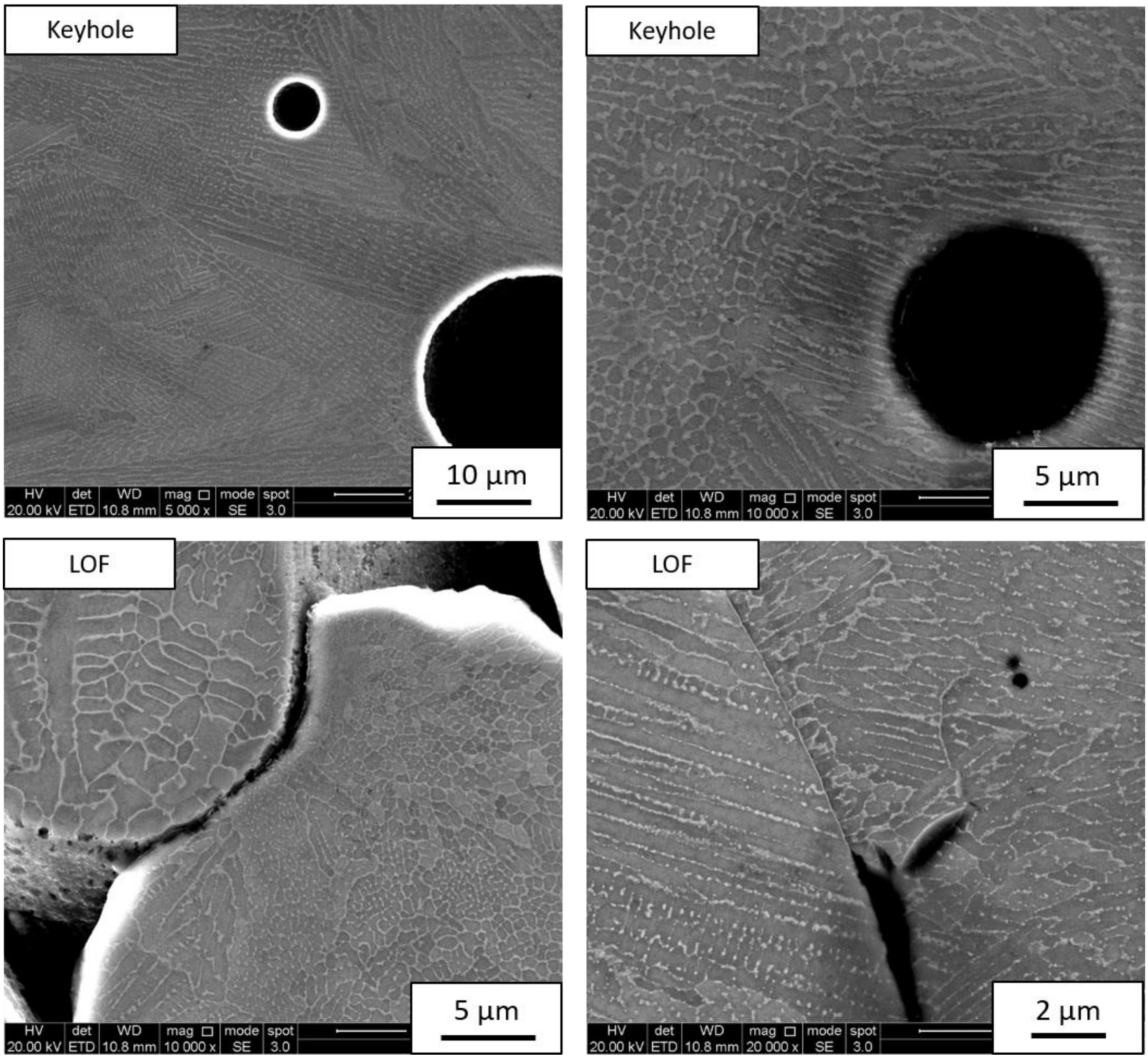

Figure 85: Etched SEM micrographs of the Keyhole and LOF samples, exhibiting the solidification structures in the vicinity of the intentionally placed voids.

7.3.2 SEM analysis on HIP Samples

Figures 86-89 contain SEM images of varying magnification of the Dense, Keyhole, LOF and Sphere samples in the HIP only condition (1160^{o}C, 102MPa, 3 hours). The dense sample still contains visible evidence of growth cells. In Figure 86a, growth cells in two different sub grains can be observed side on (revealed by parallel lines) as well as end on (revealed by a pattern of circles). This shows that not all of the segregated material was able to dissolve during the three hour HIP treatment, which is unlikely anyway at a temperature of 1160^{o}C. Figure 86c shows the presence of δ phase at the interdentritic regions, which has also been observed in several published studies after various heat treatments [176], [178], [194], [265].

It is understood that the δ phase precipitates between 780-980^{o}C [172], [176], with peak precipitation occurring around 900^{o}C [163]. The elevated temperature of 1160^{o}C applied during the HIP treatment in this study is favourable for the dissolution of Laves phase [163], diffusion of segregated elements, as well as dissolution of any γ'' precipitates that may have formed during printing, leading to the increased release of Nb. Therefore, whilst δ phase precipitation theoretically reduces at temperatures near 1020^{o}C [172], [176] the increased Nb content, in addition to the purely segregated Nb already residing at cell boundaries, enables a small amount of fine δ phase to form. At the end of the HIP process samples were air cooled leading to fast temperature reduction in the samples. Because of this, it is unlikely that the temperature remained at the optimum for γ'' precipitation for long enough for these strengthening precipitates to form. This, coupled with the presence of the δ phase, and the lack of homogenisation of the Nb to cell interiors, explains the lack of any visible γ'' phase in the SEM microstructures.

The Keyhole sample contains large regions free from growth cells or solute segregation, that directly neighbour regions that appear similar to the microstructure observed in the Dense sample. This was also observed in the EBSD analysis in Chapter 6, where only a small volume of the central defect region in the Keyohle sample recrystallised. No pores were identified in the partially recrystallised region after HIP, even through SEM analysis. The recrystallised regions, termed RX region in Figure 87a, contain non uniformly distributed white 'flecks' of two different size distributions which are believed to be carbides that have remained in the microsctructure from the as-built state [27], [188]. As well as this, a very small number of larger δ phase precipitates are present at grain boundaries. No γ'' phase precipitates are visible in the RX microstructure at this magnification.

SEM analysis of the HIP LOF microstructure (Figure 88) shows that the majority of LOF defects have been removed after HIP as discussed in Chapter 6. There are however, a few remaining pores visible as shown in Figure 88a. In addition to this, it is clear from Figure 88c that regions of unrecrystallised material can still be observed in this sample. Therefore, it is likely that further optimisation of the HIP schedule is required for this part.

The location of the pore in Figure 88a is close to a previously unmelted powder particle, providing evidence that the pore is likely at the edge of a previous LOF void. Whislt the material surrounding the powder particle has undergone recrystallisation, identified through the lack of grain sub-structures as well as the presence of recrystallisation twinning, the particle itself still contains cellular structures with intercellular segragated material. This indicates that the recrystallisation process did not occur in this region of the material, and that the growth of recrystallised grains into the region was prevented. The reason for this is potentially due to carbide and oxide based pinning of the prior particle boundaries (PPB) [57], [266]. These phases are visible in the EDS maps of the LOF sample in the HIP + HT state shown in Figure 95, and are discussed later. The recrystallised regions of material in the LOF sample, shown in Figure 88b, still contain some precipitates, some cuboidal in shape and some that look globular. It is likely that these particles are carbides as identified by Ferreri *et al.* [188].

A higher magnification image of the central region of the loose powder section of the Sphere sample is shown in Figure 89a. It is clear that fine pores are still present in the microstructure. It is also clear from this image that some PPB are still present in the microstructure. Rao *et al.* [266] identified that powder with a higher initial oxygen content led to a HIP microstructure containing a higher volume of PPB. This is due to an increased volume of oxides on the powder particle surfaces, pinning them in place. Their high hardness may also make them more difficult to deform and break-up during the HIP process. Consequently, this reduces the potential for diffusion of material and recrystallisation. Figure 97 shows EDS maps of the Sphere sample in the HIP + HT state. It is clear from these maps that Al oxides are present in the sample. These are unlikely to have formed just in the post HIP heat treatment, and therefore are also suspected to be present in the sample in the HIP only state.

The interior regions of the prior powder particles have recrystallised in some cases, as shown by the homogeneous matrix inclusive of twin structures in Figures 89b and 89c. However in other cases, observed in the HIP + HT samples introduced later in Figure 96, only partial dissolution of the as-built intra-cell precipitate structure has occurred within the sphere void region. It has been shown that as well as the oxygen content, the powder particle size also plays a large role in the formation of these prior particle boundaries, with smaller particles observing significantly more plastic strain and contact stress than larger particles. The plastic strain in the smaller particles is also more uniform throughout the particle, as compared to localised at the edges for larger particles. These effects lead to a higher level of diffusion, densification, and likely also recrystallisaion, in finer particles [267].

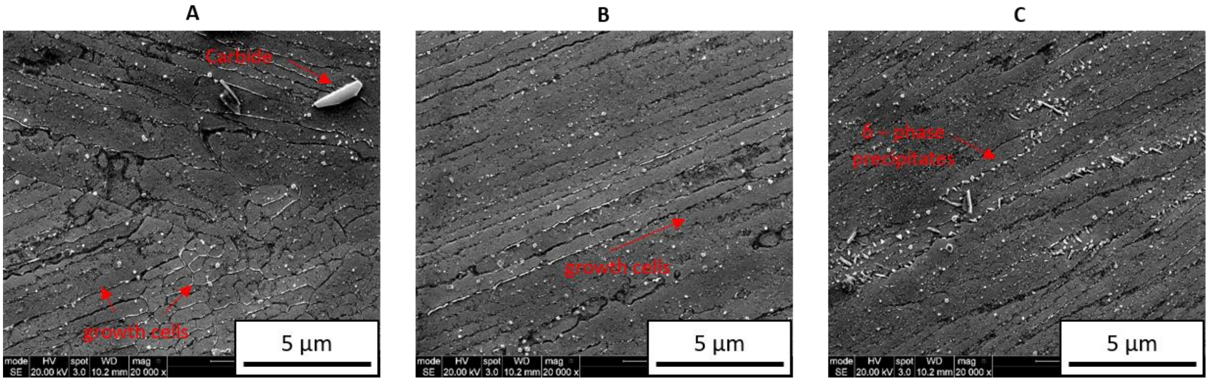

Figure 86: Etched SEM micrographs of the Dense sample after HIP only

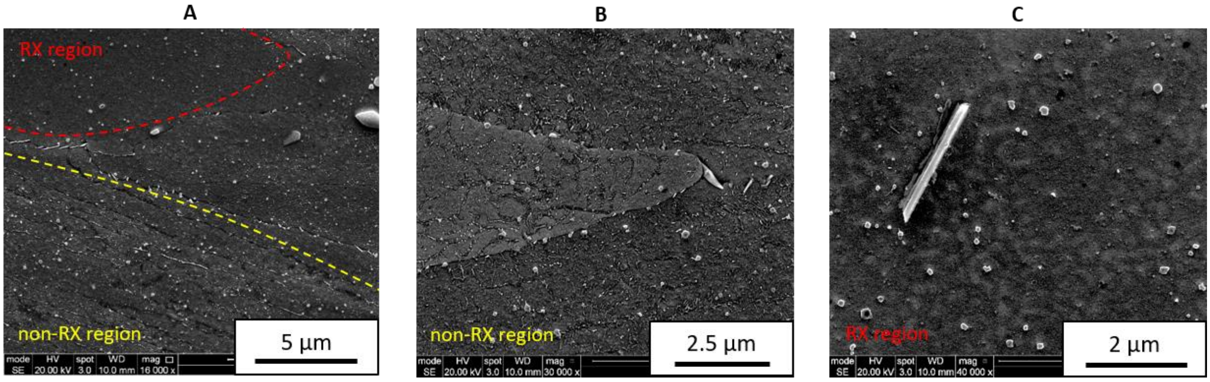

Figure 87: Etched SEM micrographs of the Keyhole sample after HIP only

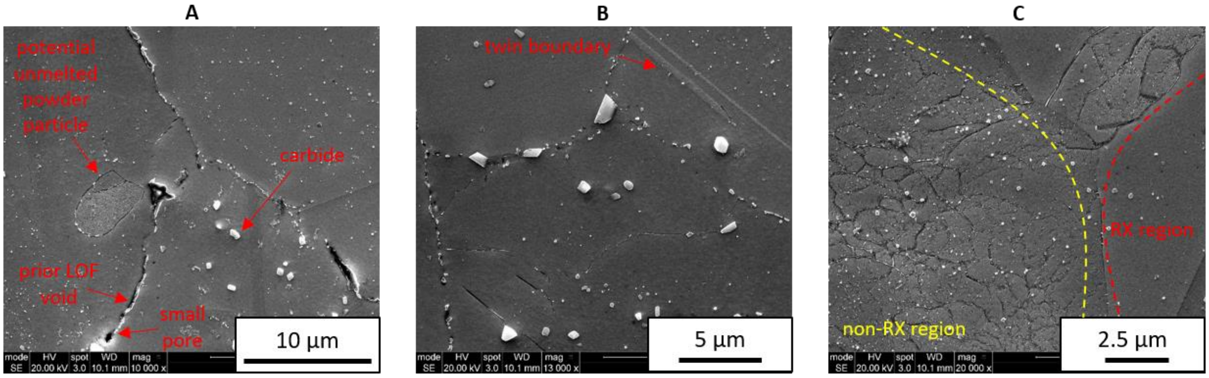

Figure 88: Etched SEM micrographs of the LOF sample after HIP only

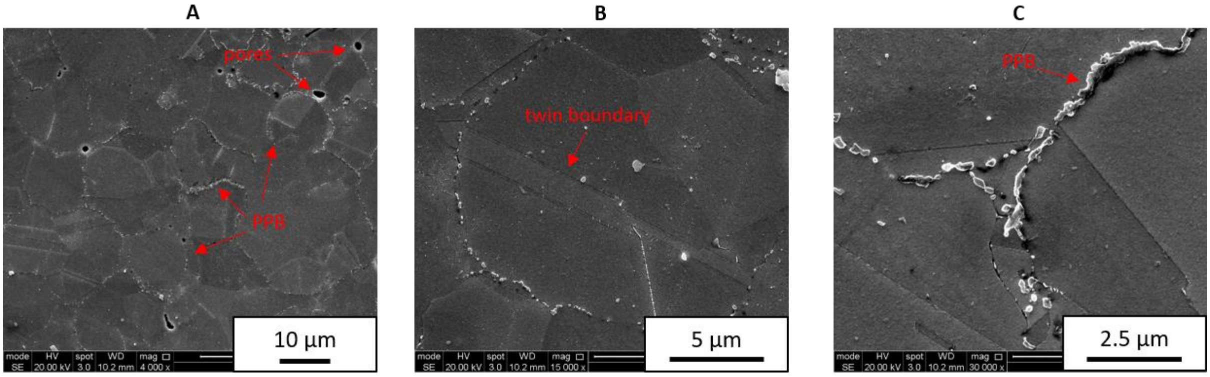

Figure 89: Etched SEM micrographs of the Sphere sample after HIP only

7.3.3 SEM and EDS Analysis on HIP + HT samples

The sample microstructures after the post HIP solution heat treatment (980°C / 1 hour / air cool) and a double age heat treatment (720°C / 8 hour / furnace cool to / 620°C / 8 hour / air cool) are shown in Figures 90-98. Significant changes can be observed compared to the HIP only state.

Whilst the Dense sample still shows evidence of cellular solidification structures, the microstructure has been replaced by long thin precipitates, both at grain boundaries, and prior cell boundaries, as shown in Figure 90. These are believed to be δ phase due to local enrichment of Nb and relative depletion of Fe and Cr in the EDS maps in Figure 91. The HIP temperature was above the dissolution temperature of the δ phase (1020°C), so large scale precipitation of this phase was not possible during HIP. Comparatively, the solution treatment of 980°C provides optimum conditions for the precipitation of this phase [176], [178], [194], [265]. The precipitates at grain boundaries are also observed to be larger than those formed between cell structures which is likely due to increased dissolution and diffusion of Nb atoms near grain boundaries compared to between cells. This reasoning has previously been attributed to increased γ'' precipitation at grain boundaries compared to between cells by Gallmeyer *et al.* [178]. The EDS map in Figure 91 show a slight depletion in Nb in the regions surrounding the grain boundary δ phase precipitates, which leads to a reduction in the possibility for any strengthening phases to precipitate in these regions. It is important to note that the 2D resolution of EDS is in the range of 1µm^2, and therefore the exact location of this qualitatively assessed depletion is not known.

Interestingly, very few carbides can be observed in the microstructure of the Dense sample. As carbides are known to form in the liquid ahead of the solidification front, these are very fine [131]. A slight compositional variation can be observed in the Ti map at positions within the grains which is potentially indicative of Ti based MC carbides. It is therefore likely that very fine carbides exist, however that they are too small to resolve at this magnification. TEM imaging discussed in Section 7.3.5 shows the presence of Nb and Ti rich MC type carbides at grain boundaries, and fine regions of Ti enrichment within the grain area. These fine regions of enrichment were not able to be correlated to features on the bright field TEM image and so no comment can be made as to the presence of MC type carbides within the grains.

The Keyhole sample microstructure shown in Figure 92 still consists of a mixture of recrystallised and non-recrystallised grains as discussed previously. However, in comparison to the internal grain structure of the non recrystallised regions visible in the Dense sample after HIP + HT, those found in the Keyhole sample are less pronounced in their retained cellular structures.

EDS maps for the Keyhole sample in Figure 93 confirm the presence of Nb and Ti rich, and Ni, Fe, Cr depleted, particles that are likely MC type metal carbides, both at grain boundaries and within the grain. Enrichment of regions of Mo suggest that M_6C carbides may also be present. Compared to the HIP only microstructures, the HIP + HT Keyhole sample contains white 'flecks' with a different morphology, cauliflower-like in shape, that are circled in Figure 92c. White flecks were proposed to be γ' particles by Kaletsch *et al.* [57] however, they could not confirm this analytically in the study they performed. A similar precipitate morphology was shown for Allvac 718Plus, a modified version of Inconel 718 that enables the primary precipitation of γ' to allow higher in service temperatures [114]. γ' precipitates contain Al [113] and Ti, and upon close inspection of the Ti map in Figure 93, local specks of Ti enrichment can subtly be observed in the same locations as some of the larger white specks in the SEM image. The presence of γ' instead of γ'' could be rationalised by the fact that a large proportion of the Nb in the material has been removed by the precipitation of the δ phase, reducing the formation of γ''. As the δ phase does not require Ti or indeed Al, the γ' phase is still able to form. However, it is also possible that the slight composition variations observed in the Ti map are just a result of carbide particles. Further EDS and TEM analysis for these precipitates is discussed in Section 7.3.5.

As well as containing fine specks of precipitates, the majority of grains in the Keyhole sample contain large scale elongated δ phase precipitation at grain boundaries. The sample also shows evidence of the phenomena of discontinuous δ phase precipitation at the recrystallised grain boundaries (Figure 92c). Precipitates an order of magnitude smaller than these grain boundary δ phase precipitates can also be observed within the grains. However, there is a clear reduction in the volume of these fine precipitates in the vicinity of the larger grain boundary δ phase precipitates. Further EDS and TEM analysis in Section 7.3.5 confirms these precipitates to be γ'' particles.

The largest difference between the LOF sample after just HIP compared to the LOF sample after both HIP and HT is the precipitation of large elongated δ phase precipitates at grain, and twin, boundaries as shown in Figure 94. There is more evidence of discontinuous precipitation in this sample compared to the Keyhole sample discussed previously, which is believed to be due to the volume of recrystallisation, and subsequent release of Nb, that occurred in the LOF sample compared to the Keyhole sample. Discontinuous precipitation occurs at moving grain boundaries [268], and as the LOF sample displayed nearly full recrystallisation, the amount of moving grain boundaries in this sample will have been greater. This is aided also by the finer initial grain size, therefore presence of more grain boundaries, observed in the as-built version of this sample. Higher resolution imaging of a region of discontinuous precipitation reveals a saw-tooth pattern along the long edge of each precipitate. The reason for this is currently unclear but is believed to be due to the partitioning of elements to the precipitate during grain boundary movement [268]. Both needle like and globular precipitates on a very small scale look to be present within the grains. These are difficult to resolve at this magnification as they produce only a slight contrast within the grains. Again, it is possible that the globular precipitates are γ'. Whilst there is evidence of this background contrast in the micrographs of other samples, the presence of larger precipitates, likely γ'' or δ phase, in those overshadows the smaller intragranular particles. Instead, in the LOF sample there is a distinctive lack of any larger scale Nb enriched γ'' or δ phase particles. Higher magnification imaging as shown in Figure 100 enables these regions of contrast to be resolved, revealing very fine, elongated, and closely located particles which are likely γ'' precipitates. The grain background contrast observed in all other samples could be indicative of similar intragranular precipitation. This is further discussed in Section 7.3.5.

EDS analysis of the LOF sample in Figure 95 shows partitioning of the Nb to the fine elongated precipitates at grain boundaries. The scale of these precipitates as well as the depletion of the Fe and Cr in this region provides evidence that the precipitates formed are the δ phase. The EDS results also show that larger MC type metal carbides, rich in Nb and Ti, and M_6C type carbides, rich in Mo, both depleted in Fe, Ni and Cr, are generally located near grain boundaries as opposed to within the grains. The large curved boundary observed in the bottom of the SEM image in Figure 95 is lined by Ti and Al oxides. This was also observed by Kaletsch et al. [57] after solidifying Inconel 718 powder to a bulk printed surface. These oxides are also identified at the region between some HIP powder particles in Figure 97. This information suggests that the large curved boundary is potentially the location of a previous LOF void. It is likely that the inclusion of oxygen on such a large level is due to the recycled nature of the powder. The work presented in this study utilised powder that was previously stored in ambient conditions and not under argon. Similarly, the powder used herein was known to have been recycled from previous builds for an unknown number of cycles. It is believed that, had the powder been stored under a protective atmosphere, and used fresh from initial manufacture, the introduction of alumina at prior void boundaries would have likely not have occurred to a similar extent.

As with the other samples (except the LOF sample), the recrystallised grain interiors of the Sphere sample, shown in Figure 96, are homogeneously filled with very fine elongated precipitates. These are either δ phase or γ''. Some of the grains contain long and thin 'spaghetti' shaped precipitates which were not identified in the HIP only microstructure. These are further discussed in Section 7.3.5 using TEM analysis.

It has been observed that the grain boundaries of the Sphere Bulk region contain fewer precipitate structures than in the Sphere Void region. The reason for this is not known, however may be due to the fact that the microstructure in the Sphere Bulk region was originally continuous and defect free, and so no diffusion of material across void regions or PPBs was required. The reduced number of grain boundary precipitates will have allowed the grains in the Sphere Bulk region to grow at a faster rate leading to the large grains observed in the EBSD images in Section 6.

In the Sphere Void region, PPBs are still visible in the microstructure after HIP + HT. The morphology of the precipitates identified seem to be unchanged from the HIP only samples, being small but closely located individual particles. In contrast to this, a single large network of precipitate is visible at the boundary between the Sphere Bulk and Sphere Void region, as shown in Figure 96a. EDS maps of a similar boundary region is shown in Figure 98. It is clear that the boundary regions between grains are depleted in the γ matrix forming elements, Ni, Fe and Cr, but enriched in Nb, Mo, Ti, Al, C and O. This shows that considerable carbide and oxide formation occurred at these regions during powder densification with the bulk cylinder. As secondary phases tend to be harder and more brittle than the bulk material matrix, regions such as this are likely to become a point of failure during loading.

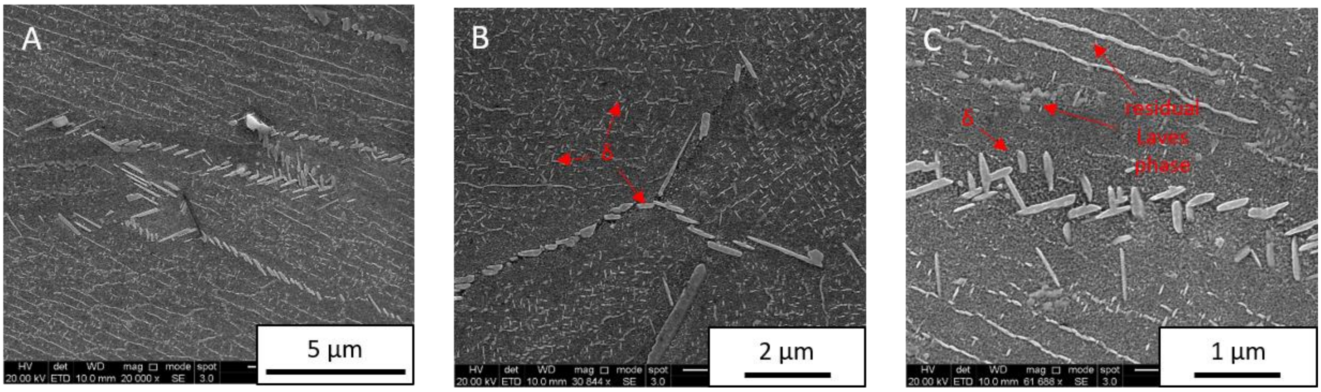

Figure 90: Etched SEM micrographs of the Dense sample after HIP and HT.

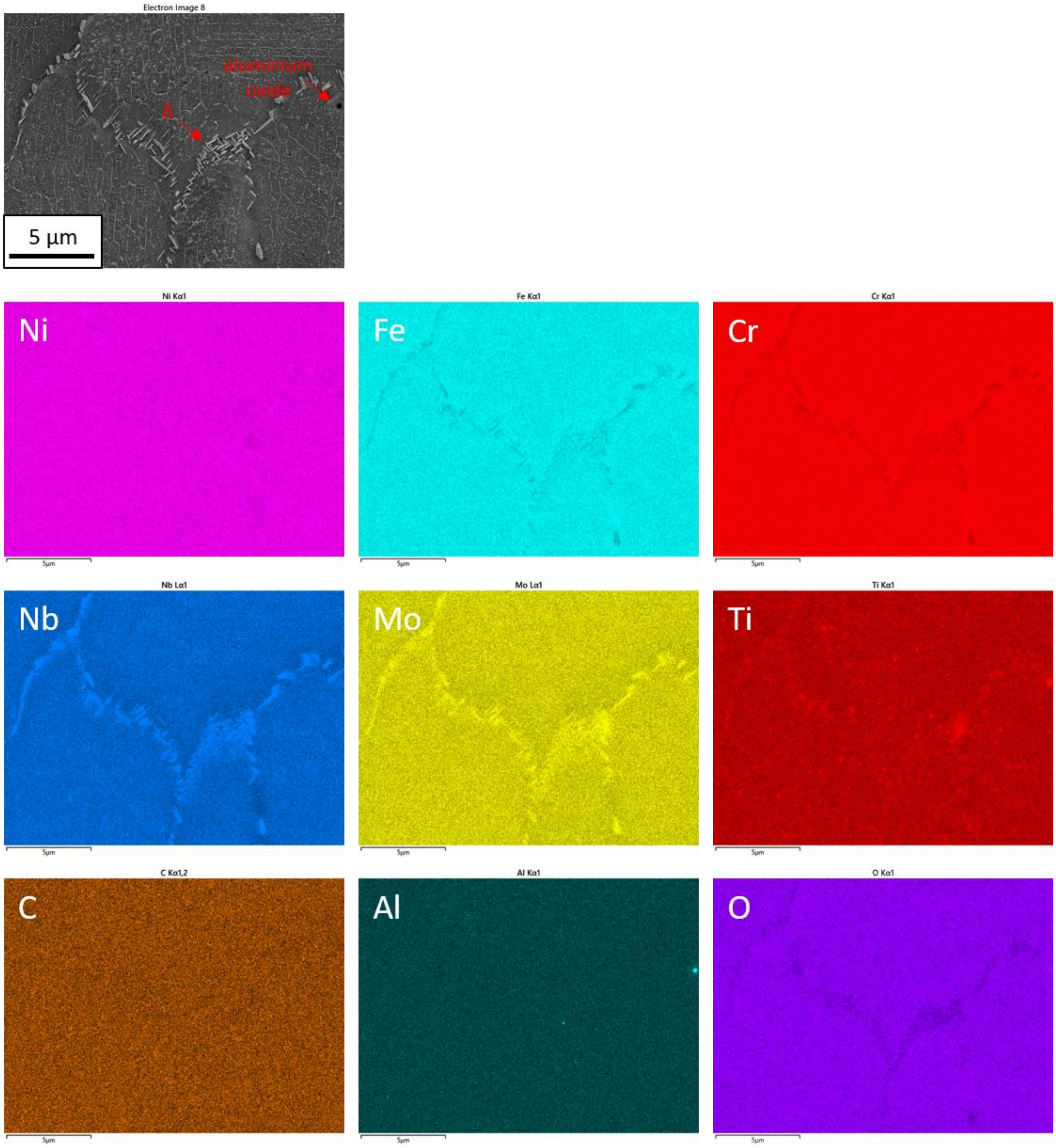

Figure 91: EDS maps of the Dense sample after HIP + HT.

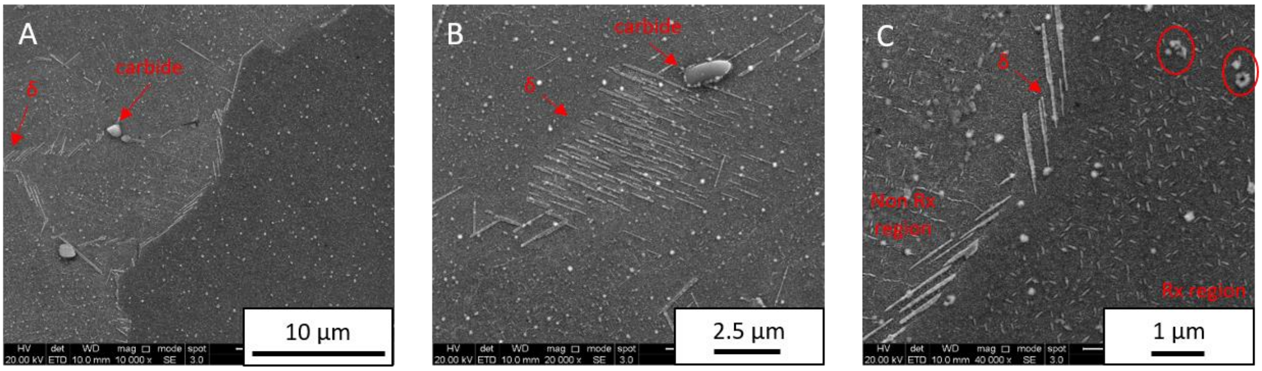

Figure 92: Etched SEM micrographs of the Keyhole sample after HIP and HT.

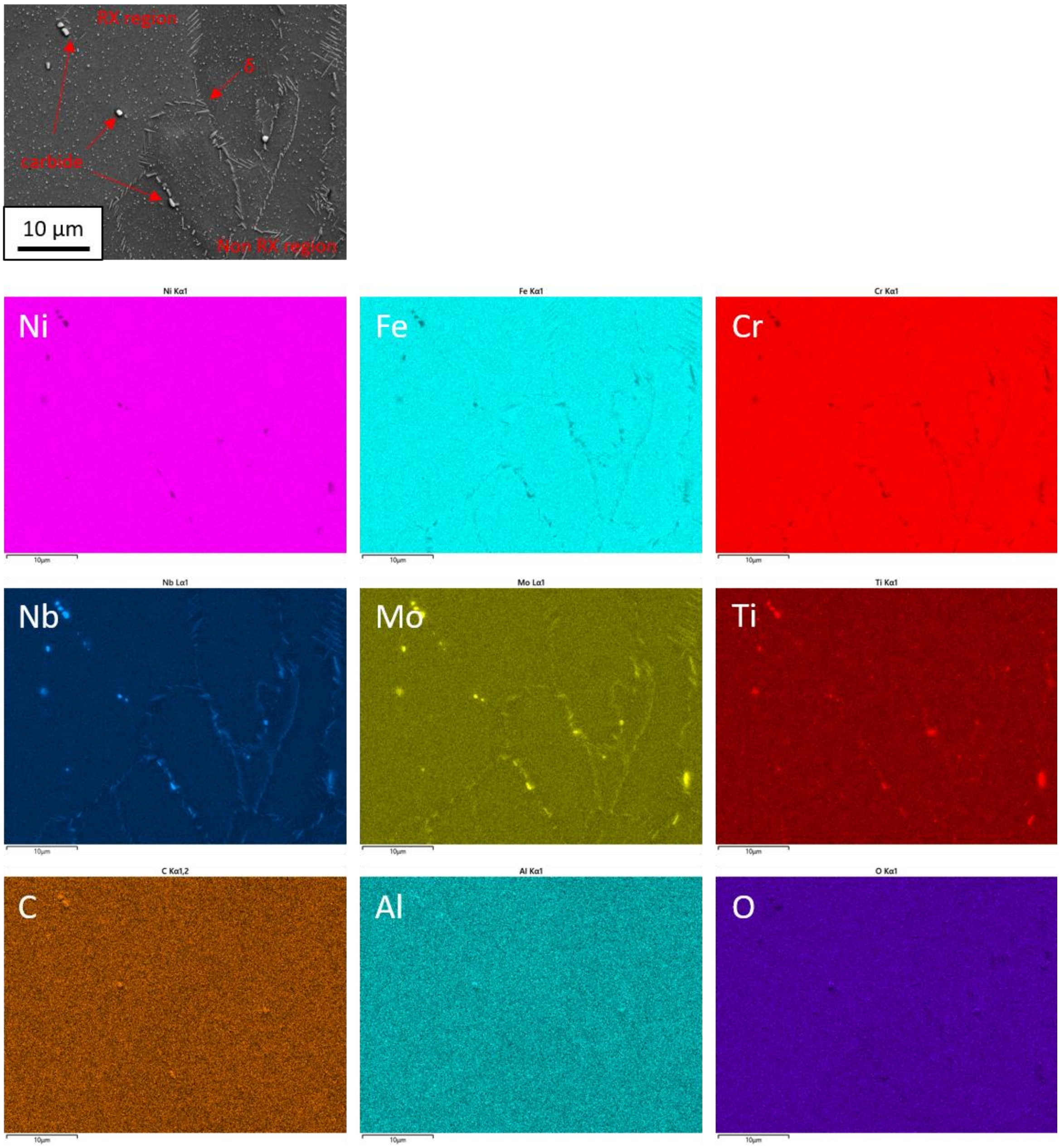

Figure 93: EDS maps of the Keyhole sample after HIP + HT. Image shows interface between large recrystallised grain and non recrystallised material.

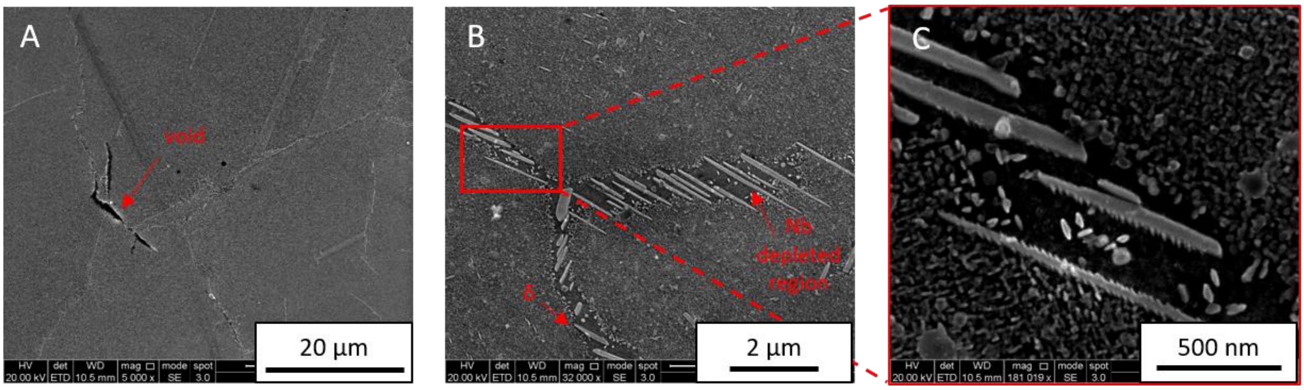

Figure 94: Etched SEM micrographs of the LOF sample after HIP and HT. Close up image of red box shows serrated precipitates.

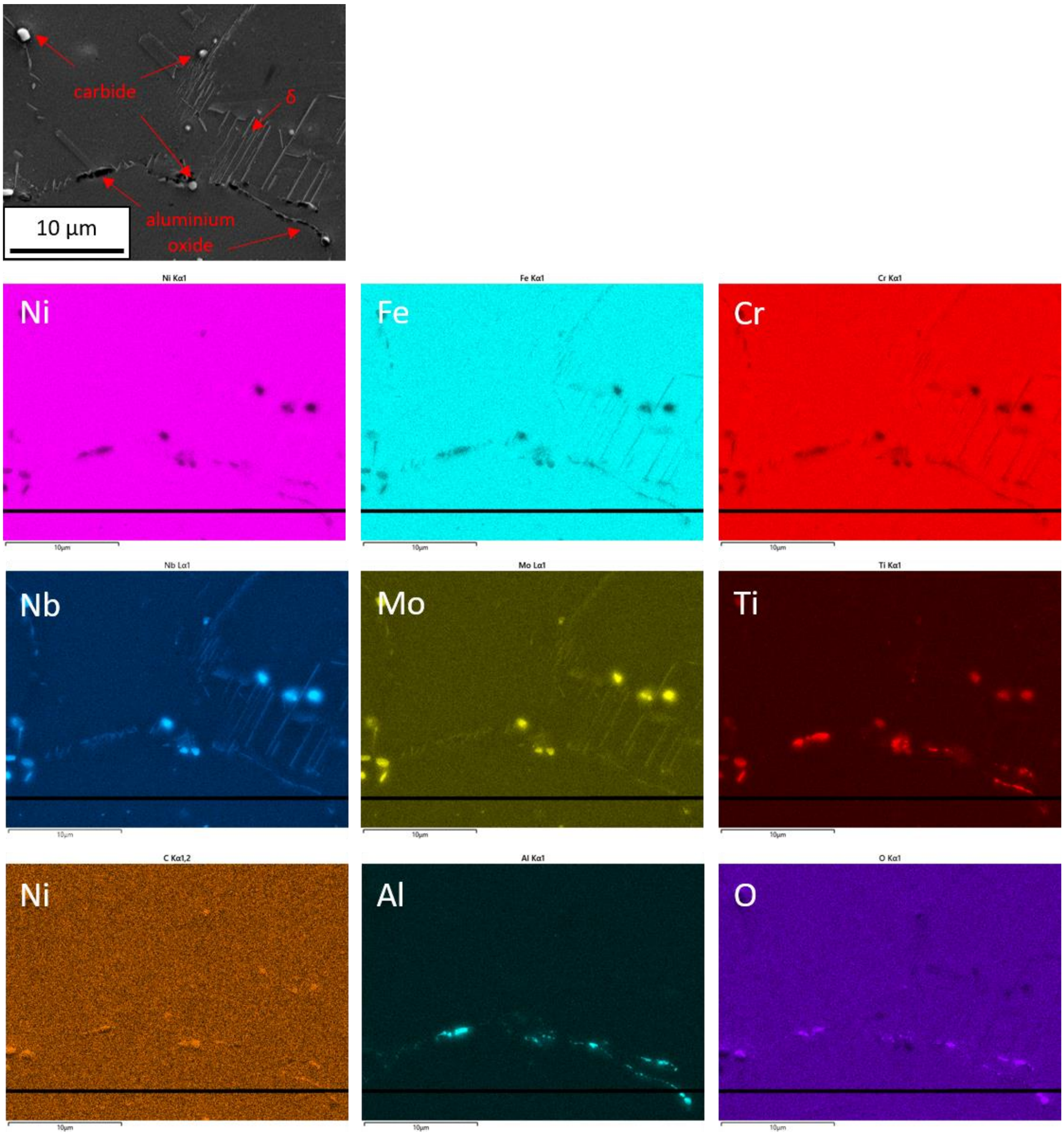

Figure 95: EDS map of LOF sample after HIP + HT. Black line due to electron beam turning off and on again during the scan.

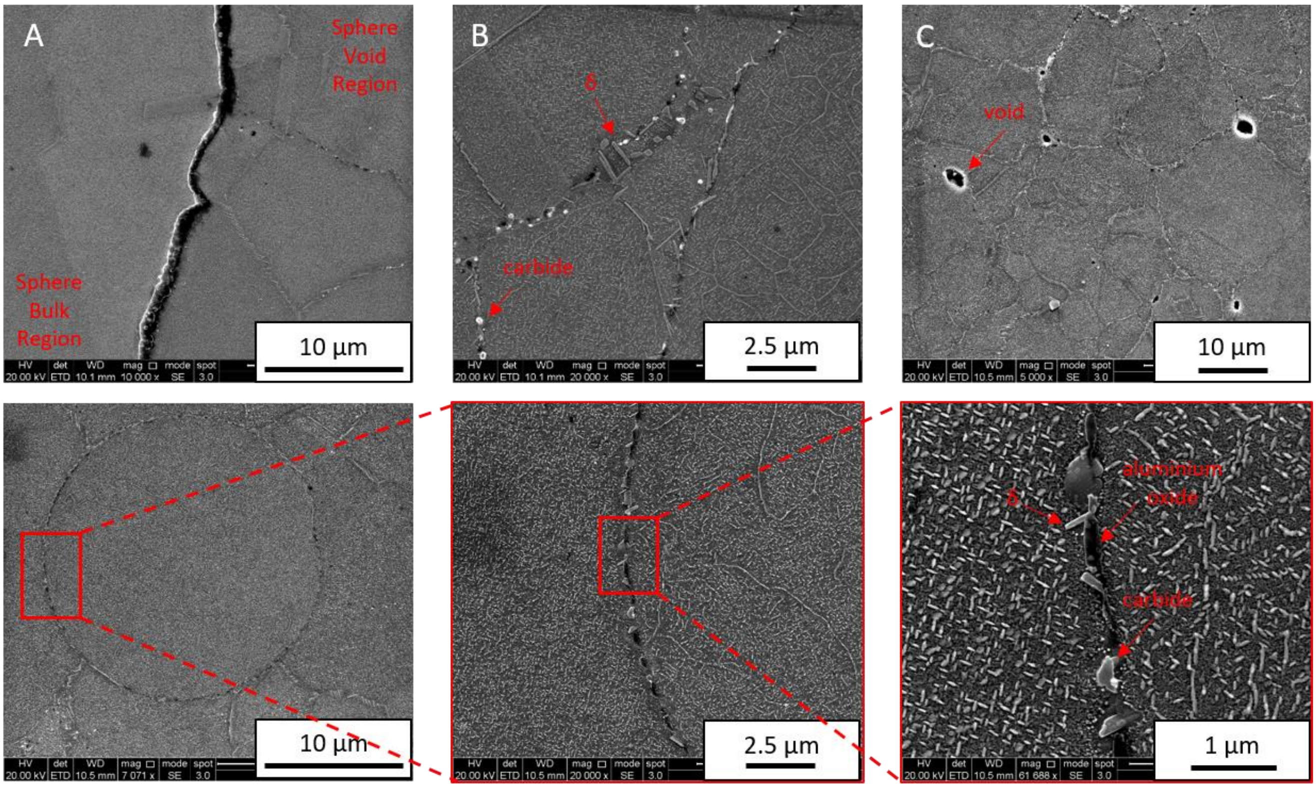

Figure 96: Etched SEM micrographs of the Sphere sample after HIP and HT. Red box shows the morphology of precipitate structures in and around a prior particle boundary (PPB). Top left micrograph shows the interface between the bulk and void regions.

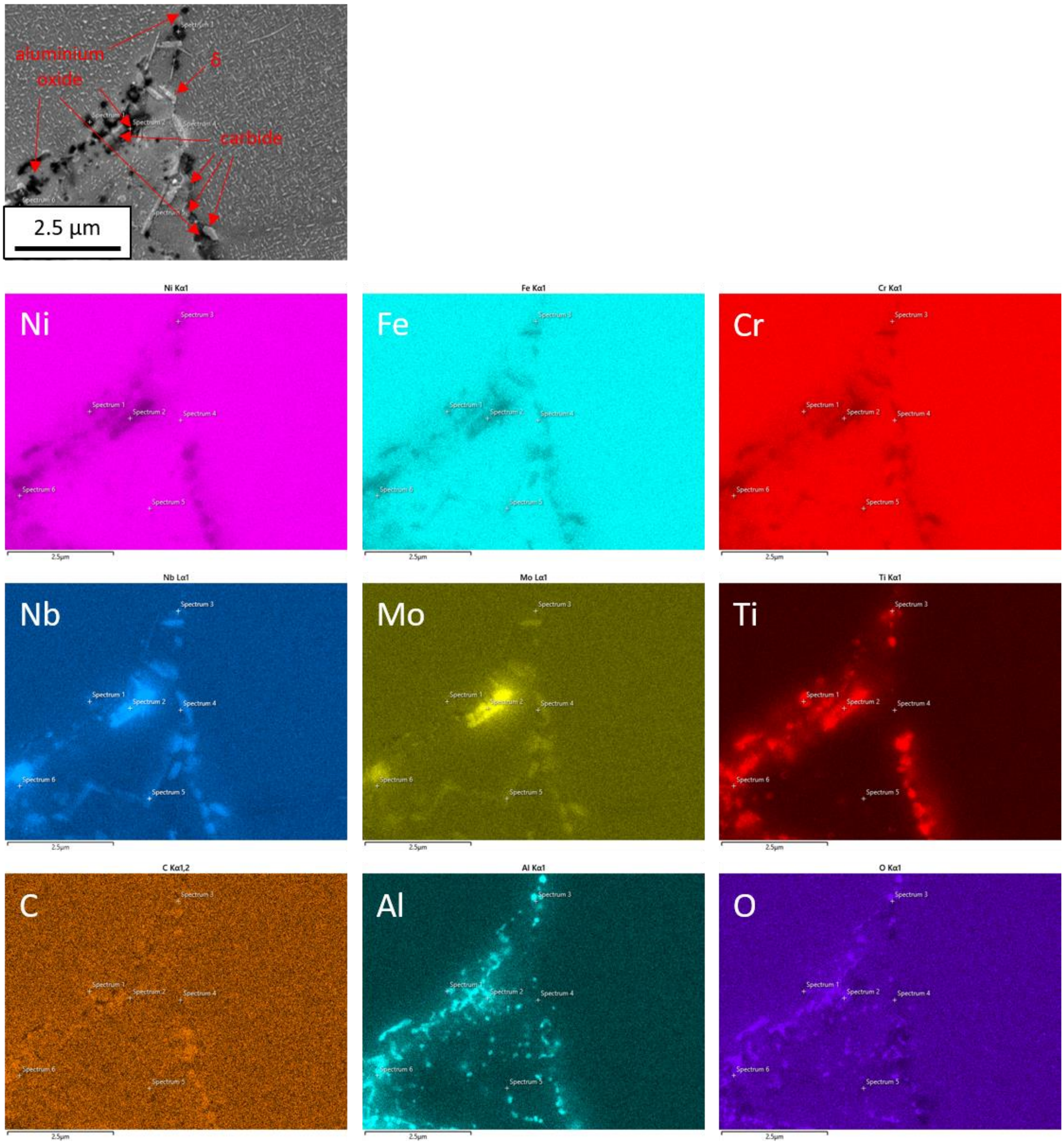

Figure 97: EDS map of Sphere Void sample after HIP + HT. Spectra locations not required for analysis.

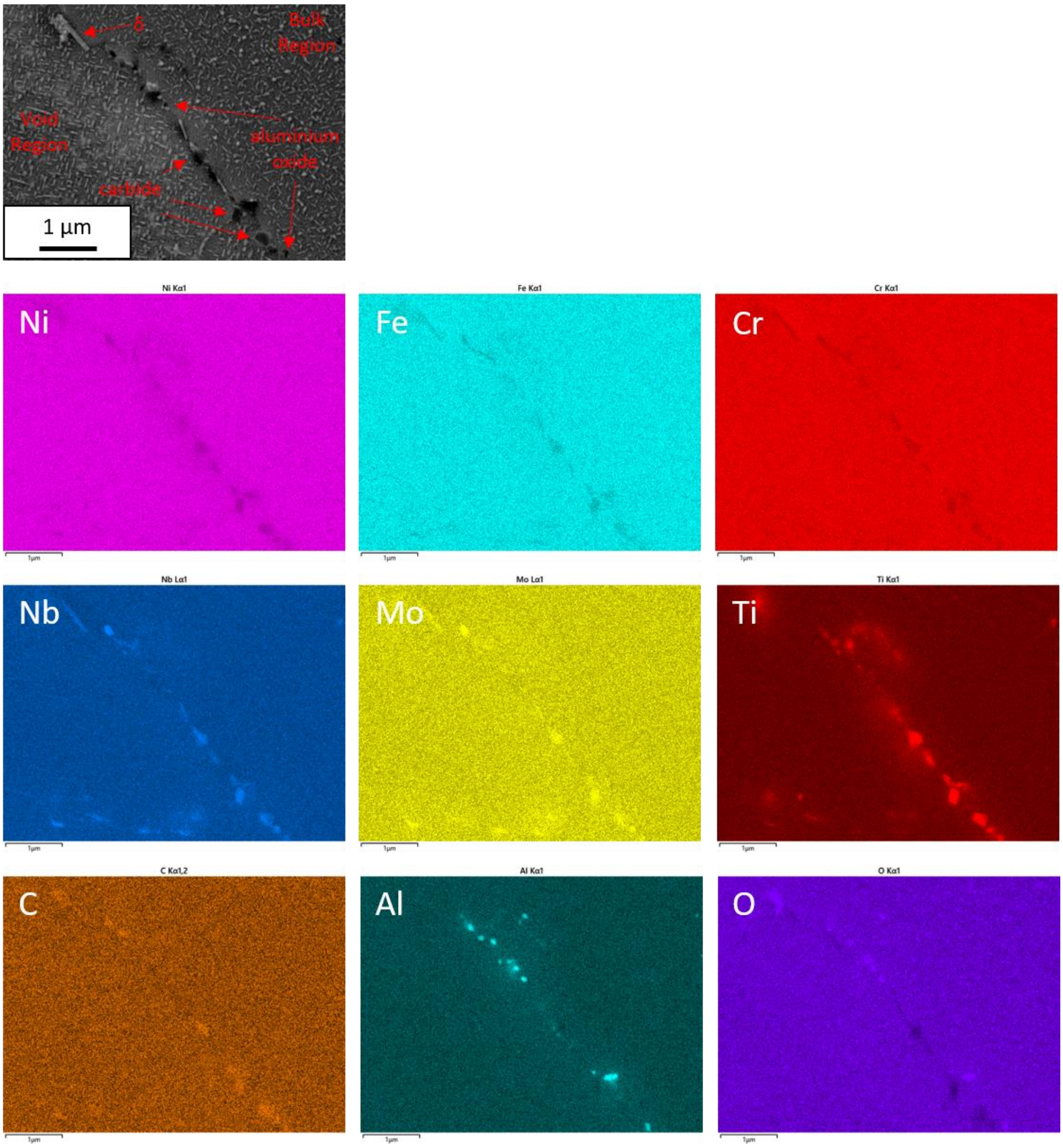

Figure 98: EDS map of Sphere Bulk/Void interface after HIP + HT.

7.3.4 SEM Analysis on HIP + HT samples at Higher Magnification

Whilst the larger scale microstructural features, particularly grain boundary phases, have been discussed in the previous section, it is worth comparing the intragranular fine scale precipitate distributions within each sample type. Figure 99 shows the etched micrographs of each sample, Dense, Keyhole, LOF, Sphere Bulk, and Sphere Void. The images obtained from the Keyhole sample are of the interior regions of the recrystallised grains. Figure 100 shows higher magnification images of the LOF sample, showing the presence of very fine precipitates that are located very close together. As discussed in the next section, 7.3.5, these phases are the strengthening γ'' phase.

Manual thresholding of 8 images similar to those presented in Figure 99 was performed in ImageJ for the Keyhole, Sphere Bulk and Sphere Void samples. The precipitates observed in the LOF sample were too fine to be resolved, and so the sample has been omitted from analysis. The Dense sample has also been omitted as it clearly exhibits a cellular structure, while the volume fraction of the needle-like phase is of interest.

Table 19 displays the data for the average number of precipitates detected in each image, the average total area fraction of precipitates in each sample, and the average precipitate diameter. All images used in the thresholding analysis, and the thresholded counterparts are shown in Appendix A.

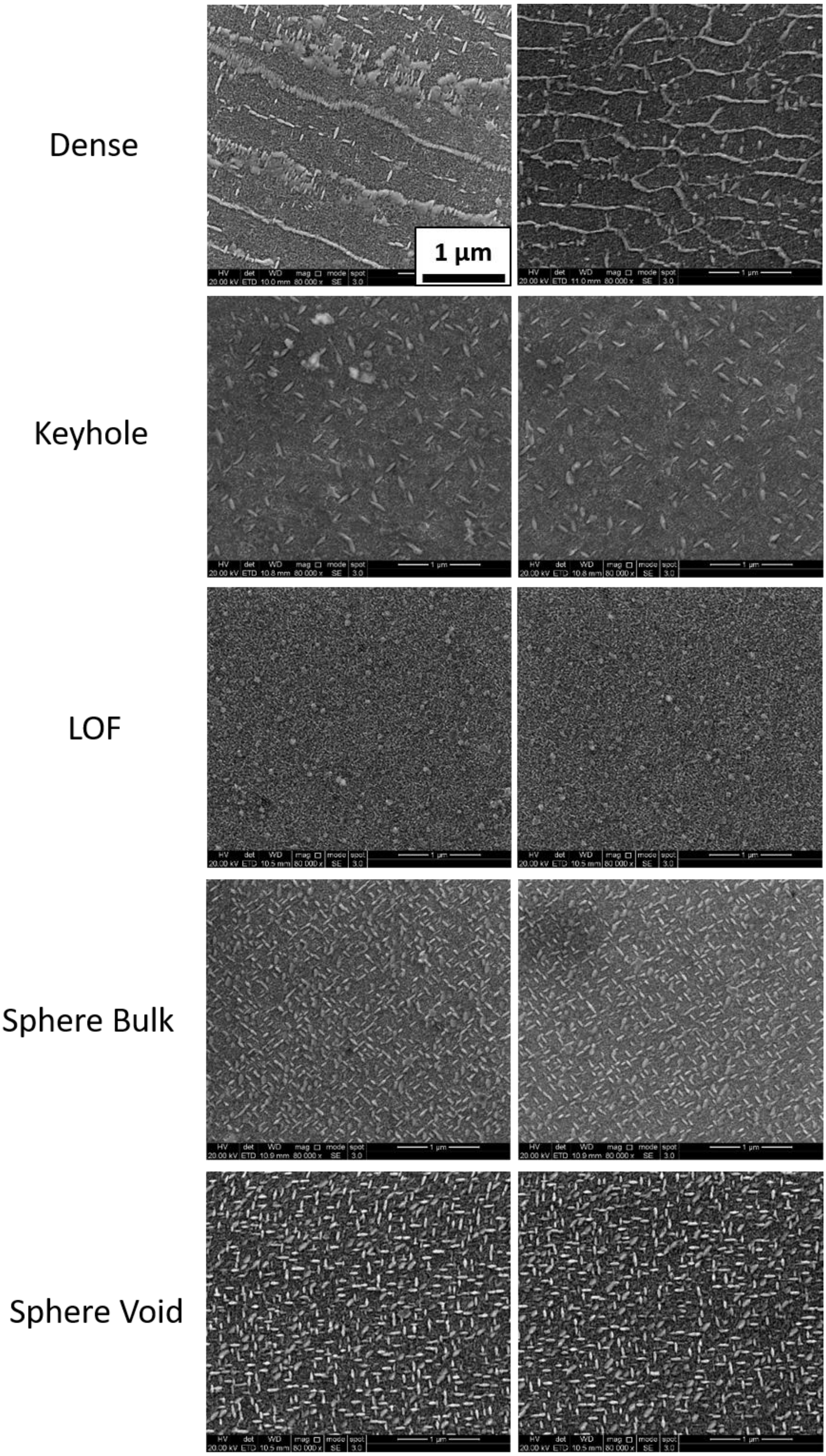

Figure 99: SEM micrographs of each sample in the HIP + HT condition to compare the precipitate structures between each microstructure type.

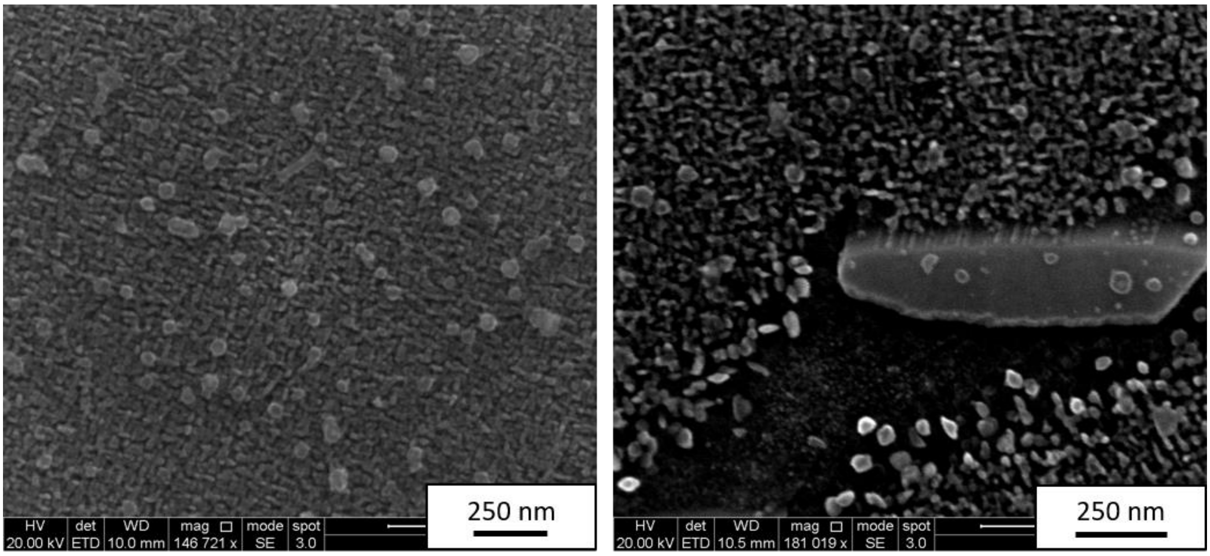

Figure 100: High magnification images of the precipitate distributions in the LOF sample.

Table 19: Summary of precipitate analysis for each sample. Errors shown as standard deviation.

	Keyhole	**Sphere Bulk**	**Sphere Void**
Number of Images Analysed	**8**	**8**	**8**
Average Counts Per Image	**312 ± 76**	**998 ± 75**	**944 ± 137**
Average % Image Area taken up by Precipitate Structures	**4.1 ± 0.7**	**7.8 ± 1.3**	**14.7 ± 2.5**
Average Precipitate Diameter (nm)	**75.8 ± 52.2**	**59.7 ± 27.9**	**81.1 ± 41.8**

As previously discussed, the Dense sample still exhibits the majority of the cellular solidification structures present in the as-built state. However, it is clear from Figure 99 that some fine needle-like γ'' precipitates have started to appear in the cell interiors. This demonstrates that sufficient Nb is present at the cell interiors to allow these precipitates to form, and is likely due to the partial dissolution of the segregated elements during the various heat treatments. In all other samples, due to the effects of recrystallisation and homogenisation of the matrix, it is assumed that sufficient Nb is present in the grain interiors to precipitate an optimum volume fraction of γ''. The Keyhole sample observes a sparse, but homogeneous, distribution of γ''. The average area percent of these particles was found to be 4.1 ± 0.7%. This value, along with the average particle diameter measurement, is slightly larger than reality due to the presence of large while 'flecks' that have been included in the thresholded images. The origin of these are currently unknown. Qualitatively, it seems as if the γ''

precipitates present in the Keyhole sample are marginally longer than those identified in both regions of the Sphere sample. This disparity between the qualitative analysis and the quantitative analysis shows the importance of taking a holistic approach to data analysis.

The Sphere Bulk and Sphere Void sample regions also contain a homogeneous distribution of these precipitates, however, at a higher area percentage of 7.8 ± 1.3% and 14.7 ± 2.5% respectively. The precipitates in the Sphere Void region are marginally larger in area than those found in the bulk region, however the difference is insignificant.

Although too difficult to resolve for quantitative analysis, images of the LOF sample shown in Figure 100 show that there is visible contrast within the γ matrix. Evidence of the identification of the γ'' phase is discussed in section 7.3.5.

7.3.5 TEM Imaging Analysis

Based on the results obtained through SEM analysis of the HIP + HT samples, a number of questions were raised which required higher resolution imaging only available using TEM analysis. The TEM was therefore used for the following:

- To confirm the presence of γ'' within the grains using electron diffraction and additional analysis performed using STEM EDS; especially in the LOF sample where it is possible that the recrystallisation process continued throughout the heat treatment cycle, leading to only very fine precipitates being present in the microstructure
- To understand what the small globular white precipitates are that were identified in the Keyhole sample.
- To further investigate the presence of alumina in regions where voids have been eliminated by diffusion
- To understand what the long thin 'spaghetti' strips of precipitates observed in some regions of the Sphere Void and LOF regions are.

Figure 101 shows the precipitate distributions in each sample using bright field STEM imaging. Whilst the Dense sample in Figure 99 shows mainly the retained cellular structure, in Figure 101, it is clear that regions of the Dense sample exhibit a similar distribution of elongated precipitates as the Keyhole sample. These are larger and more sparsely distributed compared to the Sphere Void and Sphere Bulk regions. The precipitates in the sphere void region look larger than those in the Sphere Bulk region, which corresponds well with the analysis performed in the previous section, Section 7.3.4. It is clear that the precipitate distributions in the LOF sample are very fine and difficult to resolve even using the TEM. As TEM is a transmission microscopy analysis tool, particles present throughout the thickness of the sample can be visualised. If the sample is too thick, it becomes difficult to resolve small particles that do not extent the full thickness of the sample.

Figure 102 shows the TEM selected area diffraction patterns for each sample type. The associated dark field images for the locations marked with red arrows in the diffraction patterns are shown for the Dense, Keyhole and LOF samples. It is clear that the diffraction patterns for each sample type are very similar, suggesting that each sample has similar precipitates. Diffraction dots for every orientation of γ' and γ'' precipitates are present surrounding the central γ matrix diffraction pattern [116], [117]. Upon analysis of the dark field images at the indicated locations in the diffraction patterns in Figure 102, it is clear that the precipitates have an ellipsoidal shape in all samples, indicating that these are more likely γ'' precipitates. As the δ phase is incoherent with the matrix, the diffraction pattern spacings for these would not align with those of the γ matrix [269]. Therefore, as no other pattern of spots can be observed in the diffraction patterns it can be concluded that there is no δ phase precipitation within the grain interior regions on the TEM samples [116].

Figures 104-109 show STEM EDS maps of various regions of the different samples to help discuss the bullet points above. In the majority of maps, Ni, Fe, Cr, Nb, Ti, Co, Al, and Ta have been displayed, as these are the main elements associated with Inconel 718. As the line energy of Mo is similar to Nb, this element has been excluded from the analysis. In the case where it is not confirmed if the precipitates highlighted are carbides, carbon has been added. Similarly, in regions where the presence of oxides is suspected, oxygen has been added to the analysis.

Only the Dense sample contained non-recrystallised regions within the TEM foil. Figure 103 shows that dislocations are still present in the microstructure. These provide additional strength to the γ matrix by preventing further dislocation movement. However, this is a less efficient means of strengthening than the precipitation of the strengthening γ'' and γ' phases. STEM EDS analysis of a precipitate particle at a grain boundary in the dense sample (Figure 104) shows enrichment in Nb and Ti, and a depletion in Ni, Fe, and Cr indicating the presence of MC type carbides in this sample.

Figure 105 shows STEM EDS analysis of the precipitates found in the Sphere Void region. Enrichment in Ni, Nb, and Ti, and a corresponding depletion in Fe, Cr, and Co indicates that these precipitates are likely γ'' precipitates. Upon imaging side on, these appear as long thin ellipsoids, however in 3D space, they are plate-like in shape. As TEM is a transmission imaging technique, it is possible to observe dark shadow-like circles in the matrix behind the main ellipsoidal precipitates in Figure 105. This indicates that the main precipitates are in fact circular discs and further strengthens the argument that these are γ'' precipitates. This background effect is also faintly visible in the Ni, Fe, Cr, Nb and Ti maps in Figure 107.

Although it was difficult to resolve precipitates within the LOF sample following the HIP and HT cycles using SEM imaging, the selected area diffraction pattern as well as the dark field image in Figure 102 does show the presence of γ''. In addition to this, STEM EDS analysis of the matrix region displayed in Figure 106 shows clear partitioning of the γ'' forming elements to specific, elongated regions. It is possible that the recrystallisation stage continued throughout the post HIP heat treatment in this sample, as also evidenced by the reduction in larger grains present in the analysis after HIP + HT from the EBSD data in Chapter 6, leaving only a small fraction of time for precipitates to nucleate prior to cooling. This likely resulted in the under-aged microstructure exhibited in this thesis.

Although the Dense sample does contain larger γ'' precipitates as well, the background matrix in this sample (Figure 107) also shows the same partitioning as in Figure 106 for the LOF sample. This figure also clearly shows the inclusion of Al oxide showing that even in the control sample, oxides are present.

In the SEM images, it was hypothesised that the fine white flecks observed in the LOF and Keyhole samples could be large γ' precipitates. As the diffraction pattern for γ' overlaps that for γ'', it is possible to infer from the diffraction patterns in Figure 102 that very fine γ' precipitates are present in the matrix. However, in the dark field image taken from the LOF sample, it is difficult to resolve any particles with a circular or cuboidal shape. The STEM EDS maps shown in Figure 108 for a white fleck in the dense sample confirm that these particles are depleted in Ni and so their enrichment in Nb, Al, and Ti indicate that they are more likely to be carbide (although the carbon map does not show enrichment in the location of the white fleck imaged), or oxide inclusions, within the matrix. Unfortunately, in this case the EDS map for oxygen was not recorded and so this data is not available in the analysis. Due to the nature of the AM process, which makes use of recycled powder and elevated temperature processing under an imperfect inert gas shield, the inclusion of oxygen in the material is very likely. It is important not to conclude that the samples do not contain any γ' precipitates at all as the TEM analysis was only performed on a very small fraction of the full microstructure.

TEM allows a closer look at the ‘spaghetti’ precipitates found mainly in the Sphere Void and LOF samples areas. At lower magnification, these precipitates look like residual continuous secondary phases formed during the rapid solidification of either the powder or the AM printed bulk. However, TEM and STEM EDS analysis in Figure 109 shows that these regions are made up of individual but overlapping precipitates enriched in Ni, Nb and Ti, and do not contain any enrichment in C. Therefore, it can be concluded that these regions are densely packed γ'' precipitates. The nucleation of precipitates occurs in regions where it is most energetically favourable. Solidification cell boundaries contain a high density of dislocations whilst also containing enrichment in elements required for the precipitation of γ'' and δ phases. Therefore, it is believed that these precipitates line a previous non-recrystallised solidification boundary, possibly those between sufficiently misorientated sub-grains. The matrix surrounding these overlapping precipitates is depleted in γ'' precipitates and therefore the formation of these ‘spaghetti’ precipitates is not a desirable artefact in the material.

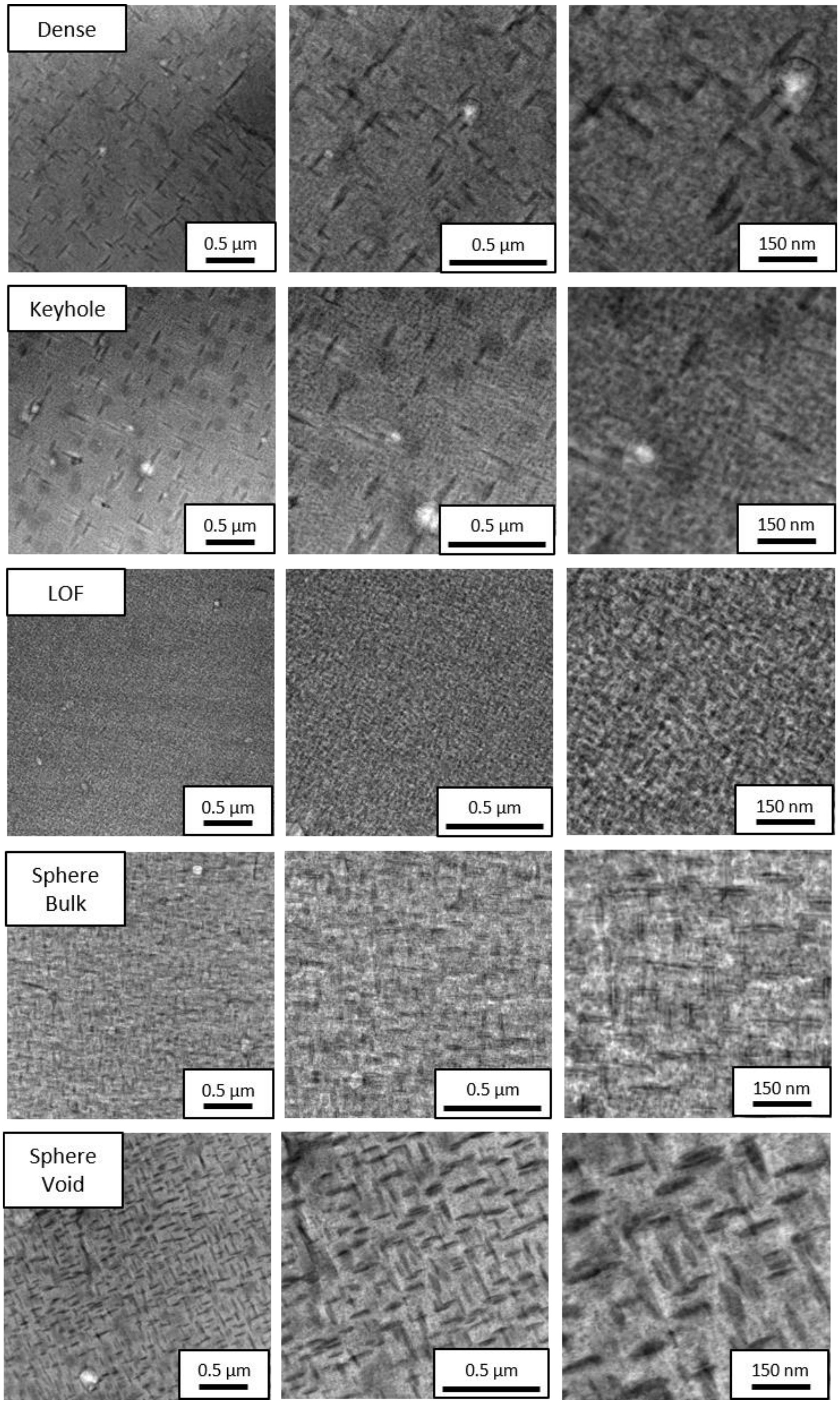

Figure 101: Bright Field STEM images of the precipitate regions found in the recrystallised regions of each sample type. A large difference in precipitate size and distribution is observed between the samples.

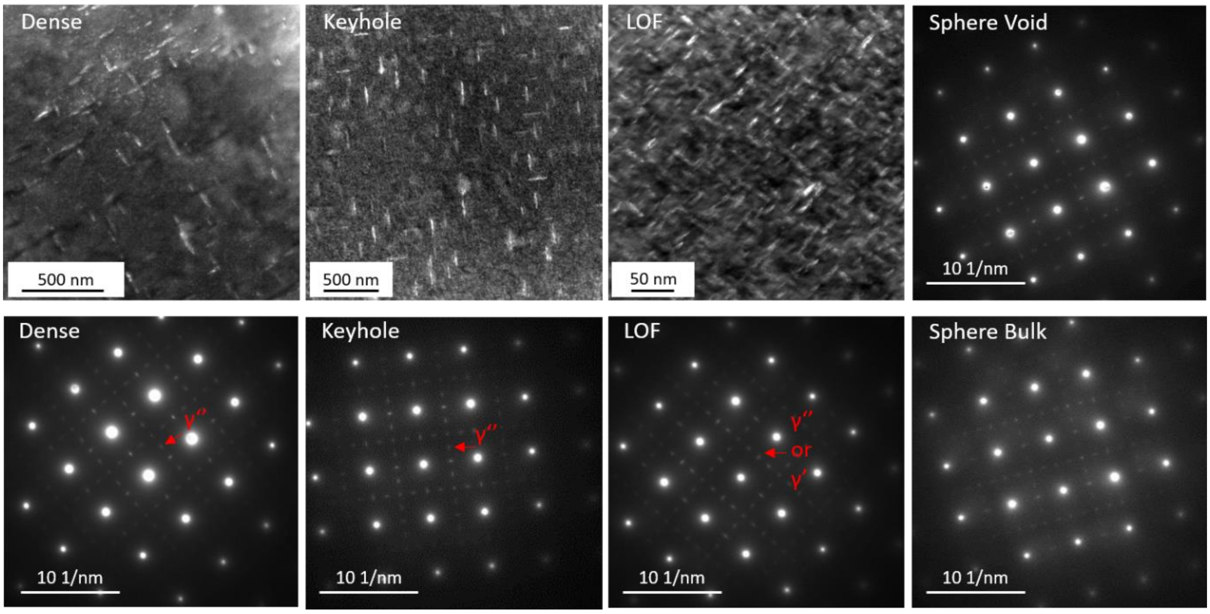

Figure 102: Selected area electron diffraction patterns for all samples along the <100> matrix zone axis showing the clear presence of γ'' precipitates. Arrows on the Dense, Keyhole and LOF diffusion patterns indicate the position of the dark field images for each. There is no clear indication of the incoherent δ phase within the imaged regions suggesting that this phase is not present within the grains.

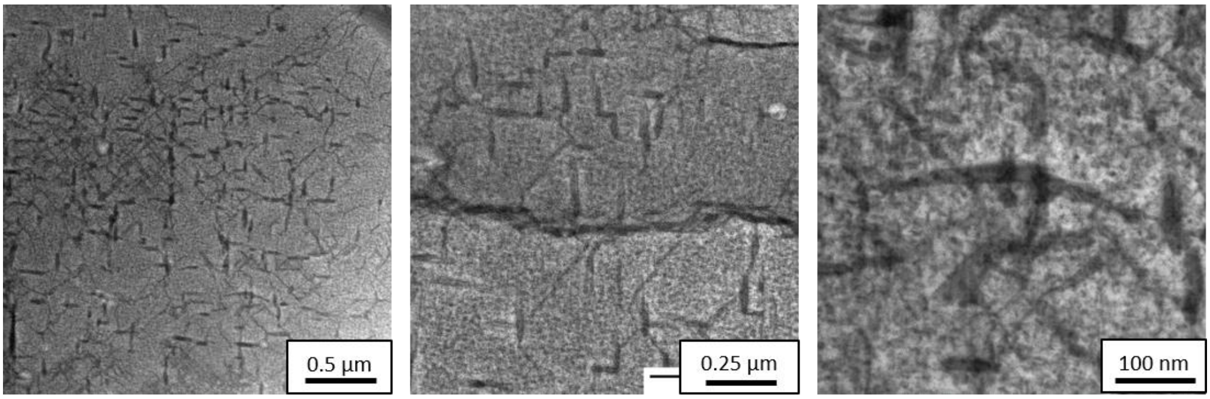

Figure 103: Bright Field STEM analysis of the Dense sample showing the dislocation network surrounding the γ'' precipitates.

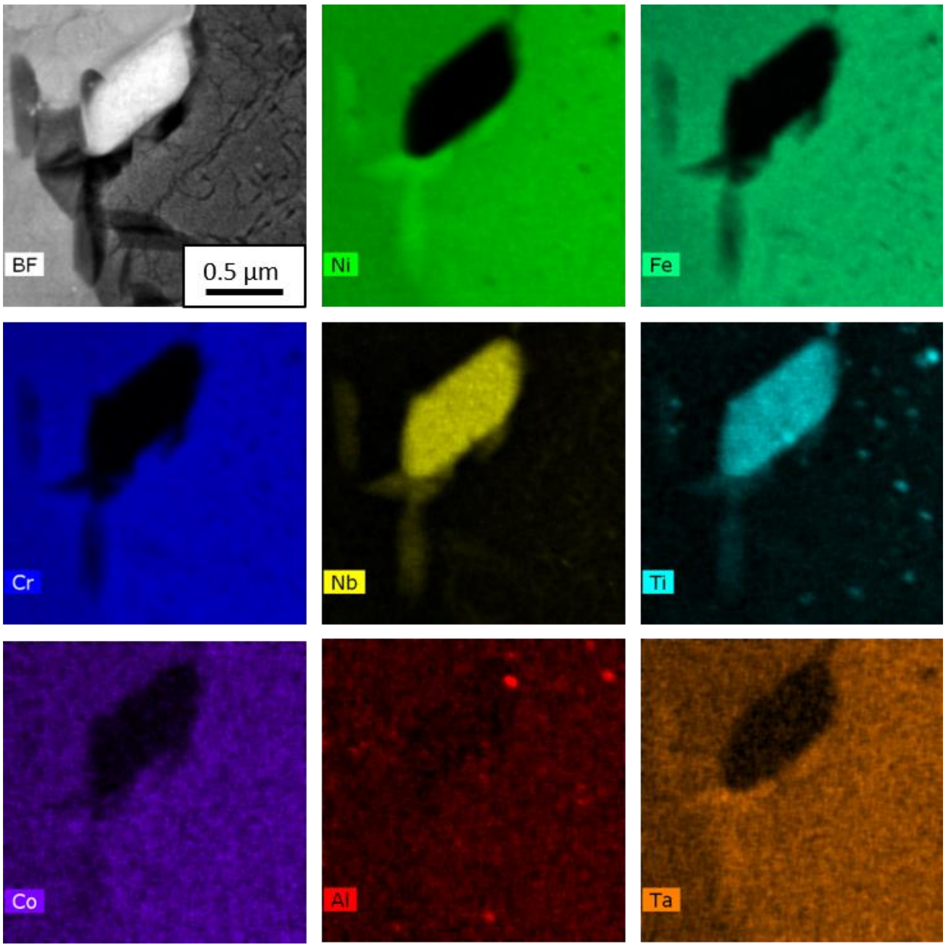

Figure 104: STEM EDS analysis of carbide at grain boundary region of the Dense sample in order to understand the composition and carbide type.

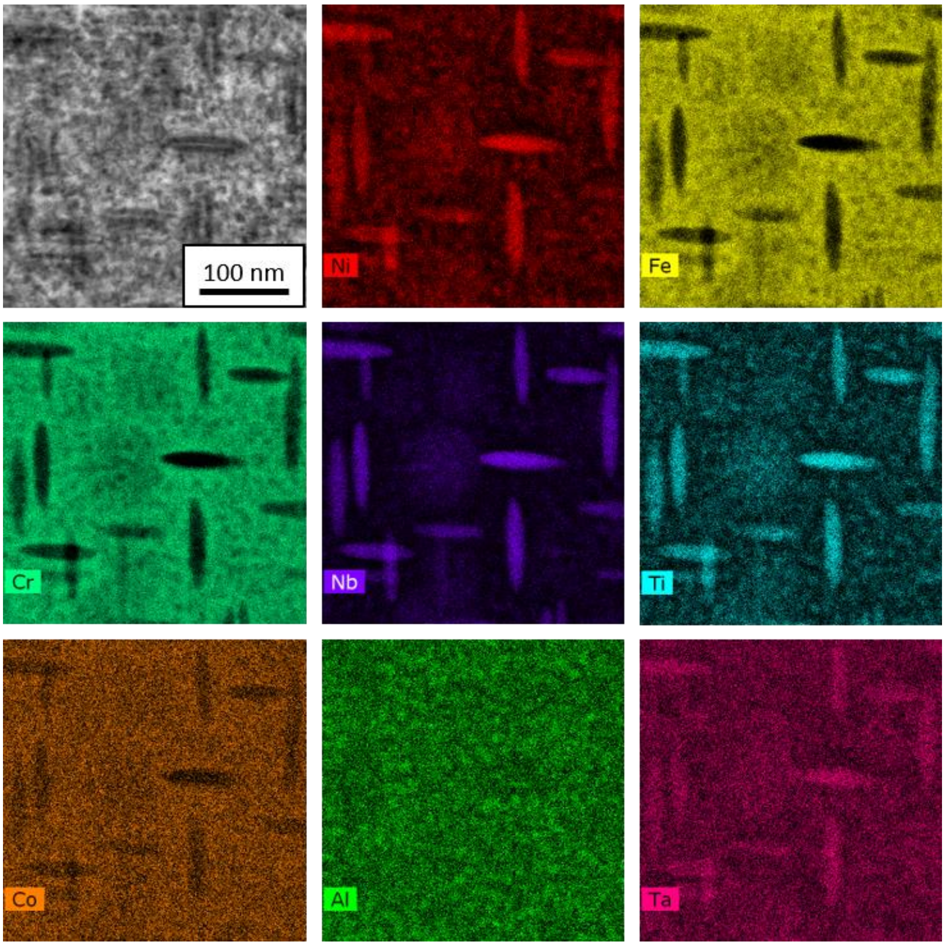

Figure 105: STEM EDS analysis of likely γ'' phase precipitates identified in the Sphere Void region showing enrichment in Ni, Nb and Ti.

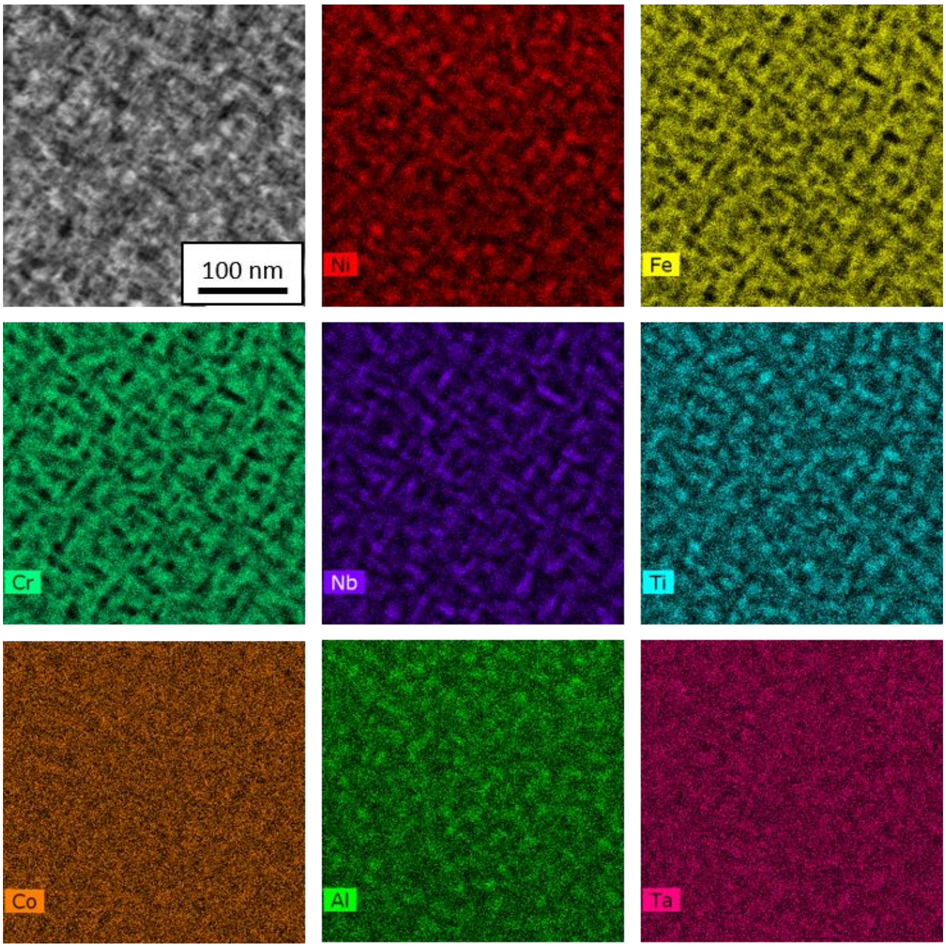

Figure 106: STEM EDS analysis of the LOF matrix showing clear partitioning of the Ni and Nb to ellipsoidal regions.

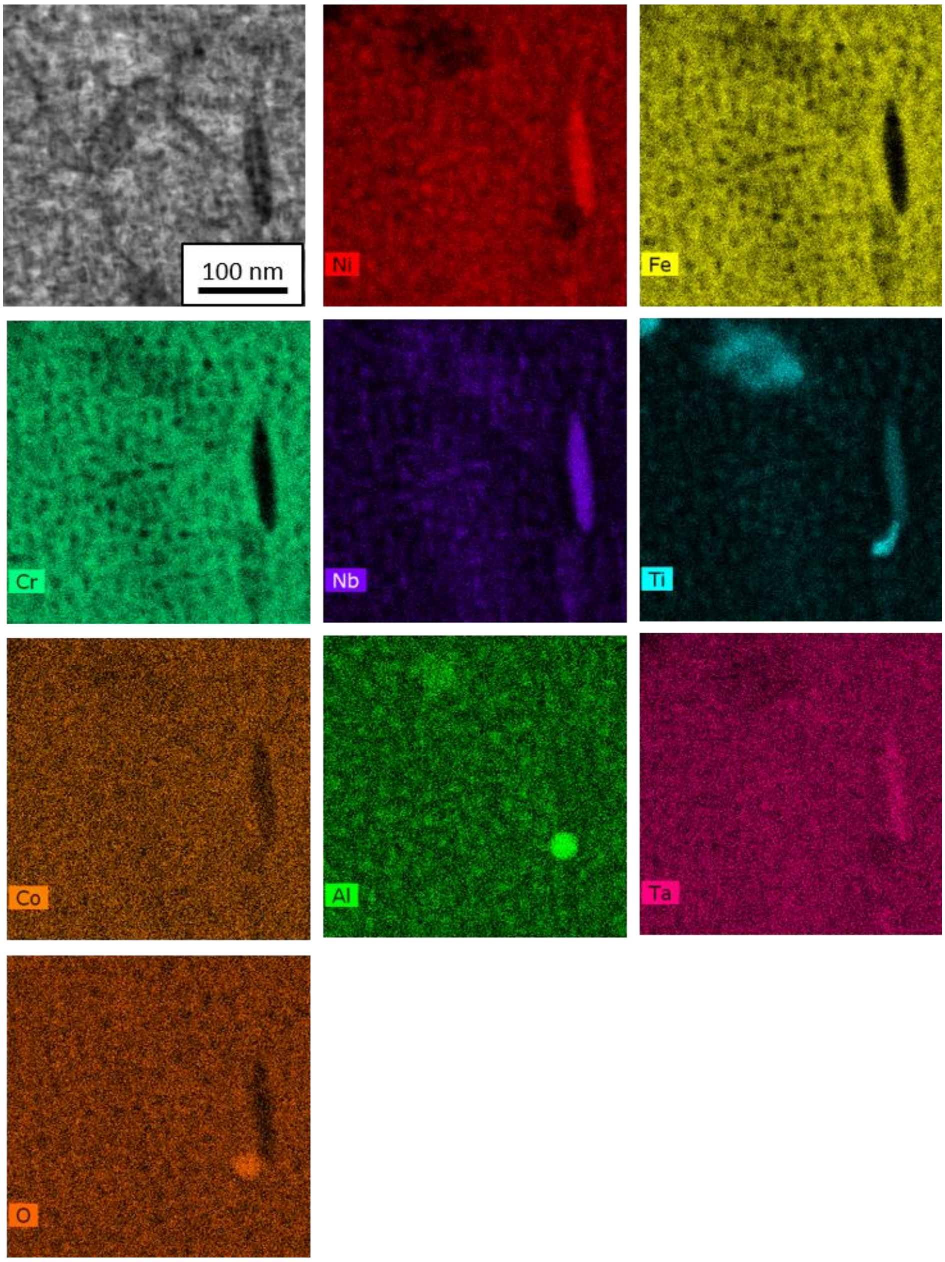

Figure 107: STEM EDS of the Dense sample showing the elemental composition of the γ'' phase, the presence of oxides in the matrix, and elemental partitioning of the background matrix.

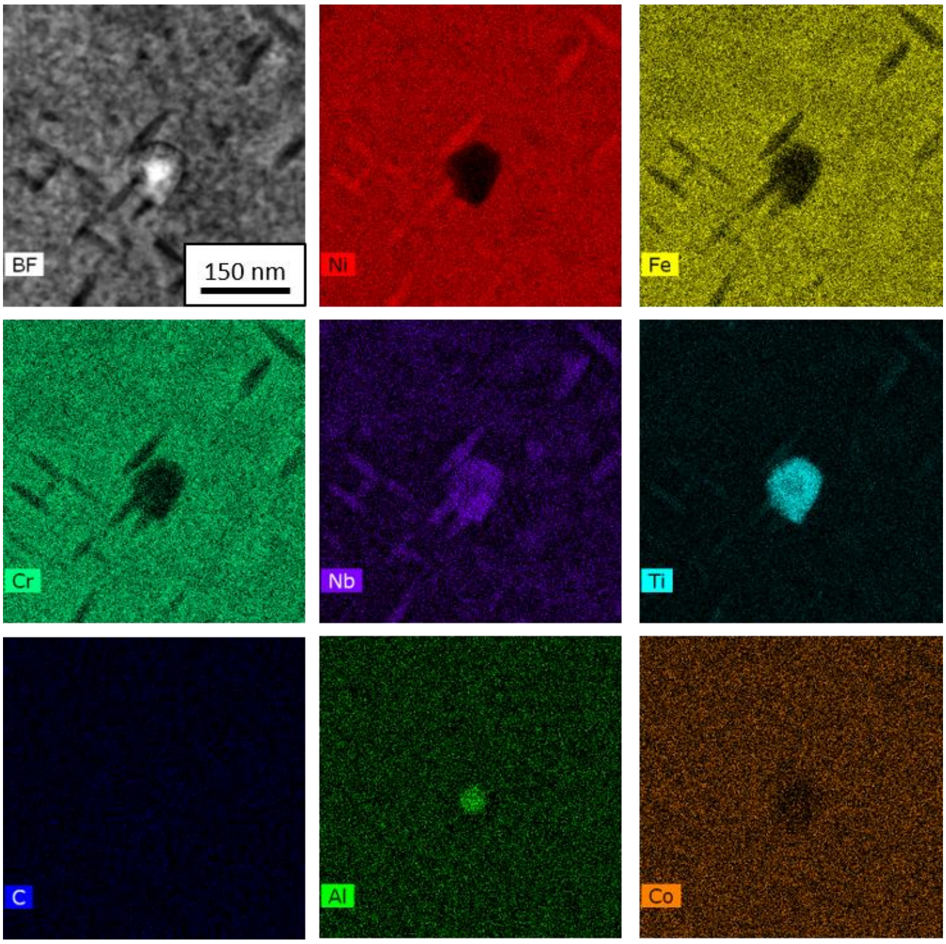

Figure 108: STEM EDS of the Dense sample showing one of the ‘white flecks’ identified from the SEM imaging. Enrichment in Nb, Ti and Al and a depletion in Ni, Fe, and Cr indicate that these are likely not γ’ particles.

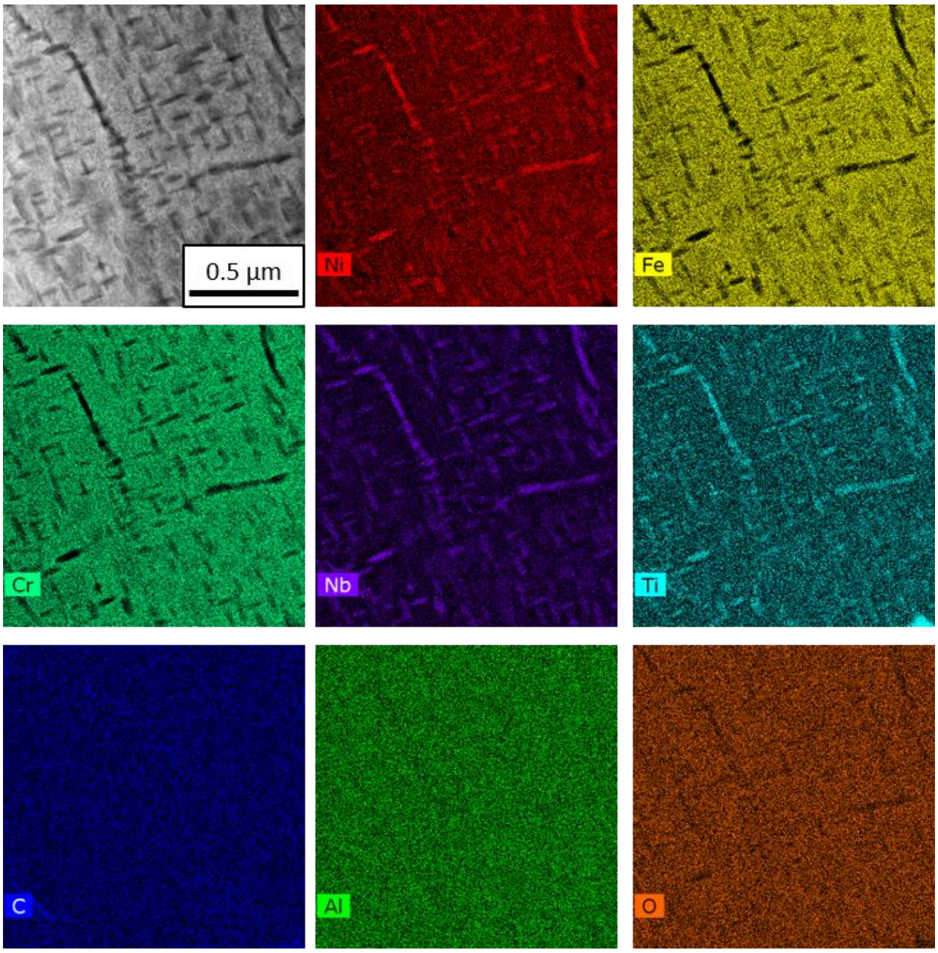

Figure 109: STEM EDS maps of the 'spaghetti' precipitates in the Sphere Void region.

7.3.6 Relationship Between Microstructure and Hardness

The microstructural results presented in this section help understand the hardness values obtained in Chapter 6. The Dense and Keyhole samples on the whole did not recrystallise and therefore retain their strength from the presence of intercellular segregated precipitates and the dislocations which were not completely eliminated by a recovery or recrystallisation process.

It is understood that the recrystallisation process produces softer material properties, however the remaining samples did not show significantly lower hardness values than the Dense and Keyhole samples in the HIP+HT state. This is because the recrystallised samples (excluding the LOF sample) were able to precipitate a high area percentage of strengthening phases from the Nb present in the γ matrix.

Out of all the samples, the LOF and Sphere Void samples obtained the lowest hardness. It is clear that the LOF sample required additional aging time to fully develop the strengthening precipitates. In addition to this, it is possible that the introduction of brittle grain boundary phases and oxides negatively influenced the hardness of both of these two sample regions.

The sphere bulk sample did not contain any of these deleterious oxygen based grain boundary particles. It also contained a high area percentage of γ'' precipitates. However, compared to the Dense and Keyhole samples, the dislocations introduced in the as-built condition were removed by the recrystallisation process. Due to the combination of these effects it makes sense that the Sphere Bulk sample showed a hardness value between that of the Dense and Keyhole samples, and the LOF and Sphere Void, samples.

7.4 Chapter Summary

The fine scale microstructure and precipitate distributions found in each of the samples presented initially in Chapter 6 have been discussed in detail in this chapter in order to understand the similarities in hardness obtained for all samples in Chapter 6, despite the greatly varying grain sizes.

The as-built microstructure in each sample is typical of AM metals; containing cellular structures and segregated material at cell boundaries. The segregated material has been shown to have an increased concentration of Nb, and also contains randomly located carbide particles. The Keyhole sample was observed to contain a larger number of larger carbide particles in the segregated region. The overall cell size for the keyhole sample is also larger than those obtained in the dense, LOF, and sphere bulk sample regions. This is due to the increased time spent at elevated temperature during solidification in this sample.

In the HIP and HIP + HT conditions, the microstructures of each sample deviate. In the HIP samples, as the required temperature conditions for the precipitation of γ'' strengthening precipitates had not been performed yet, these were not present in any of the samples. Instead, large δ phase precipitates and MC carbides of varying sizes line most grain boundaries with evidence of discontinuous precipitation of the δ phase being present in the LOF sample. Due to the lack of recrystallisation in the Dense sample, the δ phase precipitation occurred from the location of prior cell boundaries. All recrystallised grains in the keyhole, LOF and Sphere samples are dotted with the remaining carbide particles which were present in the solidification segregation zones of the as-built state, and were not able to dissolve during the HIP treatment.

Prior discontinuity boundaries in the LOF sample as well as PPB in the Sphere sample are lined with aluminium oxide particles. This is likely due to recycling of the powder and the trial should be repeated using fresh powder that has been stored, since manufacture, under a protective atmosphere to understand if this is the case.

The final heat treatment procedure allowed for the precipitation of γ'' particles to a varying extent in each sample. The LOF sample contained very refined, or not fully formed, γ'' precipitates which is due to under-aging of the sample. This was revealed by STEM EDS mapping of the grain interior. Comparatively, the Keyhole sample contained more sparsely packed, larger (qualitatively speaking) γ'' precipitates in the recrystallised region. As the majority of the microstructure did not recrystallise however, a large area of the Keyhole sample is morphologically similar to that of the Dense sample. The Sphere Bulk region contained a near ideal distribution and size of γ'' precipitation. Whilst the majority of the Sphere Void region also contained a near ideal distribution of γ'' precipitates, small areas contained strips of very densely packed or overlapping γ'' phase which led to depletion of this phase in the directly surrounding matrix. This shows that each sample type requires a different heat treatment aging time after HIP to achieve the optimum precipitate size and distribution.

Therefore, in future work it is necessary to understand the heat treatment procedure required for all sample types in order to achieve the optimum distribution of precipitates in the material. This is dependent on the geometry of the part, and so a part in question is required to further the development of this method for specific applications.

8 Mechanical Properties of Functionally Graded Samples

8.1 Introduction

It has been shown that a wide range of grain structures can be manufactured within a single LPBF build via the combined use of intentionally placed defect distributions and post build HIP processing. The next logical step is to elucidate if variations in mechanical properties can be achieved in samples manufactured by this method. In order to achieve this, simple tensile loading was performed at room temperature on a number of samples. This was performed in combination with DIC analysis in order to view variations in strain across each sample gauge length. As Inconel 718 is commonly used in gas turbine engines, a comparison between the oxidation properties of each HIP microstructure is also relevant and exhibited in this section.

8.2 Tensile Properties

Tensile specimens with intentionally placed regions of dense as-built microstructure, material inclusive of keyhole defects, material inclusive of LOF defects, and regions of unmelted powder located in the gauge length, were subject to HIP and tensile tested to determine the yield stress, ultimate tensile stress (UTS) and elongation to failure. Using these data, a comparison in the mechanical properties of each grain structure could be attained, adding to the hardness observations reported in Chapter 6. It should be noted that all samples and tests presented herein were performed on as-HIP material and not heat treated to simply determine the grain structure and grain interface boundary effects. This was due to the observations made in Chapter 7, that precipitate distributions were not optimised in each sample following the standard heat treatment schedule. Hence, the as-HIP structure was deemed to be a more representative state across samples for comparison.

Further to this, combinations of different grain size distribution regions were placed within the gauge length of the samples to observe the interaction between these under load. This test also enabled further understanding as to the possibility of introducing site specific adjustments in mechanical properties. In this case, Digital Image Correlation (DIC) was used to investigate the strain localisation in each of the samples.

8.2.1 Experimental Methods

8.2.1.1 Tensile Sample Design

Traditionally, dog-bone tensile samples are manufactured in accordance with ASTM E8 [198]. However, it was advised by the machine user in the Lea Lab (University of Sheffield), that the grip regions should be made to 25mm in width, which is larger than that stated in the standard. This was to ensure the sample could be aligned exactly with the machine grips to confirm load transfer through the centre of the gauge length.

In addition to this, the standard advises on the use of samples between 100-450mm in length. This could not be achieved for two reasons. Firstly, the build chamber of the Aconity Mini is approximately 300mm deep. Using a powder supply factor of 2.8-3, the maximum build height is approximately 100mm. Still, during a build of this height, the small powder overfill container reaches maximum capacity which causes powder spillages during cleaning and can cause health and safety issues. Secondly, the ability to alter microstructures in printed materials in the manner outlined in Chapter 6 is a largely new and experimental concept. It has been shown to work for small cylindrical cross sections, whereas here it is required in larger, cuboidal sections. In order to have more confidence in the desired outcome, small internal alternate microstructural regions were produced. Both of these factors led to the design of a tensile bar 62 mm in length.

Because of this, the experiment required the design of a new tensile bar with unique dimensions. SOLIDWORKS 2021 was utilised to design the test bars and the inbuilt Simulation Express Analysis wizard was utilised in order to visualise the stress distribution in a representative fully dense sample. The simulation was required in order to optimise the transition between the grip width and the gauge width to ensure an even stress distribution along the gauge length.

As only a simple simulation was required, the grip region of one end of the sample was fixed as a rigid body while a 200N force was applied to the through thickness face on the far side of the sample. A new material was created within the simulation wizard for Inconel 718 with a Young’s Modulus of 208GPa [270] and a Yield strength of 1.1GPa [271].

A number of iterations were considered, in which the gauge width and filet radii between the gauge section and the grip sections were altered, before the tensile bar with dimensions shown in Figure 110a was produced. The gauge length and width were 12 mm and 6mm respectively. The simulation in Figure 110b shows a uniform stress along the gauge length.

In order to produce recrystallisation conditions as close to those in the cylindrical samples discussed in Chapter 6, the defect regions required encapsulation by a layer of fully dense material. Hence, the samples were overbuilt to the dimensions shown in Figure 110c. This also allowed the removal of the rough as-built AM surface material from the gauge region during post process machining, reducing the probability of sample failure due to elevated surface roughness during testing. One bulk geometry, 15 mm thick, was printed for each microstructural condition, with several 2mm thick tensile samples to be sliced from each part.

Internal defect regions were introduced to the solid tensile bar CAD files using the Boolean logic algorithm on NetFabb Ultimate 2020. These regions were only introduced in the gauge section of the specimens as shown in Figure 111 so to allow the grip areas of each sample to be produced with identical process parameters, leading to equivalent performance in these regions across each sample type. Wall thickness on the bulk sample face was 2mm, and the bulk sample edge was 1mm. These were chosen to prevent deformation to the sample surface (enabling sufficient samples to be cut from each block) whilst allowing some deformation to occur to the sample edge (2mm of which would be removed from each side anyway) to promote recrystallisation within the sample.

Issues with the Aconity Mini at the time of printing led to a number of tensile samples not densifying during the HIP process. Reasons for this will be discussed later. Due to this, a set of 'Batch 2' samples were printed. In these, the bulk geometry thickness was reduced to 8mm, with a wall thickness of 1mm on both the face and edge of the printed sample. Two of each type of bulk sample were printed to allow for a total of four samples per defect type, two from each block. All samples in Batch 1 and 2 were printed vertically to make most efficient use of the build plate.

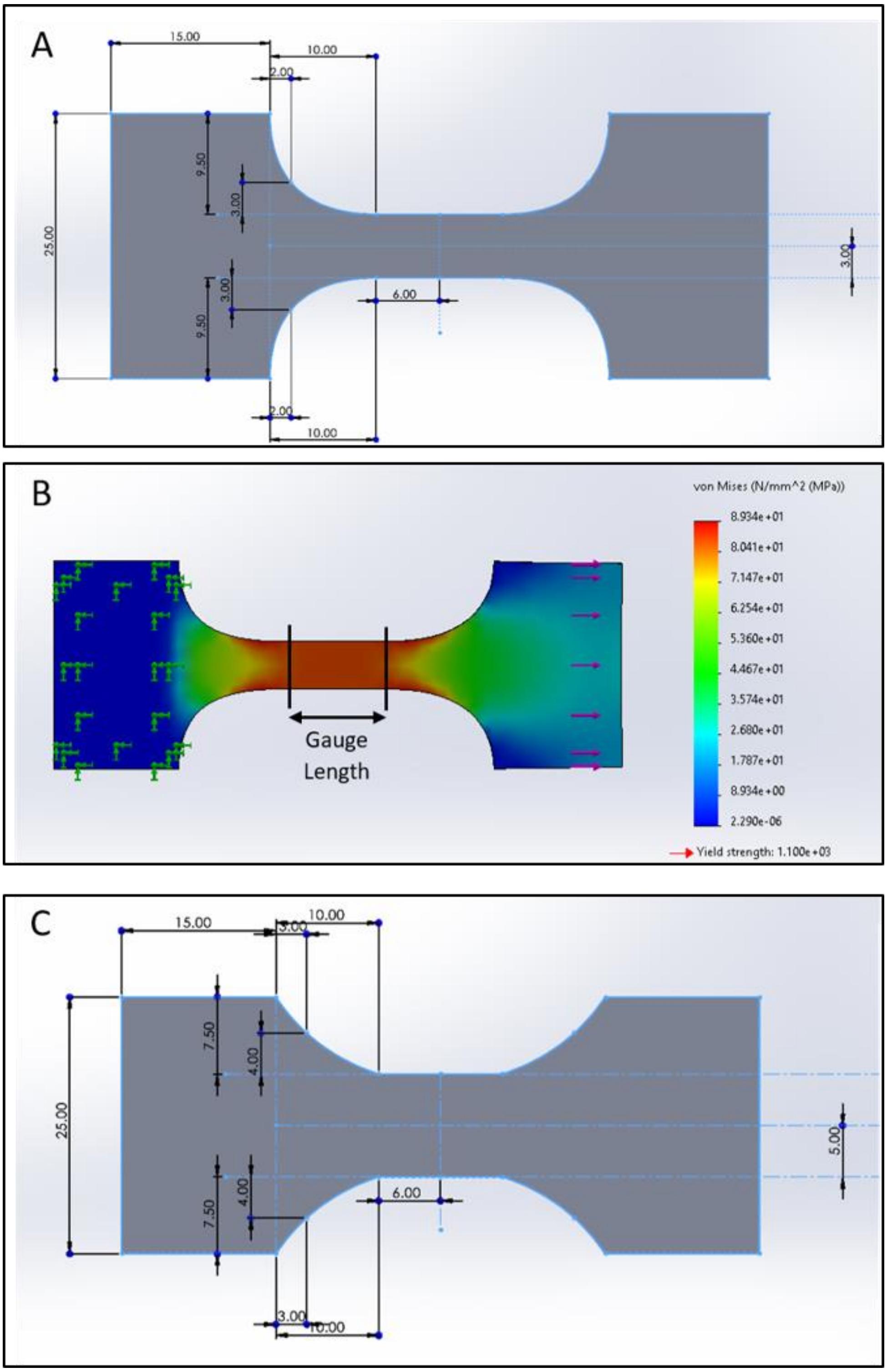

Figure 110: A: Final dimensions of tensile sample designed for experimental investigation; thickness to be 2mm, B) Solidworks Simulation Express Wizard analysis of stress distribution along the gauge length showing even distribution along gauge, C) dimensions of the tensile bar to be printed, allowing excess material for the removal of rough surface edges and dense walls encapsulating the defect regions.

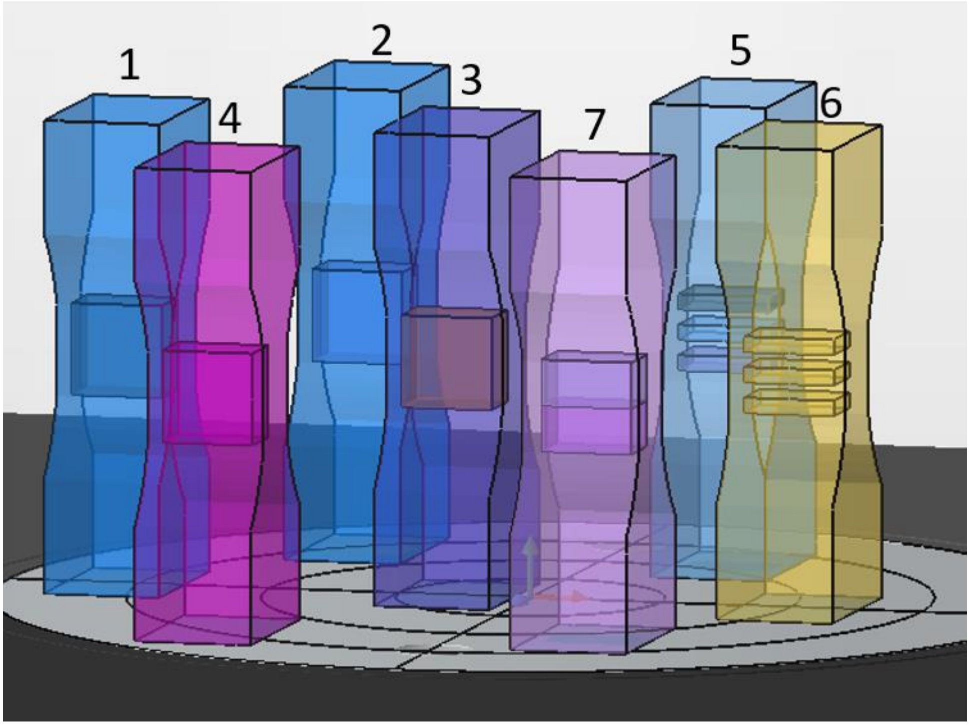

Figure 111: Schematic view of internal defect regions for each sample showing that the grip sections of each sample were produced to be identical in nature.

As part of Batch 1, seven different sample types were produced. The first four, samples 1 – 4, as labelled in Figure 111, comprised of a full gauge length containing one of the following as-built microstructures; dense material, material including keyhole porosity, material including LOF porosity, and unmelted powder. Regions containing unmelted powder will from here on called ‘sphere’ to link them to the initial experiment in Chapter 6. The dimensions of these sections were 12x12x8mm, with the 8mm dimension being the width across the gauge length. This is 2mm larger than the designed gauge width of 6mm which ensured that only the engineered microstructures would be present in the gauge section after machining.

The other three samples contained mixed regions of a combination of different defect types. Sample 5 contained an internal pattern of LOF – Loose Powder – LOF, with each section being 12x2x8mm, separated by 2mm of dense material. Sample 6 contained three loose powder sections 12x2x8mm in dimensions, separated by 2mm of dense material. Sample 7 contained a LOF section followed by a dense section, each section taking up half of the gauge length, with a dimension of 12x6x8mm each.

As part of Batch 2, the first four samples from Batch 1 were repeated with smaller internal dimensions of 12x6x8mm. All sample information and the code to each sample IDs is presented in Table 20.

Table 20: Details of naming system for each tensile sample.

Batch Number	Sample Type	Description of Sample Type (Internal microstructure in As-Built state)	Sample ID
1	**1**	Dense (control)	1D_(1 – 6)
1	**2**	LOF	1L_(1 – 6)
1	**3**	Keyhole	1K_(1 – 6)
1	**4**	Loose Powder	1S_(1 – 6)
2	**1**	Dense (control)	2D_(block number 1 or 2, (1-4))
2	**2**	LOF	2L_(block number 1 or 2, (1-4))
2	**3**	Keyhole	2K_(block number 1 or 2, (1-4))
2	**4**	Loose Powder	2S_(block number 1 or 2, (1-4))
1	**5**	Dense - LOF – Dense - Loose Powder – Dense – LOF - Dense	1LDS_(1 – 4)
1	**6**	Loose Powder – Dense – Loose Powder – Dense – Loose Powder - Dense	1SDS_(1 – 4)
1	**7**	LOF – Dense	1LD_(1 – 4)

8.2.1.2 Sample Manufacture and Heat Treatment

Samples were built on an Aconity Mini using laser parameters displayed in Table 21. Note that the parameters for the Keyhole sample are those used to produce the Higher Power Keyhole cylinders in Chapter 6.

Table 21: Laser parameters used to print the internal region of each tensile bar.

Sample Type	Laser Power (W)	Laser Velocity (mms^{-1})	Hatch Spacing (μm)	Layer Thickness (μm)
Dense	130	850	75	30
Keyhole	170	500	42	30
LOF	94	1118	108	30

Samples were removed from the baseplate and subjected to HIP using identical conditions to those previously used and outlined in Chapter 6 (1160^{o}C / 102MPa / 3 hours / air cool, with a temperature ramp up rate of 10°C/min). Each bulk section was then machined to 2mm thick sections by wire EDM. The top and bottom 2mm slices of each part were discounted to ensure that the remaining four slices contained only the intended microstructure. The surface of the gauge region of one of each sample type was prepared for optical microscopy using the standard metallographic preparation techniques. For SEM, samples were electro-etched with phosphoric acid as described in section 3.5.2.

8.2.1.3 Tensile Testing

Tensile samples to be analysed using Digital Image Correlation (DIC) were coated with a white spray paint coating followed by the production of a black ‘speckle’ pattern using standard aerosol paint cans in a fume extraction hood. Figure 112 shows an example speckle pattern achieved using this technique as captured by the DIC camera set-up.

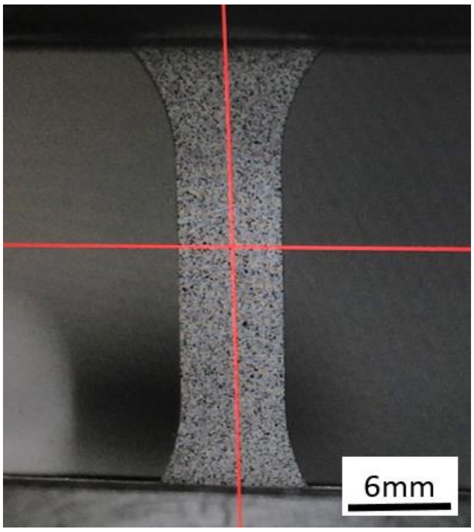

Figure 112: Tensile sample coated with speckle pattern and loaded in to the grips of the extensometer as captured by the DIC camera. Cross hares enable sample to be aligned with the camera.

The 2D DIC apparatus was set up as shown in Figure 113. Experimental assistance was kindly provided by Zilei Chen (PhD Student in Mechanical Engineering). A high resolution CCD camera was focused on the sample surface such that the camera cross hares lined up with the centre of the sample gauge. This was achieved by adjusting the height of the camera mount. Spirit levels were utilised to ensure the camera mount was parallel to the floor and that the camera was perpendicular to the sample surface. Final focusing was performed by adjusting the camera lens to ensure the speckle pattern was in perfect focus. Two standard lights were placed either side of the camera at the same height as the sample in order to illuminate the speckle pattern as well as prevent any shadows forming on the sample surface. Image capture was set up to record an image every second during the test.

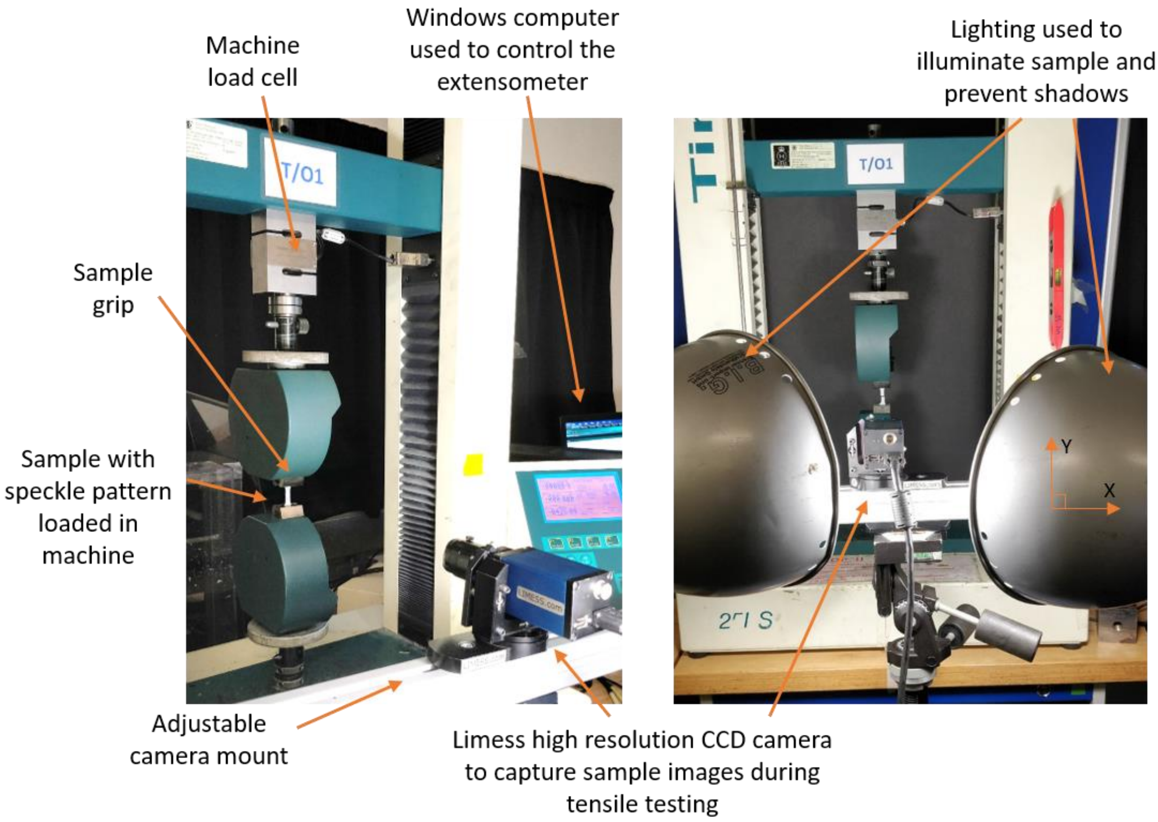

Figure 113: Tensile testing and DIC camera experimental set-up showing positions of lighting and camera with respect to the tensile testing machine loaded with a sample.

Tensile testing was performed using a Tinius Olsen 25ST benchtop universal testing rig with a maximum force of 25kN. The HW20 self-tightening wedge grips were secured to the machine using a hole and pin attachment system after which a screw thread was used to tighten them in place, preventing rotation during testing. The grips were aligned to one another using a ruler and spirit level prior to testing.

The Tinius Olsen machine was controlled using the Horizon software package installed on a local computer and linked to the extensometer. Output data from this comprised of force and elongation information along with an associated time stamp. The test crosshead speed was set to 0.01mm/s (resulting in a strain rate of 0.05mm/min) in accordance with ASTM E8 [198], and similar to [272]. All samples were tested to failure.

8.2.1.4 Strain Analysis by Digital Image Correlation (DIC)

DIC data from the 12mm long gauge length of each sample was analysed using VIC2D, version 7. DIC data was only analysed from the 12mm long gauge length of each sample. A mesh subset size of 17, step size of 4, and post process filter of 7 was used in the analysis of all images to ensure all data was comparable. A decay smoothing filter of between 9 and 15 was used after strain calculation in order to simplify the strain maps. The only exception to this is sample 1SDS_4 which, due to the poor speckle obtained after spraying, required a mesh subset size of 27, and a step size of 6 to obtain accurate strain results.

Output data from this comprised of average pixel movements in the X and Y direction, average axial strain in the X and Y directions, and average shear strain in the XY direction. Of these, the axial strain values in the loading direction (Y) were solely utilised for analysis. In addition to this, strain maps for each tensile sample at every second during the test were obtained to allow the evolution of strain to be visually interpreted. Strain distribution maps just before and after fracture were qualitatively compared.

8.2.2 Results and Discussion

8.2.2.1 Sample Manufacture

Due to a maintenance issue with the Aconity, the protective argon flow was disrupted to an unknown extent during the build of the Batch 1 samples. This issue only became known during investigative work after printing in order to understand the high levels of melt pool spatter during the build and the subsequent surface roughness on each of the built samples. It has previously been discussed that spattered particles obstruct the deposition of an even powder layer during the building of subsequent layers, and therefore can result in internal porosity.

Upon surface investigation of the polished tensile samples in Figure 114 the internal porosity was found to be present in the grip regions of sample types 1, 2, 3 and 7. As the grip regions were not printed using a contour, and so contained pathways in which air could get inside the sample, pressure equalisation occurred during HIP and these regions remained porous after HIP.

All of the internal sections recrystallised and became fully dense after HIP with the exception of the LOF regions in sample types 2 and 7 (the LOF region in sample 5 did fully recrystallise). The volume of the LOF defect region was the main difference between sample types 2 and 7, and sample 5. This recrystallisation discrepancy could be a side effect of the significant levels of spatter observed during building, with sample type 5 observing the lowest effects of spatter. The increased surface roughness produced in the presence of spatter may have led to surface reaching interlayer gaps, preventing adequate pressure in the defect region to enable recrystallisation.

The loose powder section in sample type 4 sintered in to a nugget, however did not adhere to the inner wall of the sample. However, the loose powder section in sample types 5 and 6 did recrystallise in to a fully dense microstructure within the tensile bar gauge region. The assumed large internal space produced as a result of powder packing in sample type 4 after build completion is believed to be the cause of this lack of densification.

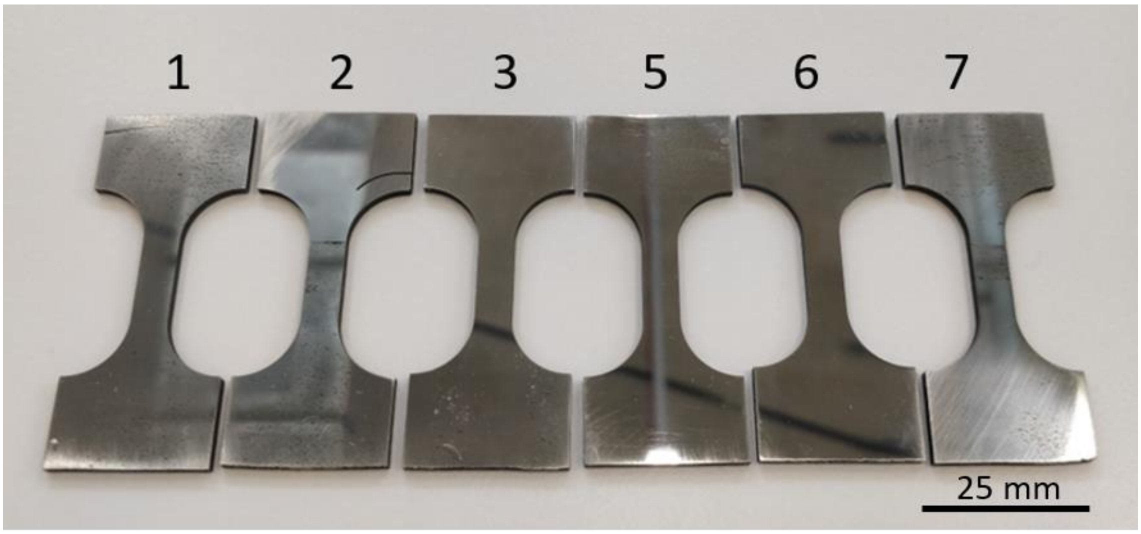

Figure 114: Completed Batch 1 tensile bars. The extra cut in the grip region of Sample 2 is due to a machining error.

Of the Batch 2 samples, only the sample types 1 and 3 fully densified. The samples containing LOF defects and loose powder did not recrystallise and could not be tested. It is possible that the rectangular shape of the internal region prevented an even amount of deformation from occurring within the whole defect region, resulting in a lack of recrystallisation in the samples that contained the more porous as-built microstructures.

Overall, of the Batch 1 samples, sample types 3, 5, and 6 were able to be tested, and of the Batch 2 samples, sample types 1 and 3 were able to be tested. Where results of individual samples are provided, they are labelled according to the key in Table 20.

8.2.2.2 Sample Microstructure

Figure 115 shows optical micrographs of the gauge region of the type 1 and 3 samples from Batch 1 as well as SEM micrographs of these samples from Batch 2. Regardless of which batch the samples were produced in, there is an evident difference in grain size between the two sample types. The type 3 samples, produced using parameters in the Keyhole melting regime, have a larger recrystallised grain size compared to the samples produced using laser parameters optimised for a fully dense build. It should be noted that in Chapter 6, the Dense sample cylinder did not recrystallise. It is believed that differences in the build geometry (spherical vs cuboidal inclusive of more 90^{o} corners), and size between the two experiments led to the differences in the lattice strain and recrystallisation kinetics, enabling the dense material to recrystallise here. The Batch 2 samples look to have a slightly larger grain size than the Batch 1 samples. This is presumed to be due to the overall smaller sample bulk size, providing a shorter laser return time and keeping the layer slightly warmer during processing.

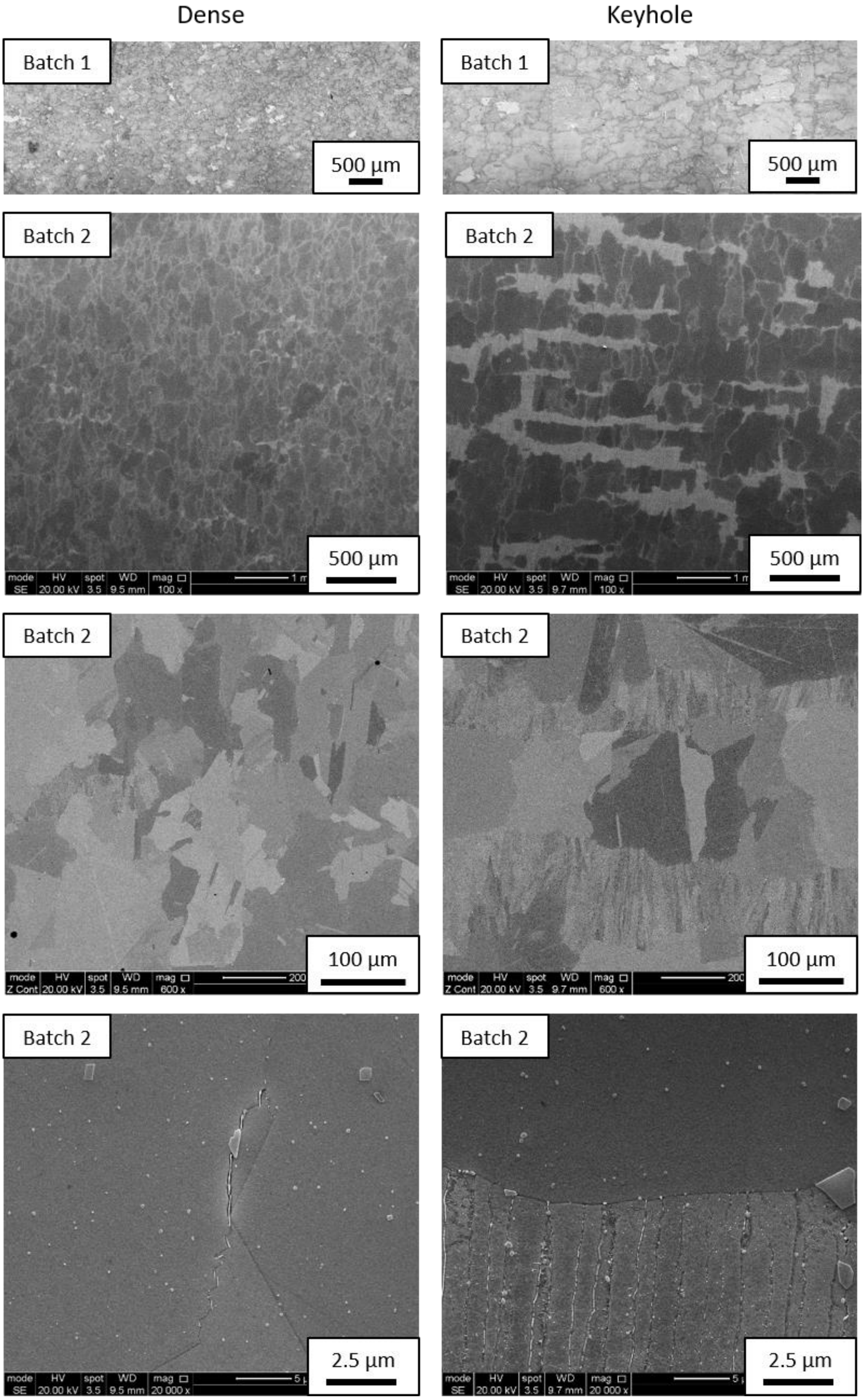

Figure 115: Optical micrographs of the gauge region of the Dense and Keyhole samples from Batch 1 and SEM micrographs from the same samples produced as part of Batch 2.

Large regions of the Keyhole sample produced as part of Batch 2 did not recrystallise, producing a striped microstructure of alternate regions containing stress free grains and as-built microstructure. This was not identified in the Batch 1 samples, showing that differences in the bulk sample size plays a large role in the recrystallisation kinetics attained in each sample.

The gauge lengths of the type 5 and 6 samples are shown in Figure 116. It is clear that the LOF regions that were built into the type 5 samples are no longer differentiable by grain size from the originally dense regions. Instead, the microstructure away from the central powder filled strip is fairly equal in size. This shows that the use of relatively thin neighbouring regions of dense and LOF material in the as-built state may only result in a narrowly differing grain structure to be obtained after HIP. It is possible that differences in texture, high and low grain boundaries, or twinning fraction, exist between these regions.

Comparatively, a clear interface exists between the dense region and the originally powder filled region in both type 5 and 6 samples. The insets show a higher magnification optical image of the central powder filled region showing the abruptness of the grain size change. It is positive that the grain sizes of the dense and sphere regions in each inset are comparable across both sample types as the central position of each gauge length should be identical for these two sample types.

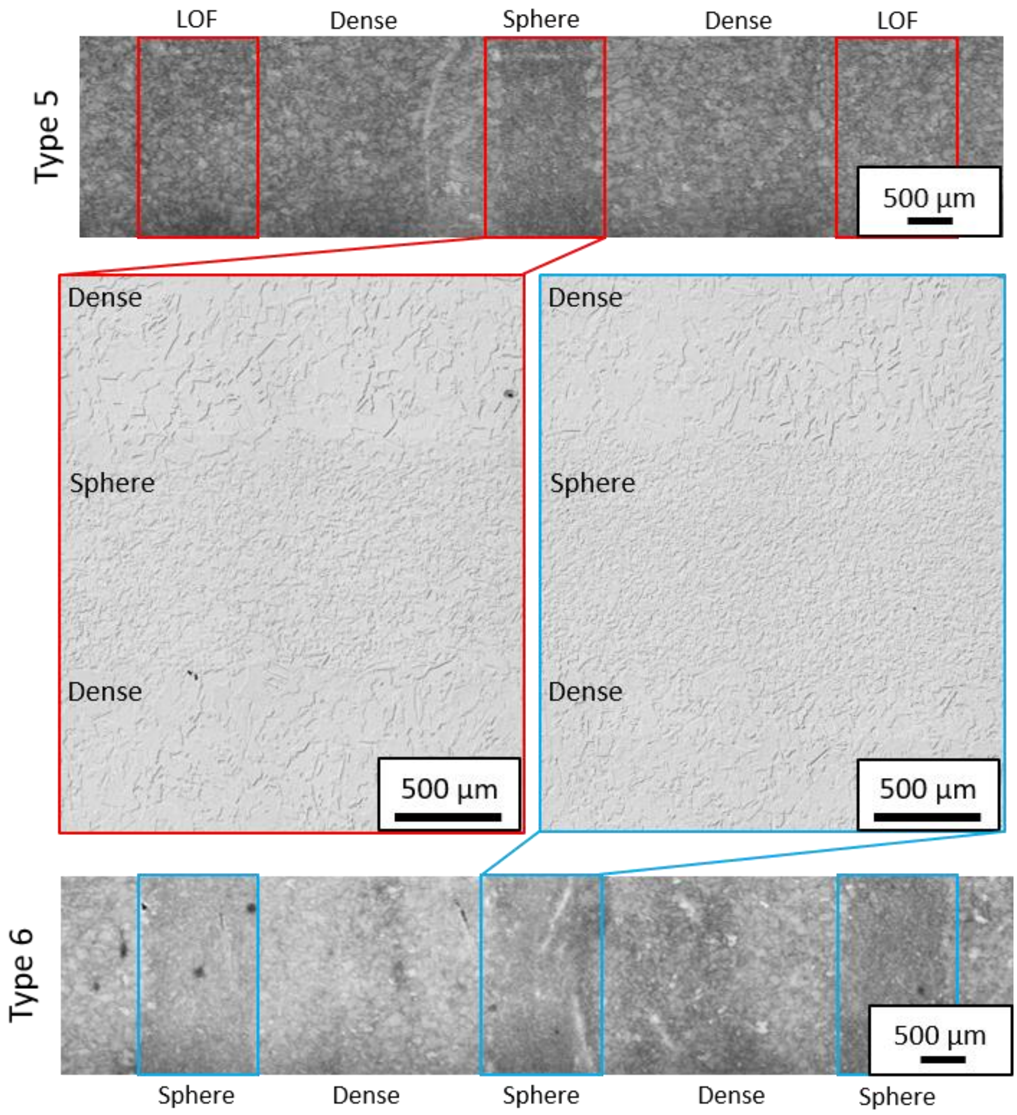

Figure 116: Optical micrographs of the etched gauge lengths of the type 5 and 6 tensile samples. The insets show the centre of the gauge region for each. A clear band of finer grain sizes can be observed in each sample, with the material surrounding this being visually equivalent in each.

8.2.2.3 Tensile Testing

Tensile Test Data

The ultimate tensile stress (UTS), yield Stress, and tensile elongation (as measured from the extensometer) was averaged over each sample type. The results are summarised in Table 22, and shown graphically in Figure 117. Figure 118 provides the raw stress/strain data for each sample tested. In Figure 118, the batch 1 keyhole samples are denoted by a dashed line to provide visual separation between the batch 1 and batch 2 keyhole samples.

Table 22: Summary data for tensile tests showing the average UTS, yield strength and tensile extension for all samples tested of each condition. Errors shown are standard deviation

	Batch 2 Dense	Batch 2 keyhole	Batch 1 Keyhole	Batch 1 LOF / Dense / Sphere	Batch 1 Sphere / Dense / Sphere
UTS (MPa)	907.6 ± 7.7	850.7 ± 7.8	879.5 ± 16.5	813.0 ± 54.2	789.4 ± 27.6
Yield Strength (MPa)	530.0 ± 10.0	513.3 ± 5.8	566.7 ± 23.1	600.0 ± 34.6	630.0 ± 10.0
Tensile Extension (mm)	9.4 ± 1.5	8.2 ± 0.5	7.9 ± 0.8	4.2 ± 0.7	3.8 ± 0.2

None of the samples underwent visible necking during testing which can also be evidenced by the lack of reduction in stress before failure for all samples shown in Figure 118. Therefore, the UTS was determined by identifying the maximum stress achieved through the sample prior to failure. The yield stress was taken by measuring by eye, the point at which the line deviated first from linear. All samples underwent hardening during yield, making the determination of the point of inflection difficult. The maximum extension refers to the largest value of displacement observed by the extensometer crosshead during each test. This includes any strain experienced by the sample away from the gauge length as well as in the extensometer system. The strain observed only within the gauge length is presented in the next section.

The type 1 and 3 (full gauge length of dense or keyhole as built material) samples obtained the highest UTS and extension at failure, with the dense sample attaining slightly higher values at 907.6MPa and 9.4mm respectively. This is compared to 865MPa and 8.0mm for the average of all the type 3 keyhole samples over batch 1 and batch 2. The tensile extension of these two sample types lay within error.

The samples that included stripes of alternating microstructure attained values of UTS and tensile extension of 813MPa and 4.2mm respectively for type 5 LDS samples and 789MPa and 3.8mm respectively for type 6 SDS samples. These values are similar within their respective error values. This suggests that the UTS and corresponding extension in these samples is likely determined by a similar microstructural region, for example, either the fine grained region, or the interface between the fine and coarse grained region.

These results show the increased ability for the Dense and keyhole samples to accumulate plastic deformation during extension prior to failure. It is likely that this result is due to the ability of these samples to extend in a uniform manner over the full gauge region, whilst this was not possible in samples that contained alternating microstructures. The fine grained regions in these samples will also have reached their maximum dislocation pile-up density achievable prior to fracture at lower levels of plastic deformation than the coarse grained regions.

These results are reflected in the overall stress vs strain graph in Figure 118. The rate of work hardening, which is given by the gradient of the slope after yield, is fairly similar for all of the sample types which is expected as the underlying material chemistry of each sample is still the same, only the grain size has been altered.

These samples were manufactured to be of custom size as they were experimental in nature and therefore should be compared to standard AM Inconel 718 properties with caution. The yield strength and UTS of as-built Inconel 718 is approximately 550MPa and 1000MPa respectively, according to Raghavan *et al.* [179] who tested seven samples across a range of different build orientations between 0^o and 90^o. The results presented in this thesis are therefore comparable to those observed in the literature. In future studies, the tests outlined in this chapter will be brought to full scale tensile tests to determine a comparative value for the tensile properties of each microstructure type. In this case, testing was performed to identify if variations in strain were obtainable within a single sample using the AM printing and HIP technique presented in Chapter 6.

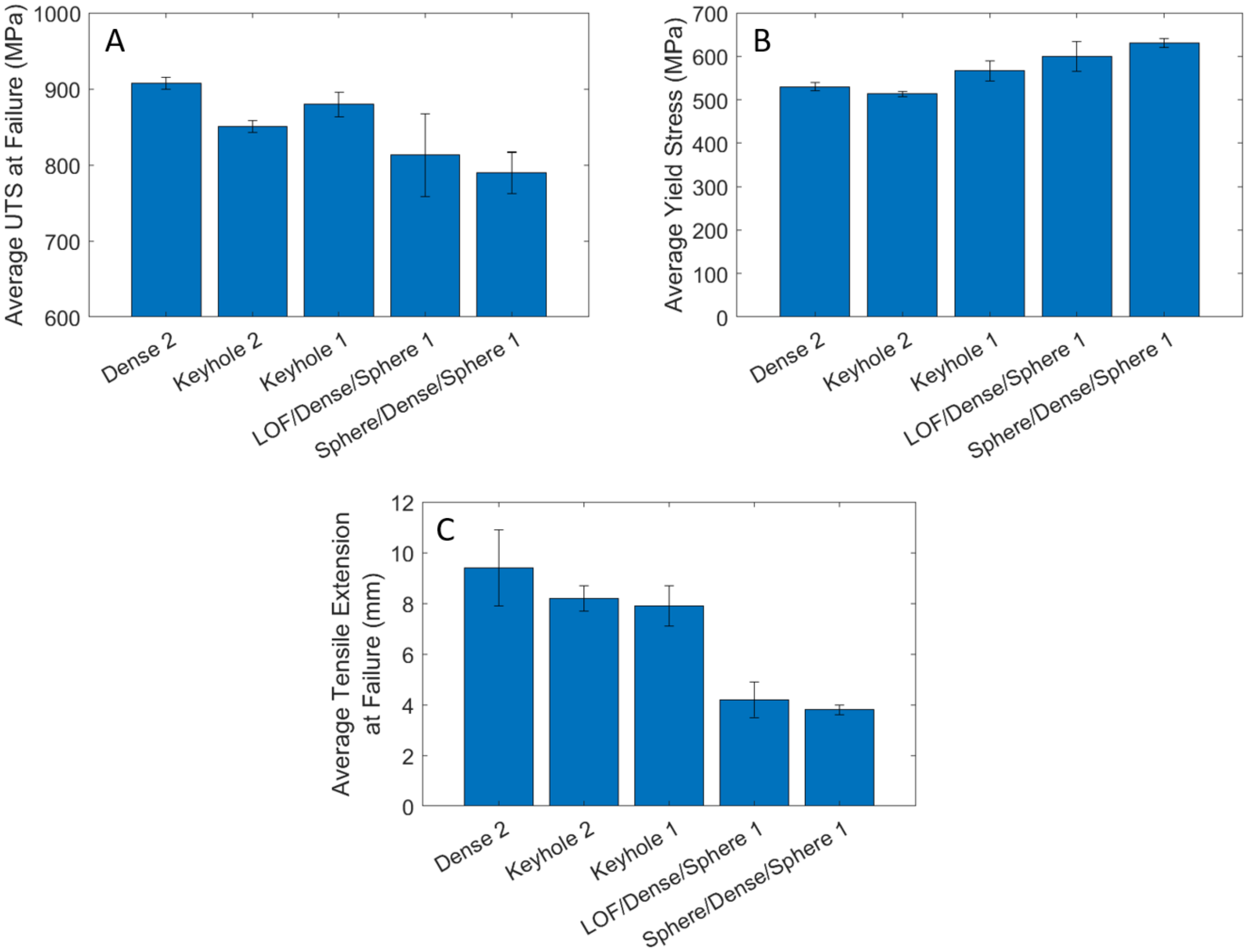

Figure 117: Summary of tensile test data for each sample type, a) ultimate tensile strength, b) Yield Stress, c) Tensile Extension of test machine. All show the average values for each test condition. The number after each bar title denotes the batch from which the samples were prepared from. Errors are given as standard deviation.

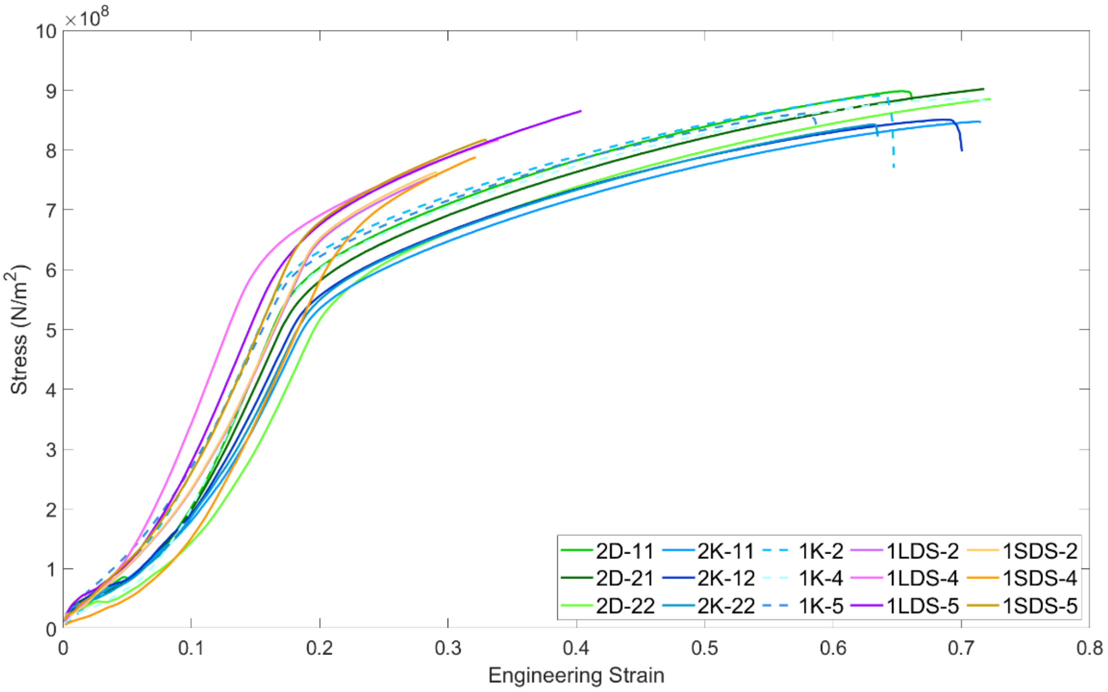

Figure 118: Stress/Strain graph for all samples tested. Samples are named according to Table 20. 2D-11 means batch 2 dense sample, block 1, sample 1. 2K-11 means batch 2 keyhole sample, block 1, sample number 1. 1K-2 means batch 1 keyhole sample, sample number 2 (all batch 1 samples were taken from a single block of material). 1LDS-2 means batch 1 (sample number 2) mixed microstructure sample containing LOF, dense and powder filled regions prior to HIP. 1SDS-2 means batch 1 (sample number 2) mixed microstructure sample containing alternating regions of loose powder and dense material prior to HIP.

Digital Image Correlation Numerical and Mapped Strain Data

Figures 121-125 show the DIC axial strain (eyy) maps in the loading direction for each tensile bar along with an image of each fracture surface. Each figure contains all the sample repeats from each sample type. Table 23 contains the average data for the minimum, maximum, average, and standard deviation of the all the axial strain values in the loading direction for each type of sample as calculated by the VIC2D software. The average mean axial strain data tabulated in Table 23 is shown in Figure 119 for visual interpretation. Figure 120 shows a comparison of the Min, Max, Mean and Median axial strain values for each individual sample.

Table 23: Strain values in the loading direction for each sample type averaged over all samples tested for that sample type.

Sample Type	Defect	Average Min Strain	Average Max Strain	Average Mean Strain	Average Sample Strain Standard Deviation
1 (Batch 2)	Dense	0.26	0.53	0.40	0.04
3 (Batch 2)	Keyhole	0.16	0.51	0.35	0.04
3 (Batch 1)	Keyhole	0.06	0.58	0.35	0.05
5 (Batch 1)	LDS	-0.01	0.28	0.11	0.01
6 (Batch 1)	SDS	0.05	0.17	0.08	0.02

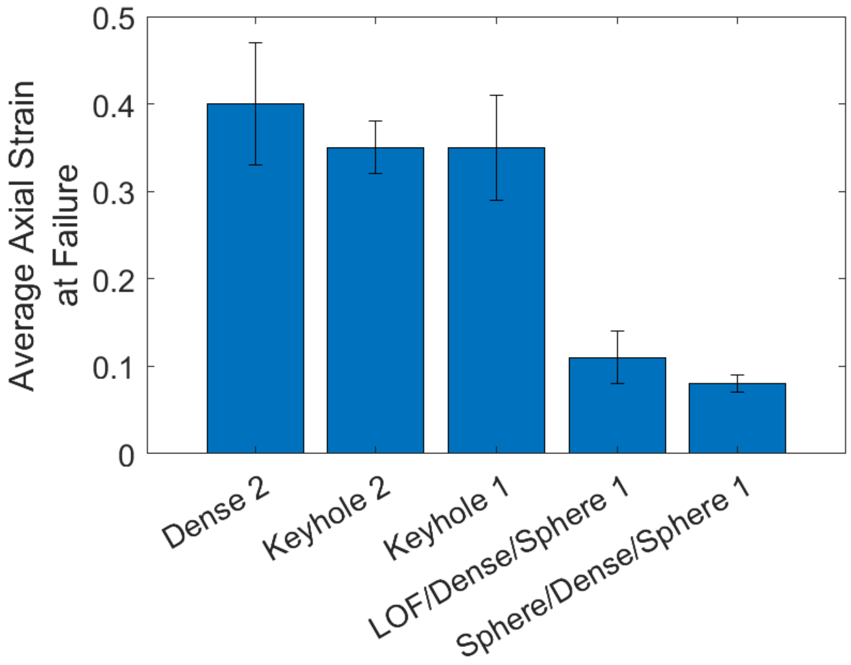

Figure 119: Bar graph showing the data for average axial strain at failure obtained from the DIC data over the gauge length of each sample only.

The Dense sample type attained the highest average mean axial strain at 40%, however this was only 5% higher than in the Keyhole sample type. The type 5 and 6 samples achieved much lower average mean strain values, at 11% and 8% mean strain. This trend is in agreement with the results from the extensometer.

It is clear that the average mean axial strain for the Batch 1 and Batch 2 Keyhole samples is identical to 2 significant figures. As these were produced as part of different builds, and therefore each had different laser return times and layer build times, this is a positive outcome as it shows that similar properties can be obtained from non-identical build geometries. Again, this result is in agreement with the tensile elongation data obtained from the extensometer Horizon software.

In the micrograph shown in Figure 116, there is a visible lack of a transition zone between the LOF and Dense regions in sample type 5 (LDS). This sample only observes two sharp microstructural transitions, these being between the Dense and loose powder regions in the centre of the gauge length. Contrary to this, the type 6 samples (SDS), visibly show six microstructural transitions. It is believed that the type 5 samples were able to achieve a higher mean strain of 28%, compared to 17% in the type 6 samples, due to the larger area present exclusive of a microstructural transition zone.

The average minimum strain in the Batch 1 type 5 (LDS) samples is a negative value. This is due to the negative strain value observed in one of the samples, 1K-4 and indicates the presence of a compressive strain. As these values are averaged pixel values over the whole map, and it was difficult to perfectly align the sample in the oversized grips, it is possible that a small shear component was present during the test, leading to a local compressive strain. Additionally, although the test grips were aligned prior to testing, slack in the hole and pin attachment system may have contributed to this effect.

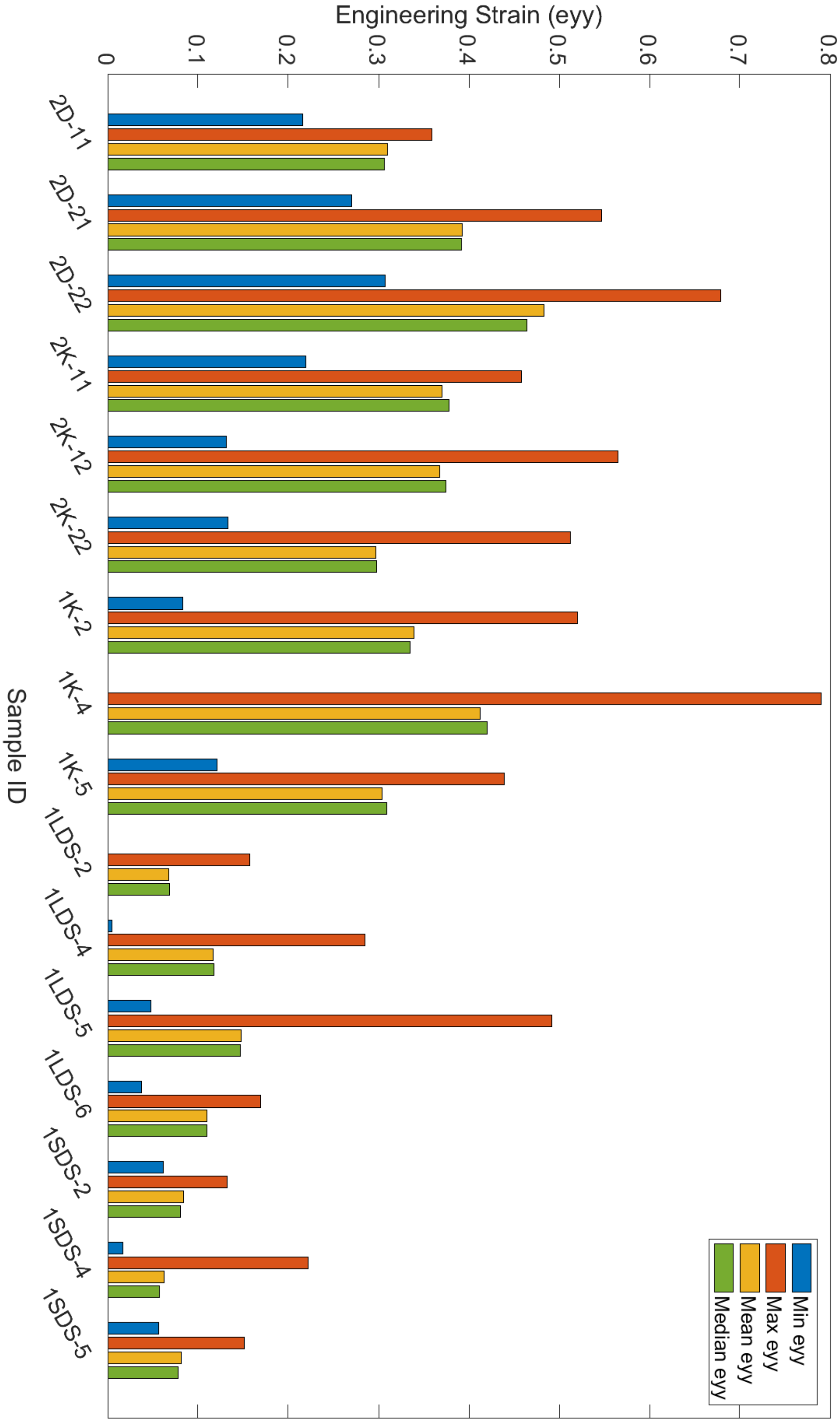

Figure 120: Min, Max, Mean and Median strain values in the y (loading) direction for each sample before fracture. Samples are named according to Table 20. As an example, 2D-11 means batch 2 dense sample, block 1, sample 1. 1LDS-2 means batch 1 (sample number 2) mixed microstructure sample containing LOF, dense and powder filled regions prior to HIP.

Upon qualitative analysis of the strain maps, it is clear that each sample behaves in a unique manner based on the type and location of the various grain distributions. The Batch 2 type 1 samples (Figure 121), which included a dense internal microstructure, show relatively homogeneous strain throughout the gauge length, apart from a localised region of increased strain that corresponded with the location of final fracture. This is typical of tensile testing whereby the material undergoes uniform elongation until a point of weakness triggers increased local strain. After this the sample necks locally until final fracture. The fracture surfaces of these samples are complex and faceted. These will be discussed in more detail in the next section.

The Batch 1 and Batch 2 type 3 samples (Figures 122 and 123), which included an internal microstructure inclusive of keyhole defects, also showed hotspots of increased strain, however these were not as finely localised as in the Dense sample. Additionally, the fracture locations of these samples only correlated with the region of highest strain in three of the six samples tested. The fracture surfaces are rougher than in the Dense samples which shows a more torturous fracture mechanism. The larger distribution of strain across the DIC map shows the potential for strain to be more evenly spread across the length of a component. This is likely due to the increased grain area in the type 3 samples as compared to the type 1, dense, samples.

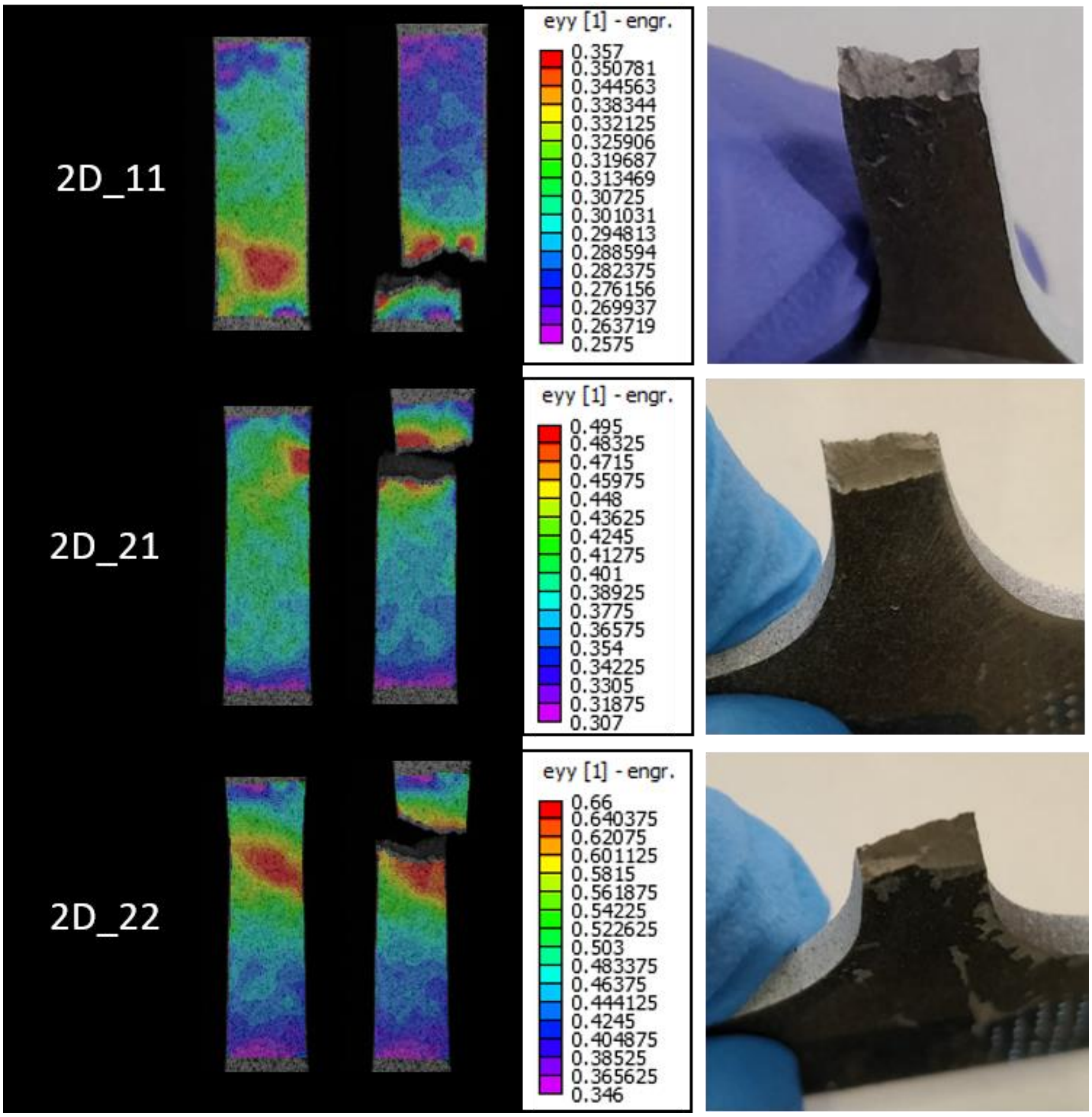

Figure 121: DIC strain data for each Batch 2 Dense sample along with images of each fracture surface.

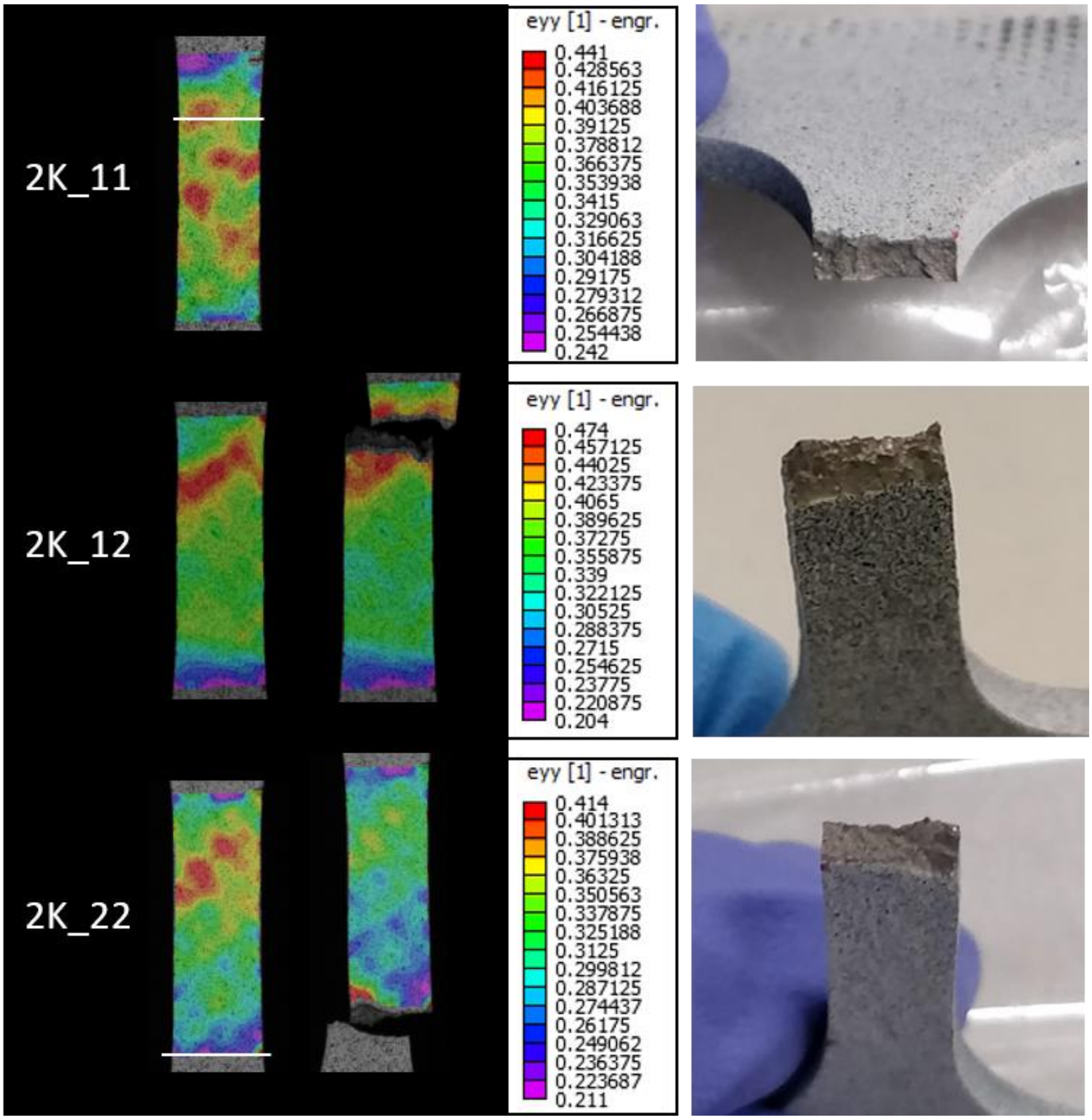

Figure 122: DIC strain data for each Batch 2 Keyhole sample along with images of each fracture surface. The white lines show the location of fracture. DIC image capture of sample 2K_11 was stopped as soon as the sample fractured, however this was done before the last image capture had occurred. Therefore, the last image captured is the image just before fracture with that of the fractured specimen not being available for analysis.

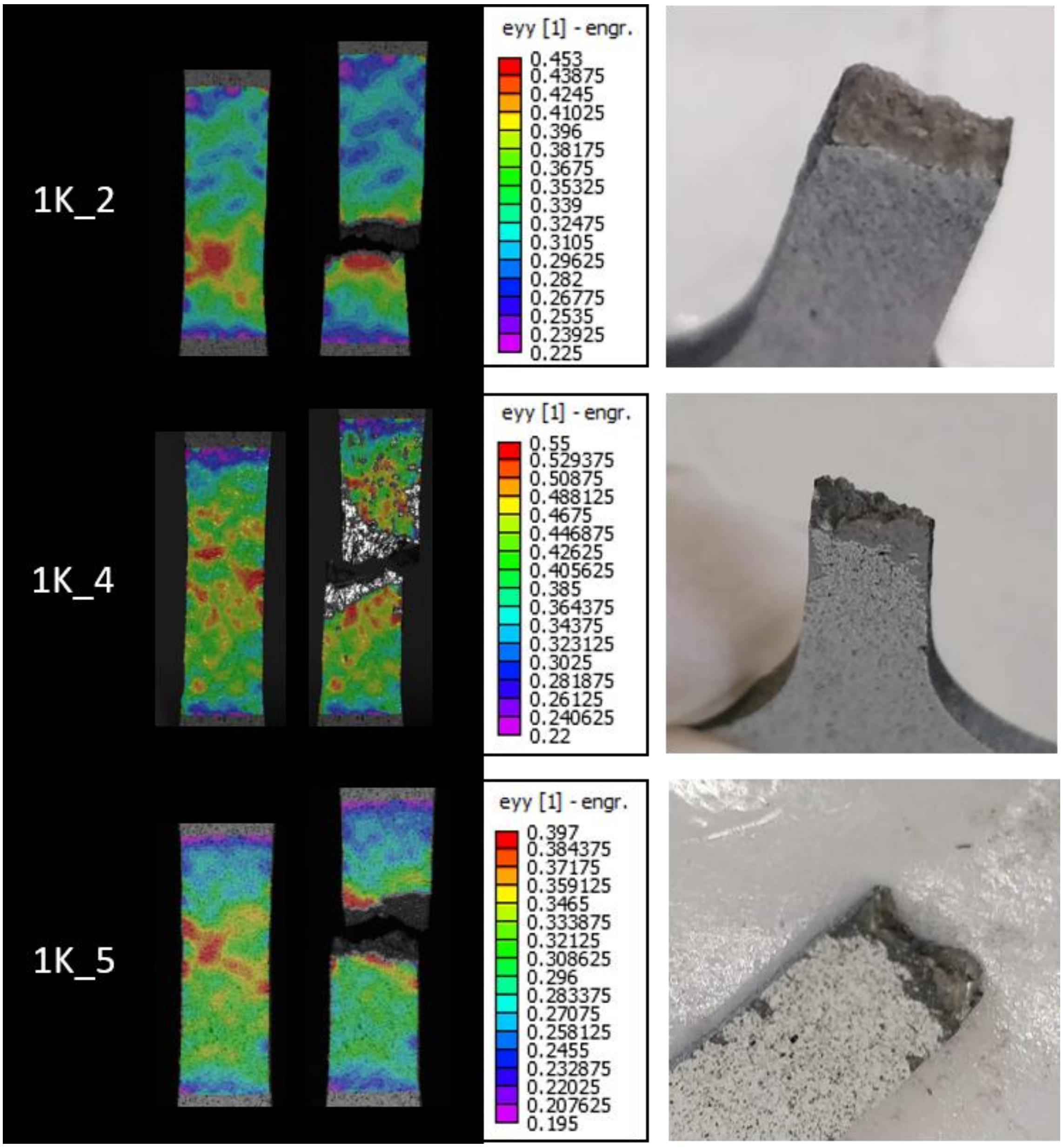

Figure 123: DIC strain data for each Batch 1 Keyhole Sample along with images of each fracture surface.

The Batch 1 type 5 samples (Figure 124), which contained three stripes of differing as-built microstructure (2x LOF and 1x loose powder), each separated by a stripe of dense as-built microstructure, all failed at or near the interface between the loose powder and the dense material sections in the mid part of the gauge length. The fracture surfaces are completely horizontal and show very fine dimples across the full fracture plane. The strain maps for each sample show a thin region of lower strain located at the mid-point of the gauge section, near the fracture location. This region of reduced strain is perpendicular to the gauge length and matches the designed location of the intentionally placed loose powder stripe. The maximum strain achieved in these samples is 48% less than in the type 1, dense, samples whilst the minimum strain is over 100% less than this. Although it should be noted that this minimum strain value is likely skewed by the slight compressive strains detected by the DIC during testing. Nevertheless, this result is interesting for two reasons; firstly, it shows the potential for specific safe failure points to be designed into components and secondly, it shows that it is possible to design functionally graded components where material strain is limited in specific regions.

The Batch 1 type 6 samples (Figure 125), which contained three stripes of loose powder separated by regions of dense material in the as-built condition, also failed near the interface region between the stripe regions. However, none failed at the gauge mid-point as in the type 5 samples. The strain maps show the presence of three distinct regions of reduced strain in each sample as opposed to the single region visible in the type 5 samples. These samples also show reduced strain levels in the regions between the stripes of HIPed powder whilst the type 5 samples show higher strain at locations away from the central stripe of HIPed powder. The type 6 samples all observed lower max axial strain than the type 5 samples, 0.17 and 0.28 respectively (68% lower max strain than the type 1, dense, samples) which is likely due to the additional two stripes of fine grain structure present in this sample. As the encapsulation of loose powder, with a nominal powder packing density of 60%, results in more open space than the printing of material inclusive of LOF defects, there may have been more deformation in the type 6 sample during HIP as compared to the type 5 sample. This results in a larger driving force for recrystallisation leading theoretically to a slightly finer overall grain size. This could be evaluated by EBSD as part of further studies.

The fracture surfaces of the type 6 (SDS) samples are visibly similar to the type 5 (LDS) samples suggesting similarities in the failure mechanism.

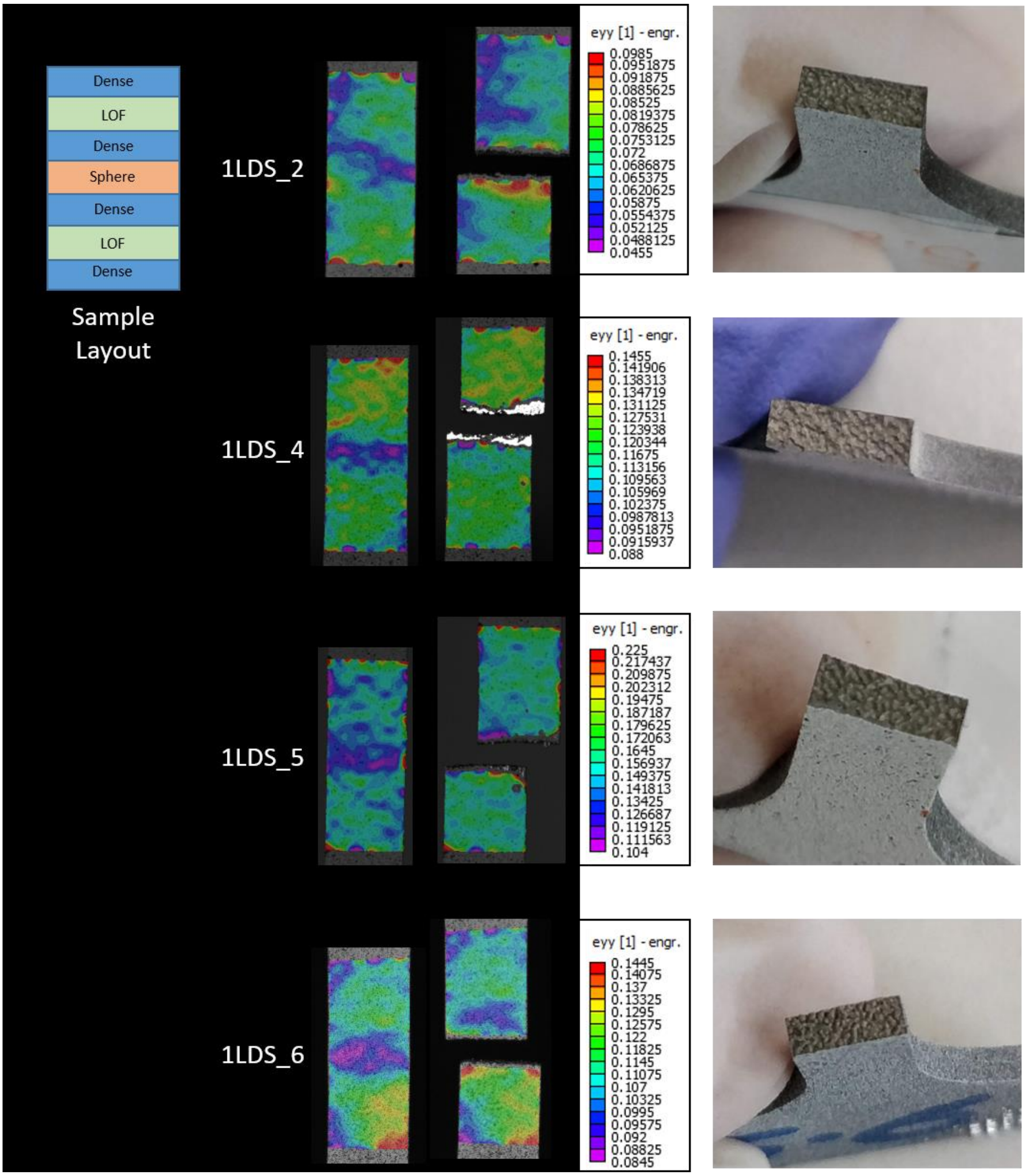

Figure 124: DIC strain data for each Batch 1, 5 series sample (Dense/LOF/Dense/Sphere/Dense/LOF/Dense) along with images of each fracture surface. Note, sample 1LDS_6 contained a large amount of slip in the grip regions and so was excluded from all analysis in Section "Tensile Test Data". This sample has been included in the data in this section "Digital Image Correlation Numerical and Mapped Strain Data"

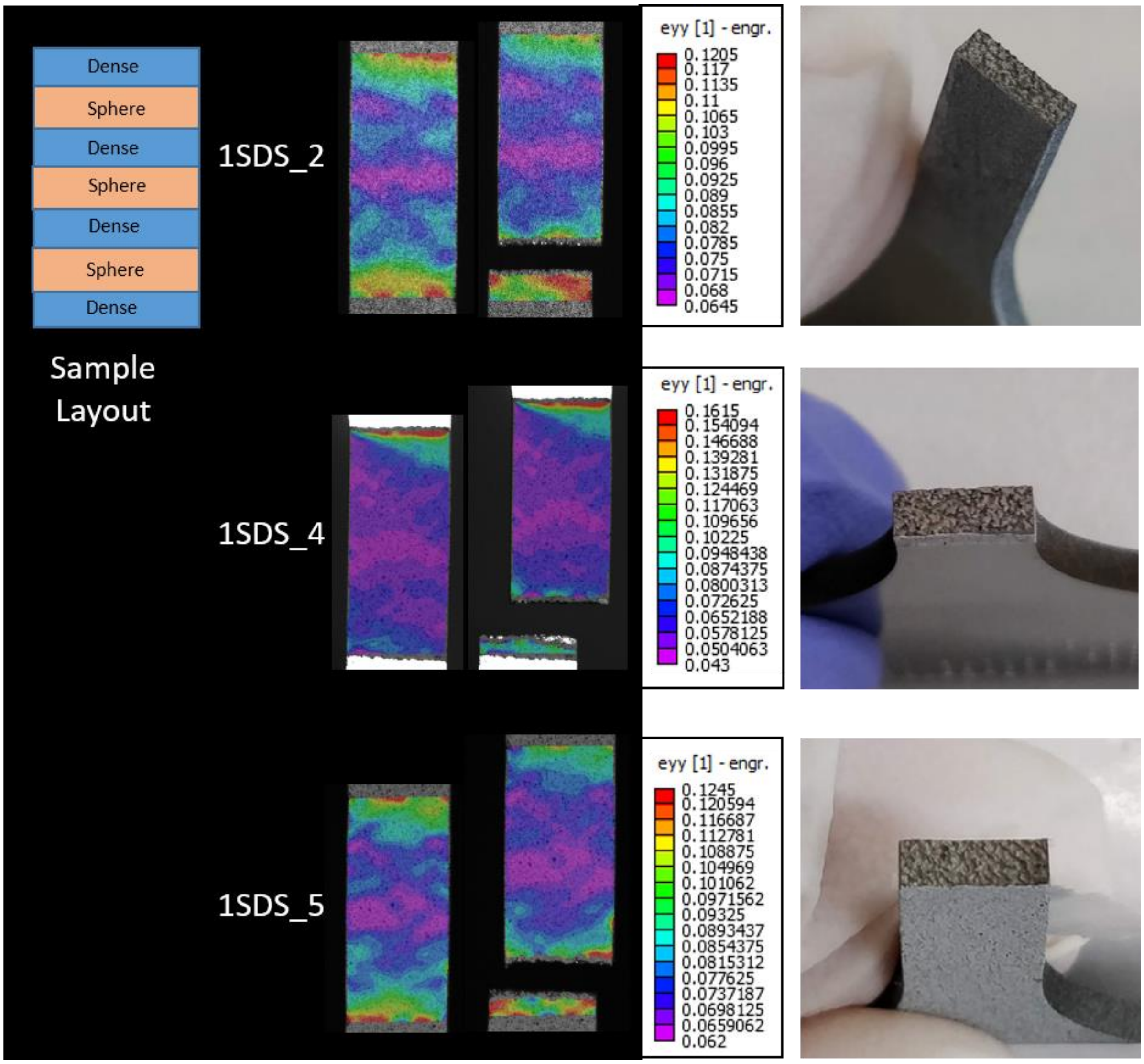

Figure 125: DIC strain data for each Batch 1, 6 series sample (Dense/Sphere/Dense/Sphere/Dense/Sphere/Dense) along with images of each fracture surface.

8.2.2.4 Sample Fracture Surfaces

The fracture surfaces for all samples tensile tested are shown in Figure 126. All images show a montaged map of the full fracture cross section apart from sample 2K_12. Initially it is clear that the fracture surface area of the LDS and SDS samples are much larger than the dense and keyhole material samples showing visually the difference in ductility observed between the two types of samples (the cross sectional area of the 2K_12 sample is comparable to sample 1K_4). There is also a marked difference in the morphology of the fracture surface between the dense and keyhole type samples, and the LDS and SDS samples, which contained stripes of HIPed powder. The dense and keyhole type samples have a fracture surface that is uneven in height, with large angled surfaces protruding the surface. In the keyhole sample, this is combined with circular regions of faceted material. In contrast, the samples inclusive of powder particles have an overall flat fracture surface, with an orientation perpendicular to the direction of tension. The surface displays large dimples, approximately 250µm in diameter. The dimple height of the SDS sample appears to be lower than that of the LDS sample, whilst the width appears to be larger, and the shape of the dimples is less circular.

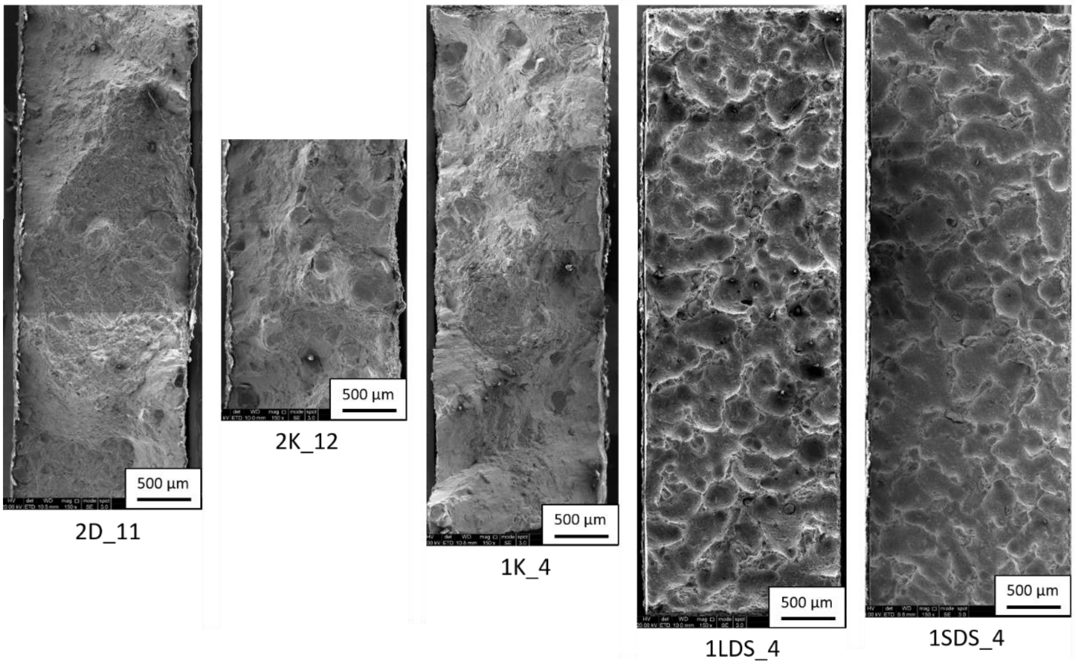

2D_11 2K_12 1K_4 1LDS_4 1SDS_4

Figure 126: Fracture surfaces of all samples. The samples initially printed with parameters optimised to create dense material, and material inclusive of Keyhole porosity, show a more ductile fracture surface than the samples initially containing loose powder. With the exception of 2K_12, the images for each sample show the full length of the fracture surface. The obvious difference in length between the dense and keyhole type samples, and the LDS and SDS samples, shows the difference in final cross sectional area. This provides visual information into the amount of necking each sample observed.

Higher magnification images of the cross sectional areas of the dense and keyhole samples in Figure 127 show the presence of very fine dimples indicating a ductile fracture [267]. No obvious difference can be observed in the dimple height between these samples, consistent with reports in the literature when comparing the fracture surface of samples exposed to different heat treatments [265]. A few regions of a more faceted fracture surface (usually circular in shape) are visible in both sample types, indicating an inter granular fracture mode [273]. From Figure 127 it can be seen that the number of occurrences of this type of region is higher in the keyhole type samples. This is possibly due to the larger grain size obtained after HIP in the keyhole samples. Overall, the dense and keyhole samples attained a mixture of inter and intra granular fractures, which is commonly seen in literature for heat treated AM parts [176].

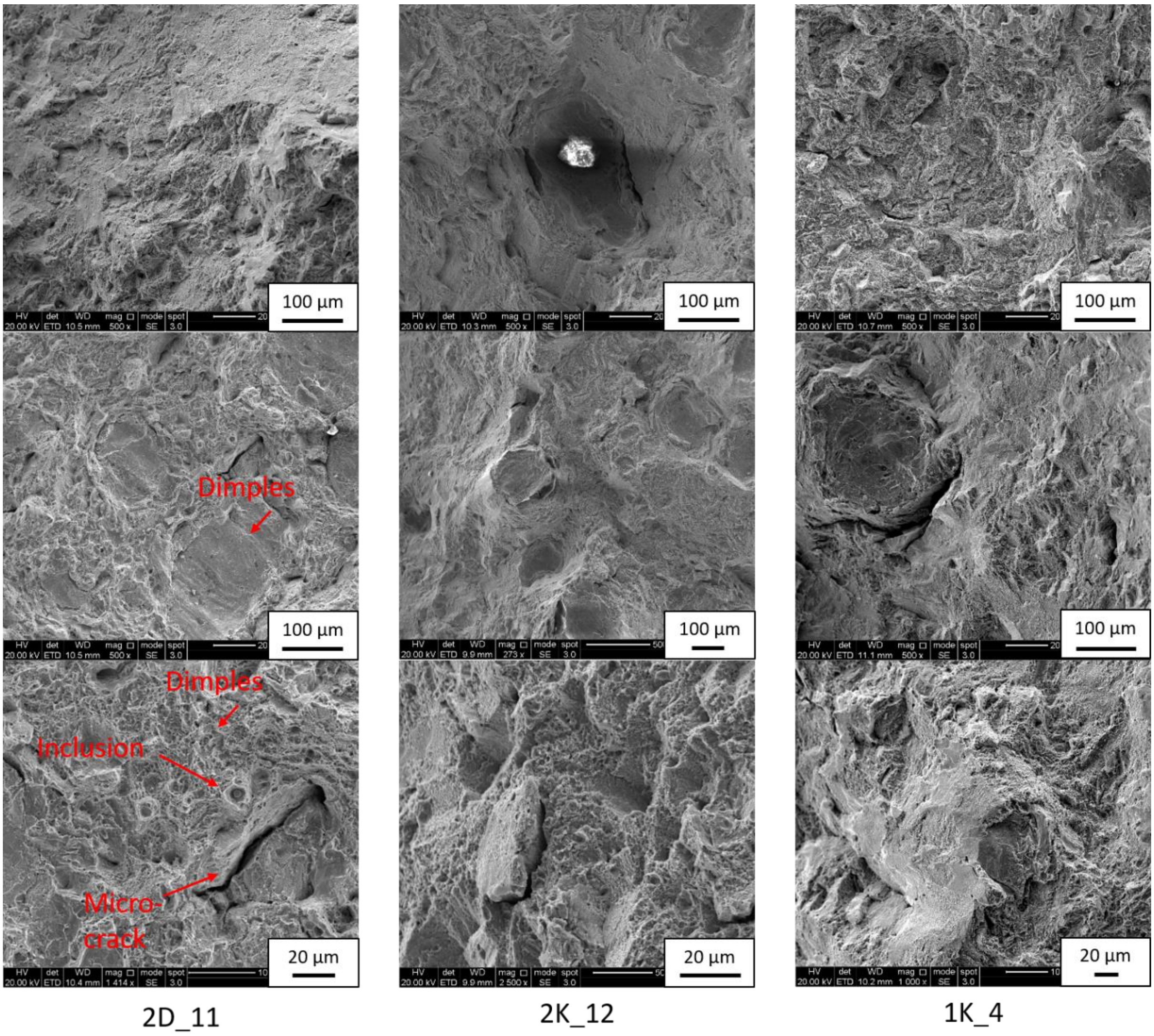

2D_11 2K_12 1K_4

Figure 127: Higher resolution fracture surfaces of the dense and keyhole samples.

In contrast to this, the samples that contained HIPed powder, shown in Figure 128, displayed very large dimples, approximately 250µm in diameter. The material within each dimple displayed a very flat and smooth fracture surface. Individual powder particles are clearly visible lining the inside of each dimple. The dimple shape is more enhanced in the LDS sample compared to the SDS sample. This sample also shows cracks and voids more prominently between the individual powder particles within each dimple. The number of voids visible between each powder particle is much larger than that observed in the SEM micrographs in Chapter 7. Because of this, is it likely that the tensile stress exerted during testing acted to create a high number of cracks and micro voids between each powder particle, leading to a comparatively more brittle fracture at the powder particle interfaces.

In the highest magnification images in Figure 128, it is clear that gaps have formed between adjacent powder particles. It has been shown in Chapter 7 that some of the PPB are lined with aluminium oxide particles. These precipitates are known to enable brittle fracture propagation, which is likely to have contributed to this effect.

It is unknown what exact phenomena is causing dimples of this size to form on the fracture surface, as the diameter of each is larger than the maximum particle size used during printing. The fracture location along the gauge length in the LDS samples was central whilst this was near the outer two bands of HIP powder in the SDS samples. It is possible that this contributes to the difference in depth and shape of the fracture dimples, however more investigation would be required to confirm this.

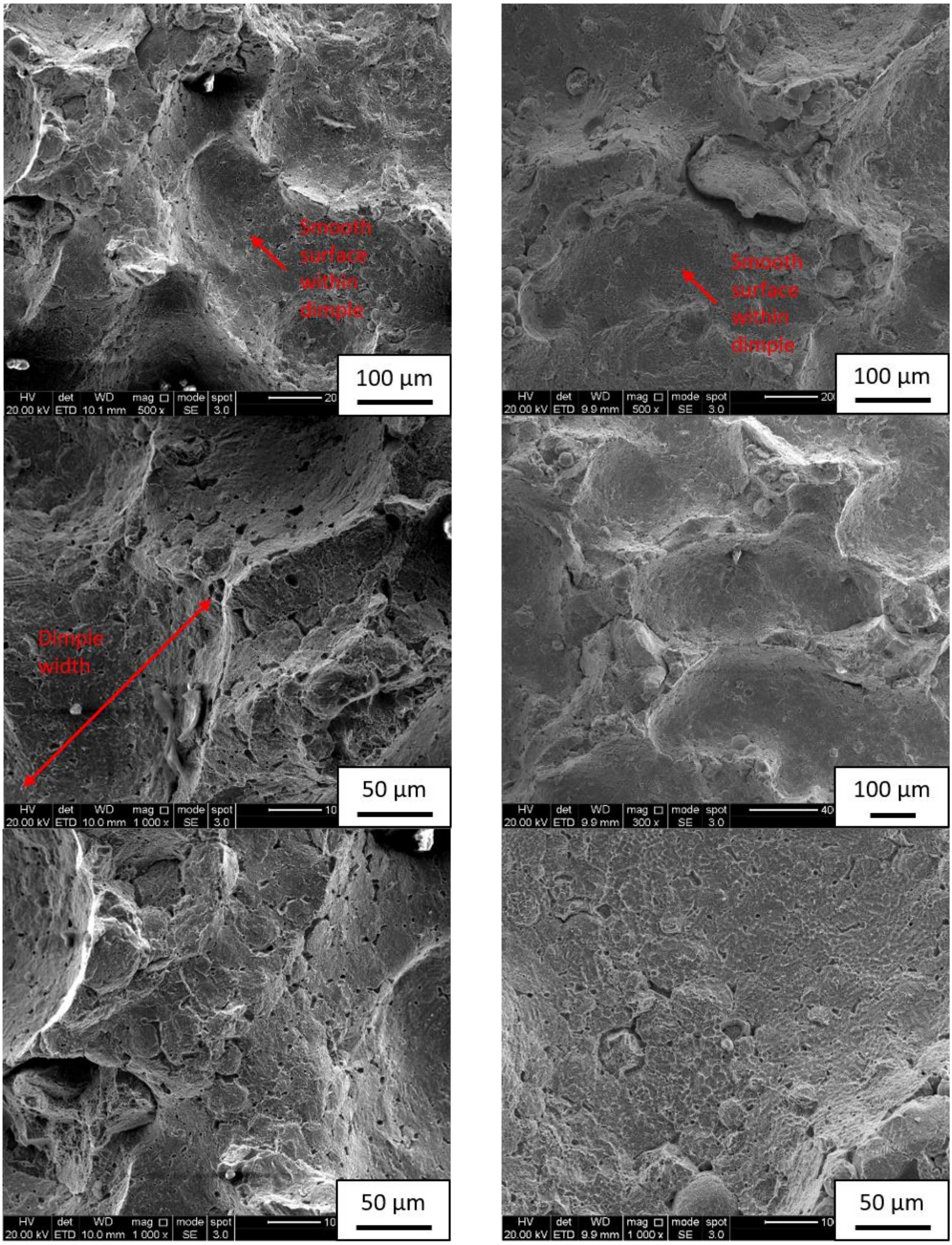

1LDS-4 1SDS-4

Figure 128: Higher resolution fracture surfaces of the LDS and SDS samples showing large scale dimples lined with visible outlines of fractured powder particles. Large pores can be seen outlining each individual powder particle.

8.2.3 Tensile Properties Summary

This section discussed the strain distribution and evolution in tensile samples where the gauge length comprises of a number of different grain morphologies and distributions. Tensile samples were designed using SolidWorks, manufactured by AM, and tested on the hydraulic test machines in the University of Sheffield Mechanical Engineering Department.

All samples underwent recrystallisation. This lead to the manufacture of a large equiaxed grain size for the Keyhole samples, and a finer equiaxed grain size for the Dense samples. In the multi-microstructure samples, a clear change in grain size is visible between the Dense, and initially loose powder, sections. This change in grain size is instant and does not take place gradually over a specific distance. Comparatively, when LOF and Dense regions are placed next to one another in the as-built condition, the effect of HIP was found to produce an approximately equal grain size across both regions. It is believed that a difference in grain size is present between the centre of the previously LOF region and the Dense region, however this difference is minor when visualised optically. Further investigation through EBSD analysis and advanced microscopy would be required to elucidate the localised effects of microstructure on the evolution of the mechanical properties in these samples.

A clear difference in tensile elongation was observed between all of the samples. The Dense samples underwent the largest elongation, followed by the Keyhole samples, and then the multi-microstructure materials. The strain did localise differently between each sample type. In the Keyhole sample, the maximum strain prior to failure exhibited a larger spread compared to the Dense samples, which showed the highest levels of strain directly at the fracture point. Much lower levels of strain were identified away from this position. In the results obtained by the tensile extensometer, the Batch 2 Keyhole samples attained lower UTS, yield stresses compared to the Batch 1 samples. Reasoning for this is believed to lie at the microstructural level and further SEM analysis should be performed on each Batch in order to understand the origins of this behaviour.

In the samples that contained HIP consolidated loose powder, the failure point was always in the vicinity of the densified loose powder region. As evidenced by the DIC data, these regions observed lower strain values. These multi-microstructural samples observed the highest yield stress which is believed to be due to the strength generated by the fine microstructure in the recrystallised powder region. The capacity for work hardening in these regions is believed to be less however, leading to inferior UTS and extension values as compared to the Dense and Keyhole samples.

These samples prove the ability of the discussed HIP technique to generate parts with varying mechanical properties, unlocking a simple route to achieving complex, functionally graded, components. Two practical benefits demonstrated in this work, are the incorporation of site specific failure points, or the production of locally stiffer component sections.

Areas for consideration if this experiment is to be repeated are as follows:

- Parts should be manufactured with a contour to provide additional protection against pressure equalisation during HIP.
- An initial experiment should be run to observe which internal defect shapes and sizes are able to be densified by HIP.
- Tensile bars should be manufactured in accordance with the ASTM standard in order to produce results comparative to those in the literature.
- Dislocation activity on either side of the fracture surface should be investigated in order to observe differences in the mechanisms of deformation and stress localisation in each sample. This is especially interesting due to the large differences in ductility observed between each sample type.

8.3 Oxidative Properties

As nickel superalloys are used in highly oxidative conditions, and the underlying grain, and grain boundary, morphology plays a large role in the oxidation kinetics of the material, it is imperative to investigate the oxidative performance of the various microstructures produced by the AM and HIP process detailed in this thesis. Oxidation occurs by the nucleation and growth of a stable oxide layer on the surface of the part. Subject to the stability of the oxide layer formed, this provides protection from further oxidation in high temperature environments.

It has been discussed in Chapter 2.5.5 that for a material with the same chemical composition, the microstructure of the base metal plays a large role in the development of a stable oxide film, with finer microstructures providing simpler diffusion paths for oxygen atoms, leading to the faster growth of a more refined, stable oxide scale [217] [218], [221]. In addition to this, microstructures with an increased number of low coincident site lattice boundaries undergo oxidation to a shorter penetration depth than those without these boundaries, helping to preserve the overall mechanical performance of the component [214].

The microstructures produced in Chapter 6 all contain different grain sizes and grain boundary morphologies. Therefore, an understanding as to how these affect the oxidation properties is important with the consideration that they may be used in gas turbine applications.

8.3.1 Experimental Methods

8.3.1.1 Sample Manufacture and heat Treatment

Samples with dimensions as shown in Figure 129 were designed on Netfabb Premium 2022. Sample geometries were designed in order to produce a hollow cuboidal dense outer shell, containing an internal cuboid manufactured with processing parameters required to produce a) a Dense microstructure, b) Keyhole defects, c) LOF defects, and d) a region of unmelted loose powder. Two samples of each type were produced. The internal cuboid has a length and width of 6mm, and a height of 5.5mm. The reduced height was incorporated in order to provide adequate wall thickness for the HIP process after the removal of the part from the baseplate by EDM. Samples were designed on this small a scale in order to fit each inside a machine that allows thermogravimetric analysis (TGA), which measures the mass of the sample with time as it undergoes oxidation. Process parameters used to produce each microstructure type are introduced in Table 21, but replicated in Table 24 for ease of viewing.

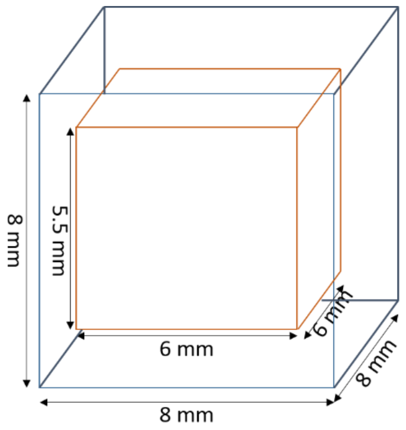

Figure 129: Sample geometry including a hollow cuboidal dense outer shell, containing an internal cuboid manufactured with processing parameters required to produce dense microstructures, keyhole defects, LOF defects, or a region of unmelted loose powder.

Table 24: Processing parameters utilised to produce each region of the samples in Figure 129.

Sample	Laser Power (W)	Laser Velocity (mms^{-1})	Hatch Spacing (μm)	Layer Thickness (μm)
Dense	130	850	75	30
Keyhole	170	500	42	30
LOF	94	1118	108	30

After removal from the baseplate, all samples were subject to HIP (1160^{0}C / 102MPa / 3 hours / air cool) with a temperature ramp up rate of 10°C/min, before the removal of 2mm of material from each surface by wire EDM. Note that the sample containing unmelted powder contracted during HIP as shown in Figure 130. The maximum contraction was approximately 0.7mm as measured using a digital Vernier calliper. With a wall thickness of 1mm, the removal of 2mm of material from each surface ensured only the internal microstructure would be present in the oxidation samples.

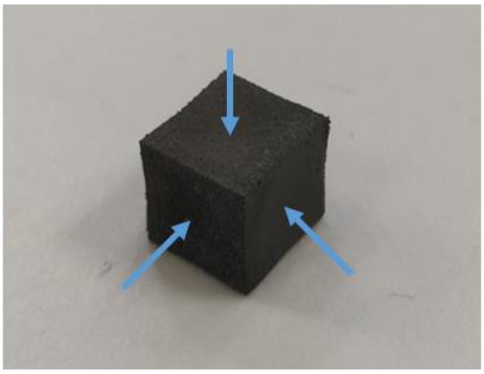

Figure 130: Sample containing loose powder after HIP showing dents in the cuboid walls due to contraction of material to the more porous region within the sample. The maximum contraction was approximately 0.7mm.

After EDM, the recast layer was removed from each surface, and all edges and corners were smoothed by hand grinding using P1200 grit paper. Samples were further polished using P2400, and P4000 grit papers. All samples were ultrasonically cleaned in Isopropan-2-ol for at least 5 minutes prior to furnace exposure.

Due to ongoing experimental concerns with the TGA at the University of Sheffield, static oxidation testing was instead completed in a box furnace. The highest sensitivity scales in the department had a resolution of 0.0001g. Using these scales, a continuous Cr_2O_3 oxide layer of approximately 0.2µm thick would have needed to form on the surface of the samples in order for a mass increase to be recorded. Therefore, it was unlikely that results for mass gain could be presented in this thesis.

As it was not known how severely the samples would oxidise and oxidation products can be dangerous to lab users, samples were initially placed in a box furnace for 100 hours with three further exposures to a total of 995 hours. For each of these furnace exposures, samples were placed in the furnace at temperature, and only removed from the furnace after they had fully cooled. After furnace treatment, the samples were mounted in conductive Bakelite, ground down to reveal the cross section using coarse grit paper, and polished using standard metallographic techniques culminating in a final polishing stage of OPS.

Oxide layers were analysed by SEM EDS and line plots were produced from the image data to show the intensity of the EDS scan for each element as the perpendicular distance from the oxide scale increases. Data was smoothed using a Savitzky-Golay filter with a smoothing factor of 0.3, and a degree of 5.

8.3.2 Results and Discussion

8.3.2.1 Mass Gain

After the first 100 hours of high temperature exposure, no visible oxide scale had formed on the surface of the samples and no mass gain could be recorded. The samples were returned to the furnace three more times for a further 125, 275, and 500 hours respectively, with samples being weighed between each interval. Comparison of the surface oxide distribution for each sample after 995 hours is shown in Figure 131. It is clear that the oxide scale is comprised of disconnected patches, and is largely underdeveloped for all samples. Due to this, no mass gain could be recorded for the samples after a total furnace time of 995 hours at 650^{o}C.

There are a number of possible reasons for this. Firstly, oxidation tests on Inconel 718 in the literature are usually performed at temperatures above 650 ^{o}C [210], [213], [214], [274]. However, this was not deemed an appropriate test temperature for the material as the upper working temperature for the alloy is 650^{o}C and so it will not be exposed to temperatures above this in service. Following discussions with sponsors, 650^{o}C was therefore deemed an appropriate temperature to conduct oxidation testing. The studies that did oxidise samples at 650 ^{o}C did so using the as-built AM grain structure and found that this led to a thicker oxide scale than the conventionally manufactured material after the same length of time. This was due to the cellular solidification structure in as-built AM samples, providing a higher volume of boundaries along which Cr atoms could diffuse. As the samples in this test were recrystallised, producing homogenised grains inclusive of twin boundaries, it is possible that the oxide scale required more time to develop [214], [215], [221].

8.3.2.2 Oxide Scale

The oxide scale seems to have developed similarly in each sample; starting from disconnected regions. It is clear that an insufficient volume of oxidation has occurred in order to fully conclude on the effects of microstructure on the oxide scale grain size, and thickness, for each sample tested.

In the optical images in Figure 131, larger oxide particles are observed in the LOF sample (red arrows), whilst these were not identified on any other sample. A larger scale image of these particles is shown in Figure 132. They look to be raised above the local region of oxide scale. It is possible that these are oxidised surface carbides that have expanded above the surface of the oxide scale [215], [219].

EDS maps of the oxide cross sections are shown for each sample in Figure 133. Only eight elements have been included in the line plots for simplicity. Ni, Cr and Fe are γ forming elements, Nb, Ti and Al are used to form the γ' and γ'' precipitates, and Ti, Nb, Al and Mo are found in various metal carbides in Inconel 718. Along with O, the inclusion of these elements was deemed sufficient for the understanding of the oxide scale formation in these samples. The other elements in Inconel 718, namely B, Co, Mn, Si and Ta, did not show any relative concentration differences across the EDS maps generated and so were not deemed to be required in this analysis.

The spatial resolution of the EDS map data acquired is influenced by the acceleration voltage of the electron beam due to the interaction volume this produces in the material. In this case, the minimum 2D resolution of the data is assumed to be approximately 1µm^2. Therefore, whilst local enrichment can be qualitatively observed in each map, the exact location and size of these regions is not quantifiable. Nevertheless, important observations can be made from the data displayed in Figure 133.

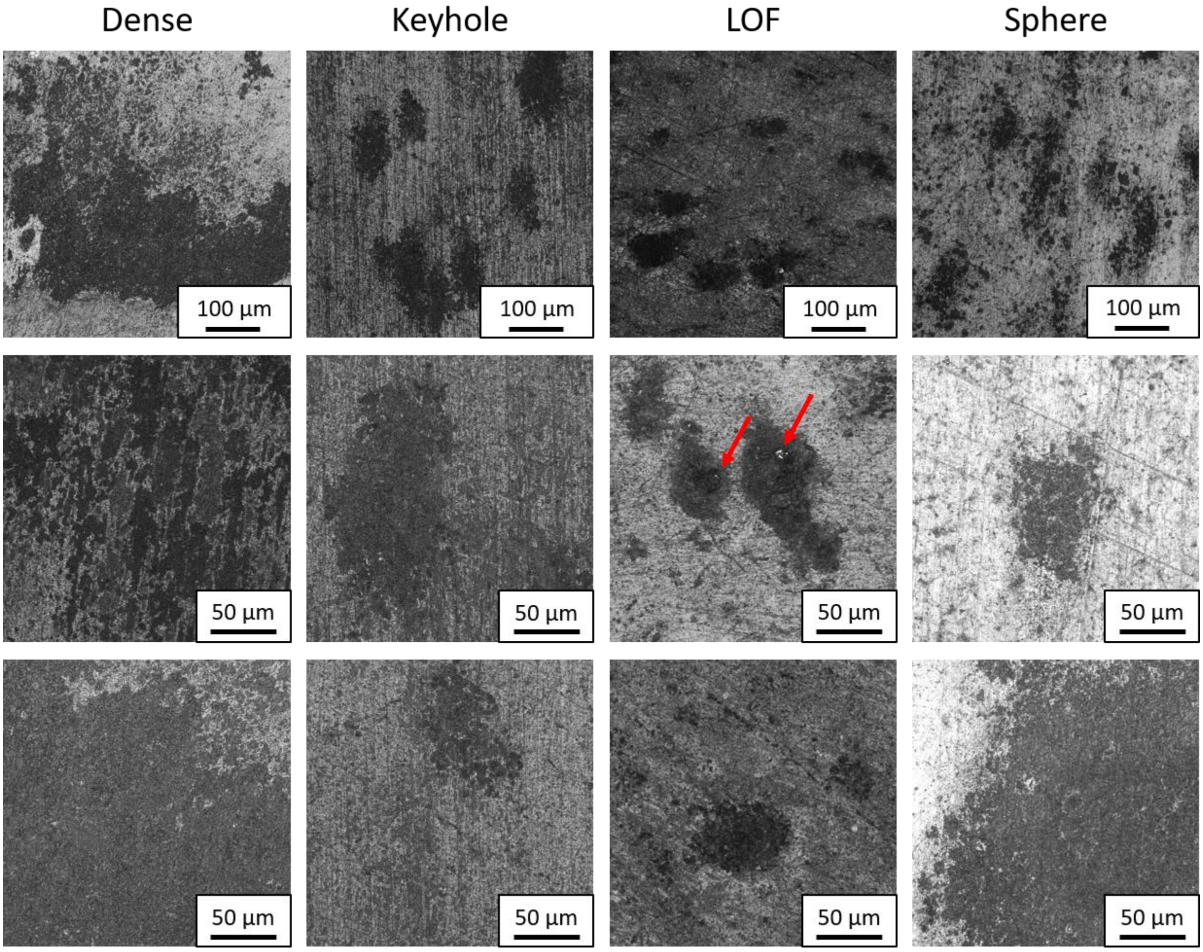

Figure 131: Optical micrographs of the surface oxides for the Dense, Keyhole, LOF and Sphere samples. The oxide scale is patchy for all samples. Red arrows in the LOF sample point to larger oxide particles that stick up above the oxide region. A closer image of these particles is shown in Figure 132.

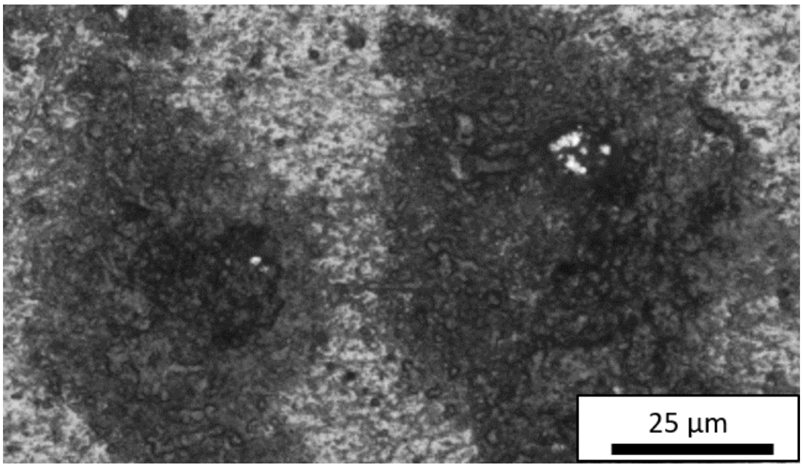

Figure 132: Close image of larger particles within the oxide scale of the LOF sample.

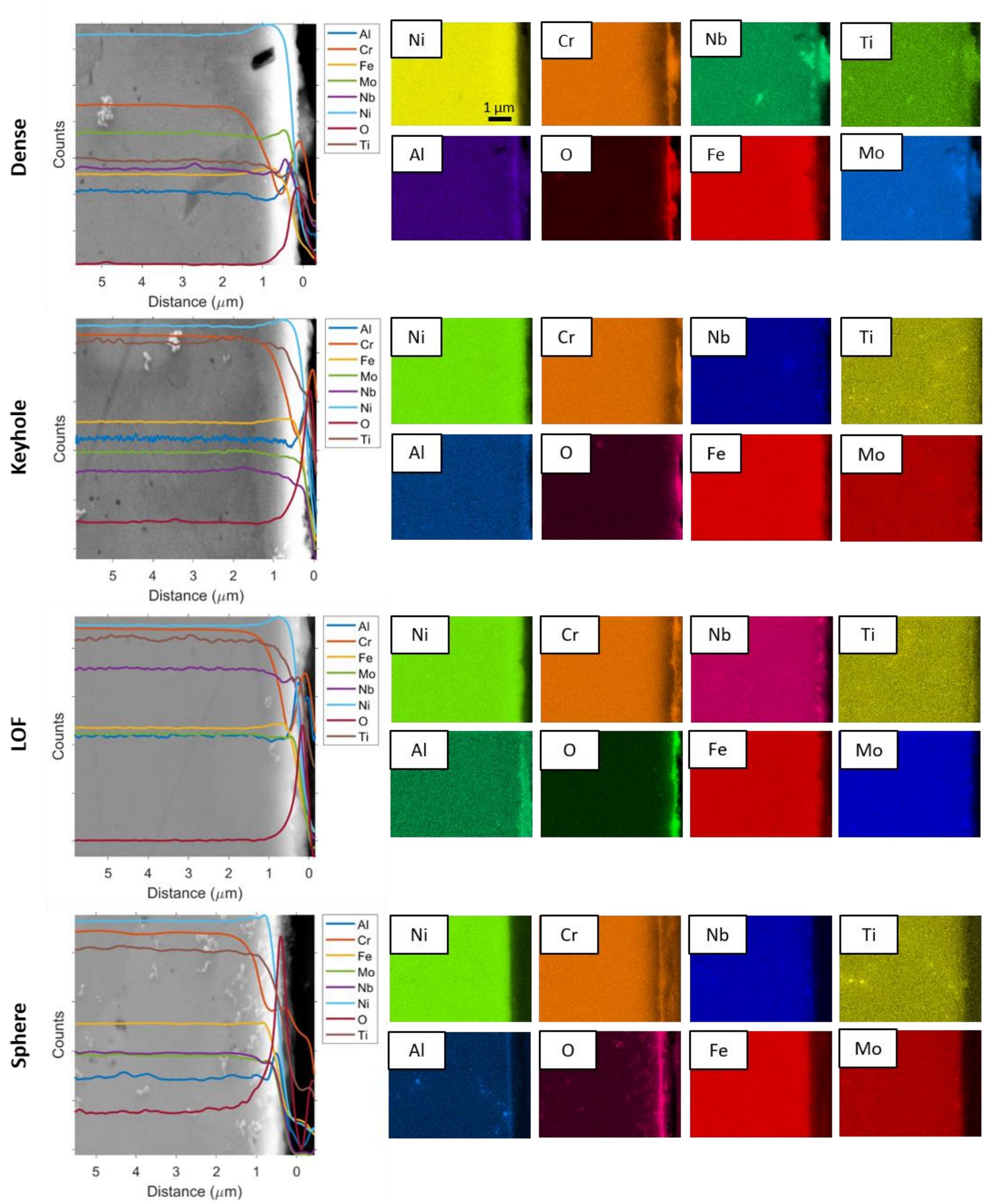

Figure 133: EDS maps and corresponding line plots for each sample showing the number of counts of each element present at specific locations from the sample surface. The axis starts at the outer edge of the oxide scale. Scale of all EDS maps are the same.

All samples show an enrichment in O and Cr at the surface of the sample. A depletion in Cr at the sub surface is also observed in each sample. This indicates the formation of a thin Cr_2O_3 oxide layer as expected.

The line plots and EDS maps show that the concentration of Al also increases from the baseline value at the material sub surface. This indicates the presence of a thin sub-oxide layer of Al_2O_3 in all samples. This has not been observed in the literature for LPBF Inconel 718 samples tested at 650°C or higher. However, not many studies have been identified that observe the oxidation behaviour of Inconel 718 manufactured by LPBF. EDS maps in a study by Parizia *et al.* [275] who studied the oxidation behaviour of LPBF Inconel 625 at 900°C do show a slight enrichment of Al at the interface between the stable chromia scale and the metal substrate. In their study, they do not report on the presence of an Al based oxide scale, however do state the presence of a minor volume of TiO_2. Comparatively, in another study, whilst NiO was not observed in as-built LPBF Inconel 718, this was observed by Raman Spectroscopy in conventionally manufactured (cast, rolled, and AMS5596 solution heat treatment - solution annealing and double ageing) Inconel 718 [217]. The authors attributed this to the efficient formation of a stable Cr_2O_3 layer in the as-built sample due to the presence of the characteristically fine solidification structure, and corresponding regions of elemental segregation. The microstructures in the samples shown in this study are understood to have fully recrystallised, and so will no longer have these fine solidification structures. Instead, they are more likely to have a microstructure similar to the conventionally manufactured material.

Once a stable Cr_2O_3 surface oxide layer has been established, further oxidation in Inconel 718 takes place by the inward movement of oxygen ions and the outward diffusion of Cr ions. As the depth into the material increases, this inward migration of oxygen is reduced to a point where there is insufficient oxygen available for the formation of Cr_2O_3. At this point, it is usual to see the formation of TiO_2, and once there is insufficient oxygen available for the formation of TiO_2, Al_2O_3 is formed [213]. None of the samples show significant enrichment of Ti near the interface between the Cr_2O_3 and the base metal. As previously mentioned, however, a slight enrichment of Al is present in this sub-oxide region. This suggests that each of the samples was able to form a very protective Cr_2O_3 scale which effectively blocked the further inward motion of oxygen ions to the base metal.

Due to the relative thickness of the oxide scale, it was necessary to perform all characterisation at high magnifications, which meant only single grains were imaged. Figure 134 shows the oxide scale of the LOF sample at a lower magnification. A line of carbides and pores is observed to extend from the surface of the sample into the bulk. This is likely a position where the as-built LOF discontinuity has not been fully consolidated by the HIP process. The EDS maps show the formation of a continuous Cr_2O_3 scale on the surface of the sample. However, it is clear from the enrichment of oxygen into the bulk of the sample that the presence of pores and carbides accelerate the ingress of oxygen into these regions. Oxidation of carbides has been shown to cause them to expand. If this occurs within the bulk of the material, this can lead to stress concentrations and cracking, which reduces the life of the part and can cause unpredicted failure.

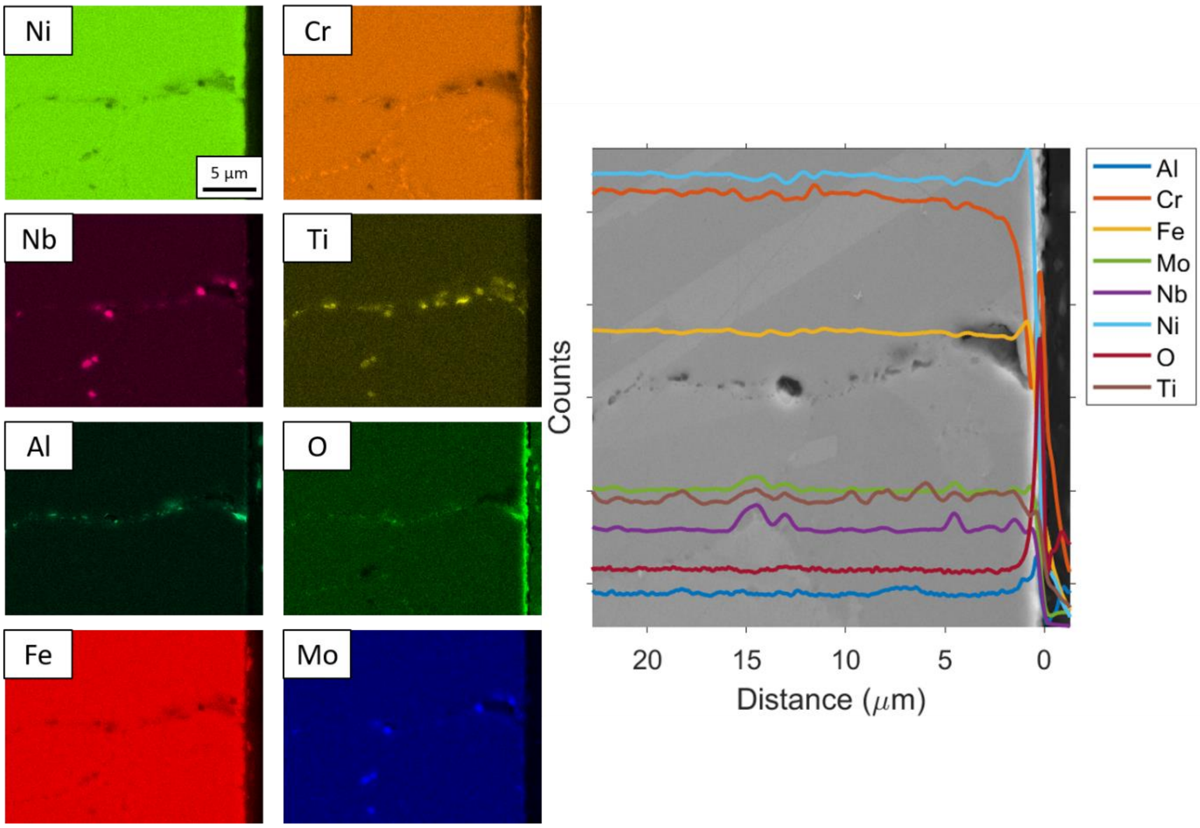

Figure 134: EDS maps and corresponding line plot showing the number of counts of each element present at specific locations from the sample surface in the LOF sample. The axis starts at the outer edge of the oxide scale. Note the scale here is larger than in Figure 133.

8.3.3 Oxidation Summary

Oxidation tests were performed on four samples, each produced with a different internal microstructure. Trials were not able to be performed in a TGA as planned. Instead, a simple box furnace was used, and samples were manually weighed. Due to the small size of the samples and minimum resolution of the available scales being 0.0001g, no mass gain values could be identified.

The temperatures used in the oxidation was below those typically used in oxidation trials of Inconel 718, however as 650°C is the highest operational temperature of Inconel 718, it was deemed appropriate to conduct all oxidation testing at this temperature.

It has been shown in the literature that samples of as-built LPBF Inconel 718 are able to form a thicker and more continuous layer of Cr_2O_3 than conventionally manufactured material [215], [217]. This is due to the fine cellular structure it exhibits compared to the coarser grained microstructure in the conventionally manufactured material. Comparatively, as-built microstructures were observed to enable oxidation deeper in to the material than conventionally manufactured samples with tighter grain boundaries.

In this study, each sample was produced to have a different grain size and so differences in the oxidation behaviour for each was expected. However, due to the unavailability of the TGA, no concrete conclusions could be made with the data available. Despite this, it can be concluded that each sample formed regions of continuous Cr_2O_3. Due to the local protection this offered, only a small volume of oxygen was able to penetrate the oxide layer, resulting in the formation of a very fine, but continuous, layer of Al_2O_3 under the main chromium-based oxide layer. This has not been previously reported on for Inconel 718 manufactured by LPBF. As there was less indication of TiO_2 formation, it can be concluded that the external Cr_2O_3 layer provided good protection against further oxygen ingress.

9 Conclusions and Further Work

Individual, more specific, conclusions have been presented at the end of each chapter. This section summarises the main conclusions drawn within this thesis and discuses some relevant ideas for further work.

9.1 Conclusions

- A new method of process control for additive manufacturing was proposed. This involves the generation of a fully optimised build file prior to building which splits hatch lines into mini hatches. Based on previously determined thermal data, each hatch line is assigned a different set of process parameters in order to achieve a homogeneous temperature across each part. This should enable multiple complex parts of identical design to be produced in an identical manner, making the qualification of parts easier in industrial applications.
- The notion that printing at a specific normalised equivalent volumetric energy density, regardless of individual parameters, produces parts of equal quality (defect population, part temperature and microstructure), was challenged. For an equal normalised equivalent energy density, varying the hatch spacing led to a larger difference in part pyrometry intensity compared to varying the laser velocity over three different part sizes. Additionally, large variations in melt pool width and depth, and pyrometry intensity data, were observed whilst printing at an equal normalised equivalent energy density. Therefore, it is believed that had the trial been performed on a more difficult to manufacture material, larger differences in porosity, grain size, and mechanical properties, would have been observed.
- A method of producing functionally graded components from a single AM print was introduced. This involves the production of as-built AM parts inclusive of a range of different intentionally placed discontinuities. Upon post processing by HIP, differences in the as-built grain size, GND distribution, and extent of sample compression, enable a range of distinct microstructures to be obtained. The method also enables the production of fully dense AM parts with a reduction in build time and input energy.
- Tensile testing of microstructurally variant samples produced using the AM and HIP technique was performed in conjunction with DIC. This demonstrated the ability to manufacture AM parts with intentionally placed differences in mechanical performance.
- Variations in the underlying distribution and size of the strengthening precipitate, γ'', was identified in all of the different functionally graded microstructures manufactured by the AM and HIP method. This was observed despite utilising an identical post HIP heat treatment.

Therefore, optimisation of the aging heat treatment is required separately for each sample type.

9.2 Further work

A deeper understanding as to the mechanisms that take place during recrystallisation in the presence of AM porosities is to be sought. This will enable closer control over the desired microstructure, and paves the way towards the production of a digital platform that is able to predict the resulting recrystallised microstructure in a given region of a build produced by this method. Initially, this involves gaining an understanding into:

- The size and shape of internal regions that may be densified by the AM and HIP method.
- The effect of the wall thickness on the fraction of recrystallised material, volume of material compaction, and the final grain morphology after HIP.
- The effect of various volume fractions of porosities of each type on the final grain morphology after HIP.
- The effect of variations in AM build 'temperature' on the final grain morphology after HIP. This aim requires the realisation of true material temperature measurement during processing.
- The effects of variations in the combination of laser power, velocity, and hatch spacing, on the final grain morphology of optimally dense samples after HIP. For example, investigating if there are combinations that enable a lower GND and strain accumulation, so to resist recrystallisation during HIP.
- The effects of different HIP process parameters on the final grain morphologies.

Once correlations between the above have been established, the creation of model linking each aspect is required in order to generate an all-encompassing build file suitable for the production of complex geometries with variations in desired post HIP grain morphologies. This includes sharp boundaries between two distinct grain sizes, bi-modal type microstructures, large and fine equiaxed grain regions, as well as regions in which the as-built AM columnar grain morphology is retained.

The majority of work within this thesis focused on evaluating the potential of using hybrid manufacturing processes to influence grain structure distributions. Further to this, it is also imperative to understand the effects of these processes on the material at higher resolutions. In precipitation hardened materials, like Inconel 718, it is crucial to understand how this manufacturing process influences the precipitation sequences. In Chapter 6, an identical heat treatment was applied to all the alternate microstructures. This produced widely differing volume fractions of γ'' precipitates in each sample. More work is to be performed to attain an optimised heat treatment route, potentially utilising multiple heat treatment cycles, to achieve a similar volume fraction of γ'' precipitates in each final microstructure.

Finally, the mechanical properties of each microstructure produced using the AM and HIP method is to be evaluated in accordance with standard testing procedures (ASTM and ISO) in order to provide comparison with traditionally manufactured materials. This includes understanding the microstructural effects of the different sample types on room or elevated temperature properties such as tensile strength, fatigue, creep, and oxidation. This includes identification of the potential damage accumulation and failure mechanisms present in each. Consideration to the effects of powder re-use is also required in the realm of mechanical property characterisation. This is especially important in samples produced using LOF porosities, where the material does not undergo full melting during the AM process.

Inconel 718 is a fairly easy material to process, however this is not the case for other Ni-based superalloys with higher γ' fractions such as Inconel 713-LC and CM247-LC, or indeed other classes of metallic materials such as Al-alloys. These materials undergo significant cracking during manufacture, as well as post processing operations where strain age cracking becomes prevalent. It would be interesting to test the AM and HIP process outlined in this thesis to these harder to process materials. It is predicted that by intentionally printing with process parameters that produce a homogeneous distribution of internal porosities, the combined effects of plastic deformation, diffusion, and recrystallisation during HIP may enable fully dense samples to be produced using the AM and HIP method, while this is difficult to achieve using laser parameters alone. This has the potential to transform the current processing route for materials that undergo strain age cracking, and lead to parts with full density and reduced susceptibility to solid state cracking.

9.3 Final Remarks

Ultimately, through this thesis, the use of hybrid manufacturing methodologies that holistically take into consideration the entirety of the manufacturing and post-manufacture landscape have been utilised to design and deliver functional microstructures. The methodologies presented herein provide an effective route towards enhancing component function from intelligent use of manufacturing processes. Consequently, components with improved lifetimes and recyclability, through the reduction in assembly operations and different alloy classes required, can be achieved. This leans towards realising the potential for additive manufacture in creating value added, sustainable, products.

References

[1] W. J. Sames, F. A. List, S. Pannala, R. R. Dehoff, and S. S. Babu, “The metallurgy and processing science of metal additive manufacturing,” *Int. Mater. Rev.*, vol. 61, no. 5, pp. 315–360, 2016, doi: 10.1080/09506608.2015.1116649.

[2] I. Gibson, D. W. Rosen, and B. Stucker, *Additive Manufacturing Technologies - Rapid Prototyping to Direct Digital Manufacturing*. Springer Science + Business Media, 2010. doi: 10.1007/978-1-4419-1120-9.

[3] ASTM, “ASTM F42/ISO TC 261 Develops Additive Manufacturing Standards,” 2017. [Online]. Available: https://www.astm.org/COMMIT/F42_AMStandardsStructureAndPrimer.pdf

[4] D. C. Hofmann *et al.*, “Developing gradient metal alloys through radial deposition additive manufacturing,” *Sci. Rep.*, vol. 4, 2014, doi: 10.1038/srep05357.

[5] S. Ford and M. Despeisse, “Additive Manufacturing and Sustainability: an exploratory study of the advantages and challenges,” *J. Clean. Prod.*, no. 137, pp. 1573–1587, 2016.

[6] Charlotte Amelia Boig, “The Application of Additive Manufacturing to Nickel-base Superalloys for Turbocharger Applications,” The University of Sheffield, 2018.

[7] M. Gupta, *3D Printing of Metals*, vol. 7, no. 10. 2017. doi: 10.3390/met7100403.

[8] M. AM, “Airbus Defence and Space develops aluminium bracket for new Eurostar E3000 satellite platforms,” 2015. https://www.metal-am.com/airbus-defence-and-space-develops-aluminium-bracket-for-new-eurostar-e3000-satellite-platforms/

[9] V. A. Popovich, E. V. Borisov, A. A. Popovich, V. S. Sufiiarov, D. V. Masaylo, and L. Alzina, “Functionally graded Inconel 718 processed by additive manufacturing: Crystallographic texture, anisotropy of microstructure and mechanical properties,” *Mater. Des.*, vol. 114, pp. 441–449, 2017, doi: 10.1016/j.matdes.2016.10.075.

[10] G. Powder Metallurgy, “GKN Additive - 3D Metal and Plastics Printing.” https://www.gknpm.com/en/our-businesses/gkn-additive/

[11] Airbus, “3D Printing - Decarbonisation meets digitalisation.” https://www.airbus.com/public-affairs/brussels/our-topics/innovation/3d-printing.html

[12] Boeing, “Additive Manufacturing Insight.” https://www.boeing.com/features/innovation-quarterly/2019_q4/btj-additive-manufacturing.page

[13] T. G. Spears and S. A. Gold, “In-process sensing in selective laser melting (SLM) additive manufacturing,” *Integr. Mater. Manuf. Innov.*, vol. 5, no. 2, 2016, doi: 10.1186/s40192-016-0045-4.

[14] J. C. Ion, H. R. Shercliff, and M. F. Ashby, “Diagrams for Laser Materials Processing,” *Acta Mater.*, vol. 40, no. 7, pp. 1539–1551, 1992.

[15] M. Grasso and B. M. Colosimo, “Process defects and in situ monitoring methods in metal powder bed fusion: A review,” *Meas. Sci. Technol.*, vol. 28, no. 4, pp. 1–40, 2017, doi: 10.1088/1361-6501/aa5c4f.

[16] A. Strondl, O. Lyckfeldt, H. Brodin, and U. Ackelid, “Characterization and Control of Powder Properties for Additive Manufacturing,” *Jom*, vol. 67, no. 3, pp. 549–554, 2015, doi: 10.1007/s11837-015-1304-0.

[17] K. N. Amato *et al.*, “Microstructures and mechanical behavior of Inconel 718 fabricated by selective laser melting,” *Acta Mater.*, vol. 60, no. 5, pp. 2229–2239, 2012, doi: 10.1016/j.actamat.2011.12.032.

[18] S. M. Thompson, L. Bian, N. Shamsaei, and A. Yadollahi, “An overview of Direct Laser Deposition for additive manufacturing; Part I: Transport phenomena, modeling and diagnostics,” *Addit. Manuf.*, vol. 8, pp. 36–62, 2015, doi: 10.1016/j.addma.2015.07.001.

[19] ASTM International, “Additive manufacturing — Design — Part 1 : Laser-based powder bed fusion of metals 1,” vol. 2019, pp. 1–15, 2019, doi: 10.1520/52911-1-19.2.

[20] M. C. Karia, M. A. Popat, and K. B. Sangani, “Selective laser melting of Inconel super alloy-a review,” *AIP Conf. Proc.*, vol. 1859, no. July, 2017, doi: 10.1063/1.4990166.

[21] B. Ferrar, L. Mullen, E. Jones, R. Stamp, and C. J. Sutcliffe, “Gas flow effects on selective laser melting (SLM) manufacturing performance,” *J. Mater. Process. Technol.*, vol. 212, no. 2, pp. 355–364, 2012, doi: 10.1016/j.jmatprotec.2011.09.020.

[22] T. Craeghs, S. Clijsters, E. Yasa, F. Bechmann, S. Berumen, and J. P. Kruth, “Determination of geometrical factors in Layerwise Laser Melting using optical process monitoring,” *Opt. Lasers Eng.*, vol. 49, no. 12, pp. 1440–1446, 2011, doi: 10.1016/j.optlaseng.2011.06.016.

[23] I. Koutiri, E. Pessard, P. Peyre, O. Amlou, and T. De Terris, “Influence of SLM process

parameters on the surface finish, porosity rate and fatigue behavior of as-built Inconel 625 parts," *J. Mater. Process. Technol.*, vol. 255, pp. 536–546, 2018, doi: 10.1016/j.jmatprotec.2017.12.043.

[24] B. Liu, R. Wildman, C. Tuck, I. Ashcroft, and R. Hague, "Investigation the effect of particle size distribution on processing parameters optimisation in selective laser melting process," *22nd Annu. Int. Solid Free. Fabr. Symp. - An Addit. Manuf. Conf. SFF 2011*, no. January 2015, pp. 227–238, 2011.

[25] U. S. Bertoli, A. J. Wolfer, M. J. Matthews, J. P. R. Delplanque, and J. M. Schoenung, "On the limitations of Volumetric Energy Density as a design parameter for Selective Laser Melting," *Mater. Des.*, vol. 113, pp. 331–340, 2017, doi: 10.1016/j.matdes.2016.10.037.

[26] S. Ghorbanpour *et al.*, "Effect of microstructure induced anisotropy on fatigue behaviour of functionally graded Inconel 718 fabricated by additive manufacturing," *Mater. Charact.*, vol. 179, no. May, p. 111350, 2021, doi: 10.1016/j.matchar.2021.111350.

[27] K. Moussaoui, W. Rubio, M. Mousseigne, T. Sultan, and F. Rezai, "Effects of Selective Laser Melting additive manufacturing parameters of Inconel 718 on porosity, microstructure and mechanical properties," *Mater. Sci. Eng. A*, vol. 735, pp. 182–190, 2018, doi: 10.1016/j.msea.2018.08.037.

[28] Q. Jia and D. Gu, "Selective laser melting additive manufactured Inconel 718 superalloy parts: High-temperature oxidation property and its mechanisms," *Opt. Laser Technol.*, vol. 62, pp. 161–171, 2014, doi: 10.1016/j.optlastec.2014.03.008.

[29] S. Y. Liu, H. Q. Li, C. X. Qin, R. Zong, and X. Y. Fang, "The effect of energy density on texture and mechanical anisotropy in selective laser melted Inconel 718," *Mater. Des.*, vol. 191, 2020, doi: 10.1016/j.matdes.2020.108642.

[30] Q. Jia and D. Gu, "Selective laser melting additive manufacturing of Inconel 718 superalloy parts: Densification, microstructure and properties," *J. Alloys Compd.*, vol. 585, pp. 713–721, 2014, doi: 10.1016/j.jallcom.2013.09.171.

[31] M. Sadowski, L. Ladani, W. Brindley, and J. Romano, "Optimizing quality of additively manufactured Inconel 718 using powder bed laser melting process," *Addit. Manuf.*, vol. 11, pp. 60–70, 2016, doi: 10.1016/j.addma.2016.03.006.

[32] M. Thomas, G. J. Baxter, and I. Todd, "Normalised model-based processing diagrams for additive layer manufacture of engineering alloys," *Acta Mater.*, vol. 108, pp. 26–35, 2016, doi:

10.1016/j.actamat.2016.02.025.

[33] G. Kasperovich, J. Haubrich, J. Gussone, and G. Requena, “Correlation between porosity and processing parameters in TiAl6V4 produced by selective laser melting,” *Mater. Des.*, vol. 105, pp. 160–170, 2016, doi: 10.1016/j.matdes.2016.09.040.

[34] T. Craeghs, L. Thijs, F. Verhaeghe, J.-P. Kruth, and J. Van Humbeeck, “A study of the microstructural evolution during selective laser melting of Ti–6Al–4V,” *Acta Mater.*, vol. 58, no. 9, pp. 3303–3312, 2010, doi: 10.1016/j.actamat.2010.02.004.

[35] C. Qiu, C. Panwisawas, M. Ward, H. C. Basoalto, J. W. Brooks, and M. M. Attallah, “On the role of melt flow into the surface structure and porosity development during selective laser melting,” *Acta Mater.*, vol. 96, pp. 72–79, 2015, doi: 10.1016/j.actamat.2015.06.004.

[36] M. N. Ahsan, R. Bradley, and A. J. Pinkerton, “Microcomputed tomography analysis of intralayer porosity generation in laser direct metal deposition and its causes,” *J. Laser Appl.*, vol. 23, no. 2, p. 022009, 2011, doi: 10.2351/1.3582311.

[37] C. L. A. Leung, S. Marussi, R. C. Atwood, M. Towrie, P. J. Withers, and P. D. Lee, “In situ X-ray imaging of defect and molten pool dynamics in laser additive manufacturing,” *Nat. Commun.*, vol. 9, no. 1, pp. 1–9, 2018, doi: 10.1038/s41467-018-03734-7.

[38] W. E. King *et al.*, “Observation of keyhole-mode laser melting in laser powder-bed fusion additive manufacturing,” *J. Mater. Process. Technol.*, vol. 214, no. 12, pp. 2915–2925, 2014, doi: 10.1016/j.jmatprotec.2014.06.005.

[39] C. L. A. Leung *et al.*, “Laser-matter interactions in additive manufacturing of stainless steel SS316L and 13-93 bioactive glass revealed by in situ X-ray imaging,” *Addit. Manuf.*, vol. 24, no. August, pp. 647–657, 2018, doi: 10.1016/j.addma.2018.08.025.

[40] S. A. Khairallah, A. T. Anderson, A. Rubenchik, and W. E. King, “Laser powder-bed fusion additive manufacturing: Physics of complex melt flow and formation mechanisms of pores, spatter, and denudation zones,” *Acta Mater.*, vol. 108, pp. 36–45, 2016, doi: 10.1016/j.actamat.2016.02.014.

[41] A. Matsunawa, J.-D. Kim, N. Seto, M. Mizutani, and S. Katayama, “Dynamics of keyhole and molten pool in laser welding,” *J. Laser Appl.*, vol. 10, no. 6, pp. 247–254, 1998, doi: 10.2351/1.521858.

[42] N. Seto, S. Katayama, and A. Matsunawa, “Porosity formation mechanism and reduction

method in CO2laser welding of stainless steel," *Yosetsu Gakkai Ronbunshu/Quarterly J. Japan Weld. Soc.*, vol. 19, no. 4, pp. 600–609, 2001, doi: 10.2207/qjjws.19.600.

[43] S. Kou, *Welding Metallurgy*, Second. Hoboken, New Jersey, 2003.

[44] S. Tammas-Williams, H. Zhao, F. Léonard, F. Derguti, I. Todd, and P. B. Prangnell, "XCT analysis of the influence of melt strategies on defect population in Ti-6Al-4V components manufactured by Selective Electron Beam Melting," *Mater. Charact.*, vol. 102, pp. 47–61, 2015, doi: 10.1016/j.matchar.2015.02.008.

[45] D. Gu, C. Ma, M. Xia, D. Dai, and Q. Shi, "A Multiscale Understanding of the Thermodynamic and Kinetic Mechanisms of Laser Additive Manufacturing," *Engineering*, vol. 3, no. 5, pp. 675–684, 2017, doi: 10.1016/J.ENG.2017.05.011.

[46] I. Zhirnov, N. Panahi, M. Åsberg, and P. Krakhmalev, "Process quality assessment with imaging and acoustic monitoring during Laser Powder Bed Fusion," *Procedia CIRP*, vol. 111, no. September 2022, pp. 363–367, 2022, doi: 10.1016/j.procir.2022.08.167.

[47] H. V Atkinson and S. Davies, "Fundamental Aspects of Hot Isostatic Pressing : An Overview," *Metall. Mater. Trans. A*, vol. 31, no. December, pp. 2981–3000, 2000, doi: 10.1007/s11661-000-0078-2.

[48] H. V Atkinson and S. Davies, "Fundamental Aspects of Hot Isostatic Pressing : An Overview," vol. m, no. December, 2000.

[49] Kobelco, "What is Hot Isostatic Pressing?" https://www.kobelco.co.jp/english/products/ip/technology/hip.html (accessed Jul. 20, 2023).

[50] W. Tillmann, C. Schaak, J. Nellesen, M. Schaper, M. E. Aydinöz, and K. P. Hoyer, "Hot isostatic pressing of IN718 components manufactured by selective laser melting," *Addit. Manuf.*, vol. 13, no. November, pp. 93–102, 2017, doi: 10.1016/j.addma.2016.11.006.

[51] A. du Plessis and E. Macdonald, "Hot isostatic pressing in metal additive manufacturing: X-ray tomography reveals details of pore closure," *Addit. Manuf.*, vol. 34, no. February, p. 101191, 2020, doi: 10.1016/j.addma.2020.101191.

[52] W. Tillmann *et al.*, "Functional encapsulation of laser melted Inconel 718 by Arc-PVD and HVOF for post compacting by hot isostatic pressing Functional encapsulation of laser melted Inconel 718 by Arc-PVD and HVOF for post compacting by hot isostatic pressing," *Powder Metall.*, vol. 58, no. 4, pp. 259–264, 2015, doi: 10.1179/0032589915Z.000000000250.

[53] A. du Plessis and P. Rossouw, “Investigation of Porosity Changes in Cast Ti6Al4V Rods After Hot Isostatic Pressing,” *J. Mater. Eng. Perform.*, vol. 24, no. 8, pp. 3137–3141, 2015, doi: 10.1007/s11665-015-1580-4.

[54] S. Tammas-williams, P. J. Withers, I. Todd, and P. B. Prangnell, “The Effectiveness of Hot Isostatic Pressing for Closing Porosity in Selective Electron Beam Melting,” *Metall. Mater. Trans. A*, vol. 47A, no. 5, pp. 1939–1946, 2016, doi: 10.1007/s11661-016-3429-3.

[55] S. Tammas-Williams, P. J. Withers, I. Todd, and P. B. Prangnell, “Porosity regrowth during heat treatment of hot isostatically pressed additively manufactured titanium components,” *Scr. Mater.*, vol. 122, pp. 72–76, 2016, doi: 10.1016/j.scriptamat.2016.05.002.

[56] J. Bustillos, J. Kim, and A. Moridi, “Exploiting lack of fusion defects for microstructural engineering in additive manufacturing,” *Addit. Manuf.*, vol. 48, p. 102399, 2021, doi: 10.1016/j.addma.2021.102399.

[57] A. Kaletsch, S. Qin, S. Herzog, and C. Broeckmann, “Influence of high initial porosity introduced by laser powder bed fusion on the fatigue strength of Inconel 718 after post-processing with hot isostatic pressing,” *Addit. Manuf.*, vol. 47, 2021, doi: 10.1016/j.addma.2021.102331.

[58] I. Yadroitsev, P. Bertrand, G. Antonenkova, S. Grigoriev, and I. Smurov, “Use of track/layer morphology to develop functional parts by selective laser melting,” *J. Laser Appl.*, vol. 25, no. 5, p. 052003, 2013, doi: 10.2351/1.4811838.

[59] M. J. Matthews, G. Guss, S. A. Khairallah, A. M. Rubenchik, P. J. Depond, and W. E. King, “Denudation of metal powder layers in laser powder-bed fusion processes,” *Acta Mater.*, vol. 114, pp. 33–42, 2016, doi: 10.1201/9781315119106.

[60] I. Yadroitsev, A. Gusarov, I. Yadroitsava, and I. Smurov, “Single track formation in selective laser melting of metal powders,” *J. Mater. Process. Technol.*, vol. 210, no. 12, pp. 1624–1631, 2010, doi: 10.1016/j.jmatprotec.2010.05.010.

[61] P. Bidare, I. Bitharas, R. M. Ward, M. M. Attallah, and A. J. Moore, “Fluid and particle dynamics in laser powder bed fusion,” *Acta Mater.*, vol. 142, pp. 107–120, 2018, doi: 10.1016/j.actamat.2017.09.051.

[62] M. J. Matthews, G. Guss, S. A. Khairallah, A. M. Rubenchik, P. J. Depond, and W. E. King, “Denudation of metal powder layers in laser powder bed fusion processes,” *Acta Mater.*, vol. 114, pp. 33–42, 2016, doi: .1037//0033-2909.I26.1.78.

[63] P. J. DePond *et al.*, “In situ measurements of layer roughness during laser powder bed fusion additive manufacturing using low coherence scanning interferometry,” *Mater. Des.*, vol. 154, pp. 347–359, 2018, doi: 10.1016/j.matdes.2018.05.050.

[64] R. Li, J. Liu, Y. Shi, L. Wang, and W. Jiang, “Balling behavior of stainless steel and nickel powder during selective laser melting process,” *Int. J. Adv. Manuf. Technol.*, vol. 59, no. 9–12, pp. 1025–1035, 2012, doi: 10.1007/s00170-011-3566-1.

[65] S. A. Khairallah and A. Anderson, “Mesoscopic simulation model of selective laser melting of stainless steel powder,” *J. Mater. Process. Technol.*, vol. 214, no. 11, pp. 2627–2636, 2014, doi: 10.1016/j.jmatprotec.2014.06.001.

[66] S. Kleszczynski, J. Zur Jacobsmühlen, J. T. Sehrt, and G. Witt, “Error detection in laser beam melting systems by high resolution imaging,” *23rd Annu. Int. Solid Free. Fabr. Symp. - An Addit. Manuf. Conf. SFF 2012*, no. August, pp. 975–987, 2012.

[67] C. Li, Z. Y. Liu, X. Y. Fang, and Y. B. Guo, “Residual Stress in Metal Additive Manufacturing,” *Procedia CIRP 71*, vol. 72, pp. 348–353, 2018, doi: 10.1016/j.procir.2018.03.131.

[68] S. Periane *et al.*, “Influence of heat treatment on the fatigue resistance of Inconel 718 fabricated by selective laser melting (SLM),” *Mater. Today Proc.*, vol. 46, no. March, pp. 7860–7865, 2021, doi: 10.1016/j.matpr.2021.02.447.

[69] P. Mercelis and J. P. Kruth, “Residual stresses in selective laser sintering and selective laser melting,” *Rapid Prototyp. J.*, vol. 12, no. 5, pp. 254–265, 2006, doi: 10.1108/13552540610707013.

[70] T. Mishurova *et al.*, “The Influence of the Support Structure on Residual Stress and Distortion in SLM Inconel 718 Parts,” *Metall. Mater. Trans. A Phys. Metall. Mater. Sci.*, vol. 49, no. 7, pp. 3038–3046, 2018, doi: 10.1007/s11661-018-4653-9.

[71] Special Metals Corporation, “Inconel Alloy 718,” *Tech. Bull.*, no. SMC-045, pp. 1–28, 2007, [Online]. Available: https://www.specialmetals.com/documents/technical-bulletins/inconel/inconel-alloy-718.pdf

[72] R. Barros *et al.*, “Laser powder bed fusion of inconel 718: Residual stress analysis before and after heat treatment,” *Metals (Basel).*, vol. 9, no. 12, 2019, doi: 10.3390/met9121290.

[73] N. J. Harrison, I. Todd, and K. Mumtaz, “Reduction of micro-cracking in nickel superalloys processed by Selective Laser Melting: A fundamental alloy design approach,” *Acta Mater.*,

vol. 94, pp. 59–68, 2015, doi: 10.1016/j.actamat.2015.04.035.

[74] A. J. Dunbar *et al.*, “Development of experimental method for in situ distortion and temperature measurements during the laser powder bed fusion additive manufacturing process,” *Addit. Manuf.*, vol. 12, pp. 25–30, 2016, doi: 10.1016/j.addma.2016.04.007.

[75] T. Mukherjee, W. Zhang, and T. DebRoy, “An improved prediction of residual stresses and distortion in additive manufacturing,” *Comput. Mater. Sci.*, vol. 126, pp. 360–372, 2017, doi: 10.1016/j.commatsci.2016.10.003.

[76] M. M. S. N. for R. C. of A. M. P. B. F. P. N. I. R. (NISTIR)-8036 Mani, B. Lane, M. A. Donmez, S. C. Feng, S. P. Moylan, and R. Fesperman, “Measurement Science Needs for Real-time Control of Additive Manufacturing Powder Bed Fusion Processes (NISTIR) - 8036,” *NIST Interagency/Internal Rep.*, vol. 8036, no. September, p. 50, 2015, doi: 10.6028/NIST.IR.8036.

[77] M. Mani, B. M. Lane, M. A. Donmez, S. C. Feng, and S. P. Moylan, “A review on measurement science needs for real-time control of additive manufacturing metal powder bed fusion processes,” *Int. J. Prod. Res.*, vol. 55, no. 5, pp. 1400–1418, 2017, doi: 10.1080/00207543.2016.1223378.

[78] P. Lott, H. Schleifenbaum, W. Meiners, K. Wissenbach, C. Hinke, and J. Bültmann, “Design of an optical system for the in situ process monitoring of Selective Laser Melting (SLM),” *Phys. Procedia*, vol. 12, no. PART 1, pp. 683–690, 2011, doi: 10.1016/j.phpro.2011.03.085.

[79] S. K. Everton, M. Hirsch, P. I. Stavroulakis, R. K. Leach, and A. T. Clare, “Review of in-situ process monitoring and in-situ metrology for metal additive manufacturing,” *Mater. Des.*, vol. 95, pp. 431–445, 2016, doi: 10.1016/j.matdes.2016.01.099.

[80] G. Tapia and A. Elwany, “A Review on Process Monitoring and Control in Metal-Based Additive Manufacturing,” *J. Manuf. Sci. Eng.*, vol. 136, no. 6, p. 060801, 2014, doi: 10.1115/1.4028540.

[81] M. Pavlov, M. Doubenskaia, and I. Smurov, “Pyrometric analysis of thermal processes in SLM technology,” *Physics Procedia*, vol. 5, no. PART 2. pp. 523–531, 2010. doi: 10.1016/j.phpro.2010.08.080.

[82] P. A. Hooper, “Melt pool temperature and cooling rates in laser powder bed fusion,” *Addit. Manuf.*, vol. 22, no. May, pp. 548–559, 2018, doi: 10.1016/j.addma.2018.05.032.

[83] S. Clijsters, T. Craeghs, S. Buls, K. Kempen, and J. P. Kruth, “In situ quality control of the

selective laser melting process using a high-speed, real-time melt pool monitoring system," *Int. J. Adv. Manuf. Technol.*, vol. 75, no. 5–8, pp. 1089–1101, 2014, doi: 10.1007/s00170-014-6214-8.

[84] T. Craeghs, S. Clijsters, J. P. Kruth, F. Bechmann, and M. C. Ebert, "Detection of Process Failures in Layerwise Laser Melting with Optical Process Monitoring," *Phys. Procedia*, vol. 39, pp. 753–759, 2012, doi: 10.1016/j.phpro.2012.10.097.

[85] J.-P. Kruth, J. Duflou, P. Mercelis, J. Van Vaerenbergh, T. Craeghs, and J. De Keuster, "On-line monitoring and process control in selective laser melting and laser cutting," in *Proceedings of the 5th Lane Conference, Laser Assisted Net Shape Engineering*, 2007, vol. 1, no. 1, pp. 23–37. [Online]. Available: https://lirias.kuleuven.be/bitstream/123456789/163155/1/07PP090.pdf

[86] J. Kruth and P. Mercelis, "Procedure and Apparatus for In-situ Monitoring and Feedback Control of Selective Laser Powder Processing," 2009

[87] P. Mercelis, J. P. Kruth, and J. Van Vaerenbergh, "Feedback control of selective laser melting," *Proc. 15th Int. Symp. Electromachining, ISEM 2007*, pp. 421–426, 2007.

[88] T. Craeghs, F. Bechmann, S. Berumen, and J. P. Kruth, "Feedback control of Layerwise Laser Melting using optical sensors," *Phys. Procedia*, vol. 5, no. PART 2, pp. 505–514, 2010, doi: 10.1016/j.phpro.2010.08.078.

[89] M. Doubenskaia, M. Pavlov, S. Grigoriev, E. Tikhonova, and I. Smurov, "Comprehensive Optical Monitoring of Selective Laser Melting," *JLMN-Journal of Laser Micro/Nanoengineering*, vol. 7, no. 3, pp. 236–243, 2012, doi: 10.2961/j1mn.2012.03.001.

[90] F. Bayle and M. Doubenskaia, "Selective Laser Melting process monitoring with high speed infra-red camera and pyrometer," *Fundam. Laser Assist. Micro- Nanotechnologies*, vol. 6985, no. 698505, pp. 1–8, 2008, doi: 10.1117/12.786940.

[91] C. Barrett, C. Carradero, E. Harris, K. Rogers, E. MacDonald, and B. Conner, "Statistical analysis of spatter velocity with high-speed stereovision in laser powder bed fusion," *Prog. Addit. Manuf.*, vol. 4, no. 4, pp. 423–430, 2019, doi: 10.1007/s40964-019-00094-6.

[92] M. Bisht, N. Ray, F. Verbist, and S. Coeck, "Correlation of selective laser melting-melt pool events with the tensile properties of Ti-6Al-4V ELI processed by laser powder bed fusion," *Addit. Manuf.*, vol. 22, no. May, pp. 302–306, 2018, doi: 10.1016/j.addma.2018.05.004.

[93] S. Coeck, M. Bisht, J. Plas, and F. Verbist, "Prediction of lack of fusion porosity in selective

laser melting based on melt pool monitoring data," *Addit. Manuf.*, vol. 25, no. October 2018, pp. 347–356, 2019, doi: 10.1016/j.addma.2018.11.015.

[94] B. K. Foster, E. W. Reutzel, A. R. Nassar, B. T. Hall, S. W. Brown, and C. J. Dickman, "Optical, layerwise monitoring of powder bed fusion," pp. 295–307.

[95] M. Mahmoudi, A. A. Ezzat, and A. Elwany, "Layerwise Anomaly Detection in Laser Powder-Bed Fusion Metal Additive Manufacturing," *J. Manuf. Sci. Eng. Trans. ASME*, vol. 141, no. 3, pp. 1–13, 2019, doi: 10.1115/1.4042108.

[96] M. Grasso, V. Laguzza, Q. Semeraro, and B. M. Colosimo, "In-Process Monitoring of Selective Laser Melting: Spatial Detection of Defects Via Image Data Analysis," *J. Manuf. Sci. Eng. Trans. ASME*, vol. 139, no. 5, 2017, doi: 10.1115/1.4034715.

[97] A. R. Nassar, J. S. Keist, E. W. Reutzel, and T. J. Spurgeon, "Intra-layer closed-loop control of build plan during directed energy additive manufacturing of Ti-6Al-4V," *Addit. Manuf.*, vol. 6, pp. 39–52, 2015, doi: 10.1016/j.addma.2015.03.005.

[98] A. Neef, V. Seyda, D. Herzog, C. Emmelmann, M. Schönleber, and M. Kogel-Hollacher, "Low coherence interferometry in selective laser melting," *Phys. Procedia*, vol. 56, no. C, pp. 82–89, 2014, doi: 10.1016/j.phpro.2014.08.100.

[99] J. A. Kanko, A. P. Sibley, and J. M. Fraser, "In situ morphology-based defect detection of selective laser melting through inline coherent imaging," *J. Mater. Process. Technol.*, vol. 231, pp. 488–500, 2016, doi: 10.1016/j.jmatprotec.2015.12.024.

[100] T. G. Fleming, S. G. L. Nestor, M. A. Boukhaled, T. R. Allen, N. J. Smith, and J. M. Fraser, "Tracking the Morphology Evolution of 3D Selective Laser Melting in situ using Inline Coherent Imaging," *2018 Conf. Lasers Electro-Optics, CLEO 2018 - Proc.*, vol. 1, no. c, pp. 4–5, 2018.

[101] A. J. Dunbar and A. R. Nassar, "Assessment of optical emission analysis for in-process monitoring of powder bed fusion additive manufacturing," *Virtual Phys. Prototyp.*, vol. 13, no. 1, pp. 14–19, 2018, doi: 10.1080/17452759.2017.1392683.

[102] W. Ya, A. R. Konuk, R. Aarts, B. Pathiraj, and B. Huis In 'T Veld, "Spectroscopic monitoring of metallic bonding in laser metal deposition," *J. Mater. Process. Technol.*, vol. 220, pp. 276–284, 2015, doi: 10.1016/j.jmatprotec.2015.01.026.

[103] M. Montazeri, A. R. Nassar, A. J. Dunbar, and P. Rao, "In-process monitoring of porosity in

additive manufacturing using optical emission spectroscopy," *IISE Trans.*, vol. 52, no. 5, pp. 500–515, 2020, doi: 10.1080/24725854.2019.1659525.

[104] M. J. Donachie and S. J. Donachie, "Superalloys: A Technical Guide," in *ASM International*, 2nd Editio., 2002, pp. 26–28. doi: 10.1361.

[105] R. C. Reed, "The Physical Metallurgy of Nickel and its Alloys," in *The Superalloys: Fundamentals and Applications*, Cambridge University Press, 2008, pp. 49–50.

[106] H. I. H. Saravanamutto, G. F. C. Rogers, H. Cohen, and P. V. Straznicky, *Gas Turbine Theory*, Sixth Edit. Edinburgh: Pearson Education Limited, 2009.

[107] T. Sonar, V. Balasubramanian, S. Malarvizhi, T. Venkateswaran, and D. Sivakumar, "An overview on welding of Inconel 718 alloy - Effect of welding processes on microstructural evolution and mechanical properties of joints," *Mater. Charact.*, vol. 174, no. February, p. 110997, 2021, doi: 10.1016/j.matchar.2021.110997.

[108] T. DebRoy *et al.*, "Additive manufacturing of metallic components – Process, structure and properties," *Prog. Mater. Sci.*, vol. 92, no. October, pp. 112–224, 2018, doi: 10.1016/j.pmatsci.2017.10.001.

[109] National Speciality Alloys, "718/Inconel® Nickel Alloy Bar." http://www.nsalloys.com/products/nickel-alloy-bar/718inconel-nickel-alloy-bar.html

[110] A. International, "Standard Specification for Additive Manufacturing Nickel Alloy (UNS N07718) with Powder Bed Fusion F3055," *ASTM Stand.*, no. March, pp. 1–8, 2014, doi: 10.1520/F3055-14A.Copyright.

[111] R. C. Reed and R. C. Reed, "The physical metallurgy of nickel and its alloys," in *The Superalloys*, 2009, pp. 33–120. doi: 10.1017/cbo9780511541285.004.

[112] S. Sanchez, G. Gaspard, C. J. Hyde, I. A. Ashcroft, G. A. Ravi, and A. T. Clare, "The creep behaviour of nickel alloy 718 manufactured by laser powder bed fusion," *Mater. Des.*, vol. 204, p. 109647, 2021, doi: 10.1016/j.matdes.2021.109647.

[113] P. M. Mignanelli *et al.*, "Gamma-gamma prime-gamma double prime dual-superlattice superalloys," *Scr. Mater.*, vol. 136, pp. 136–140, 2017, doi: 10.1016/j.scriptamat.2017.04.029.

[114] K. Löhnert and F. Pyczak, "Microstructure evolution in the nickel base superalloy Allvac® 718Plus^{TM}," *7th Int. Symp. Superalloy 718 Deriv. 2010*, vol. 2, no. January, pp. 877–891, 2010, doi: 10.1002/9781118495223.ch67.

[115] H. K. D. H. Bhadeshia, “Nickel Based Superalloys,” *University of Cambridge*. https://www.phase-trans.msm.cam.ac.uk/2003/Superalloys/superalloys.html (accessed Sep. 13, 2022).

[116] G. H. Cao *et al.*, “Investigations of γ′ γ″ and δ precipitates in heat-treated Inconel 718 alloy fabricated by selective laser melting,” *Mater. Charact.*, vol. 136, no. January, pp. 398–406, 2018, doi: 10.1016/j.matchar.2018.01.006.

[117] W. M. Tucho and V. Hansen, “Characterization of SLM-fabricated Inconel 718 after solid solution and precipitation hardening heat treatments,” *J. Mater. Sci.*, vol. 54, no. 1, pp. 823–839, 2019, doi: 10.1007/s10853-018-2851-x.

[118] S. R. Shatynski, “The thermochemistry of transition metal carbides,” *Oxid. Met.*, vol. 13, no. 2, pp. 105–118, 1979, doi: 10.1007/BF00611975.

[119] C. T. Sims, N. S. Stoloff, and W. C. Hagel, *Superalloys II: High Temperature Materials for Aerospace and Industrial Power*. John Wiley & Sons, 1987.

[120] J. William D. Callister and D. G. Rethwisch, *Materials Science and Engineering*, Ninth. John Wiley & Sons (Asia) Pte Ltd, 2011.

[121] F. J. Humphreys and M. Hatherly, *Recrystallization and Related Annealing Phenomena*, 2nd ed. Elsevier Ltd, 2004.

[122] L. R. Owen and N. G. Jones, “Lattice distortions in high-entropy alloys,” *J. Mater. Res.*, vol. 33, no. 19, pp. 2954–2969, 2018, doi: 10.1557/jmr.2018.322.

[123] J. W. T. Read, *Dislocations in Crystals*. McGraw-Hill Book Company, Inc, 1953.

[124] A. Rollett, F. J. Humphreys, G. S. Rohrer, and M. Hatherly, “Chapter 2: The Deformed State,” in *Recrystallization and Related Annealing Phenomena*, 2004.

[125] S. Gao *et al.*, “Recrystallization-based grain boundary engineering of 316L stainless steel produced via selective laser melting,” *Acta Mater.*, vol. 200, pp. 366–377, 2020, doi: 10.1016/j.actamat.2020.09.015.

[126] R. W. K. Honeycombe, *The Plastic Deformation of Metals*. Edward Arnold (Publishers) Ltd., 1968.

[127] D. Raabe, “Recovery and Recrystallization: Phenomena, Physics, Models, Simulation,” in *Physical Metallurgy*, Fifth Edit., vol. 1, D. E. Laughlin and K. Hono, Eds. Elsevier, 2014, pp. 2291–2397. doi: 10.1016/B978-0-444-53770-6.00023-X.

[128] I. Z. Awan and A. Q. Khan, “Recovery, Recrystallization, and Grain-Growth,” *Chem. Soc. Pakistan*, vol. 41, no. January, 2019, doi: 10.52568/000707/JCSP/41.01.2019.

[129] K. Huang and R. E. Logé, “A review of dynamic recrystallization phenomena in metallic materials,” *Mater. Des.*, vol. 111, pp. 548–574, 2016, doi: 10.1016/j.matdes.2016.09.012.

[130] A. Kelly and G. W. Groves, *Crystallography and Crystal Defects*. Bristol: J. W. Arrowsmith Ltd., 1970.

[131] E. Chlebus, K. Gruber, B. Kuźnicka, J. Kurzac, and T. Kurzynowski, “Effect of heat treatment on the microstructure and mechanical properties of Inconel 718 processed by selective laser melting,” *Mater. Sci. Eng. A*, vol. 639, pp. 647–655, 2015, doi: 10.1016/j.msea.2015.05.035.

[132] K. K. Alaneme and E. A. Okotete, “Recrystallization mechanisms and microstructure development in emerging metallic materials: A review,” *J. Sci. Adv. Mater. Devices*, vol. 4, no. 1, pp. 19–33, 2019, doi: 10.1016/j.jsamd.2018.12.007.

[133] N. Hansen, “Hall-petch relation and boundary strengthening,” *Scr. Mater.*, vol. 51, no. 8 SPEC. ISS., pp. 801–806, 2004, doi: 10.1016/j.scriptamat.2004.06.002.

[134] R. D. Doherty, “Recrystallisation and Texture,” *Prog. Mater. Sci.*, vol. 42, pp. 39–58, 1997.

[135] R. W. Cahn, “Recovery and Recrystallization,” in *Physical Metallurgy*, North-Holland Printing Company, 1965, pp. 925–985.

[136] P. A. Beck and P. R. Sperry, “Strain induced grain boundary migration in high purity aluminum,” *J. Appl. Phys.*, vol. 21, no. 2, pp. 150–152, 1950, doi: 10.1063/1.1699614.

[137] H. Beladi, P. Cizek, and P. D. Hodgson, “Dynamic recrystallization of austenite in Ni-30 Pct Fe model alloy: Microstructure and texture evolution,” *Metall. Mater. Trans. A Phys. Metall. Mater. Sci.*, vol. 40, no. 5, pp. 1175–1189, 2009, doi: 10.1007/s11661-009-9799-z.

[138] M. Azarbarmas, M. Aghaie-Khafri, J. M. Cabrera, and J. Calvo, “Dynamic recrystallization mechanisms and twining evolution during hot deformation of Inconel 718,” *Mater. Sci. Eng. A*, vol. 678, no. September, pp. 137–152, 2016, doi: 10.1016/j.msea.2016.09.100.

[139] Y. In, B. Lin, A. D. Rollett, G. S. Rohrer, M. Bernacki, and N. Bozzolo, “Thermo-mechanical factors influencing annealing twin development in nickel during recrystallization,” *J. Mater. Sci.*, vol. 50, no. 15, pp. 5191–5203, 2015, doi: 10.1007/s10853-015-9067-0.

[140] Y. C. Lin *et al.*, “EBSD study of a hot deformed nickel-based superalloy,” *J. Alloys Compd.*, vol. 640, pp. 101–113, 2015, doi: 10.1016/j.jallcom.2015.04.008.

[141] A. M. Wusatowska-Sarnek, H. Miura, and T. Sakai, “Nucleation and microtexture development under dynamic recrystallization of copper,” *Mater. Sci. Eng. A*, vol. 323, no. 1–2, pp. 177–186, 2002, doi: 10.1016/S0921-5093(01)01336-3.

[142] D. A. Porter, K. E. Easterling, and M. Y. Sherif, “Crystal Interfaces and Microstructure,” in *Phase Transformations in Metals and Alloys*, Chapman & Hall, 2009.

[143] S. Mahajan, C. S. Pande, M. A. Imam, and B. B. Rath, “Formation of annealing twins in FCC crystals,” *Acta Mater.*, vol. 45, no. 6, pp. 2633–2638, 1997.

[144] M. A. Meyers and C. McCowan, “The formation of annealing twins: overview and new thoughts,” 1984.

[145] N. Bozzolo and M. Bernacki, “Viewpoint on the Formation and Evolution of Annealing Twins During Thermomechanical Processing of FCC Metals and Alloys,” *Metall. Mater. Trans. A*, vol. 51, no. 6, pp. 2665–2684, 2020, doi: 10.1007/s11661-020-05772-7.

[146] V. Randle, “Twinning-related grain boundary engineering,” *Acta Mater.*, vol. 52, no. 14, pp. 4067–4081, 2004, doi: 10.1016/j.actamat.2004.05.031.

[147] G. Palumbo, E. M. Lehockey, and P. Lin, “Applications for grain boundary engineered materials,” *Jom*, vol. 50, no. 2, pp. 40–43, 1998, doi: 10.1007/s11837-998-0248-z.

[148] V. Randle, “Mechanism of Twinning-Induced Grain Boundary Engineering in Low Stacking-Fault Energy Materials,” *Acta Metall. Inc*, vol. 47, no. 15, pp. 4187–4196, 1999, doi: 10.1016/S1359-6454(99)00277-3.

[149] U. Krupp, “Improving the resistance to intergranular cracking and corrosion at elevated temperatures by grain-boundary-engineering-type processing,” *J. Mater. Sci.*, vol. 43, pp. 3908–3916, 2008, doi: 10.1007/s10853-007-2363-6.

[150] W. M. Tucho and V. Hansen, “Studies of Post-Fabrication Heat Treatment of L-PBF-Inconel 718: Effects of Hold Time on Microstructure, Annealing Twins, and Hardness,” *Metals (Basel).*, vol. 11, no. 266, 2021, doi: 10.3390/met11020266.

[151] B. Lin *et al.*, “Observation of annealing twin nucleation at triple lines in nickel during grain growth,” *Acta Mater.*, vol. 99, pp. 63–68, 2015, doi: 10.1016/j.actamat.2015.07.041.

[152] D. D. R. Peachey *et al.*, “Directional recrystallization of an additively manufactured Ni-base superalloy,” *Addit. Manuf.*, vol. 60, no. PA, p. 103198, 2022, doi: 10.1016/j.addma.2022.103198.

[153] W. Kurz and D. J. Fisher, *Fundamentals of Solidification*, 4th ed. Trans Tech Publications Ltd, 1998.

[154] W. Losert, B. Q. Shi, and H. Z. Cummins, “Evolution of dendritic patterns during alloy solidification: From the initial instability to the steady state,” *Proc. Natl. Acad. Sci. U. S. A.*, vol. 95, no. 2, pp. 439–442, 1998, doi: 10.1073/pnas.95.2.439.

[155] D. A. Porter and K. E. Easterling, “Solidification,” in *Phase Transformations in Metals and Alloys*, Chapman & Hall, 1981, pp. 185–249.

[156] S. Kou, *WELDING METALLURGY*, Second Edi. John Wiley & Sons, 2003.

[157] Y. Yehorov, L. J. da Silva, and A. Scotti, “Exploring the use of switchback for mitigating homoepitaxial unidirectional grain growth and porosity in WAAM of aluminium alloys,” *Int. J. Adv. Manuf. Technol.*, vol. 104, no. 1–4, pp. 1581–1592, 2019, doi: 10.1007/s00170-019-03959-w.

[158] X. Wang, X. Gong, and K. Chou, “Review on powder-bed laser additive manufacturing of Inconel 718 parts,” *Proc IMechE Part B; J. Eng. Manuf.*, pp. 1890–1903, 2015, doi: 10.1177/0954405415619883.

[159] E. Hosseini and V. A. Popovich, “A review of mechanical properties of additively manufactured Inconel 718,” *Addit. Manuf.*, vol. 30, 2019, doi: 10.1016/j.addma.2019.100877.

[160] Q. B. Nguyen, M. L. S. Nai, Z. Zhu, C. N. Sun, J. Wei, and W. Zhou, “Characteristics of Inconel Powders for Powder-Bed Additive Manufacturing,” *Engineering*, vol. 3, no. 5, pp. 695–700, 2017, doi: 10.1016/J.ENG.2017.05.012.

[161] L. C. Ardila *et al.*, “Effect of IN718 recycled powder reuse on properties of parts manufactured by means of Selective Laser Melting,” *Phys. Procedia*, vol. 56, no. C, pp. 99–107, 2014, doi: 10.1016/j.phpro.2014.08.152.

[162] E. Paccou *et al.*, “Investigations of powder reusing on microstructure and mechanical properties of Inconel 718 obtained by additive manufacturing,” *Mater. Sci. Eng. A*, vol. 828, no. June, 2021, doi: 10.1016/j.msea.2021.142113.

[163] Z. Wang, K. Guan, M. Gao, X. Li, X. Chen, and X. Zeng, “The microstructure and mechanical properties of deposited-IN718 by selective laser melting,” *J. Alloys Compd.*, vol. 513, pp. 518–523, 2012, doi: 10.1016/j.jallcom.2011.10.107.

[164] E. Malekipour and H. El-Mounayri, *Mechanics of Additive and Advanced Manufacturing,*

Volume 8 - Chapter 12, no. October. Springer, 2017. doi: 10.1007/978-3-319-95083-9.

[165] L. L. Parimi, G. Ravi, D. Clark, and M. M. Attallah, "Microstructural and texture development in direct laser fabricated IN718," *Mater. Charact.*, vol. 89, pp. 102–111, 2014, doi: 10.1016/j.matchar.2013.12.012.

[166] L. N. Carter, C. Martin, P. J. Withers, and M. M. Attallah, "The influence of the laser scan strategy on grain structure and cracking behaviour in SLM powder-bed fabricated nickel superalloy," *J. Alloys Compd.*, vol. 615, pp. 338–347, 2014, doi: 10.1016/j.jallcom.2014.06.172.

[167] F. Liu *et al.*, "The effect of laser scanning path on microstructures and mechanical properties of laser solid formed nickel-base superalloy Inconel 718," *J. Alloys Compd.*, vol. 509, no. 13, pp. 4505–4509, 2011, doi: 10.1016/j.jallcom.2010.11.176.

[168] L. Parry, I. A. Ashcroft, and R. D. Wildman, "Understanding the effect of laser scan strategy on residual stress in selective laser melting through thermo-mechanical simulation," *Addit. Manuf.*, vol. 12, pp. 1–15, 2016, doi: 10.1016/j.addma.2016.05.014.

[169] G. E. Bean, D. B. Witkin, T. D. McLouth, D. N. Patel, and R. J. Zaldivar, "Effect of laser focus shift on surface quality and density of Inconel 718 parts produced via selective laser melting," *Addit. Manuf.*, vol. 22, no. April, pp. 207–215, 2018, doi: 10.1016/j.addma.2018.04.024.

[170] X. Shi *et al.*, "Performance of high layer thickness in selective laser melting of Ti6Al4V," *Materials (Basel).*, vol. 9, no. 12, pp. 1–15, 2016, doi: 10.3390/ma9120975.

[171] A. A. Popovich, V. S. Sufiiarov, I. A. Polozov, and E. V. Borisov, "Microstructure and mechanical properties of Inconel 718 produced by SLM and subsequent heat treatment," *Key Eng. Mater.*, vol. 651–653, no. February, pp. 665–670, 2015, doi: 10.4028/www.scientific.net/KEM.651-653.665.

[172] Y. Gao *et al.*, "Effect of δ phase on high temperature mechanical performances of Inconel 718 fabricated with SLM process," *Mater. Sci. Eng. A*, vol. 767, no. 100, 2019, doi: 10.1016/j.msea.2019.138327.

[173] M. E. Aydinöz *et al.*, "On the microstructural and mechanical properties of post-treated additively manufactured Inconel 718 superalloy under quasi-static and cyclic loading," *Mater. Sci. Eng. A*, vol. 669, no. May, pp. 246–258, 2016, doi: 10.1016/j.msea.2016.05.089.

[174] S. Y. Park, K. S. Kim, M. C. Kim, M. E. Kassner, and K. A. Lee, "Effect of Post-heat Treatment on

the Tensile and Cryogenic Impact Toughness Properties of Inconel 718 Manufactured by Selective Laser Melting," *Adv. Eng. Mater.*, vol. 23, no. 3, 2021, doi: 10.1002/adem.202001005.

[175] K. A. Sofinowski, S. Raman, X. Wang, B. Gaskey, and M. Seita, "Layer-wise engineering of grain orientation (LEGO) in laser powder bed fusion of stainless steel 316L," *Addit. Manuf.*, vol. 38, p. 101809, 2021, doi: 10.1016/j.addma.2020.101809.

[176] D. Deng, R. L. Peng, H. Brodin, and J. Moverare, "Microstructure and mechanical properties of Inconel 718 produced by selective laser melting: Sample orientation dependence and effects of post heat treatments," *Mater. Sci. Eng. A*, vol. 713, no. December, pp. 294–306, 2018, doi: 10.1016/j.msea.2017.12.043.

[177] W. M. Tucho, P. Cuvillier, A. Sjolyst-Kverneland, and V. Hansen, "Microstructure and hardness studies of Inconel 718 manufactured by selective laser melting before and after solution heat treatment," *Mater. Sci. Eng. A*, vol. 689, no. December 2016, pp. 220–232, 2017, doi: 10.1016/j.msea.2017.02.062.

[178] T. G. Gallmeyer, S. Moorthy, B. B. Kappes, M. J. Mills, B. Amin-Ahmadi, and A. P. Stebner, "Knowledge of process-structure-property relationships to engineer better heat treatments for laser powder bed fusion additive manufactured Inconel 718," *Addit. Manuf.*, vol. 31, no. August 2019, p. 100977, 2020, doi: 10.1016/j.addma.2019.100977.

[179] S. Raghavan *et al.*, "Effect of different heat treatments on the microstructure and mechanical properties in selective laser melted INCONEL 718 alloy," *Mater. Manuf. Process.*, vol. 32, no. 14, pp. 1588–1595, 2017, doi: 10.1080/10426914.2016.1257805.

[180] F. Brenne *et al.*, "Microstructural design of Ni-base alloys for high-temperature applications: impact of heat treatment on microstructure and mechanical properties after selective laser melting," *Prog. Addit. Manuf.*, vol. 1, no. 3–4, pp. 141–151, 2016, doi: 10.1007/s40964-016-0013-8.

[181] J. Strößner, M. Terock, and U. Glatzel, "Mechanical and Microstructural Investigation of Nickel-Based Superalloy IN718 Manufactured by Selective Laser Melting (SLM)," *Adv. Eng. Mater.*, vol. 17, no. 8, pp. 1099–1105, 2015, doi: 10.1002/adem.201500158.

[182] J. N. DuPont, C. V. Robino, J. R. Michael, M. R. Nous, and A. R. Marder, "Solidification of Nb-bearing superalloys: Part I. Reaction sequences," *Metall. Mater. Trans. A Phys. Metall. Mater. Sci.*, vol. 29, no. 11, pp. 2785–2796, 1998, doi: 10.1007/s11661-998-0319-3.

[183] N. Kouraytem *et al.*, “A recrystallization heat-treatment to reduce deformation anisotropy of additively manufactured Inconel 718,” *Mater. Des.*, vol. 198, 2021, doi: 10.1016/j.matdes.2020.109228.

[184] F. Xiao, R. Yang, L. Fang, and C. Zhang, “Solidification shrinkage of Ni-Cr alloys,” *Mater. Sci. Eng. B Solid-State Mater. Adv. Technol.*, vol. 132, no. 1–2, pp. 193–196, 2006, doi: 10.1016/j.mseb.2006.02.019.

[185] X. Gong, X. Wang, Z. Jones, K. Cooper, V. Cole, and K. Chou, “Characterization of Microstructure and Mechanical Property of Inconel 718 from Selective Laser Melting,” in *ASME 2015 Internaltional Manufacturing Science and Engineering Conference*, 2015, pp. 1–7.

[186] T. Antonsson and H.Fredriksson, “Effect of cooling rate on the solidification of INCONEL 718,” *Metall. Mater. Trans. B*, vol. 36B, pp. 85–96, 2005, doi: 10.1007/bf03024544.

[187] K. Gruber, R. Dziedzic, B. Kuźnicka, B. Madejski, and M. Malicki, “Impact of high temperature stress relieving on final properties of Inconel 718 processed by laser powder bed fusion,” *Mater. Sci. Eng. A*, vol. 813, no. March, 2021, doi: 10.1016/j.msea.2021.141111.

[188] N. C. Ferreri, S. C. Vogel, and M. Knezevic, “Determining volume fractions of γ, γ′, γ″, δ, and MC-carbide phases in Inconel 718 as a function of its processing history using an advanced neutron diffraction procedure,” *Mater. Sci. Eng. A*, vol. 781, no. January, p. 139228, 2020, doi: 10.1016/j.msea.2020.139228.

[189] D. A. Lesyk, S. Martinez, O. O. Pedash, V. V. Dzhemelinskyi, and A. Lamikiz, “Porosity and surface defects characterization of hot isostatically pressed Inconel 718 alloy turbine blades printed by 3D laser metal fusion technology,” *MRS Adv.*, no. 0123456789, 2022, doi: 10.1557/s43580-021-00187-x.

[190] Y. J. Kang, S. Yang, Y. K. Kim, B. AlMangour, and K. A. Lee, “Effect of post-treatment on the microstructure and high-temperature oxidation behaviour of additively manufactured inconel 718 alloy,” *Corros. Sci.*, vol. 158, no. June, p. 108082, 2019, doi: 10.1016/j.corsci.2019.06.030.

[191] J. Schneider, B. Lund, and M. Fullen, “Effect of heat treatment variations on the mechanical properties of Inconel 718 selective laser melted specimens,” *Addit. Manuf.*, vol. 21, no. December 2017, pp. 248–254, 2018, doi: 10.1016/j.addma.2018.03.005.

[192] V. A. Popovich, E. V. Borisov, A. A. Popovich, V. S. Sufiiarov, D. V. Masaylo, and L. Alzina, “Impact of heat treatment on mechanical behaviour of Inconel 718 processed with tailored microstructure by selective laser melting,” *Mater. Des.*, vol. 131, no. January, pp. 12–22,

2017, doi: 10.1016/j.matdes.2017.05.065.

[193] S. Zhang *et al.*, “Precipitation behavior of δ phase and its effect on stress rupture properties of selective laser-melted Inconel 718 superalloy,” *Compos. Part B Eng.*, vol. 224, no. June, p. 109202, 2021, doi: 10.1016/j.compositesb.2021.109202.

[194] F. Liu, F. Lyu, F. Liu, X. Lin, and C. Huang, “Laves phase control of inconel 718 superalloy fabricated by laser direct energy deposition via ı aging and solution treatment,” *J. Mater. Res. Technol.*, vol. 9, no. 5, pp. 9753–9765, 2020, doi: 10.1016/j.jmrt.2020.06.061.

[195] Y. Zhao, K. Li, M. Gargani, and W. Xiong, “A comparative analysis of Inconel 718 made by additive manufacturing and suction casting: Microstructure evolution in homogenization,” *Addit. Manuf.*, vol. 36, pp. 17–22, 2020, doi: 10.1016/j.addma.2020.101404.

[196] F. Liu, X. Lin, G. Yang, M. Song, J. Chen, and W. Huang, “Microstructure and residual stress of laser rapid formed Inconel 718 nickel-base superalloy,” *Opt. Laser Technol.*, vol. 43, no. 1, pp. 208–213, 2011, doi: 10.1016/j.optlastec.2010.06.015.

[197] D. A. Porter, K. E. Easterling, and M. Y. Sherif, *Phase Transformations in Metals and Alloys*, 3rd Editio. CRC Press, 2009.

[198] A. S. for T. and M. I. (ASTM), “E 8/E 8M – 08: Standard Test Methods for Tension Testing of Metallic Materials,” 2008. [Online]. Available: http://www.astm.org/Standards/E8.htm

[199] T. Trosch, J. Strößner, R. Völkl, and U. Glatzel, “Microstructure and mechanical properties of selective laser melted Inconel 718 compared to forging and casting,” *Mater. Lett.*, vol. 164, pp. 428–431, 2016, doi: 10.1016/j.matlet.2015.10.136.

[200] R. E. Reed-Hill, “Chapter 20 - Creep,” in *Physical Metallurgy Principles*, Litton Educational Publishin, 1973, pp. 840–850.

[201] Z. Xu, J. W. Murray, C. J. Hyde, and A. T. Clare, “Effect of post processing on the creep performance of laser powder bed fused Inconel 718,” *Addit. Manuf.*, vol. 24, no. October, pp. 486–497, 2018, doi: 10.1016/j.addma.2018.10.027.

[202] S. Wu *et al.*, “Improving creep property of additively manufactured Inconel 718 through specifically-designed post heat treatments,” *Mater. Sci. Eng. A*, vol. 857, no. August, pp. 15–17, 2022, doi: 10.1016/j.msea.2022.144047.

[203] J. J. Shi *et al.*, “Microstructure and creep anisotropy of Inconel 718 alloy processed by selective laser melting,” *Mater. Sci. Eng. A*, vol. 805, no. June 2020, 2021, doi:

10.1016/j.msea.2020.140583.

[204] M. F. Ashby, H. Shercliff, and D. Cebon, “Running hot: using materials at high temperatures,” in *Materials: Engineering, Science, Processing and Design*, Elsevier Science, 2023, pp. 276–309.

[205] M. Pröbstle *et al.*, “Superior creep strength of a nickel-based superalloy produced by selective laser melting,” *Mater. Sci. Eng. A*, vol. 674, pp. 299–307, 2016.

[206] Q. Wang *et al.*, “Evolution of microstructural characteristics during creep behavior of Inconel 718 alloy,” *Mater. Sci. Eng. A*, vol. 857, no. August, 2022.

[207] Y. Kuo, S. Horikawa, and K. Kakehi, “Effects of build direction and heat treatment on creep properties of Ni-base superalloy built up by additive manufacturing,” *Scr. Mater.*, vol. 129, pp. 74–78, 2017, doi: 10.1016/j.scriptamat.2016.10.035.

[208] A. S. Khanna, “High Temperature Oxidation,” in *Handbook of Environmental Degradation of Materials*, 2012, pp. 127–194.

[209] J. Young, “Chapter 1 The Nature of High Temperature Oxidation,” in *High Temperature Oxidation and Corrosion of Metals*, vol. 1, no. C, 2008, pp. 1–27. doi: 10.1016/S1875-9491(08)00001-X.

[210] S. Kathiravan, G. Saravanan, A. M. K. Kirubaharan, and R. Ranjan, “Study of oxide layer formation on Inconel 718 during isothermal oxidation between 800 ◦ C to 1200 ◦ C in hot air,” *Ceram. Int.*, vol. 48, no. August, pp. 36012–36020, 2022.

[211] R. Wang, D. Gu, H. Zhang, and M. Guo, “High temperature oxidation behavior of laser powder bed fusion printed WC/Inconel 718 composites,” *J. Mater. Sci.*, vol. 57, no. 29, pp. 14119–14134, 2022, doi: 10.1007/s10853-022-07520-1.

[212] J. J. Valencia and P. N. Quested, “Thermophysical Properties,” 2008. doi: 10.1361/asmhba0005240.

[213] M. Calandri *et al.*, “Solution Treatment Study of Inconel 718 Produced by SLM Additive Technique in View of the Oxidation Resistance,” *Adv. Eng. Mater.*, vol. 20, no. 11, pp. 1–16, 2018, doi: 10.1002/adem.201800351.

[214] T. Sanviemvongsak, D. Monceau, C. Desgranges, and B. Macquaire, “Intergranular oxidation of Ni-base alloy 718 with a focus on additive manufacturing,” *Corros. Sci.*, vol. 170, no. April, 2020, doi: 10.1016/j.corsci.2020.108684.

[215] Y. Luo, B. Zhang, Z. Song, C. Li, G. Chen, and G.-P. Zhang, “A comparative investigation of long-term oxidation behavior of selective laser melting – fabricated Inconel 718 at 650 ° C,” *J. Mater. Res.*, vol. 35, no. 15, 2020, doi: 10.1557/jmr.2020.98.

[216] D. J. Young, “Chapter 5 - Oxidation of Alloys 1: Single Phase Scales,” in *High Temperature Oxidation and Corrosion of Metals*, vol. 1, no. 1, 2008, pp. 111–125.

[217] M. Beyhaghi, M. Rouhani, J. Hobley, and Y. Jeng, “In-situ and ex-situ comparison of oxidation of Inconel 718 manufactured by selective laser melting and conventional methods up to 650 ◦ C,” *Appl. Surf. Sci.*, vol. 569, no. August, p. 151037, 2021, doi: 10.1016/j.apsusc.2021.151037.

[218] L. Li *et al.*, “Influence of building direction on the oxidation behavior of Inconel 718 alloy fabricated by additive manufacture of electron beam melting,” *Materials (Basel).*, vol. 11, no. 12, 2018, doi: 10.3390/ma11122549.

[219] J. Hong, N. Park, S. Kim, and C. Kang, “Microstructures of Oxidized Primary Carbides on Superalloy Inconel 718,” *Mater. Sci. Forum*, vol. 502, no. December 2005, pp. 249–256, 2005, doi: 10.4028/www.scientific.net/MSF.502.249.

[220] E. Sadegimeresht *et al.*, “Isothermal Oxidation Behavior of EBM-Additive Manufactured Alloy 718,” in *Proceedings of the 9th International Symposium on Superalloy 718 & Derivatives: Energy, Aerospace, and Industrial Applications*, 2018, pp. 219–240.

[221] M. Beyhaghi, M. Rouhani, J. Hobley, and Y. R. Jeng, “In-situ and ex-situ comparison of oxidation of Inconel 718 manufactured by selective laser melting and conventional methods up to 650 °C,” *Appl. Surf. Sci.*, vol. 569, no. April, p. 151037, 2021, doi: 10.1016/j.apsusc.2021.151037.

[222] Z. Luo and Y. Zhao, “Efficient thermal finite element modeling of selective laser melting of Inconel 718,” *Comput. Mech.*, vol. 65, no. 3, pp. 763–787, 2020, doi: 10.1007/s00466-019-01794-0.

[223] R. E. Reed-Hill, “Fracture,” in *Physical Metallurgy Principles*, Second Edi., Litton Educational Publishing Inc, 1973, pp. 809–824.

[224] A. R. Balachandramurthi, J. Moverare, N. Dixit, and R. Pederson, “Influence of defects and as-built surface roughness on fatigue properties of additively manufactured Alloy 718,” *Mater. Sci. Eng. A*, vol. 735, no. June, pp. 463–474, 2018, doi: 10.1016/j.msea.2018.08.072.

[225] L. Sheridan, O. E. Scott-Emuakpor, T. George, and J. E. Gockel, “Relating porosity to fatigue

failure in additively manufactured alloy 718," *Mater. Sci. Eng. A*, vol. 727, no. April, pp. 170–176, 2018, doi: 10.1016/j.msea.2018.04.075.

[226] K. Solberg, D. Wan, and F. Berto, "Fatigue assessment of as-built and heat-treated Inconel 718 specimens produced by additive manufacturing including notch effects," *Fatigue Fract. Eng. Mater. Struct.*, vol. 43, no. 10, pp. 2326–2336, 2020, doi: 10.1111/ffe.13300.

[227] R. Konečná, G. Nicoletto, L. Kunz, and A. Bača, "Microstructure and directional fatigue behavior of Inconel 718 produced by selective laser melting," *Procedia Struct. Integr.*, vol. 2, pp. 2381–2388, 2016, doi: 10.1016/j.prostr.2016.06.298.

[228] D. B. Witkin, D. N. Patel, and G. E. Bean, "Notched fatigue testing of Inconel 718 prepared by selective laser melting," *Fatigue Fract. Eng. Mater. Struct.*, vol. 42, no. 1, pp. 166–177, 2019, doi: 10.1111/ffe.12880.

[229] C. Tan *et al.*, "Additive manufacturing of steel–copper functionally graded material with ultrahigh bonding strength," *J. Mater. Sci. Technol.*, vol. 72, pp. 217–222, 2021, doi: 10.1016/j.jmst.2020.07.044.

[230] G. H. Loh, E. Pei, D. Harrison, and M. D. Monzón, "An overview of functionally graded additive manufacturing," *Addit. Manuf.*, vol. 23, no. June, pp. 34–44, 2018, doi: 10.1016/j.addma.2018.06.023.

[231] S. Tammas-Williams and I. Todd, "Design for additive manufacturing with site-specific properties in metals and alloys," *Scr. Mater.*, vol. 135, pp. 105–110, 2017, doi: 10.1016/j.scriptamat.2016.10.030.

[232] K. A. Mumtaz and N. Hopkinson, "Laser melting functionally graded composition of Waspaloy® and Zirconia powders," *J. Mater. Sci.*, vol. 42, no. 18, pp. 7647–7656, 2007, doi: 10.1007/s10853-007-1661-3.

[233] R. Esmaeilizadeh *et al.*, "Customizing mechanical properties of additively manufactured Hastelloy X parts by adjusting laser scanning speed," *J. Alloys Compd.*, vol. 812, p. 152097, 2020, doi: 10.1016/j.jallcom.2019.152097.

[234] V. A. Popovich, E. V. Borisov, V. S. Sufiyarov, and A. A. Popovich, "Tailoring the Properties in Functionally Graded Alloy Inconel 718 Using Additive Technologies," *Met. Sci. Heat Treat.*, vol. 60, no. 11–12, pp. 701–709, 2019, doi: 10.1007/s11041-019-00343-z.

[235] V. Popovich, E. Borisov, T. Riemslag, and V. Sufiiarov, "Creep and Thermomechanical Fatigue

of Functionally Graded Inconel 718 Produced by Additive Manufacturing," in *TMS 2018 - 147th Annual Meeting and Exhibition*, 2018, no. February. doi: 10.1007/978-3-319-72526-0.

[236] S. H. Sun, T. Ishimoto, K. Hagihara, Y. Tsutsumi, T. Hanawa, and T. Nakano, "Excellent mechanical and corrosion properties of austenitic stainless steel with a unique crystallographic lamellar microstructure via selective laser melting," *Scr. Mater.*, vol. 159, pp. 89–93, 2019, doi: 10.1016/j.scriptamat.2018.09.017.

[237] S. Gao, R. Liu, R. Huang, X. Song, and M. Seita, "A hybrid directed energy deposition process to manipulate microstructure and properties of austenitic stainless steel," *Mater. Des.*, vol. 213, p. 110360, 2022, doi: 10.1016/j.matdes.2021.110360.

[238] F. Liu, X. Lin, G. Yang, M. Song, J. Chen, and W. Huang, "Microstructure and residual stress of laser rapid formed Inconel 718 nickel-base superalloy," *Opt. Laser Technol.*, vol. 43, no. 1, pp. 208–213, 2011, doi: 10.1016/j.optlastec.2010.06.015.

[239] E. Hernández-Nava, P. Mahoney, C. J. Smith, J. Donoghue, I. Todd, and S. Tammas-Williams, "Additive manufacturing titanium components with isotropic or graded properties by hybrid electron beam melting/hot isostatic pressing powder processing," *Sci. Rep.*, vol. 9, no. 1, pp. 1–11, 2019, doi: 10.1038/s41598-019-40722-3.

[240] Y. L. Kuo and K. Kakehi, "Influence of powder surface contamination in the Ni-based superalloy alloy718 fabricated by selective laser melting and hot isostatic pressing," *Metals (Basel).*, vol. 7, no. 9, 2017, doi: 10.3390/met7090367.

[241] D. Jiang, Y. Tian, Y. Zhu, S. Huang, and A. Huang, "On the microstructure and tensile property of core-shell structured nickel-based superalloy part produced by laser powder bed fusion and hot isostatic pressing," *Mater. Sci. Eng. A*, vol. 870, no. February, p. 144833, 2023, doi: 10.1016/j.msea.2023.144833.

[242] R. Xin, J. Luo, and Q. Ma, "Effect of parameters on internal crack healing in 30Cr2Ni4MoV steel for 600-ton ultra-super ingots," *Metals (Basel).*, vol. 7, no. 4, pp. 1–12, 2017, doi: 10.3390/met7040149.

[243] RAECO Detect Measure Analyse, "Refractive Index." http://www.raeco.com/training/refractive-index-values.htm

[244] A. S. Agazhanov, D. A. Samoshkin, and Y. M. Kozlovskii, "Thermophysical properties of Inconel 718 alloy," *J. Phys. Conf. Ser.*, vol. 1382, no. 1, 2019, doi: 10.1088/1742-6596/1382/1/012175.

[245] N. Raghavan *et al.*, “Numerical modeling of heat-transfer and the influence of process parameters on tailoring the grain morphology of IN718 in electron beam additive manufacturing,” *Acta Mater.*, vol. 112, pp. 303–314, 2016, doi: 10.1016/j.actamat.2016.03.063.

[246] J. Metelkova, Y. Kinds, K. Kempen, C. de Formanoir, A. Witvrouw, and B. Van Hooreweder, “On the influence of laser defocusing in Selective Laser Melting of 316L,” *Addit. Manuf.*, vol. 23, no. April, pp. 161–169, 2018, doi: 10.1016/j.addma.2018.08.006.

[247] T. D. McLouth *et al.*, “The effect of laser focus shift on microstructural variation of Inconel 718 produced by selective laser melting,” *Mater. Des.*, vol. 149, pp. 205–213, 2018, doi: 10.1016/j.matdes.2018.04.019.

[248] Aconity, “Aconity Mini Laser Quality Measurement - 500096-2.”

[249] Q. Zhong, K. Wei, Z. Lu, X. Yue, T. Ouyang, and X. Zeng, “High power laser powder bed fusion of Inconel 718 alloy: Effect of laser focus shift on formability, microstructure and mechanical properties,” *J. Mater. Process. Technol.*, vol. 311, no. August 2022, p. 117824, 2023, doi: 10.1016/j.jmatprotec.2022.117824.

[250] K. S. Ramani, C. He, Y. L. Tsai, and C. E. Okwudire, “SmartScan: An intelligent scanning approach for uniform thermal distribution, reduced residual stresses and deformations in PBF additive manufacturing,” *Addit. Manuf.*, vol. 52, no. October 2021, p. 102643, 2022, doi: 10.1016/j.addma.2022.102643.

[251] M. Qin *et al.*, “Adaptive toolpath generation for distortion reduction in laser powder bed fusion process,” *Addit. Manuf.*, vol. 64, no. January, p. 103432, 2023, doi: 10.1016/j.addma.2023.103432.

[252] M. Ester, H.-P. Kriegel, J. Sander, and X. Xu, “Density-Based Algorithm for Discovering Clusters in Large Spatial Databases with Noise,” *KDD-96*, vol. 2, pp. 635–654, 2009, doi: 10.1016/B978-044452701-1.00067-3.

[253] Fiji, “Auto Threshold.” https://imagej.net/plugins/auto-threshold

[254] G. Sanchez Chavez, S. Farid Estefen, T. Gurova, A. Leontiev, L. Silva Gomes, and S. Bottega Peripolli, “Redistribution of grain boundary misorientation and residual stresses of thermomechanically simulated welding in an intercritically reheated coarse grained heat affected zone,” *Metals (Basel).*, vol. 11, no. 11, 2021, doi: 10.3390/met11111850.

[255] S. I. Wright, M. M. Nowell, and D. P. Field, "A review of strain analysis using electron backscatter diffraction," *Microsc. Microanal.*, vol. 17, no. 3, pp. 316–329, 2011, doi: 10.1017/S1431927611000055.

[256] S. Holland, X. Wang, X. Y. Fang, Y. B. Guo, F. Yan, and L. Li, "Grain boundary network evolution in Inconel 718 from selective laser melting to heat treatment," *Mater. Sci. Eng. A*, vol. 725, no. April, pp. 406–418, 2018, doi: 10.1016/j.msea.2018.04.045.

[257] G. A. Rao, M. Kumar, M. Srinivas, and D. S. Sarma, "Effect of standard heat treatment on the microstructure and mechanical properties of hot isostatically pressed superalloy inconel 718," *Mater. Sci. Eng. A*, vol. 355, no. 1–2, pp. 114–125, 2003, doi: 10.1016/S0921-5093(03)00079-0.

[258] A. P. Shabanov, "Mechanism of Fatigue-Crack Growth Under Compressive External Stresses," *J. Appl. Mech. Tech. Phys.*, vol. 46, no. 6, pp. 861–866, 2005, doi: 0021-8944/05/4606-0861.

[259] H. Yu, X. Liu, X. Li, and A. Godbole, "Crack healing in a low-carbon steel under hot plastic deformation," *Metall. Mater. Trans. A Phys. Metall. Mater. Sci.*, vol. 45, no. 2, pp. 1001–1009, 2014, doi: 10.1007/s11661-013-2049-4.

[260] W. M. Tucho and V. Hansen, "Studies of post-fabrication heat treatment of L-PBF-inconel 718: Effects of hold time on microstructure, annealing twins, and hardness," *Metals (Basel).*, vol. 11, no. 2, pp. 1–20, 2021, doi: 10.3390/met11020266.

[261] W. Duan, Y. Yin, J. Zhou, M. Wang, H. Nan, and P. Zhang, "Dynamic research on Ti6Al4V powder HIP densification process based on intermittent experiments," *J. Alloys Compd.*, vol. 771, pp. 489–497, 2019, doi: 10.1016/j.jallcom.2018.08.261.

[262] Y. C. Lin *et al.*, "EBSD analysis of evolution of dynamic recrystallization grains and δ phase in a nickel-based superalloy during hot compressive deformation," *Mater. Des.*, vol. 97, pp. 13–24, 2016, doi: 10.1016/j.matdes.2016.02.052.

[263] W. Yinmin, C. Mingwei, Z. Fenghua, and M. En, "High tensile ductility in a nanostructured metal," *Nature*, vol. 419, no. 6910, pp. 912–914, 2002, [Online]. Available: http://dx.doi.org/10.1038/nature01133

[264] M. Zouari, R. E. Logé, and N. Bozzolo, "In situ characterization of inconel 718 post-dynamic recrystallization within a scanning electron microscope," *Metals (Basel).*, vol. 7, no. 266, 2017, doi: 10.3390/met7110476.

[265] D. Zhang, W. Niu, X. Cao, and Z. Liu, “Effect of standard heat treatment on the microstructure and mechanical properties of selective laser melting manufactured Inconel 718 superalloy,” *Mater. Sci. Eng. A*, vol. 644, pp. 32–40, 2015, doi: 10.1016/j.msea.2015.06.021.

[266] G. A. Rao, M. Srinivas, and D. S. Sarma, “Effect of oxygen content of powder on microstructure and mechanical properties of hot isostatically pressed superalloy Inconel 718,” *Mater. Sci. Eng. A*, vol. 435–436, pp. 84–99, 2006, doi: 10.1016/j.msea.2006.07.053.

[267] X. Tian, J. Wu, Z. Lu, R. Yang, and L. Xu, “Effect of powder size segregation on the mechanical properties of hot isostatic pressing Inconel 718 alloys,” *J. Mater. Res. Technol.*, vol. 21, pp. 84–96, 2022, doi: 10.1016/j.jmrt.2022.09.009.

[268] I. Manna, S. K. Pabi, and W. Gust, “Discontinuous reactions in solids,” *Int. Mater. Rev.*, vol. 46, no. 2, pp. 53–91, 2001, doi: 10.1179/095066001101528402.

[269] E. J. Pickering *et al.*, “Grain-boundary precipitation in Allvac 718Plus,” *Acta Mater.*, vol. 60, no. 6–7, pp. 2757–2769, 2012, doi: 10.1016/j.actamat.2012.01.042.

[270] High Temp Metals, “INCONEL 718 TECHNICAL DATA.” https://www.hightempmetals.com/techdata/hitempInconel718data.php

[271] ASM Aerospace Specification Metals Inc., “Special Metals INCONEL® Alloy 718.” http://asm.matweb.com/search/SpecificMaterial.asp?bassnum=NINC34%0A

[272] Y. Zhai, D. A. Lados, E. J. Brown, and G. N. Vigilante, “Understanding the microstructure and mechanical properties of Ti-6Al-4V and Inconel 718 alloys manufactured by Laser Engineered Net Shaping,” *Addit. Manuf.*, vol. 27, no. March, pp. 334–344, 2019, doi: 10.1016/j.addma.2019.02.017.

[273] L. Chang, W. Sun, Y. Cui, F. Zhang, and R. Yang, “Effect of heat treatment on microstructure and mechanical properties of the hot-isostatic-pressed Inconel 718 powder compact,” *J. Alloys Compd.*, vol. 590, pp. 227–232, 2014, doi: 10.1016/j.jallcom.2013.12.107.

[274] J. W. X. Wo, H. T. Pang, A. S. Wilson, M. C. Hardy, and H. J. Stone, “The Isothermal Oxidation of a New Polycrystalline Turbine Disk Ni-Based Superalloy at 800 °C and Its Modification with Pre-oxidation,” *Metall. Mater. Trans. A Phys. Metall. Mater. Sci.*, vol. 54, no. 5, pp. 1946–1960, 2023, doi: 10.1007/s11661-022-06896-8.

[275] S. Parizia *et al.*, “Effect of heat treatment on microstructure and oxidation properties of Inconel 625 processed by LPBF,” *J. Alloys Compd.*, vol. 846, p. 156418, 2020, doi:

10.1016/j.jallcom.2020.156418.

Appendix A

This appendix contains the secondary electron SEM, and the corresponding thresholded, images for all the samples analysed as part of Chapter 7. All images outlined in red are the keyhole sample, all images outlined in orange are of the Sphere Bulk, and all images outlined in blue are of the Sphere Void.

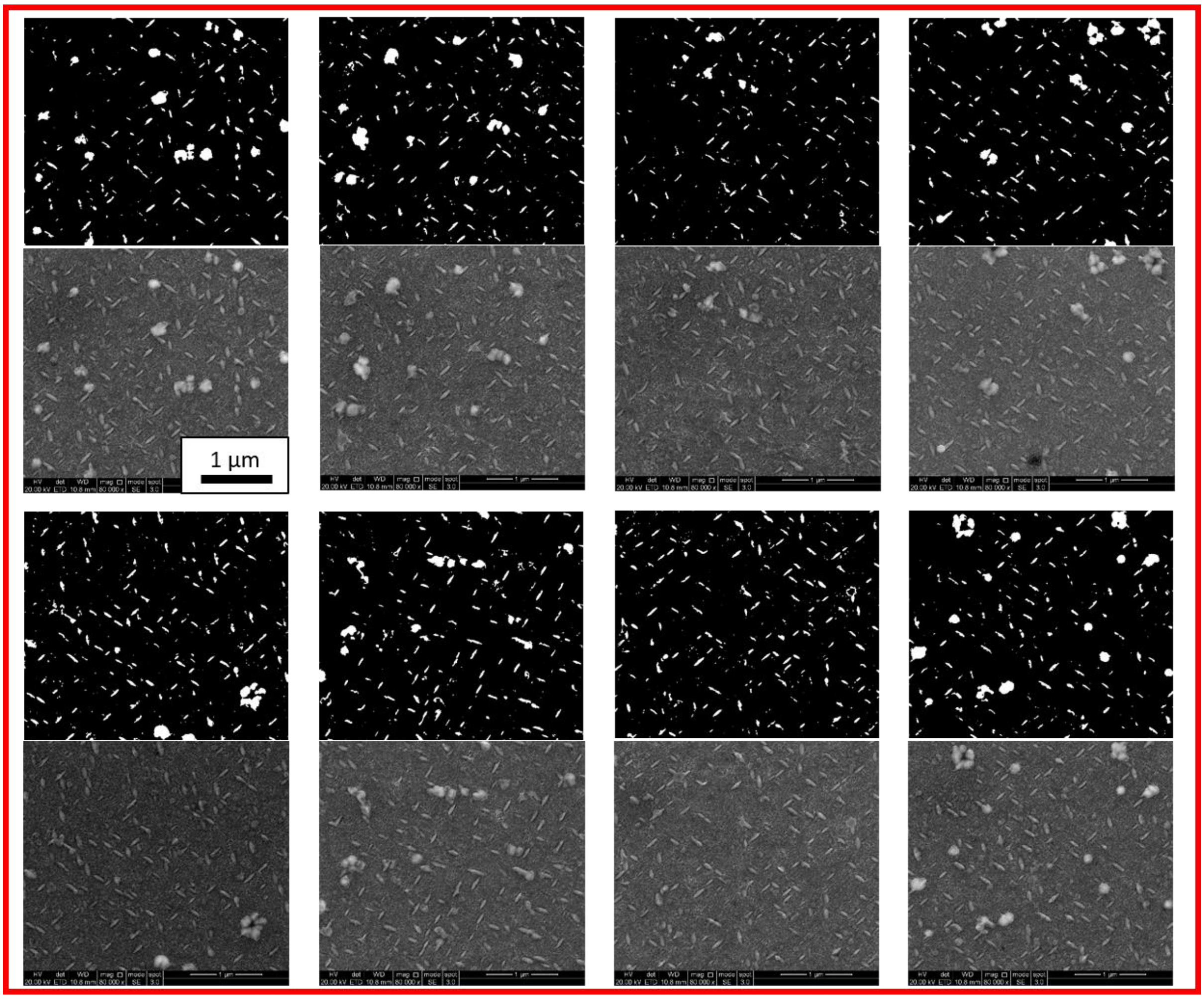

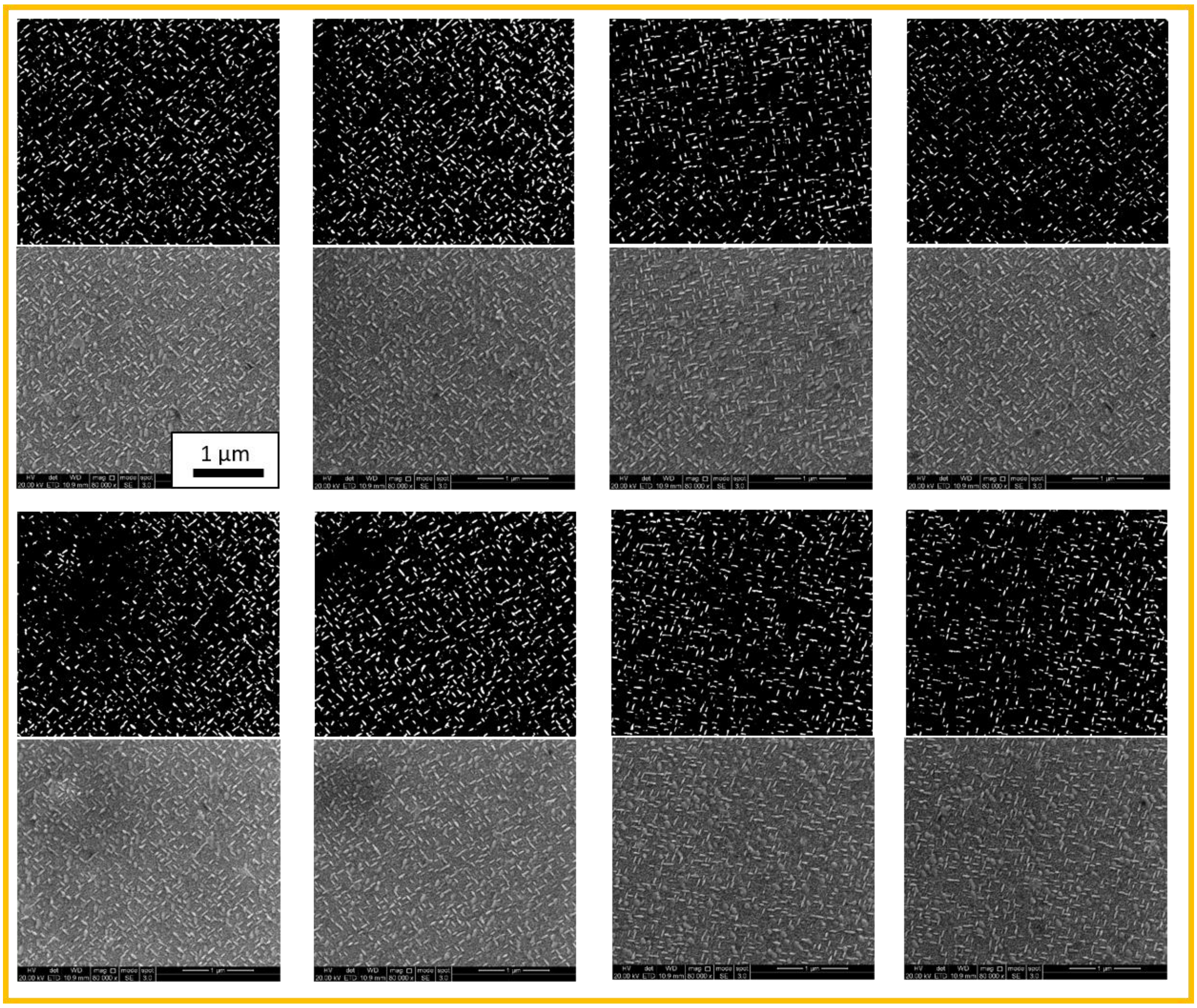
1 µm

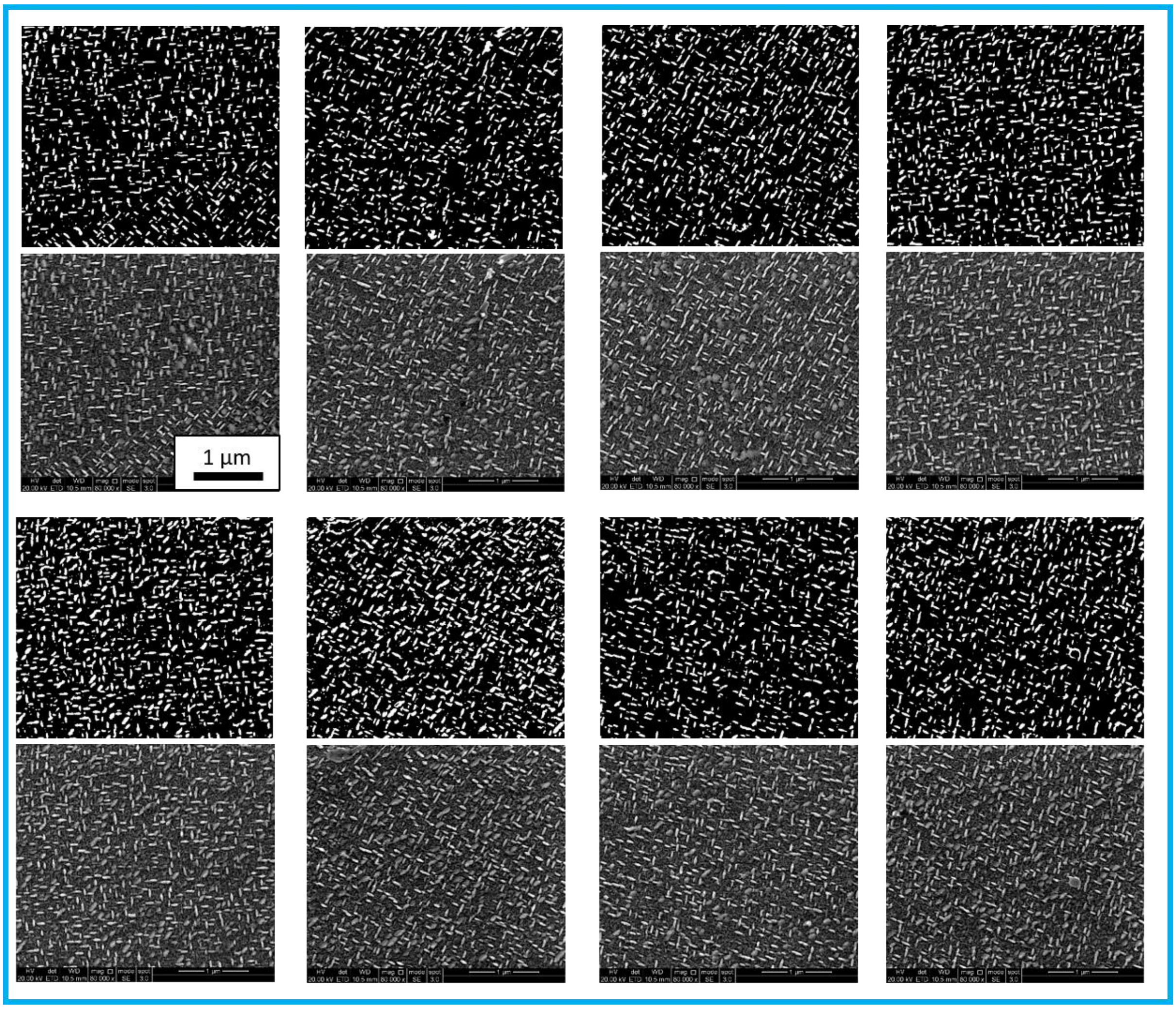
1 µm
HV det WD mag mode spot
20.00 kV ETD 10.5 mm 80 000 x SE 3.0
1 µm